The Dissertation Committee for Swagata Das
certifies that this is the approved version of the following dissertation:

Fault Location and Analysis in Transmission and Distribution Networks

Committee:

Surya Santoso, Supervisor

Ross Baldick

Michael F. Becker

Matt Hersh

Thomas A. Short

Fault Location and Analysis in Transmission and Distribution Networks

by

Swagata Das, B.Tech, M.S.E

DISSERTATION

Presented to the Faculty of the Graduate School of

The University of Texas at Austin

in Partial Fulfillment

of the Requirements

for the Degree of

DOCTOR OF PHILOSOPHY

THE UNIVERSITY OF TEXAS AT AUSTIN

May 2015

Dedicated to my parents and to the loving memory of my grandparents.

Acknowledgments

I wish to thank my advisor, Dr. Surya Santoso, for his invaluable guidance and support throughout my years at UT-Austin. Working under him has been an absolute honor and privilege. Everything that I know about power systems, technical writing, and technical presentation, I have learned from him. Thank you for believing in me and giving me this incredible opportunity; I am very grateful and very proud to be your student.

I would like to thank Dr. Ross Baldick, Dr. Matt Hersh, Dr. Michael Becker, and Mr. Thomas A. Short for taking time off their busy schedules and serving on my dissertation committee. Their comments and suggestions have been invaluable towards completing this dissertation.

My sincere thanks to Electric Power Research Institute for providing financial support and actual fault event data used in this research.

I am also very grateful to all the staff members at the Electrical and Computer Engineering Department and the International Office. Special thanks to Melanie Gulick and Melody Singleton for being so encouraging and helpful all the time.

Many thanks go out to my fellow labmates with whom I have had a lot of fun over the last five years. Thank you, Neeraj Karnik, Thekla Boutsika, Pisitpol Chirapongsananurak, Anamika Dubey, Min Lwin, David Jonsson, Tuan Ngo, Kyung Woo Min, Jules Campbell, Yichuan Niu, Suma Basu, and Jonas Traphöner.

Finally, I would like to express my sincere gratitude to my parents for their love, encouragement, support, and immense patience.

Fault Location and Analysis in Transmission and Distribution Networks

Swagata Das, Ph.D.
The University of Texas at Austin, 2015

Supervisor: Surya Santoso

Short-circuit faults are inevitable on transmission and distribution networks. In an effort to provide system operators with an accurate location estimate and reduce service restoration times, several impedance-based fault location algorithms have been developed for transmission and distribution networks. Each algorithm has specific input data requirements and make certain assumptions that may or may not hold true in a particular scenario. Identifying the best fault location approach, therefore, requires a thorough understanding of the working principle behind each algorithm. Moreover, impedance-based fault location algorithms require voltage and current phasors, captured by intelligent electronic devices (IEDs), to estimate the fault location. Unfortunately, voltage phasors are not always available due to operational constraints or equipment failure. Furthermore, impedance-based fault location algorithms assume a radial distribution feeder. With increased interconnection of distributed generators (DGs) to the feeder, this assumption is violated. DGs also contribute to the fault and severely compromise the accuracy of location estimates. In addition, the variability of certain DGs such as the fixed-speed wind turbine can alter fault current levels and result in relay misoperations. Finally, data recorded by IEDs during a fault contain a wealth of information and are prime for use in other applications that improve power system reliability.

Based on the above background, the first objective of this dissertation is to present a comprehensive theory of impedance-based fault location algorithms. The contributions lie in clearly specifying the input data requirement of each algorithm and identifying their strengths and weaknesses. The following criteria are recommended for selecting the most suitable fault location algorithm: (a) data availability and (b) application scenario. The second objective is to develop fault location algorithms that use only the current to estimate the fault location. The simple but powerful algorithms allow system operators to locate faults even in the absence of voltage data. The third objective is to investigate the shortcomings of existing fault location algorithms when DGs are interconnected to the distribution feeder and develop an improved solution. A novel algorithm is proposed that require only the voltage and current phasors at the substation, is straightforward to implement, and is capable of locating all fault types. The fourth objective is to examine the effects of wind speed variation on the maximum and minimum fault current levels of a wind turbine and investigate the impact on relay settings. Contributions include developing an accurate time-domain model of a fixed-speed wind turbine with tower shadow and wind shear and verifying that the variation in wind speed does not violate relay settings calculated using the IEC 60909-0 Standard. The final objective is to exploit intelligent electronic device data for improving power system reliability. Contributions include validating the zero-sequence impedance of multi-terminal transmission lines with unsynchronized measurements, reconstructing the sequence of events, assessing relay performance, estimating the fault resistance, and verifying the accuracy of the system model.

Overall, the research presented in this dissertation aims to describe the theory of impedance-based fault location, identify the sources of fault location error, propose solutions to overcome those error sources, and share lessons learned from analyzing intelligent electronic device data. The research is expected to reduce service downtime, prevent protection system misoperations, and improve power quality.

Table of Contents

List of Tables

List of Figures

Chapter 1

Introduction

This chapter outlines the research carried out in this dissertation to locate and analyze transmission and distribution faults using intelligent electronic device data. It begins with an overview of existing techniques to analyze and compute the location of faults in Section 1.1. The shortcomings of these techniques are identified, and the motivation to develop improved solutions is justified. Next, the research objectives are explicitly stated in Section 1.2. The original research contributions along with the resulting publications are summarized in Section 1.3.

1.1 Background and Motivation

Despite the recent efforts to modernize the electrical grid, short-circuit faults are inevitable on overhead transmission and distribution feeders. Faults are caused by animals, trees or foreign objects coming in contact with the overhead line, lightning strikes during inclement weather, or insulation failure in power system equipment. In the event of a fault, protective devices operate to interrupt the fault current and limit the damage to power system equipment. Depending on the nature of the fault (temporary or permanent), and the utility fault clearing practice, customers downstream from the protective device may experience momentary or sustained interruptions [11]. In either case, the operation of sensitive customer loads is completely disrupted. In fact, a study published by the Lawrence Berkeley National Laboratory in 2006 conclude that power outages cost the US economy $80 billion per year [12]. Therefore, it is crucial for system

operators to find the fault location as quickly as possible so as to perform maintenance repair and restore power back to the customers.

Guidelines for Choosing the Most Suitable Fault Location Algorithm

Utilities commonly use impedance-based fault location algorithms to track down the exact location of a fault [13, 14]. These fault-locating algorithms are straightforward to implement and yield reasonable location estimates. Voltage and current waveforms captured by digital relays, digital fault recorders, and other intelligent electronic devices (IEDs) during a fault are used to estimate the impedance between the IED device and location of the fault. Given the line impedance in ohms, the per-unit distance to the fault can be easily obtained. A number of impedance-based fault location algorithms have been developed for transmission and distribution network applications [4, 13–21]. Fault-locating algorithms using data captured at one end of the line are commonly referred to as one-ended algorithms while those using data captured at both ends of a line are referred to as two-ended algorithms. Each algorithm has specific input data requirements and makes certain assumptions when computing the distance to a fault. These assumptions may or may not hold true in a particular fault location scenario. Put another way, no single fault-locating algorithm works best in several different fault location scenarios. Choosing the best fault-locating approach from such a wide selection of impedance-based fault location algorithms is, therefore, an overwhelming task and requires a detailed understanding of the working principle behind each algorithm.

Fault Location with Current Measurements Only

Impedance-based fault location algorithms require the input of the voltage and current phasors to estimate the distance to a fault. Unfortunately, most relays in distribution networks are of the overcurrent type and record only the current. Voltage

measurements are, thus, simply not recorded. SEL-551 is an example of such an over-current distribution relay [8]. Voltage measurements can also be missing when a fuse protecting the voltage transformer blows and results in a loss-of-potential [22]. In such scenarios, existing impedance-based algorithms cannot be used to estimate the fault location. A similar problem explored in [23] and [24] develops current-only algorithms that are valid for locating single line-to-ground faults only. Authors in [25] develop current-only algorithms for a transmission network that require the fault current in one or more branches (not a single point measurement). The algorithms are complex and have been evaluated by a trivial four-bus simulation model. Based on this discussion, it is essential to develop fault location algorithms that use only the current to estimate the distance to a fault. The current-only algorithms must be straightforward to implement, capable of locating all fault types, and validated with actual fault event data.

Fault Location Error due to DGs and the Need for Improved Solutions

Existing impedance-based fault location algorithms assume a radial distribution feeder where the power flows unidirectionally from the substation to the load. With the integration of distributed generators (DGs) to the distribution circuit, however, distribution feeders are no longer radial. Short-circuit current to a fault comes from two sources, the utility substation and the distributed generators. Since the DG penetration level is expected to increase over the next few years, neglecting the fault current contribution from DGs will certainly compromise the accuracy of location estimates. Algorithms proposed by [26–28] aim to improve the fault location accuracy in the presence of DGs. Unfortunately, these algorithms require additional measurements at the DG terminal that may not be available. Authors in [29] present an interesting, but iterative approach that utilize measurements captured at the substation only. Algorithms in [30] and [31] also make use of substation measurements; however, their application

is limited to line-to-line and three-phase faults, respectively. Therefore, this discussion highlights the need to understand how DGs affect the accuracy of existing fault location algorithms and then develop an improved algorithm. The improved algorithm must be capable of locating faults with only the voltage and current waveforms at the substation, be straightforward to implement, and be successful in locating all fault types.

Impact of DGs on System Protection

Besides fault location, the presence of distributed generators can also affect the maximum and minimum fault current levels in a distribution network. The minimum fault current is used for determining the relay pickup current while the maximum fault current is used for determining the power system equipment rating [32]. Among the available DG technologies, synchronous DGs (diesel generators, gas turbines, and hydro generators) and induction DGs (fixed-speed and wide-slip wind turbines) contribute a significant fault current [33, 34]. Inverter-based DGs (photovoltaic generators, doubly-fed induction generator, and permanent magnet wind turbines), on the other hand, contribute a fault current one or two times the rated current for less than half a cycle and can be neglected. To ensure that the system protection remains well coordinated and that the maximum rating of power system equipment are not exceeded, the IEC 60909-0 Standard [32] is popularly used for calculating the minimum and maximum fault currents in networks interconnected with DGs [35]. Unfortunately, this Standard has been developed for a traditional power system with conventional generators. However, fixed-speed and wide-slip wind turbines have specific features that distinguish them from conventional generators, the fundamental difference being that the primary drive source, the wind speed, is variable and intermittent. In addition, tower shadow and wind shear also cause periodic fluctuations in the wind speed [36]. Tower shadow is the obstruction of the tower to the wind and wind shear is the variation of the wind speed

with height. The periodic fluctuations are further pronounced in a wind farm where all the wind turbines are synchronized with each other. Authors in [37, 38] conclude that the periodic variations in wind speed may have a substantial effect on short-circuit currents. But they provide no guidelines on how such wind speed variations affect the relay pickup current and equipment ratings. Based on this discussion, it is critical to investigate the effects of wind speed variation (stochastic and periodic) on the maximum and minimum fault current levels of a wind turbine and associated protection settings.

Knowledge Gained by Analyzing Intelligent Electronic Data

So far, the discussion focuses on using intelligent electronic device (IED) data to pinpoint the exact location of a fault and is only one part of the solution to improving the power system performance and reliability. Because IEDs provide a snapshot of the power system during a fault and contain a wealth of information, the second part of the effort focuses on gleaning additional information from the IED data. Knowledge gained from analyzing IED data can help system operators understand what happened, why it happened, and how to prevent it from happening again [39–41]. Momentary faults can be detected and repaired before they evolve into a system-wide blackout. Furthermore, a study by North Electric Reliability Corporation (NERC) [42] identifies relay setting error as one of the major causes of relay misoperations. Therefore, assessing relay performance is one of the major benefits of event report analysis. Any undesired operation due to incorrect settings can be identified and corrected. Even if the subject relay did not misoperate, routine analysis of events is a good practice to ensure that the relay operated with due consideration to selectivity, dependability, and security. Analysis of fault events is also helpful in evaluating the performance of circuit breakers.

Another major benefit of analyzing IED data is to validate the zero-sequence impedance of overhead transmission and distribution feeders. The zero-sequence line

impedance is a user-defined setting in distance and directional overcurrent relays [43,44], and plays an important role in system protection. An accurate value of the zero-sequence line impedance is also required by impedance-based fault location algorithms to estimate the distance to a fault. Unfortunately, the accuracy of the zero-sequence line impedance is subject to much uncertainty since it depends on earth resistivity. Although utilities use a typical value of 100 Ω-m, the earth resistivity is difficult to measure and changes with soil type, temperature, and moisture content in soils. Consequently, authors in [15] attempt to validate the zero-sequence line impedance using IED data captured at one end of the line. However, they assume a known fault location and a zero fault resistance. To avoid making such assumptions, authors in [43] use synchronized IED data from both ends of a transmission line to verify the zero-sequence impedance. Because IEDs can have different sampling rates, or detect the fault at slightly different time instants, waveforms captured by IED devices at both ends of a transmission line may not be synchronized with each other [4]. Furthermore, three-terminal transmission lines are frequently used by utilities to increase operational support and meet system demand [45]. Very little work, if any, has been conducted on validating the zero-sequence line impedance of three-terminal transmission lines. Therefore, it is necessary to devise a methodology that can use unsynchronized measurements to confirm the zero-sequence impedance of two- and three-terminal transmission lines.

Voltage and current waveforms captured during a fault can also be used to estimate the fault resistance and gain insight into the root cause of a fault. Analysis of 148 fault events in utility circuits reveals that trees with a large diameter present a fault resistance greater than 20 ohms when they fall on overhead lines [46]. Animals like squirrel, birds, or snakes coming in contact with the transmission line have the least resistance while lightning induced faults have a resistance equal to the tower footing resistance. In addition to identifying the root cause of the fault, fault resistance also

plays an important role in replicating the fault in the system circuit model and verifying the model accuracy. The circuit model in PSCAD [47], CAPE [48], OpenDSS [49], and other power system software is used by system operators to conduct short-circuit studies, determine protective relay settings, and choose the maximum rating of circuit breakers and other power system equipment. Incorrect short-circuit model parameters can lead to erroneous relay settings and relay misoperations, an example of which is described in [50]. As a result, it is vital to ensure that the system model is accurate and continually updated to reflect any system additions, repair, or modifications.

1.2 Objectives

The overall objective of this dissertation is to assist system operators in tracking down the exact location of a fault with available data and in taking preventive measures to avoid system-wide blackouts and protection system misoperations. The research is expected to reduce service downtime and improve service reliability and power quality. The specific research objectives are stated below:

Objective 1: Present the Theory of Impedance-based Fault Location Algorithms and Evaluate their Sensitivity to the Sources of Fault Location Error

This objective presents the underlying theory of one-ended fault location algorithms (simple reactance, Takagi, modified Takagi, Eriksson, and Novosel *et al.* methods) and two-ended fault location algorithms (synchronized, unsynchronized, and current-only methods). IEEE C37.114 Standard [13] was used as a benchmark for determining which algorithms to evaluate. The aim is to identify the input data requirement of each algorithm, evaluate the impact of various sources of fault location error, demonstrate the application of each algorithm in locating field data, and provide recommendations for choosing the best fault-locating approach.

Objective 2: Develop Algorithms Capable of Locating Faults with Current Only

This objective develops fault location algorithms that use current data as the only input for estimating the distance to a fault. Depending on whether the current phasor or the current magnitude is available during a fault, the current-only algorithms will be developed in two parts: fault location using current phasor and fault location using current magnitude only. The developed algorithms will complement existing impedance-based fault location algorithms and will allow system operators to perform fault location even in the absence of voltage data.

Objective 3: Investigate the Effects of Distributed Generators on Impedance-based Fault Location and Develop Improved Solutions

This objective investigates the shortcomings of existing impedance-based fault location algorithms to locate faults that occur downstream from distributed generators (DGs). The goal is to understand how different factors such as DG technology, DG MVA capacity, DG interconnect transformer, tapped loads, distance between the DG unit and the fault, and fault resistance affect fault location in the presence of distributed generators. This objective also entails developing a methodology that uses the voltage and current waveform data at the substation to improve the accuracy of locating faults in distribution networks with DGs.

Objective 4: Evaluate the Impact of Distributed Generators on Relay Settings

This objective involves evaluating the effects of wind speed variation (stochastic and periodic) on the maximum and minimum fault current levels of a wind turbine and the subsequent impact on system protection settings. The focus is on fixed-speed wind turbines since they contribute the maximum fault current, six or more times the rated current, as compared to other distributed generator technologies.

Objective 5: Demonstrate the Potential of Intelligent Electronic Device Data in Improving Power System Performance and Reliability

This objective demonstrates the potential of intelligent electronic device data in improving power system performance and reliability through fault event data collected from transmission and distribution networks. Potential applications include reconstructing the sequence of events, assessing relay and circuit breaker performance, validating the zero-sequence line impedance, estimating the fault resistance and identifying the root cause of the fault, and confirming the accuracy of the system circuit model. This objective also focuses on developing a methodology that can validate the zero-sequence line impedance of two- and three-terminal transmission lines using unsynchronized measurements.

1.3 Original Research Contributions and Dissertation Outline

This Section identifies the original research contributions made while achieving the objectives of this dissertation. The Section also provides a list of all the publications resulting from this research work and outlines the organization of this dissertation.

Contributions to Objective 1

The contribution made while achieving Objective 1 is to present a comprehensive theory of impedance-based fault-location algorithms. The theory includes detailed derivations that are useful in understanding the motivation behind the development of each algorithm, identifying their input data requirements, and distinguishing their strengths and weaknesses. Chapter 2 describes the theory of fault location algorithms and provides a qualitative discussion on the sources of fault location error. Chapter 3 uses simple test systems to evaluate the sensitivity of the fault location algorithms to the following error sources: inaccurate voltage and current phasors, inaccurate line impe-

dance parameters, system load, non-homogeneous system, parallel lines, three-terminal lines, and tapped radial lines. The approach is to introduce the error sources one by one and study the corresponding impact on location estimates. Since simple test systems are being used, the fault location error is strictly proportional to the inaccuracies introduced. From the analysis conducted on simulation and field data, the following criteria is recommended for selecting the most suitable fault location algorithm: (a) data availability and (b) application scenario. This research work has been published in [51–55].

- S. Das, S. Santoso, A. Gaikwad, and M. Patel, "Impedance-based fault location in transmission networks: theory and application," *IEEE Access*, vol. 2, pp. 537-557, 2014.

- S. Das, S. Santoso, R. Horton, and A. Gaikwad, "Effect of earth current return model on transmission line fault location - a case study," in *Proc. IEEE Power Energy Soc. General Meeting*, Jul. 2013, pp. 1-6.

- J. Traphöner, S. Das, S. Santoso, and A. Gaikwad, "Impact of grounded shield wire assumption on impedance-based fault location algorithms," in *Proc. IEEE PES General Meeting Conf. Expo.*, Jul. 2014, pp. 1-5.

- N. Karnik, S. Das, S. Kulkarni, and S. Santoso, "Effect of load current on fault location estimates of impedance-based methods," in *Proc. IEEE Power Energy Soc. General Meeting*, San Diego, CA, Jul. 2011, pp. 1-6.

- S. Kulkarni, N. Karnik, S. Das, and S. Santoso, "Fault location using impedance-based algorithms on non-homogeneous feeders," in *Proc. IEEE Power Energy Soc. General Meeting*, San Diego, CA, Jul. 2011, pp. 1-6.

Contributions to Objective 2

The contributions made while achieving Objective 2 are developing fault location algorithms that use only the current to estimate the distance to a fault. Since overcurrent relays in distribution networks may record the fault current waveforms (magnitude and phase angle) or the fault current magnitude only, the algorithms are developed in two parts: fault location using current phasors and fault location using current magnitude only. Source impedance parameters and Kirchhoff's circuit laws are used to estimate the missing fault voltage at the monitoring location. Once the missing fault voltage is available, impedance-based fault location principles can be applied from the monitoring location to estimate the distance to fault. Another method uses the system circuit model for fault location purposes. The location at which the short-circuit current matches the measured fault current is declared to be the fault location. The proposed algorithms are computationally simple and capable of locating all fault types. Chapter 4 presents a derivation of the current-only algorithms and demonstrates their efficacy with field data collected from utility distribution networks. The work is published in [56, 57].

– S. Das, N. Karnik, and S. Santoso, "Distribution fault location using current only," *IEEE Trans. Power Del.*, vol. 27, no. 3, pp. 1144-1153, Jul. 2012.

– S. Das, S. Kulkarni, N. Karnik, and S. Santoso, "Distribution fault location using short-circuit fault current profile approach," in *Proc. IEEE Power Energy Soc. General Meeting*, San Diego, CA, Jul. 2011, pp. 1-7.

Contributions to Objective 3

The contribution made when working toward Objective 3 is to provide a detailed insight into how distributed generators (DGs) affect the accuracy of existing impedance-based fault location algorithms in distribution networks interconnected with DGs. In

particular, the effects of DG technology, DG MVA capacity, DG interconnect transformer, tapped loads, distance between the DG unit and the fault, and fault resistance on the accuracy of fault location are examined in details. An understanding of these critical error sources will be useful for developing improved fault-locating solutions. The analysis is described in Chapter 5 and has been published in [58]. Another contribution is based on developing a novel algorithm that improves the accuracy of locating faults downstream from DGs. The approach consists of using the voltage and current at the substation, and the distributed generator impedance to estimate the missing fault current at the DG terminal. The estimated current is then included in the fault location calculation to improve the fault location accuracy. The simple but powerful algorithm is capable of locating all fault types and was validated against an actual 34.5-kV distribution feeder serving utility customers in rural New York. The algorithm is described in Chapter 6.

– S. Das, S. Santoso, and A. Maitra, "Effects of distributed generators on impedance-based fault location algorithms," in *Proc. IEEE PES General Meeting Conf. Expo.*, Jul. 2014, pp. 1-5.

Contributions to Objective 4

The contribution made while working towards Objective 4 is to develop a high-resolution time-domain model of a fixed-speed wind turbine with a detailed representation of tower shadow and wind shear effects. These effects are often approximated or neglected in typical fixed-speed models published in the literature. The proposed model, described in Chapter 7, can be used to perform any power quality analysis, and has been published in [59]. Another contribution lies in verifying the suitability of using the IEC 60909-0 Standard in calculating the maximum and minimum fault currents for networks interconnected with DG. A comprehensive analysis conducted in Chapter 7 concludes

that the IEC Standard uses a voltage factor to account for the wind speed variation in fixed speed wind turbines and has been published in [60].

– S. Das, N. Karnik, and S. Santoso,"Time-domain modeling of tower shadow and wind shear in wind turbines," *ISRN Renewable Energy*, vol. 2011, no. 890582, Jul. 2011.

– S. Das and S. Santoso, "Effect of wind speed variation on the short-circuit contribution of a wind turbine," in *Proc. IEEE Power Energy Soc. General Meeting*, Jul. 2012, pp. 1-8.

Contributions to Objective 5

The contribution made while achieving Objective 5 consists of developing algorithms to validate the zero-sequence impedance of two- and three-terminal transmission lines using unsynchronized IED data. For two-terminal lines, the negative-sequence network is used to align the voltage and current of one terminal with those at the other terminal. Next, the fact that the zero-sequence fault voltage at the fault point is equal when calculated from either line terminal is used to estimate the zero-sequence line impedance. For three-terminal transmission lines, in addition to the line experiencing the fault, it is also necessary to validate the zero-sequence impedance of the line that connects the third terminal to the tap point. Because the third terminal operates in parallel with one of the terminals to feed the fault, the voltage at the tap point is equal when calculated from either of those two terminals. This principle is used to validate the zero-sequence impedance of the tapped line. Since measurements at the third terminal may not be always available, two approaches are developed. The first approach uses unsynchronized measurements at all the three terminals while the second approach uses unsynchronized measurements at any of the two terminals. The proposed algorithms

are described in Chapter 8 and verified with field data in Chapter 9. Other contributions include proposing and demonstrating the potential of IED data in improving power system performance and reliability. Fault data collected from utility transmission and distribution networks are successfully used to reconstruct the sequence of events, assess the performance of relays and circuit breakers, estimate the fault resistance, and verify the accuracy of the system model. The theory is described in Chapter 8 and illustrated with actual fault event data in Chapter 9. Parts of this analysis are published in [51].

– S. Das, S. Santoso, A. Gaikwad, and M. Patel, "Impedance-based fault location in transmission networks: theory and application," *IEEE Access*, vol. 2, pp. 537-557, 2014.

Chapter 2

Theory of Impedance-based Fault Location Algorithms

Transmission and distribution circuits often experience short-circuit faults due to lightning strikes during inclement weather, animal and tree contact with an overhead line, and insulation failure in power system equipment. It is common to use impedance-based fault location algorithms to track the location of such faults so as to expedite service restoration and improve system reliability [13, 14]. These fault-locating algorithms are straightforward to implement and yield reasonable location estimates. Voltage and current waveforms captured by digital relays, digital fault recorders, and other intelligent electronic devices (IEDs) during a fault are used to estimate the apparent impedance between the IED device and location of the short-circuit fault. Given the line impedance in ohms, the per-unit distance to the fault can be estimated accurately.

A number of impedance-based fault location algorithms have been developed for transmission and distribution network applications. Fault-locating algorithms using data captured by an IED device at one end of the line are commonly referred to as one-ended algorithms, while those using data captured by IEDs at both ends of a transmission line are referred to as two-ended algorithms. Each algorithm has specific input data requirements and makes certain assumptions when computing the distance to a fault. These assumptions may or may not hold true in a particular fault location scenario. Put another way, no single fault-locating algorithm works best in several different fault location scenarios. Choosing the best fault-locating approach from such a wide selection of impedance-based fault location algorithms is, therefore, an overwhelming task and

requires a detailed understanding of the working principle behind each algorithm.

Based on the aforementioned background, the ***objective*** of this Chapter is to present the underlying theory of one-ended impedance-based fault location algorithms (simple reactance, Takagi, modified Takagi, Eriksson, and Novosel *et al.* methods) and two-ended impedance-based fault location algorithms (synchronized, unsynchronized, and current-only methods). IEEE C37.114 Standard [13] served as a benchmark for determining which algorithms to evaluate. The goal is to lay down a strong technical foundation for determining the most suitable fault-locating algorithm with available data.

Contributions of this Chapter were identified as follows: (a) presented a detailed theory of impedance-based fault-locating algorithms for locating all fault types, (b) highlighted the motivation behind the development of each fault-locating algorithm, (c) defined input data requirement of each algorithm, and (d) identified the strength and weakness of each algorithm.

Publication:

– S. Das, S. Santoso, A. Gaikwad, and M. Patel, "Impedance-based fault location in transmission networks: theory and application," *IEEE Access*, vol. 2, pp. 537-557, 2014.

2.1 One-ended Impedance-based Fault Location Algorithms

One-ended impedance-based fault location algorithms estimate the location of a fault by looking into a transmission or distribution feeder from one end [13]. Voltage and current waveforms captured during a fault by an intelligent electronic device (IED) at one end of the line are used to determine the apparent impedance between the IED device and the location of the short-circuit fault. Given the line impedance in ohms, the per-unit distance to a fault can be easily obtained. The advantages of using one-ended

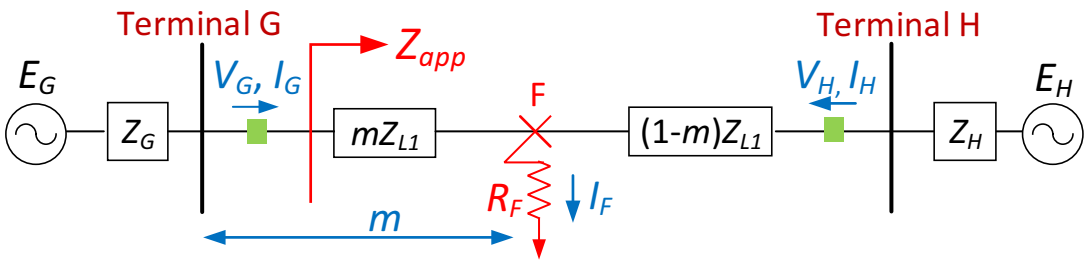

Figure 2.1: One-line diagram of a two-terminal network.

algorithms are that they are straightforward to implement, yield reasonable location estimates, and require data from only one end of a line. There is no need for any communication channel or remote data and hence, fault location can be implemented at the line terminal by any microprocessor-based numerical relay.

To illustrate the principle of one-ended methods, consider the two-terminal network shown in Fig. 2.1. The overhead line is homogeneous and has a total positive-sequence impedance of Z_{L1} between terminals G and H. Networks upstream from terminals G and H are represented by their respective Thevenin equivalents having impedances Z_G and Z_H. When a fault with a resistance value of R_F occurs at a distance m per unit from terminal G, both sources contribute to the total fault current I_F. The voltage and current phasors at terminal G during the fault are V_G and I_G, respectively. Similarly, the voltage and current phasors at terminal H during the fault are V_H and I_H, respectively. Note that although measurements are available at both ends of the line, one-ended methods use voltage and current captured at either terminal G or at terminal H. Using Kirchhoff's laws, the voltage drop from terminal G can be expressed as

$$V_G = mZ_{L1}I_G + R_F I_F \tag{2.1}$$

where V_G and I_G depend on the fault type and are defined in Table 2.1.

Table 2.1: Definition of V_G, I_G, and ΔI_G for Different Fault Types

Fault Type	V_G	I_G	ΔI_G
A-G	V_{AF}	$I_{AF} + kI_{G0}$	$I_{AF} - I_{Apre}$
B-G	V_{BF}	$I_{BF} + kI_{G0}$	$I_{BF} - I_{Bpre}$
C-G	V_{CF}	$I_{CF} + kI_{G0}$	$I_{CF} - I_{Cpre}$
AB, AB-G, ABC	$V_{AF} - V_{BF}$	$I_{AF} - I_{BF}$	$(I_{AF} - I_{Apre}) - (I_{BF} - I_{Bpre})$
BC, BC-G, ABC	$V_{BF} - V_{CF}$	$I_{BF} - I_{CF}$	$(I_{BF} - I_{Bpre}) - (I_{CF} - I_{Cpre})$
CA, CA-G, ABC	$V_{CF} - V_{AF}$	$I_{CF} - I_{AF}$	$(I_{CF} - I_{Cpre}) - (I_{AF} - I_{Apre})$
where $k = \dfrac{Z_{L0}}{Z_{L1}} - 1$			

Notations in the table can be defined as follows:

I_{G0}	is the zero-sequence fault current phasor (kA)
Z_{L0}	is the zero-sequence line impedance (Ω)
Z_{L1}	is the positive-sequence line impedance (Ω)
ΔI_G	is the "pure" fault current discussed in Section 2.1.2 (kA)
V_{AF}, V_{BF}, V_{CF}	are the fault voltage phasors in phases A, B, and C (kV)
I_{AF}, I_{BF}, I_{CF}	are the fault current phasors in phases A, B, and C (kA)
I_{Apre}, I_{Bpre}, I_{Cpre}	are the prefault current phasors in phases A, B, and C (kA)

Dividing (2.1) throughout by I_G, the apparent impedance to the fault (Z_{app}) measured from terminal G can be expressed as

$$Z_{app} = \frac{V_G}{I_G} = mZ_{L1} + R_F \left(\frac{I_F}{I_G} \right) \tag{2.2}$$

Equation 2.2 is the fundamental equation that governs one-ended impedance-based fault location algorithms. Unfortunately, because measurements from only one end of the line are used, (2.2) has three unknowns, namely, m, R_F, and I_F. To eliminate R_F and I_F from the fault location computation, several one-ended algorithms have been developed and are discussed in details below.

2.1.1 Simple Reactance Method

The simple reactance method takes advantage of the fact that the fault resistance, R_F, is resistive in nature [13]. Therefore, if currents I_F and I_G are assumed to be in phase, the term $R_F\,(I_F/I_G)$ in (2.2) reduces to a real number as illustrated in Fig. 2.2 (a). Considering only the imaginary components of (2.2), the distance to a fault is given by

$$m = \frac{\text{imag}\left(\dfrac{V_G}{I_G}\right)}{\text{imag}\,(Z_{L1})} \tag{2.3}$$

Put another way, the simple reactance method estimates the reactance to a fault in order to eliminate the effect of fault resistance from the fault location calculation.

Although the simple reactance method is computationally simple and requires minimum data for fault location, the accuracy of fault location deteriorates when I_F and I_G are not in phase. The phase angle mismatch occurs under two conditions: system load and system non-homogeneity. When the system load is significant, the phase angle of current at the substation, I_G, is not exactly equal to the phase angle of current at the fault point, I_F. Furthermore, in a non-homogeneous system, wherein the source impedances have a different phase angle than the line impedance, fault currents I_H and I_G do not have the same phase angle. Because I_F is the summation of I_G and I_H, the phase angle of I_F is also not equal to that of I_G. As a result, $R_F\,(I_F/I_G)$ is a complex number and presents an additional reactance to the fault. Neglecting this reactance introduces an error in the location estimates and is referred to as the reactance error [13]. When I_F leads I_G, the term $R_F\,(I_F/I_G)$ is inductive and increases the apparent impedance to the fault as shown in Fig. 2.2 (b). One-ended methods will, therefore, overestimate the location of the fault. When I_F lags I_G, the term $R_F\,(I_F/I_G)$ is capacitive and decreases the apparent impedance to the fault as shown in Fig. 2.2 (c). In such cases, one-ended methods will underestimate the location of the fault.

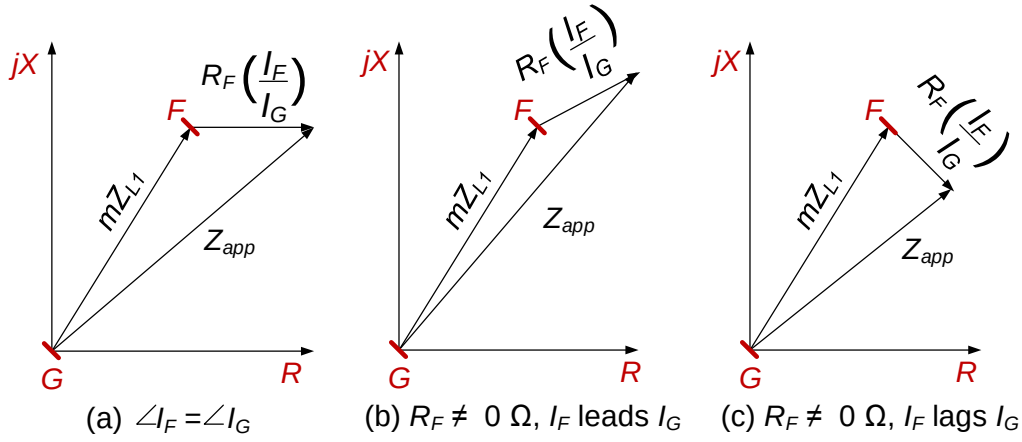

Figure 2.2: Reactance error in the simple reactance method [4].

2.1.2 Takagi Method

The Takagi method improves upon the performance of the simple reactance method by "subtracting out" [14] the load current from the total fault current. Superposition principle is used for decomposing a network during fault into a prefault and "pure fault" network as illustrated for a three-phase fault in Fig. 2.3. In a "pure fault" network, all voltage sources are short-circuited and a voltage source, V_{F1pre}, is inserted at the fault point F, where V_{F1pre} is the positive-sequence prefault voltage at the fault point. Next, the fault current I_F is calculated by applying the current division rule to the "pure fault" network as [17]

$$I_F = \left(\frac{Z_{G1} + Z_{L1} + Z_{H1}}{(1-m)Z_{L1} + Z_{H1}} \right) \Delta I_G = \frac{1}{|d_s| \angle \beta} \times \Delta I_G \tag{2.4}$$

where Z_{G1} and Z_{H1} are the positive-sequence source impedances behind terminals G and H, d_s is the current distribution factor, β is the angle of the current distribution factor, and ΔI_G is the "pure" fault current at terminal G. Substituting the expression for I_F in (2.1) and multiplying both sides by ΔI_G^*, the following is obtained:

$$V_G \times \Delta I_G^* = m Z_{L1} I_G \Delta I_G^* + R_F \times \left(\frac{1}{d_s} \right) \tag{2.5}$$

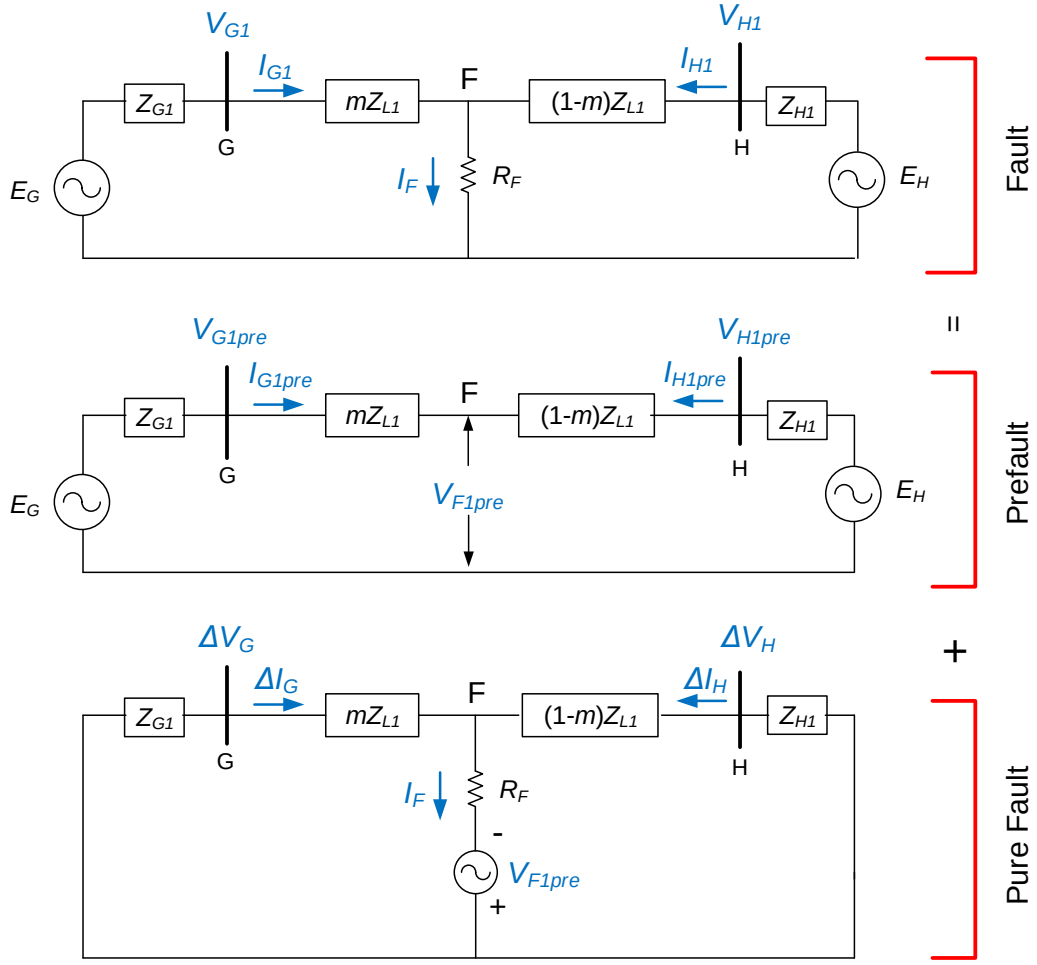

Figure 2.3: Superposition theorem used to decomposes the network in Fig. 2.1 into a prefault and a "pure" fault during a three-phase fault.

To eliminate R_F from the fault location computation in (2.5), the Takagi method assumes a homogeneous network, i.e., the local and remote source impedances, Z_{G1} and Z_{H1}, have the same impedance angle as the overhead line. This assumption implies that d_s is a real number with β equal to zero. As a result, $R_F(1/d_S)$ reduces to a real number. Equating only the imaginary components of (2.5), the distance to a fault is given as

$$m = \frac{\text{imag}\left(V_G \times \Delta I_G^*\right)}{\text{imag}\left(Z_{L1} \times I_G \times \Delta I_G^*\right)} \tag{2.6}$$

where V_G, I_G, and ΔI_G depend on the fault type and are defined in Table 2.1.

Although the Takagi method uses the "pure fault" current ΔI_G to minimize any reactance error due to system load, the success of this method relies on the network being homogeneous in nature. If the network is non-homogeneous, $R_F(1/d_S)$ is no longer a real number and will cause a reactance error in the location estimates. The error is proportional to the degree of non-homogeneity. In addition, when calculating ΔI_G, the method assumes that the load current remains equal both before and during the fault. This holds true for a constant current load model only. In practice, loads are a mix of constant power and constant impedance loads with very few loads being constant current in nature.

2.1.3 Modified Takagi Method

The number of prefault cycles to be included in the event report is a relay setting and may not be always available for fault location purposes. Therefore, to avoid using the prefault current, the modified Takagi method uses the zero-sequence current, I_{G0}, instead of ΔI_G to account for load current during a single line-to-ground fault [16, 61]. This substitution is possible since I_{G0}, similar to ΔI_G, exists only during a ground fault and is zero under balanced operating conditions. The distance to a fault is computed as

$$m = \frac{\text{imag}\left(V_G \times 3I_{G0}^*\right)}{\text{imag}\left(Z_{L1} \times I_G \times \ 3I_{G0}^*\right)} \tag{2.7}$$

Furthermore, the modified Takagi method compensates for a non-homogeneous system by using the zero-sequence network shown in Fig. 2.4 to calculate d_s as

$$|d_s| \angle\beta = \frac{Z_{G0} + Z_{L0} + Z_{H0}}{(1-m)Z_{L0} + Z_{H0}} \tag{2.8}$$

where Z_{G0} and Z_{H0} are the zero-sequence source impedances behind terminals G and H. Since β represents the degree of non-homogeneity, applying an angle correction of $e^{-j\beta}$ to the fault location computation in (2.7) would force the system to be homogeneous and improve the accuracy of location estimates. However, to calculate β, the distance

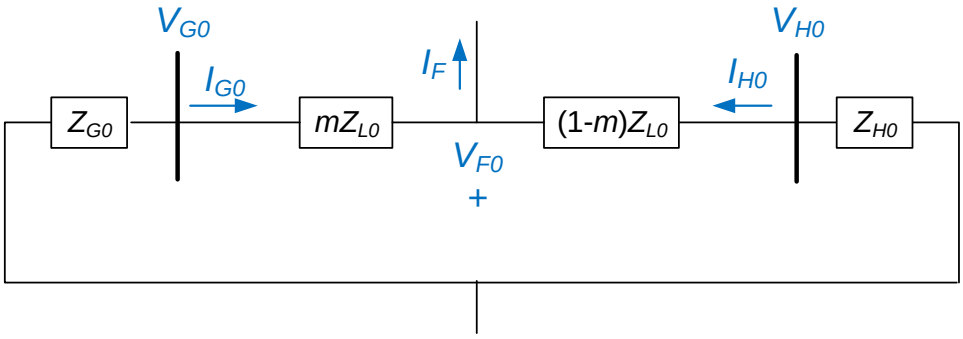

Figure 2.4: Zero-sequence network during a ground fault.

to fault, m, must be known. Therefore, the modified Takagi method proceeds by first calculating a preliminary estimate of m using (2.7). This value of m is then used to calculate the angle correction factor in (2.8). The final fault location estimate that accounts for both load and system non-homogeneity is

$$m = \frac{\text{imag}\left(V_G \times 3I_{G0}^{*} \times e^{-j\beta}\right)}{\text{imag}\left(Z_{L1} \times I_G \times \ 3I_{G0}^{*} \times e^{-j\beta}\right)} \tag{2.9}$$

Although the modified Takagi method has a superior performance over the Takagi method, the accuracy of location estimates depends on accurately knowing the source impedance parameters. If the zero-sequence impedance of the local source is not available, it can be estimated from the fault data using (8.43). The remote zero-sequence source impedance, Z_{H0}, however, must be known.

2.1.4 Eriksson Method

This fault-locating technique is applicable for locating faults in a two-terminal transmission line only and uses source impedance parameters to overcome any reactance error caused by fault resistance, load, or system non-homogeneity [18]. The positive-sequence network is used to calculate the current distribution factor d_s as

$$|d_s| \angle\beta = \frac{Z_{G1} + Z_{L1} + Z_{H1}}{(1-m)Z_{L1} + Z_{H1}} \tag{2.10}$$

Substituting (2.10) in (2.5) as

$$V_G = mZ_{L1}I_G + R_F\left(\frac{Z_{G1}+Z_{L1}+Z_{H1}}{(1-m)Z_{L1}+Z_{H1}}\right)\Delta I_G \tag{2.11}$$

Simplifying and rearranging the terms results in the following expression:

$$m^2 - k_1 m + k_2 - k_3 R_F = 0 \tag{2.12}$$

where constants k_1, k_2, and k_3 are complex multiplications of voltage, current, line impedance, and source impedances and are defined as follows:

$$k_1 = a + jb = 1 + \frac{Z_{H1}}{Z_{L1}} + \left(\frac{V_G}{Z_{L1}\times I_G}\right)$$

$$k_2 = c + jd = \frac{V_G}{Z_{L1}\times I_G}\left(1 + \frac{Z_{H1}}{Z_{L1}}\right)$$

$$k_3 = e + jf = \frac{\Delta I_G}{Z_{L1}\times I_G}\left(1 + \frac{Z_{H1}+Z_{G1}}{Z_{L1}}\right)$$

Separating (2.12) into real and imaginary parts, the distance to fault m can be solved from the following quadratic equation:

$$m = \frac{\left(a - \frac{eb}{f}\right) \pm \sqrt{\left(a - \frac{eb}{f}\right)^2 - 4\left(c - \frac{ed}{f}\right)}}{2} \tag{2.13}$$

where m can take two possible values. Since the fault location estimate must be less that the total line length, the value of m that lies between 0 and 1 per unit should be chosen as the location estimate. If the local source impedance, Z_{G1}, is not available, it can be calculated from the fault event data using (8.44). The remote positive-sequence source impedance, Z_{H1}, must be known.

2.1.5 Novosel *et al.* Method

This fault-locating technique is a modified version of the Eriksson method and is applicable for locating faults on (a) distribution feeders and (b) radial transmission

lines [19]. This method should not be used for locating faults on multi-terminal transmission lines. All loads are lumped at the end of the feeder as shown in Fig. 2.5.

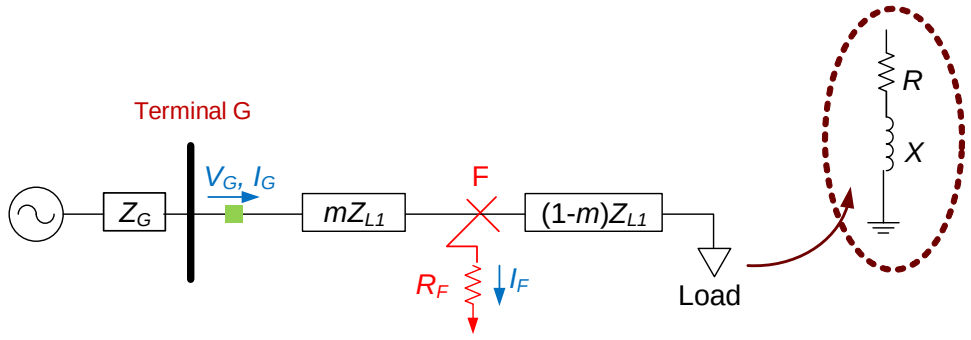

Figure 2.5: Novosel *et al.* method assumes a constant impedance load model and lumps it at the end of the feeder.

The load is assumed to be constant impedance in nature and can be estimated from the prefault voltage and current phasors, V_{G1pre} and I_{G1pre}, as

$$Z_{Load} = R + jX = \frac{V_{G1pre}}{I_{G1pre}} - Z_{L1} \tag{2.14}$$

The per-unit distance to the fault can then be solved from the quadratic equation in (2.13), where the constants are defined as

$$k_1 = a + jb = 1{+}1 + \frac{Z_{Load}}{Z_{L1}} + \left(\frac{V_G}{Z_{L1} \times I_G}\right)$$

$$k_2 = c + jd = \frac{V_G}{Z_{L1} \times I_G}\left(1 + \frac{Z_{Load}}{Z_{L1}}\right)$$

$$k_3 = e + jf = \frac{\Delta I_G}{Z_{L1} \times I_G}\left(1 + \frac{Z_{Load} + Z_{G1}}{Z_{L1}}\right)$$

The value of m between 0 and 1 per unit should be chosen as the location estimate. If the local source impedance Z_{G1} is not known, it can be estimated from (8.44). Similar to the Eriksson method, the Novosel *et al.* method is also robust to any reactance error due to fault resistance and load.

2.2 Two-ended Impedance-based Fault Location Algorithms

Two-ended impedance-based algorithms require waveform data captured at both ends of an overhead line and are more suited towards locating faults on networked transmission systems where measurements from multiple monitors may be available. The fault-locating principle is similar to that of one-ended methods, i.e., using the voltage and current during a fault to estimate the apparent impedance from the monitoring location to the fault. Additional measurements from the remote end of a transmission line are used to eliminate any reactance error caused by fault resistance, load current, or system non-homogeneity. Fault type classification is also not required. A communication channel transfers data from one IED device to the other. Alternatively, data from both IEDs can be collected and processed at a central location. Depending on data availability, two-ended impedance-based methods are further classified as described below.

2.2.1 Synchronized Two-ended Method

This method assumes that measurements from both ends of a transmission line are synchronized to a common time reference via a global positioning system (GPS). Any one of the three symmetrical components can be used for fault location computation. Using the negative-sequence components are, however, more advantageous since they are not affected by load current, zero-sequence mutual coupling, uncertainty in zero-sequence line impedance, or infeed from zero-sequence tapped loads [15,43]. To illustrate the fault-locating principle, consider the negative-sequence network during an unbalanced fault as shown in Fig. 2.6. The negative-sequence voltage at the fault point F, V_{F2}, can be calculated from terminal G and H as

$$\text{Terminal G:} \quad V_{F2} = V_{G2} - mZ_{L2}I_{G2} \tag{2.15}$$

$$\text{Terminal H:} \quad V_{F2} = V_{H2} - (1-m)Z_{L2}I_{H2} \tag{2.16}$$

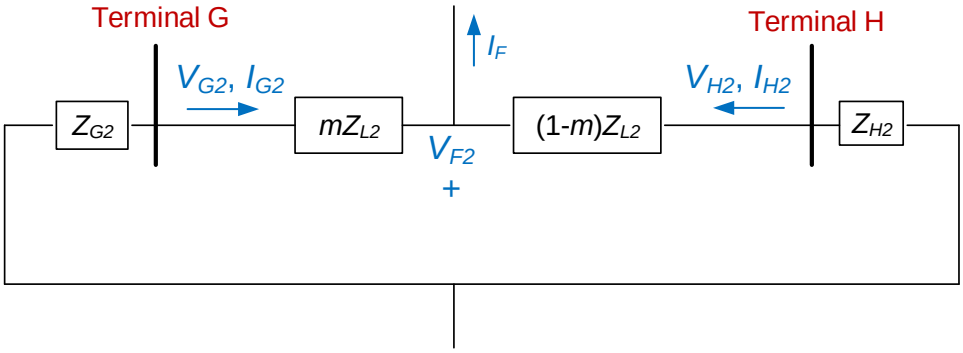

Figure 2.6: Negative-sequence network during an unbalanced fault.

where V_{G2} and I_{G2} are the negative-sequence fault voltage and current phasors at terminal G, V_{H2} and I_{H2} are the negative-sequence fault voltage and current phasors at terminal H, and Z_{L2} is the negative-sequence line impedance which is equal to the positive-sequence line impedance, Z_{L1}. Since V_{F2} is equal when calculated from either line terminal, equate (2.17) and (2.16) to solve for the distance to fault m as

$$m = \frac{V_{G2} - V_{H2} + Z_{L2} I_{H2}}{(I_{G2} + I_{H2})\, Z_{L2}} \tag{2.17}$$

Equation 2.17 is applicable for locating any unbalanced fault such as a single line-to-ground, line-to-line, or double line-to-ground fault. However, during a three-phase balanced fault, negative-sequence components do not exist. In such a case, the same fault-locating principle is applied to a positive-sequence network and the distance to fault is computed as [20]

$$m = \frac{V_{G1} - V_{H1} + Z_{L1} I_{H1}}{(I_{G1} + I_{H1})\, Z_{L1}} \tag{2.18}$$

where V_{G1} and I_{G1} are the positive-sequence fault voltage and current phasors at terminal G, and V_{H1} and I_{H1} are the positive-sequence fault voltage and current phasors at terminal H. Note that there is no need to know the fault type. The presence or absence of negative-sequence components can be used to differentiate between an unbalanced or a balanced fault.

2.2.2 Unsynchronized Two-ended Method

Waveforms captured by IED devices at both ends of a transmission line may not be synchronized with each other. The GPS device may be absent or not functioning correctly. Alternatively, IEDs can have different sampling rates or they may detect the fault at slightly different time instants. The communication channel, which transfers data from one IED to the other, can also introduce a phase shift. Therefore, to align the voltage and current measurements of terminal G with respect to terminal H, authors in [4] use a synchronizing operator $e^{j\delta}$ as,

$$\text{Terminal G:} \quad V_{Fi} = V_{Gi}e^{j\delta} - mZ_{Li}I_{Gi}e^{j\delta} \tag{2.19}$$

$$\text{Terminal H:} \quad V_{Fi} = V_{Hi} - (1-m)Z_{Li}I_{Hi} \tag{2.20}$$

where the subscript i refers to the i^{th} symmetrical component. Negative-sequence components are used to compute the location of an unbalanced fault while positive-sequence components are used to compute the location of a balanced three-phase fault. Equating (2.21) and (2.20), the synchronizing operator takes the form of

$$e^{j\delta} = \frac{V_{Hi} - (1-m)Z_{Li}I_{Hi}}{V_{Gi} - mZ_{Li}I_{Gi}} \tag{2.21}$$

Now, $e^{j\delta}$ can be eliminated from the fault location computation by taking the absolute value on both sides of (2.21) as

$$\left|e^{j\delta}\right| = 1 = \left|\frac{V_{Hi} - (1-m)Z_{Li}I_{Hi}}{V_{Gi} - mZ_{Li}I_{Gi}}\right| \tag{2.22}$$

Simplifying and rearranging the terms, the distance to fault m is a quadratic equation given by

$$m = \frac{-B \pm \sqrt{B^2 - 4AC}}{2A} \tag{2.23}$$

where the constants are defined as

$A = |Z_{Li}I_{Gi}|^2 - |Z_{Li}I_{Hi}|^2$

$$B = -2 \times \mathrm{Re}\left[V_{Gi}\left(Z_{Li}I_{Gi}\right)^{*} + \left(V_{Hi} - Z_{Li}I_{Hi}\right)\left(Z_{Li}I_{Hi}\right)^{*}\right]$$

$$C = \left|V_{Gi}\right|^{2} - \left|V_{Hi} - Z_{Li}I_{Hi}\right|^{2}$$

Solving the quadratic equation in (2.23) yields two values of m. The value between 0 and 1 per unit should be chosen as the location estimate.

2.2.3 Unsynchronized Current-only Two-ended Method

Due to limitations in data availability, suppose that only the current waveforms at terminals G and H are available for fault location. Voltage phasors V_{G2} and V_{H2} are missing or simply not available. Using only the current and source impedance parameters, the negative-sequence fault voltage can be calculated from either terminal as [21]

$$\text{Terminal G:} \qquad V_{F2} = -\left(Z_{G2} + mZ_{L2}\right)I_{G2} \tag{2.24}$$

$$\text{Terminal H:} \qquad V_{F2} = -\left(Z_{H2} + (1-m)Z_{L2}\right)I_{H2} \tag{2.25}$$

where Z_{G2} and Z_{H2} are the negative-sequence source impedance parameters behind terminals G and H. Equate (2.26) with (2.25) to eliminate V_{F2}. Also, to avoid any alignment issues with data sets from both ends of a transmission line, consider only the absolute values as

$$\left|I_{H2}\right| = \left|\frac{\left(Z_{G2} + mZ_{L2}\right)}{\left(Z_{H2} + (1-m)Z_{L2}\right)} \times I_{G2}\right| \tag{2.26}$$

Squaring and rearranging the terms, the distance to fault m can be solved by solving the quadratic equation in (2.23), where the constants are defined as

$a + jb = I_{G2}Z_{G2}$

$c + jd = Z_{L2}I_{G2}$

$e + jf = Z_{H2} + Z_{L2}$

$g + jh = Z_{L2}$

$A = \left|I_{H2}\right|^{2} \times \left(g^{2} + h^{2}\right) - \left(c^{2} + d^{2}\right)$

$$B = -2 \times |I_{H2}|^2 (eg + fh) - 2 (ac + bd)$$

$$C = |I_{H2}|^2 \times (e^2 + f^2) - (a^2 + b^2)$$

The value of m that lies between 0 and 1 per unit should be chosen as the final location estimate. This method is applicable for locating unbalanced faults only. Furthermore, the accuracy of location estimates depends on accurately knowing the source impedance parameters.

2.3 Summary

This Chapter presents the theory of one- and two-ended impedance-based fault location algorithms. The input data requirement of each algorithm is summarized in Table 2.2.

Table 2.2: Summary of Input Data Requirements of Impedance-based Fault Location Algorithms

Input Data	Simple Reactance	Takagi	Modified Takagi	Eriksson	Novosel *et al.*	Synchronized Two-ended	Unsynchronized Two-ended	Unsynchronized Current-only Two-ended
Fault Event Data								
Fault Type	✓	✓	✓	✓	✓			
Fault Voltage[1] (Local End)	✓	✓	✓	✓	✓	✓	✓	
Fault Current (Local End)	✓	✓	✓	✓	✓	✓	✓	✓
Fault Voltage[1] (Remote End)						✓	✓	
Fault Current (Remote End)						✓	✓	✓
Synchronized Data						✓		
Prefault Current		✓		✓	✓			
Prefault Voltage					✓			
Line Parameters								
Line Length	✓	✓	✓	✓	✓	✓	✓	✓
Positive-sequence Line Impedance	✓	✓	✓	✓	✓	✓	✓	✓
Zero-sequence Line Impedance	✓	✓	✓	✓	✓			
Source Impedance Parameters								
Positive-sequence Source Impedance (Local End)				Optional	Optional			
Positive-sequence Source Impedance (Remote End)				✓				
Negative-sequence Source Impedance (Local End)								✓
Negative-sequence Source Impedance (Remote End)								✓
Zero-sequence Source Impedance (Local End)			Optional					
Zero-sequence Source Impedance (Remote End)			✓					

[1] Voltages measured between the line and the ground.

Chapter 3

Error Analysis of Impedance-based Fault Location

Impedance-based fault location algorithms described in Chapter 2 make certain simplifying assumptions when computing the distance to a fault. Accuracy is affected when these assumptions do not hold true because of load, fault resistance, current infeed from a remote source, zero-sequence mutual coupling in parallel lines to name a few. In addition, impedance-based fault-locating algorithms require the input of the voltage and current phasors during a fault, and line impedance parameters when estimating the fault location. Inaccuracy in the input parameters further adds to the error in fault location. Three-terminal and tapped radial lines can also challenge the application of impedance-based algorithms. Therefore, the ***objective*** of this Chapter is to evaluate the sensitivity of fault-locating algorithms to the error sources mentioned above. The ***contribution*** lies in using simulation test systems and field data to perform a thorough error analysis and to gauge the significance of each error source.

Publications:

- S. Das, S. Santoso, A. Gaikwad, and M. Patel, "Impedance-based fault location in transmission networks: theory and application," *IEEE Access*, vol. 2, pp. 537-557, 2014.
- S. Das, S. Santoso, R. Horton, A. Gaikwad, "Effect of earth current return model on transmission line fault location - a case study," in *Proc. IEEE Power Energy Soc. General Meeting*, Jul. 2013, pp. 1-6.

– J. Traphöner, S. Das, S. Santoso, and A. Gaikwad, "Impact of grounded shield wire assumption on impedance-based fault location algorithms," in *Proc. IEEE PES General Meeting Conf. Expo.*, Jul. 2014, pp. 1-5.

– N. Karnik, S. Das, S. Kulkarni, and S. Santoso, "Effect of load current on fault location estimates of impedance-based methods," in *Proc. IEEE Power Energy Soc. General Meeting*, San Diego, CA, Jul. 2011, pp. 1-6.

– S. Kulkarni, N. Karnik, S. Das, and S. Santoso, "Fault location using impedance-based algorithms on non-homogeneous feeders," in *Proc. IEEE Power Energy Soc. General Meeting*, San Diego, CA, Jul. 2011, pp. 1-6.

3.1 Benchmark Test Case

To evaluate the sensitivity of impedance-based fault location algorithms to various sources of fault-locating error, a two-terminal transmission network shown in Fig. 2.1 was modeled in PSCAD simulation software [47]. The model will be used to replicate actual short-circuit faults that occur on a transmission line and generate the corresponding voltage and current waveforms. The rated voltage at terminals G and H is 69 kV. Relays, present at both terminals for line protection, record the three-phase line-to-ground voltages and currents at 128 samples per cycle. The network upstream from terminal G is represented by an ideal voltage source $E_G = 1\angle 10^\circ$ per unit behind an equivalent positive- and zero-sequence impedance of $Z_{G1} = 3.75\angle 71^\circ\,\Omega$ and $Z_{G0} = 11.25\angle 65^\circ\,\Omega$, respectively. The network upstream from terminal H is also represented by an ideal voltage source $E_H = 1\angle 0^\circ$ per unit behind an equivalent positive- and zero-sequence impedance of $Z_{H1} = 12\angle 71^\circ\,\Omega$ and $Z_{H0} = 30\angle 65^\circ\,\Omega$, respectively. The angle by which E_G leads E_H is known as the power angle, δ, and represents the net load served by the transmission line. The transmission line connecting terminals G and H is 18 miles long and was modeled using the frequency dependent model in PSCAD. The tower configuration of

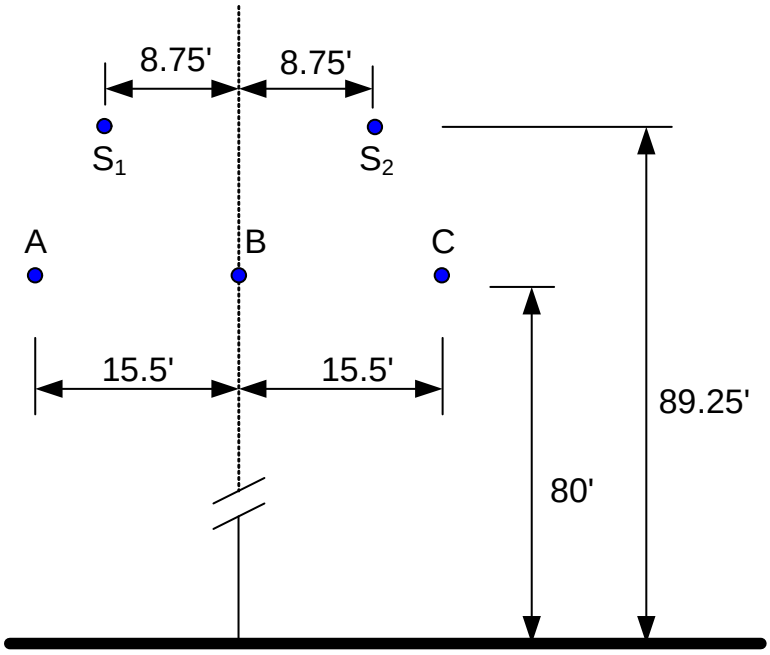

Figure 3.1: Tower configuration of an actual 69-kV transmission line.

an actual 69-kV transmission line was used as shown in Fig. 3.1. Shield wires S_1 and S_2 protect phase conductors A, B, and C from direct lightning strikes. The material used to build the conductors is described in Table 3.1. Using modified Carson's model [3] and an earth resistivity value of 100 Ω m, the positive- and zero-sequence line impedances were calculated to be $Z_{L1} = 15.55\angle 69.9^\circ\,\Omega$ and $Z_{L0} = 35.46\angle 63.4^\circ\,\Omega$, respectively. Details on how to solve line constants have been described in Appendix A.

Note that the test feeder has been intentionally designed to be simple, homogeneous, and compliant with all the assumptions made by impedance-based fault location algorithms. The goal is to introduce the fault-locating error sources one by one and study the impact on fault location estimates. Since a simple test system is being used, the error in location estimates is strictly proportional to the inaccuracies introduced. The analysis will, therefore, give an accurate measure of how significant a particular error source is and whether the error source should be considered for fault location purposes.

Table 3.1: Conductor Data

	Material	Resistance (Ω/mi)	Diameter (inch)	GMR (feet)
Phase	ACSR Linnet 336,400 26/7	0.294	0.720	0.024
Shield	ACSR Grouse 80,000 8/1	1.404	0.367	0.009

3.2 Fault Location Error due to Inaccurate Input Data

Impedance-based fault location algorithms require the input of fundamental frequency fault voltage and current phasors to calculate the distance to a fault. Unfortunately, because of DC offset and CT saturation, fault current phasors may not be accurate and will result in a substantial error in location estimates. A delta-connected potential transformer can introduce error in the calculation of the fault voltage phasor. In addition, all impedance-based fault location algorithms estimate the impedance to fault in ohms. Line impedance parameters in ohms per unit distance are required to obtain a corresponding distance estimate. Uncertainty about these line parameters, particularly the zero-sequence line impedance further adds to the error in location estimates. This Section discusses these factors and their impact on fault location accuracy in details.

3.2.1 Inaccurate Current Phasor: DC Offset and CT Saturation

Impedance-based fault location algorithms employ phasor quantities of voltage and current to compute the distance to a fault. The calculation of these phasor quantities are complicated by the presence of an exponentially decaying DC offset which makes the fault current asymmetrical during the first few cycles as shown in Fig. 3.2. The asymmetry is maximum when a fault occurs at the zero-crossing of a voltage waveform and minimum when a fault occurs near the voltage peak. Fortunately, most single line-to-ground faults are caused by an animal or a tree coming into contact with a transmission line during peak voltage conditions [7]. In such cases, the DC offset is negligible. Faults

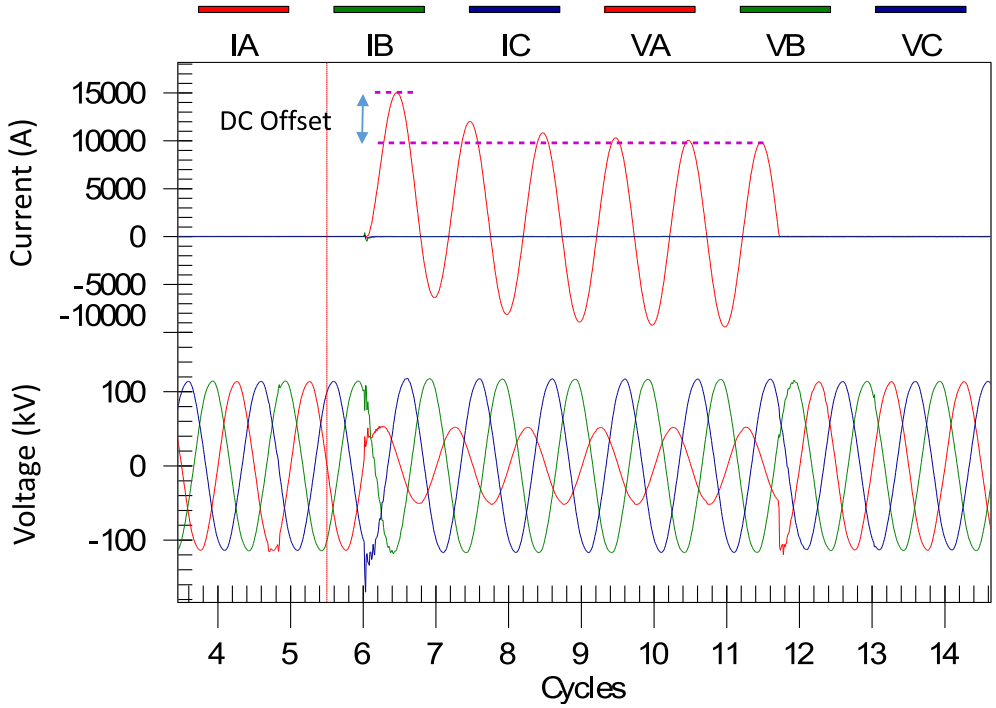

Figure 3.2: Fault current with a significant DC offset.

due to lightning strikes are, however, random and can occur at any point on the voltage waveform, resulting in a significant asymmetry in the fault current.

To filter out the decaying DC offset and calculate the fault current phasor, Fast Fourier transforms (FFT) are commonly used [14]. A window length of one cycle is used to extract the fundamental-frequency magnitude and phase angle, and discard all harmonics. As an example, a rolling FFT filter is applied to the waveform in Fig. 3.2. In a rolling FFT, the FFT operation is performed repeatedly by a one-cycle long window sweeping across the entire waveform. Figure 3.3 shows that the FFT operation is successful in filtering out most, but not all of the DC offset. The fault current magnitude fluctuates and reaches steady-state only when the DC offset decays. The corresponding variation in location estimates from the simple reactance method is shown in Fig. 3.4.

The cosine filter is another phasor estimation technique commonly used in Schweitzer relays [62]. The coefficients of this filter are sampled from a cosine wave and require

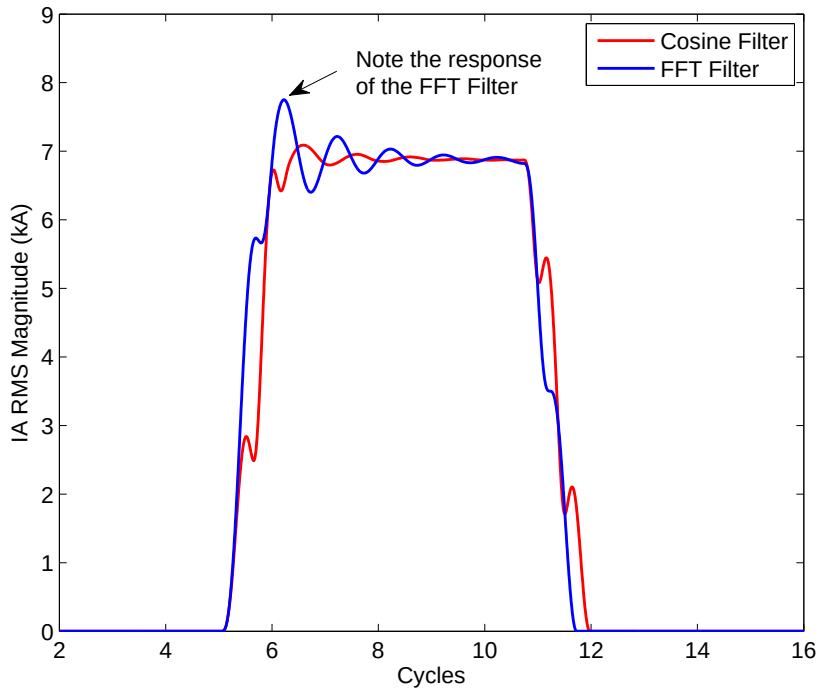

Figure 3.3: Cosine filter is more effective in filtering out the DC offset than the FFT filter.

a minimum response time of one and a quarter cycles. The quarter-cycle delay is used to calculate the phase angle. As seen in Fig. 3.3, the cosine filter does a better job of eliminating the DC offset than the FFT filter. The front and tail end of the signal are, however, severely distorted. This distortion can offset the accuracy of fault current phasor calculation during short-duration faults, resulting in erroneous location estimates.

In addition to DC offset, saturation of a current transformer (CT) can also distort the fault current waveforms and introduce a significant error in location estimates. CT saturation is often caused by fault currents having a significant DC offset [7]. As the DC offset decays down within two or three cycles, the saturated CT may return to normal operating conditions. Therefore, for faults that last for a number of cycles, the best way to handle CT saturation is to wait for the DC offset to decay before applying

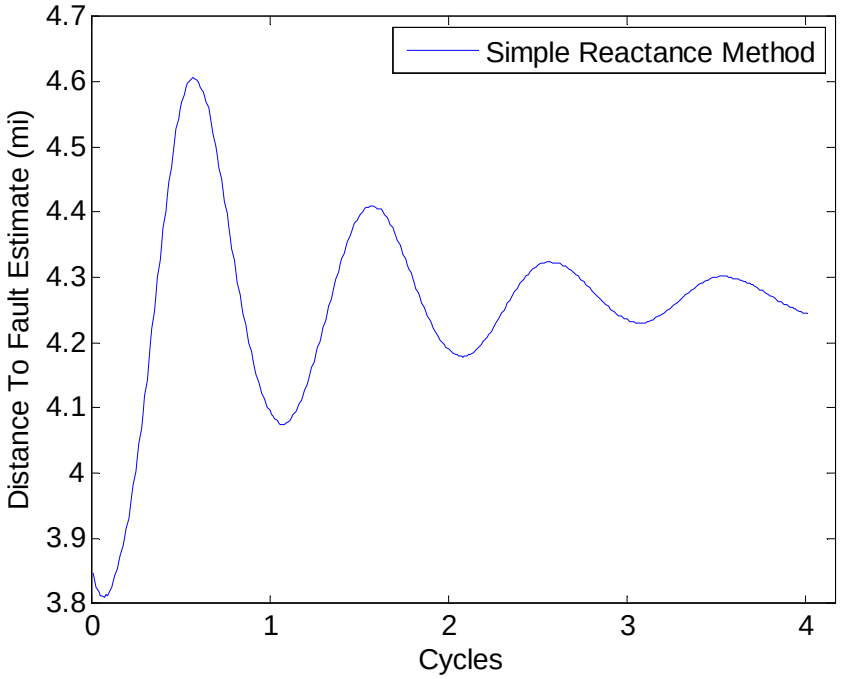

Figure 3.4: Variation in location estimates from the simple reactance method due to DC Offset. Voltage and current phasors were calculated using the FFT filter.

fault location algorithms.

3.2.2 Inaccurate Voltage Phasor: Delta-connected Potential Transformer

Impedance-based fault location algorithms require the input of line-to-ground voltages when computing the distance to a fault. When potential transformers are connected in a delta configuration, line-to-line voltages are available instead. The measured line-to-line voltages can be used by one-ended algorithms to estimate the location of line-to-line, double line-to-ground, or three-phase faults with no loss in accuracy. Line-to-ground voltages are, however, necessary to estimate the location of single line-to-ground faults [15]. If the zero-sequence impedance of the source, Z_{GO}, is available, then the line-to-ground voltage during a A-G fault can be estimated as

$$V_{AF} = \frac{1}{3}\left(V_{AB} - V_{CA}\right) - Z_{G0}I_{G0} \tag{3.1}$$

where V_{AF} is the estimated line-to-ground voltage of the faulted phase (phase A), V_{AB} is the line-to-line fault voltage measured between phases A and B, and V_{CA} is the line-to-line fault voltage measured between phases C and A. Accuracy of the estimated line-to-ground fault voltage depends on the accuracy of the zero-sequence source impedance.

3.2.3 Inaccurate Line Parameters: Untransposed Lines

Impedance-based fault location algorithms require the positive- and zero-sequence impedances of a transmission line to estimate the distance to a fault. When calculating the sequence line parameters, transmission lines are assumed to be transposed as explained in Appendix A. Transposition is the principle of physically exchanging the position of phase conductors at periodic intervals such that a particular conductor occupies all positions of a particular line configuration. This principle is illustrated in Fig. 3.5, where the positions of phase conductors A, B, and C are rotated every one-third of the total line length. Transposition equalizes the mutual coupling between the three phases and reduces the sequence impedance matrix, Z_{012}, to a diagonal matrix as shown in (3.2). The diagonal elements are formed by the sequence line impedances while the off-diagonal elements are zero, indicating no coupling between the sequence networks.

$$Z_{012} = \begin{bmatrix} Z_{L0} & 0 & 0 \\ 0 & Z_{L1} & 0 \\ 0 & 0 & Z_{L2} \end{bmatrix} \Omega \tag{3.2}$$

Although transposing a line is advantageous, it introduces complications in the design of a transmission line, and increases the overall design cost due to additional support structures and insulator string requirements. As a result, many transmission lines are not transposed. The sequence impedance matrix of an 18-mile long untransposed line having the same line configuration shown in Fig. 3.1 is:

$$Z_{012} = \begin{bmatrix} 15.47 + j32.52 & 0.26 + j0.00 & 0.26 + j0.00 \\ 0.26 + j0.00 & 5.33 + j15.15 & 0.00 - j1.02 \\ 0.26 + j0.00 & 0.00 - j1.02 & 5.33 + j15.15 \end{bmatrix} \Omega$$

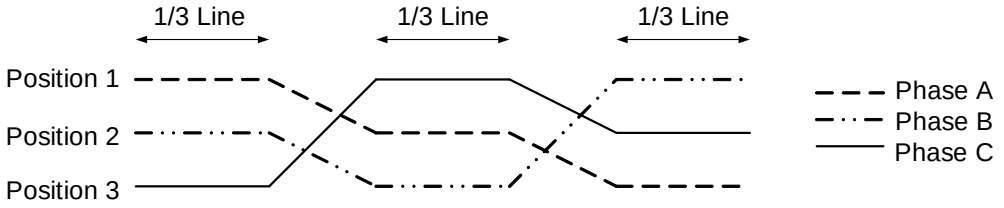

Figure 3.5: A transposed transmission line [5].

Observe that the off-diagonal elements are no longer zero. For example, $0.26+j0.00\,\Omega$ represents the coupling between the positive- and zero-sequence network. Since impedance-based fault location algorithms assume the sequence networks to be decoupled from each other, an untransposed transmission line will affect the accuracy of location estimates.

Figure 3.6 demonstrates the impact of untransposed lines on one- and two-ended fault-locating techniques. In the reference case (transposed line), single line-to-ground faults were simulated along the length of the transmission line in the 69-kV test case with $R_F = 0\,\Omega$. Distances to faults were computed by applying one-ended methods to the voltage and current recorded at terminal G. To apply two-ended methods, measurements captured at both terminals were used. Next, the transmission line in the test case was intentionally changed to an untransposed line and faults were simulated with the same value of R_F. Distances to faults were computed using the new set of voltage and current waveforms. The fault-location error was calculated as

$$\text{Error } (\%) = \frac{\text{Actual Location} - \text{Estimated Location}}{\text{Total Line Length}} \tag{3.3}$$

Because of the line transposition assumption, one-ended methods underestimate the location of a fault when compared against the reference case as shown in Fig. 3.6. The fault-location error increases as faults move farther away from the monitoring location. Two-ended methods are also affected by the line transposition assumption, the fault-location error being around 1.2%.

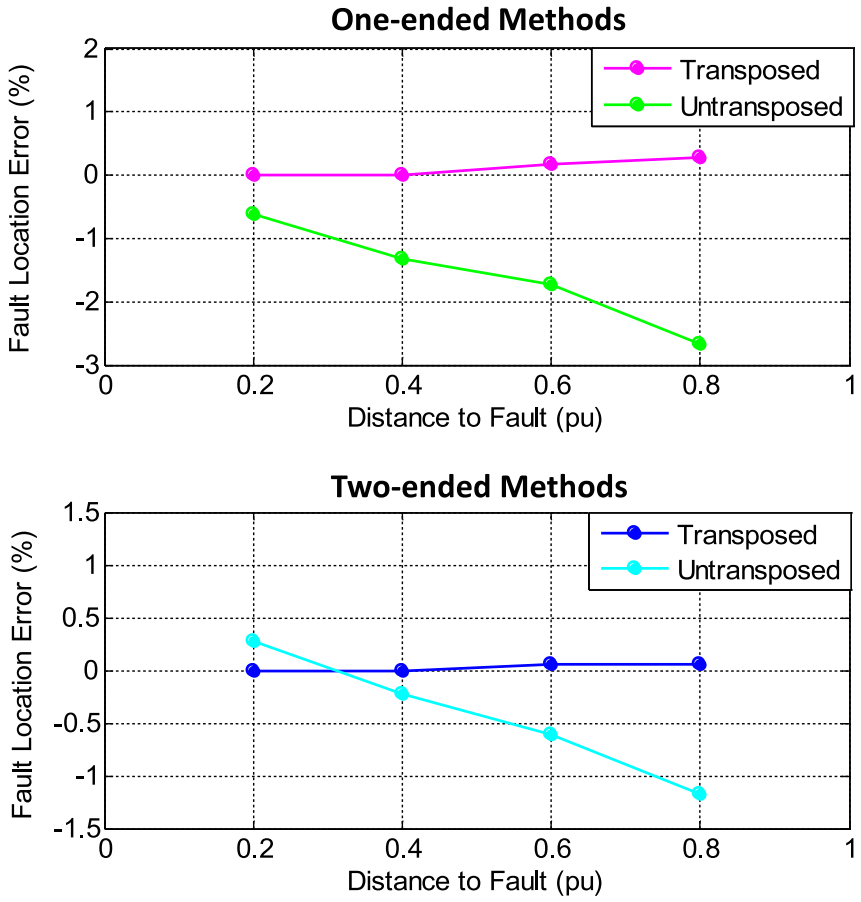

Figure 3.6: Error in fault location due to untransposed transmission lines.

3.2.4 Inaccurate Line Parameters: Uncertainty in Earth Resistivity

Earth resistivity ρ is the resistance with which the earth opposes the flow of electric current. It is an electrical characteristic of the ground and plays a critical role when calculating the zero-sequence impedance of a transmission line [3]. Determining the exact value of ρ is difficult since it varies greatly with the soil type as shown in Table 3.2. Most utilities use a standard earth resistivity value of 100 Ω m while others use the Wenner four-point method to measure ρ with great accuracy [43]. In addition to soil type, the value of ρ is also dictated by the moisture content in soils, temperature, and season of the year. Under extremely high or low temperatures, the soil is dry and

Table 3.2: Variation of Earth Resistivity with Soil Type [1]

Soil Type	Earth Resistivity (Ω m)	
	Range	Average
Peat	>1200	200
Adobe clay	2-200	40
Boggy ground	2-50	30
Gravel (moist)	50-3000	1000 (moist)
Sand and sandy ground	50-3000	200 (moist)
Stony and rocky ground	100-8000	2000
Concrete: 1 part cement + 3 parts sand	50-300	150

Table 3.3: Effect of Earth Resistivity on Line Impedance Parameters

ρ (Ω m)	Z_{L1} (Ω)	Z_{L0} (Ω)
10	$5.33 + j15.15$	$13.59 + j30.34$
100	$5.33 + j15.15$	$15.47 + j32.53$
500	$5.33 + j15.15$	$16.74 + j33.87$
1000	$5.33 + j15.15$	$17.28 + j34.40$

ρ increases ↓ ; Z_{L0} increases ↓

has a very high earth resistivity value. During the rainy season, the value of ρ decreases. Minerals, salts, and other electrolytes make soils more conductive and tend to lower the earth resistivity value. Put another way, earth resistivity is never constant and is never known accurately. Table 3.3 shows the impact of a varying earth resistivity value on the positive- and zero-sequence impedances of the 69-kV transmission line described in Section 3.1. The positive-sequence line impedance remains unaffected by changes in the value of earth resistivity. The zero-sequence line impedance, on the other hand, increases as ρ increases. Since one-ended fault location algorithms require the zero-sequence line impedance to compute the location of single line-to-ground faults, these methods are sensitive to any changes in earth resistivity.

As an example, the 69-kV test case was used to demonstrate the detrimental effect of ρ on one-ended methods. Single line-to-ground faults were simulated along the

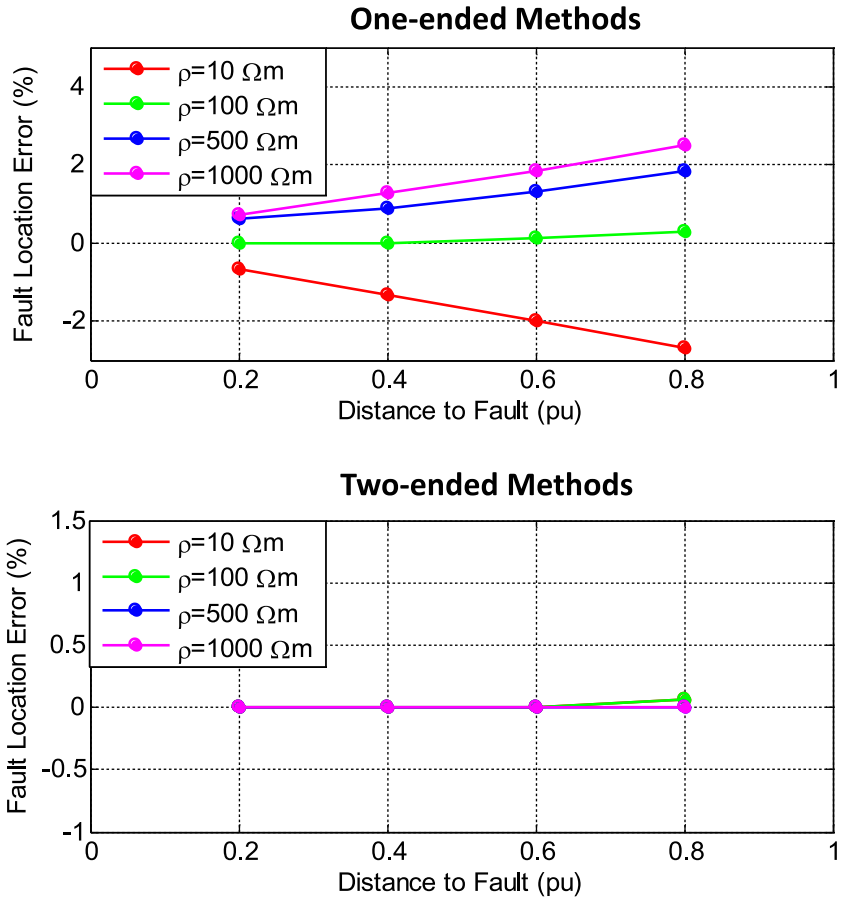

Figure 3.7: Error in fault location due to uncertainty in earth resistivity.

entire length of the transmission line with earth resistivity values ranging from 10 to 1000 Ω m. Line impedance parameters, used as an input to the fault location algorithms, were, however, calculated using the standard earth resistivity value of 100 Ω m. This case study reflects a practical scenario in which the resistivity of the soil can indeed vary over such a wide range. However, line impedance settings in a digital relay or a fault locator are computed using a particular value of ρ and do not reflect that change. As expected, the accuracy of one-ended methods are affected by the uncertainty in earth resistivity as shown in Fig. 3.7. When the actual value of earth resistivity is greater than the one used in the fault location computation, i.e., 100 Ω m, the distance to fault is overestimated.

Similarly, when ρ is lower than the value used in the fault location computation, the distance to fault is underestimated. Also observe that the fault-location error increases linearly as the fault moves farther away from the monitoring location. This is because the error due to inaccurate zero-sequence line impedance adds up as the line length between the monitoring location and the fault increases. In contrast, two-ended methods do not use zero-sequence line impedance when estimating the distance to fault and are hence, not affected by any variation in earth resistivity.

3.2.5 Inaccurate Line Parameters: Tower Footing Resistance

When calculating the phase impedance matrix of the transmission line, the neutral conductor is assumed to be perfectly grounded to the earth as described in Appendix A. In practice, shield wires are grounded to the earth through a finite tower footing resistance which has a value between 25 and 100 ohms as illustrated in Fig. 3.8. In the figure, span is the length of the transmission line between two adjacent towers and R_T is the tower footing resistance. The network formed by the shield wire and tower footing resistance is shown in Fig. 3.9 where Z_{nn} is the self-impedance of the earth wire per span. Since the neutral is no longer at earth potential, line impedance calculated using Kron reduction will be different from the actual line impedance and will affect the accuracy of fault location estimates.

To analyze the impact of tower footing resistance on the accuracy of impedance-based fault location algorithms, the test case described in Section 3.1 was used with certain additional modifications. The transmission line is 3.73 miles long and supported by transmission towers every 1000 feet as shown in Fig. 3.10. Arrangement of the phase and neutral conductors, and conductor material remain the same as those given by Fig. 3.1 and Table 3.1. Since the objective is to investigate the effect of tower grounding resistances on the accuracy of fault location algorithms, the transmission line is built as

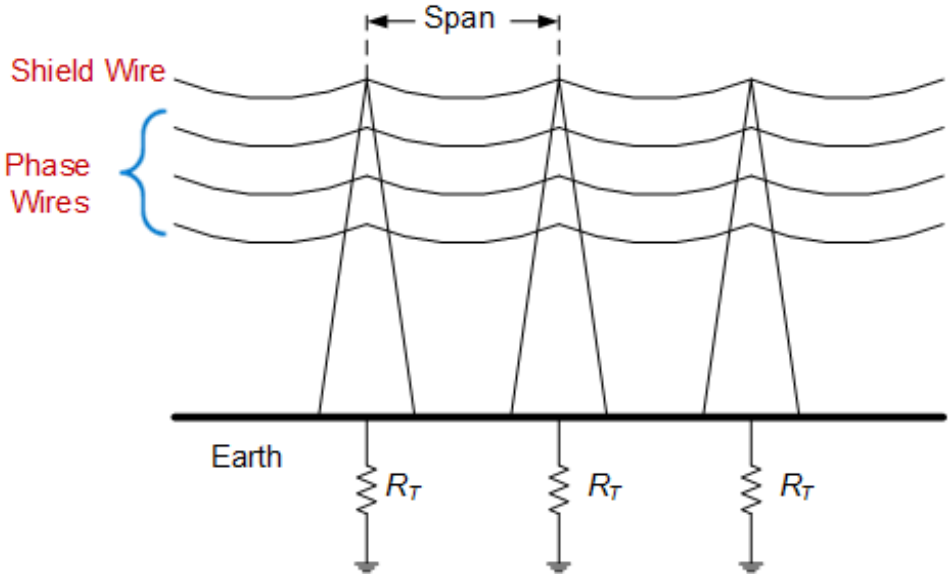

Figure 3.8: Shield wire grounded through tower footing resistances, R_T [6].

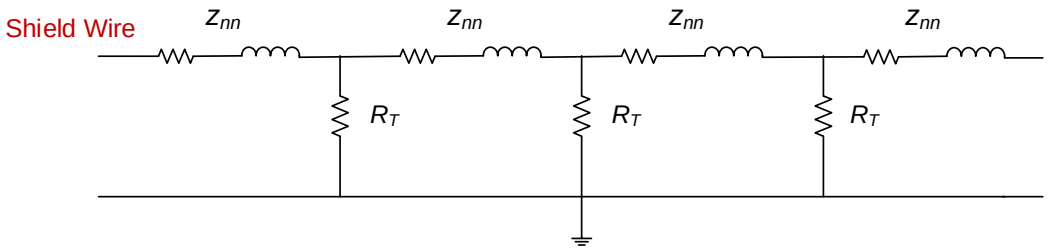

Figure 3.9: Network of the tower footing resistance and the shield wire impedance.

an n-phase model with a detailed representation of tower footing resistances as shown in Fig. 3.11. Note that in an n-phase model, all conductors are modeled explicitly in the simulation model. For example, in a three-phase system with two neutral conductors, the n-phase model will be modeled as a 5-conductor system.

Next, single line-to-ground faults were simulated at 0.75 mi, 1.86 mi, and 2.80 mi from the monitor. For each fault, the tower footing resistance at every tower was varied at the following values: $0\,\Omega$, $5\,\Omega$, and $20\,\Omega$. The goal was to investigate whether the magnitude of the tower footing resistance and the number of towers between the monitor and the fault play a significant role in the fault location accuracy. As seen in

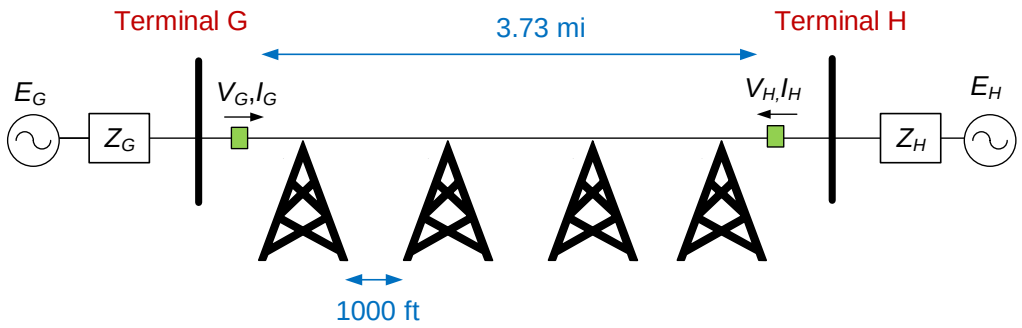

Figure 3.10: Transmission line of benchmark test case reduced to 3.73 miles and supported by towers every 1000 feet.

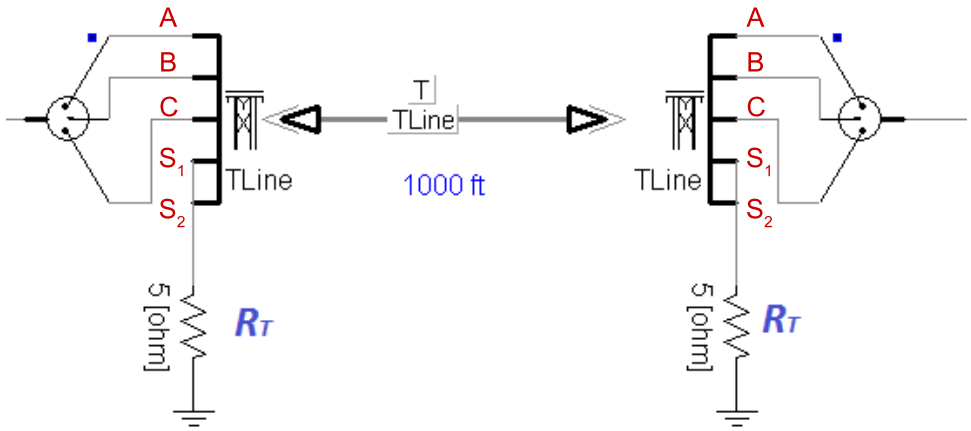

Figure 3.11: Transmission line modeled as an n-phase model in PSCAD with the two shield wires, S_1 and S_2, grounded through a tower footing resistance R_T.

Table 3.4, when the tower footing resistance is 0 Ω, estimates from the Eriksson method are accurate. However, for non-zero values of tower footing resistance, the fault location error increases. The percent error depends on how far the fault is from the monitor rather than on the magnitude of the tower footing resistance.

Fault location error from the one-ended methods can be explained by the fact that the tower footing resistance affects the value of the zero-sequence line impedance as shown in Fig. 3.5. The positive-sequence impedance of the line remains unchanged.

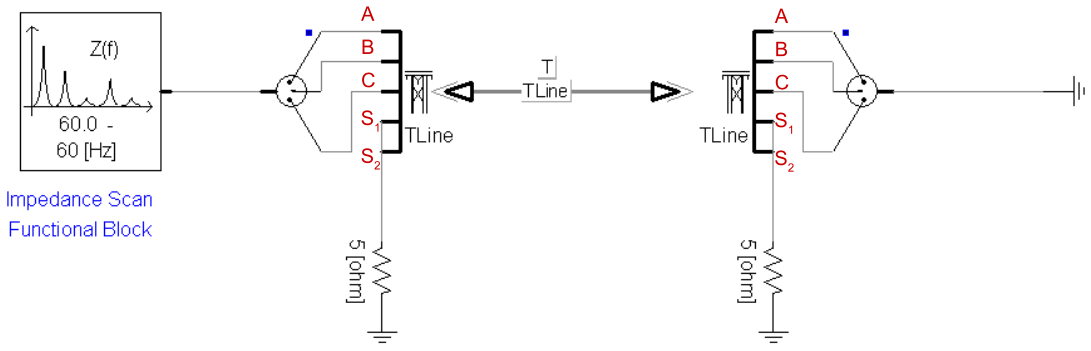

Figure 3.12: The impedance scan block in PSCAD was used to calculate the zero-sequence line impedance at different tower footing resistance values.

It should be noted that the impedance scan function block in PSCAD [47] was used to calculate the sequence line impedances at different values of tower footing resistance. This block is a powerful feature of PSCAD and generates the equivalent impedance matrix as seen from the interface point as shown in Fig. 3.12.

Distance to fault estimates from the two-ended unsynchronized negative-sequence method are shown in Table 3.6. Accuracy of this method is not affected by the presence of the tower footing resistance. This is because two-ended methods do not use zero-sequence line impedance in their fault location computation.

From the analysis described above, it can be concluded that the tower footing resistance affects the magnitude of the zero-sequence line impedance. Because the zero-sequence line impedance is required by one-ended methods to locate single line-to-ground faults, the accuracy of these methods are affected by the tower footing resistance. The increase in error is, however, marginal, around 4%. The analysis also concludes that the size of the tower footing resistance and the number of towers between the monitor and the fault have a negligible impact on one-ended methods. In contrast, two-ended methods are robust to the presence of the tower footing resistance.

Table 3.4: Impact of R_T on the Eriksson Method

Actual Location (mi)	Estimated Location (mi)		
	$R_T = 0\ \Omega$	$R_T = 5\ \Omega$	$R_T = 20\ \Omega$
0.75	0.74	0.78	0.78
1.86	1.85	1.96	1.96
2.80	2.78	2.94	2.95

Table 3.5: Effect of R_T on the Positive- and Zero-sequence Line Impedances

	$R_T = 0\ \Omega$	$R_T = 5\ \Omega$	$R_T = 20\ \Omega$
Zero-sequence Line Impedance (Ω)	$9.50\angle 70.8°$	$10.02\angle 78.3°$	$10.03\angle 78.5°$
Positive-sequence Line Impedance (Ω)	$3.25\angle 73.0°$	$3.25\angle 73.0°$	$3.25\angle 73.0°$

Table 3.6: Impact of R_T on the Unsynchronized Two-ended Method

Actual Location (mi)	Estimated Location (mi)		
	$R_T = 0\ \Omega$	$R_T = 5\ \Omega$	$R_T = 20\ \Omega$
0.75	0.75	0.75	0.75
1.86	1.86	1.86	1.86
2.80	2.80	2.80	2.80

3.2.6 Inaccurate Line Parameters: Earth Current Return Model

Transmission networks are not perfectly balanced due to untransposed lines, loads, and unbalanced faults. As a result, the residual current, which is the summation

of currents in all the three phases, flows back to the source through the neutral. Since transmission lines are multi-grounded systems, i.e., the neutral conductor is grounded at multiple points along the length of a transmission line, this return current is shared between the earth and neutral [63]. The current through the earth cannot penetrate deep into the ground due to a condition similar to skin effect [64]. Instead, they flow along the surface just underneath the conductor as shown in Fig. 3.13.

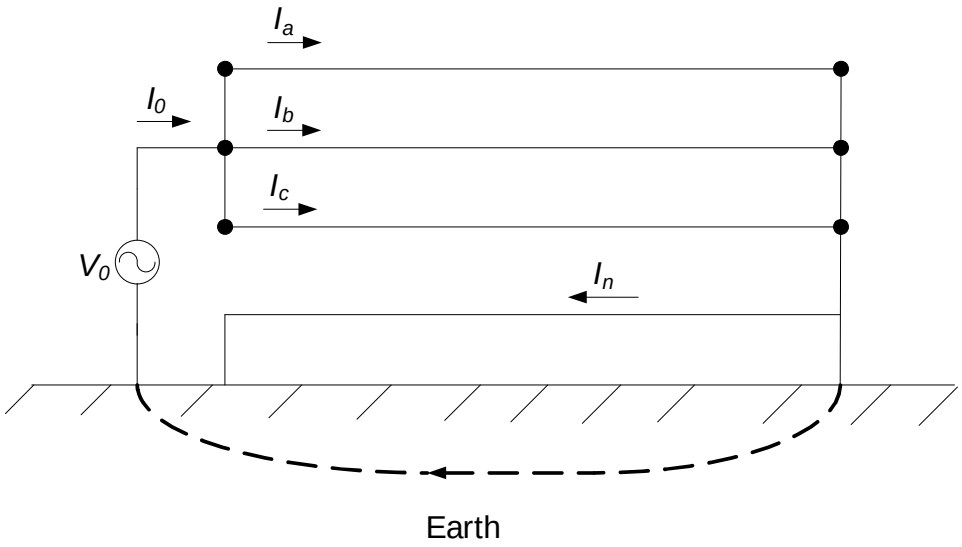

Figure 3.13: Earth current return in a three-phase four wire multi-grounded system [7].

To account for earth current return, three well known modeling methods are Full Carson's model, modified Carson's model, and Deri model. Equations governing each model are described in Appendix A. The motivation for the study stems from the fact that line constants calculated using each of the three models are not exactly identical. For example, Table 3.7 shows the line impedances of the transmission line in Fig. 9.19, solved using the different earth current return models at an earth resistivity value of 100 Ω-m. The positive-sequence line impedance from all the three models match relatively well. This is because the positive-sequence currents do not flow through the earth and is, hence, not affected by the earth model. The zero-sequence impedance, particularly

Table 3.7: Line Parameters using Different Earth Current Return Models

Earth Return Model	Z_{L1} (Ω/mi)	Z_{L0} (Ω/mi)
Full Carson's Model	$6.01 + j19.00$	$19.72 + j56.23$
Modified Carson's Model	$6.01 + j19.00$	$19.82 + j55.93$
Deri Model	$5.92 + j19.00$	$19.95 + j56.53$

the zero-sequence reactance, show minor differences. Since transmission lines travel over wide geographical distances, seemingly minor differences in line constant values can affect the accuracy of fault location estimates.

To investigate how line constants calculated using different earth return models affect the accuracy of impedance-based fault location algorithms, actual fault event data described in Section 9.4 was used. Using actual fault data is advantageous since no assumptions about the earth need to be made. Results are, therefore, not biased. The approach consists of using line constants, calculated using each of the three earth models, as an input to the Takagi method. As observed from Table 3.8, estimates using each of the three modeling methods yield almost identical results and are close to the actual location of the fault. Also note that the results are not consistent for the same fault event. For example, for events 1 and 2, the modified Carson's model yields location estimates that are close to the actual fault location. In events 3 and 4, on the other hand, Deri model is more accurate. The inconsistency is due to other factors such as DC offset which influence the accuracy of location estimates. Therefore, the analysis concludes that any of the three earth modeling techniques can be used for fault location computation without any significant variation in accuracy.

Table 3.8: Fault Location Estimates using Line Parameters Computed by Different Earth Return Models

Event	Earth Return Model	Fault Location (mi)	
		Estimated	Actual
Event 1	Full Carson's Model	14.20	
1/10/2012	Modified Carson's Model	14.24	
12:44:38.413	Deri Model	14.15	
Event 2	Full Carson's Model	14.07	
1/10/2012	Modified Carson's Model	14.12	
12:44:38.897	Deri Model	14.03	14.37
Event 3	Full Carson's Model	14.46	
1/10/2012	Modified Carson's Model	14.50	
12:59:41.532	Deri Model	14.41	
Event 4	Full Carson's Model	14.63	
1/10/2012	Modified Carson's Model	14.68	
12:59:41.999	Deri Model	14.59	

3.2.7 Inaccurate Line Parameters: Non-homogeneous Lines

Both one- and two-ended impedance-based fault location algorithms assume a homogeneous overhead feeder with a uniform impedance per unit mile. However, practical utility distribution feeders are constructed using different conductor types and pole configurations. As an example, a 7.6-mile long utility circuit can be constructed as follows: 0.13 miles using 2-ACSR phase and neutral conductors, 1.25 miles using 336-AAC phase and 1/0-ACSR neutral conductors, and 6.23 miles using 556-AAC phase and 336-AAC neutral conductors. Such a non-homogeneous feeder can affect the accuracy of impedance-based fault location algorithms. A comprehensive analysis conducted in [55] concludes that the fault location accuracy in non-homogeneous feeders may be preserved by using the line impedance parameters of the most commonly occurring line conductor. In this example, this means using the positive- and zero-sequence line impedances of the 556-AAC phase and 336-AAC neutral configuration.

3.3 Fault Location Error due to Application Challenges

Impedance-based fault location techniques described in Chapter 2 make certain simplifying assumptions. The accuracies of location estimates are compromised when these assumptions do not hold true because of load, non-homogeneous system, and double-circuit transmission lines. The task of locating faults is further complicated by tapped radial lines or three-terminal transmission networks. The objective of this Section is to evaluate the error in fault location due to such application related challenges.

3.3.1 System Load

This Section investigates the impact of system load on the accuracy of impedance-based fault location algorithms. System load as an error source is particularly dominant in distribution feeders. To conduct the analysis, the 69-kV case was used to simulate single line-to-ground faults at several locations of the 18-mile long transmission line with different values of δ and R_F. Recall that δ represents the net load served by the transmission network. One-ended fault location algorithms use voltage and current captured at terminal G while two-ended algorithms use waveforms captured at both line ends.

When the fault resistance is zero, location estimates from the simple reactance method are accurate, even under heavily loaded conditions as shown in Fig. 3.14. Note that a power angle of 20° corresponds to a load current of 430 A. For non-zero values of fault resistance, however, the same values of load current cause a reactance error in the simple reactance method. The reactance error is capacitive and the simple reactance method underestimates the location of faults. The fault-location error is further magnified when the load and fault resistance is increased to 40° and 15 Ω, respectively. It is also interesting to observe the increase in reactance error as the distance to fault increases in Fig. 3.14. When faults occur towards the end of the transmission line, the fault current contribution from the local terminal decreases. The load current constitutes a significant

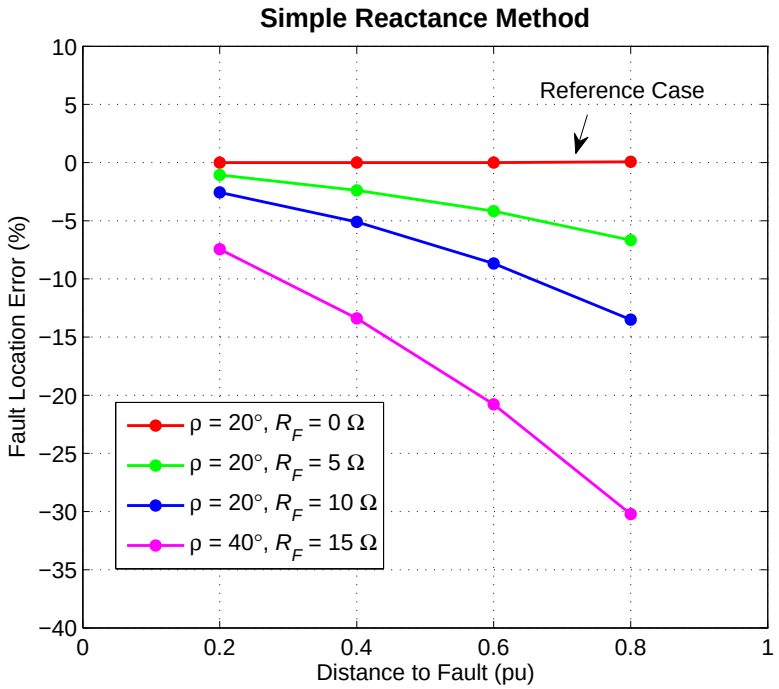

Figure 3.14: Reactance error due to load in the simple reactance method.

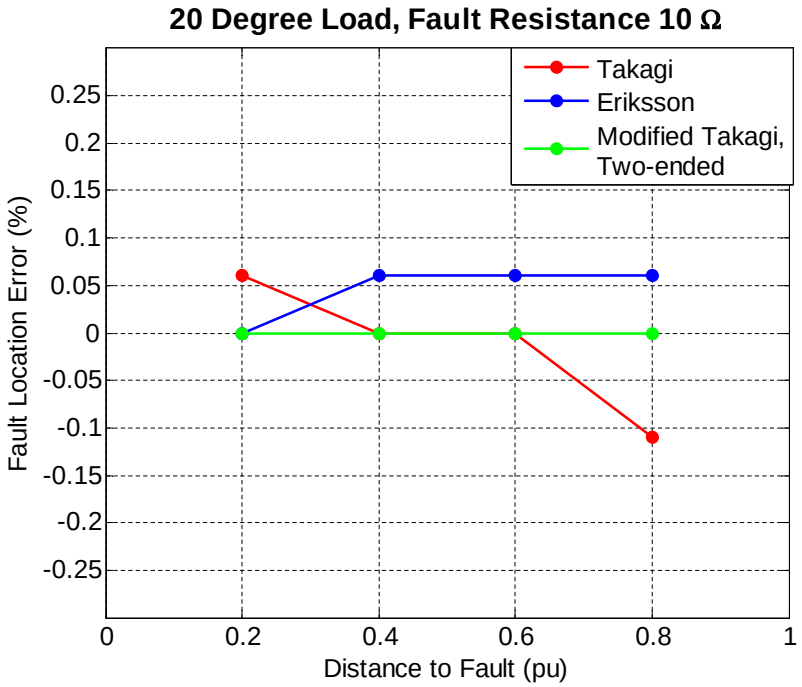

Figure 3.15: Load has no impact on the Takagi, Modified Takagi, Eriksson, and Two-ended methods.

percent of the total fault current and increases the phase angle mismatch between I_F and I_G. For example, when a fault occurs at 0.8 per unit from terminal G, the load current is 28% of the fault current recorded at terminal G. As a result, the reactance error increases.

Takagi method uses the "pure fault" current to minimize the reactance error due to load. As shown in Fig. 3.15, the reactance error is negligible when $R_F = 10\,\Omega$ and $\delta = 20°$. Modified Takagi, Eriksson, and two-ended methods are also not affected by an increase in the system load.

3.3.2 Non-homogeneous System

To demonstrate the effect of a non-homogeneous system on impedance-based fault location algorithms, the 69-kV benchmark test case was used. The test case is homogeneous since the local and remote source impedances have the same angle as the line impedance and hence, serves as the reference case. Single line-to-ground faults were simulated along the entire length of the transmission line with $\delta = 1°$ and $R_F = 5\,\Omega$. To compute the location of faults, one-ended methods use voltage and current waveforms at terminal G while two-ended methods use voltage and current measurements at both terminals. Next, the system is intentionally made non-homogeneous by changing the value of Z_{G1} to $15\angle 50°\,\Omega$. Faults were simulated using the same values of fault resistance and load. Location estimates from one and two-ended methods, computed using the new set of voltage and current measurements, were compared with those obtained in the reference case (homogeneous system) as shown in Fig. 3.16. As expected, the accuracy of simple reactance and Takagi methods deteriorate in a non-homogeneous system. The Eriksson method uses the remote source impedance to improve upon the performance of the Takagi method. The modified Takagi and two-ended methods are also robust to the increase in non-homogeneity and remain unaffected.

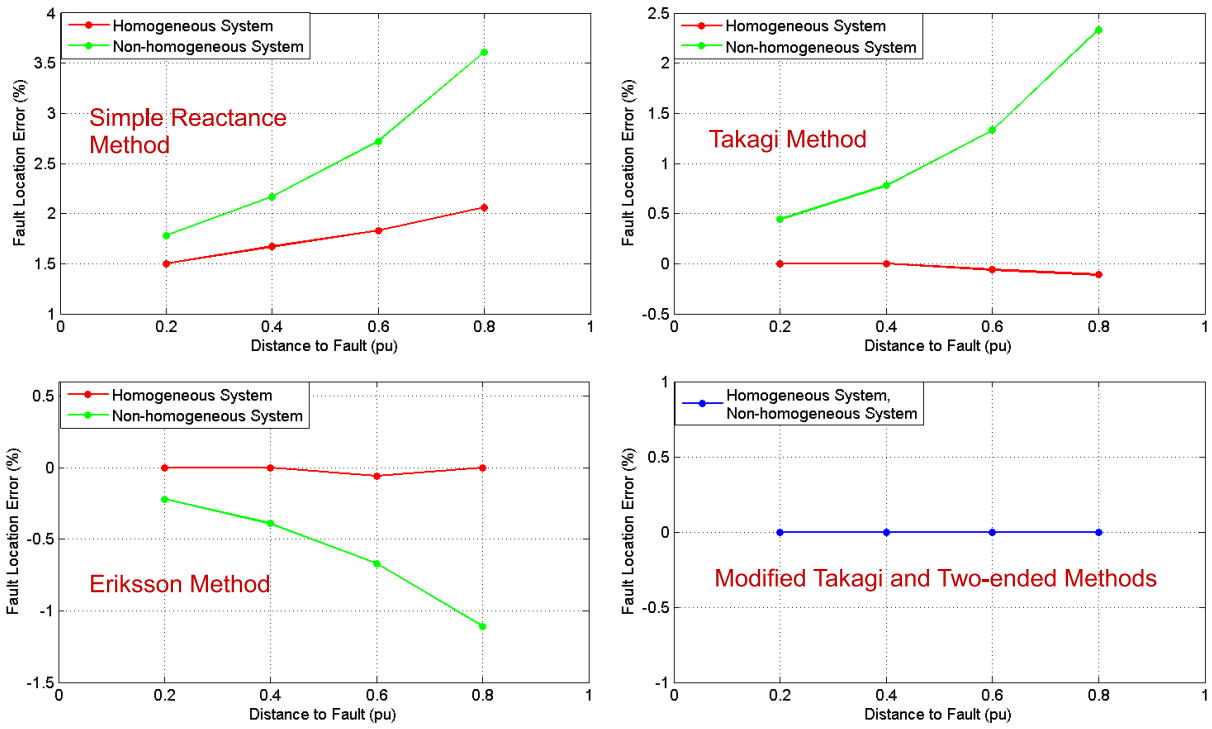

Figure 3.16: Effect of a non-homogeneous system on impedance-based fault location algorithms.

3.3.3 Parallel Lines

In transmission networks, it is common to find transmission lines that are physically parallel to each other. Two three-phase lines may be supported by the same tower or they may run on two separate towers but share the same right of way. Because of the mutual coupling between two lines, the impedance to fault calculation is influenced by currents flowing in the parallel line, thereby compromising the accuracy of location estimates. As an example, consider the double-circuit transmission network shown in Fig. 3.17. The rated voltage at terminals G and H is 69 kV. Source impedance parameters Z_G and Z_H have the same values as those used in Section 3.1. The transmission line is 18 miles long and has the configuration of an actual 69-kV double-circuit transmission line as shown in Fig. 3.18. Phase conductors A, B, and C represent Line 1 in Fig. 3.17 while phase conductors A', B', and C' represent Line 2. Materials used to build

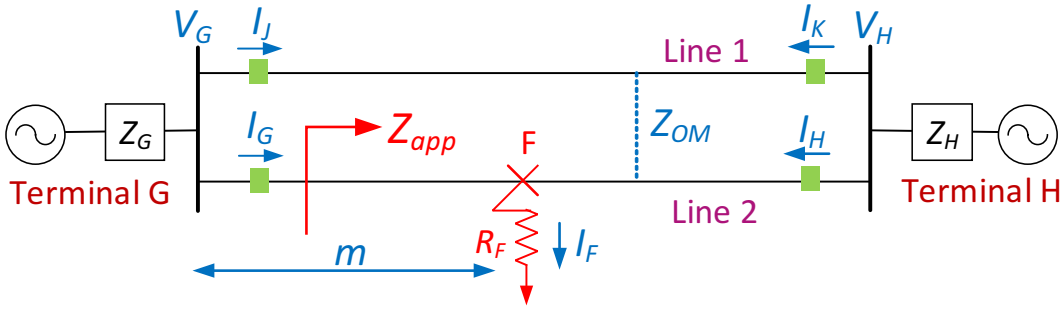

Figure 3.17: Double-circuit transmission network.

the conductors are the same as those described in Table 3.1. Assuming both lines to be completely transposed and using an earth resistivity value of 100 Ω m, the sequence impedance matrix Z_{012} of the transmission line is given as

$$Z_{012} = \begin{bmatrix} 15.82 + j40.91 & 0 & 0 & 10.52 + j25.77 & 0 & 0 \\ 0 & 5.33 + j12.92 & 0 & 0 & 0 & 0 \\ 0 & 0 & 5.33 + j12.92 & 0 & 0 & 0 \\ 10.52 + j25.77 & 0 & 0 & 15.82 + j40.91 & 0 & 0 \\ 0 & 0 & 0 & 0 & 5.33 + j12.92 & 0 \\ 0 & 0 & 0 & 0 & 0 & 5.33 + j12.92 \end{bmatrix} \Omega$$

Here, the off-diagonal term $10.52 + j25.77\ \Omega$ represents the zero-sequence mutual coupling (Z_{0M}) between two parallel lines and will always be present, regardless of whether the line is transposed or not. Observe that Z_{0M} is significant, around 63% of the zero-sequence line impedance. Because of Z_{0M}, the apparent impedance measured at terminal G during a fault on Line 2 changes and can be written as

$$Z_{app} = \frac{V_G}{I_G} = mZ_{L1} + mZ_{0M}\left(\frac{I_{J0}}{I_G}\right) + R_F\left(\frac{I_F}{I_G}\right) \tag{3.4}$$

where I_{J0} is the zero-sequence current in the parallel transmission line. If the two lines are parallel to each other for the entire line length, then Z_{0M} can be taken into consideration by simply measuring I_{J0} and inputting the value to (3.4). However, many different configurations of parallel lines are possible. For example, two lines may start parallel to each other from one terminal but end at two different terminals [65]. In such cases, the term $mZ_{0M}\,(I_{J0}/I_G)$ will affect the accuracy of distance-to-fault estimates.

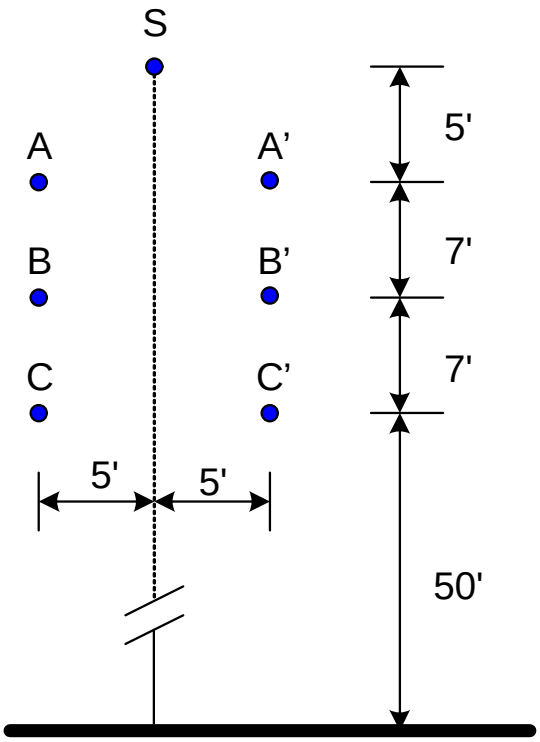

Figure 3.18: Configuration of an actual 69-kV double-circuit transmission line.

If current I_G flows in the same direction as the current in the parallel line, I_J, then one-ended fault locating techniques will overestimate the location of the fault. On the other hand, if currents I_G and I_J flow in opposite directions, one-ended methods will underestimate the location of the fault [13].

To evaluate the impact of Z_{OM} on impedance-based fault location algorithms, the test case described in Fig. 3.17 was used. Analysis begins by first developing a reference case wherein there is no zero-sequence mutual coupling between the two lines. In reality, this is possible only when the two parallel lines are far apart from each other. Single line-to-ground faults were simulated at various locations of Line 2 with $R_F = 0\,\Omega$ and a load angle of $\delta = 10°$. To compute the location of faults, one-ended methods use the voltage and current waveforms at terminal G while two-ended methods use waveforms at both ends of the line. Next, Z_{0M} was intentionally introduced in the base case and the same

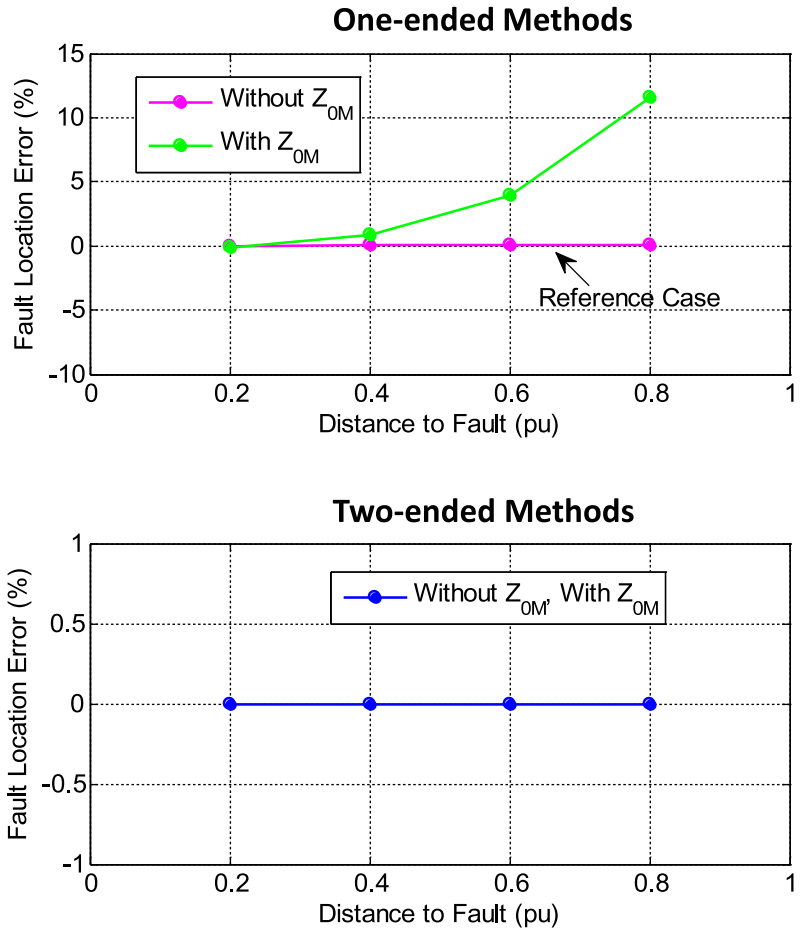

Figure 3.19: Impact of zero-sequence mutual coupling on impedance-based fault location algorithms.

faults were simulated on Line 2. Location estimates computed using the new waveforms were then compared with those obtained in the reference case to obtain the increase in fault-locating error due to Z_{0M}. As shown in Fig. 3.19, all one-ended methods are equally affected by Z_{0M}. The increase in fault-locating error is around 10% at the far end of the line. Note that in this analysis, Z_{0M} was not compensated by I_{J0} in the parallel line.

The two-ended synchronized or the two-ended unsynchronized methods do not use the zero-sequence network when computing the distance to a fault. As a result, they are not affected by Z_{0M} as shown in Fig. 3.19. The unsynchronized current-only

two-ended method is also not affected by Z_{0M}. However, this method does require the knowledge of negative-sequence currents I_{J2} and I_{K2} flowing in the parallel transmission line. This is because I_{J2} and I_{K2} cause an additional voltage drop across the source impedances Z_G and Z_H and if neglected, will cause an error in the location estimates. Recall from Section 2.2.3 that the unsynchronized current-only two-ended method solves for the distance to fault m by the quadratic equation given in (2.23). For double circuit lines, constants a and b change and are defined as follows:

$$a + jb = I_{G2}Z_{G2} + I_{J2}Z_{G2} - I_{K2}Z_{H2}$$

The other constants remain the same. The unsynchronized current-only two-ended method is not affected by the different configurations of parallel transmission lines.

3.3.4 Three-terminal Lines

Impedance-based fault location algorithms in Chapter 2 have been primarily developed for a two-terminal transmission line and can be extended to locate faults on a radial distribution feeder. However, the application scenario changes in the case of a three-terminal line as shown in Fig. 3.20. One-ended fault location algorithms are accurate up to the tap point only. When a fault occurs beyond the tap point, the fault current contributed by the third terminal (terminal T) modifies the impedance to fault equation and results in a significant error in location estimates. For example, consider the fault shown in Fig. 3.20. The apparent impedance measured from terminal G is:

$$Z_{app} = \frac{V_G}{I_G} = mZ_{L1} + (m - D)\, Z_{L1}\frac{I_T}{I_G} + R_F\left(\frac{I_F}{I_G}\right) \tag{3.5}$$

where I_T is the fault current contributed by terminal T and D is the distance of the tap point from terminal G. Since one-ended algorithms at terminal G have no knowledge about I_T, the term $(m - D)\, Z_{L1}\, (I_T/I_G)$ will cause one-ended methods to overestimate the location of the fault. Moreover, current I_F is the summation of I_G, I_H, and I_T. As

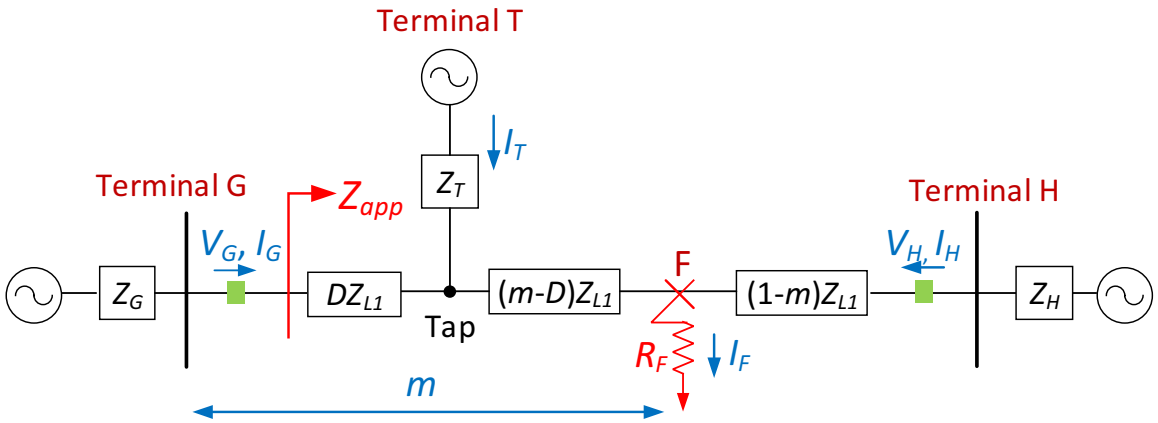

Figure 3.20: Three-terminal transmission line.

a result, I_F and I_G have different phase angles in a non-homogeneous system and will introduce an additional reactance error. Depending on whether the reactance error is inductive or capacitive, distance to fault is over or underestimated. One-ended methods applied from terminal H, on the other hand, can successfully estimate the location of fault F. Since the fault is located before the tap point, the fault current contributed by terminals G and T act as remote infeed only and do not alter the apparent impedance measured from terminal H. Therefore, the solution in the case of three-terminal lines is to apply one-ended methods from each terminal. One of the three estimates will successfully pinpoint the exact location of the fault as demonstrated in the case study described in Section 3.4.3. Two-ended algorithms can be extended for application to three-terminal lines with certain additional modifications. For instance, authors in [21] transform a three-terminal line into an equivalent two-terminal line and then apply the unsynchronized current-only two-ended method.

3.3.5 Tapped Radial Line

Locating faults on a radial feeder tapped from a two-terminal transmission line is a challenging task for impedance-based fault location algorithms. When a fault occurs

in the line section between the tap point and the load, as illustrated by F in Fig. 3.21, the apparent impedance measured from terminal G is the same as that given by (3.5). One-ended algorithms make use of measurements captured at only one end of the line. Therefore, neglecting the fault current contributed by terminal H will cause one-ended methods to overestimate the fault location.

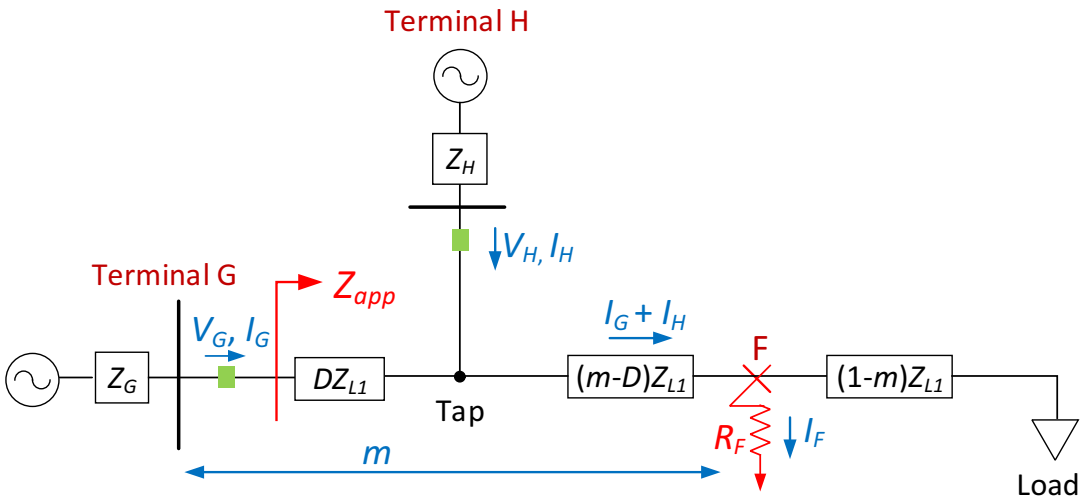

Figure 3.21: Fault on a radial feeder tapped from a two-terminal line.

Measurements captured at both ends of a line can be used to improve the accuracy of location estimates. The first step is to confirm whether the fault is located on the radial line. This is achieved by calculating the voltage at the tap point during fault, V_{Tap}, from terminals G and H as shown below:

$$\text{Terminal G:} \qquad V_{Tap} = V_G - DZ_{L1}I_G \tag{3.6}$$

$$\text{Terminal H:} \qquad V_{Tap} = V_H \tag{3.7}$$

If the fault is on the radial line, V_{Tap} calculated from terminal G will equal that calculated from terminal H. This is because terminals G and H operate in parallel to feed the fault on the radial line. Next, (3.5) can be used to compute the distance to fault.

3.4 Application of Impedance-based Fault Location Algorithms to Field Data

This Section demonstrates the application of impedance-based fault location algorithms on actual fault event data captured in utility transmission and distribution networks. Data consists of voltage and current waveforms recorded by digital relays and digital fault recorders, line impedance parameters, and known location of the fault. Each event was chosen to highlight a unique aspect of impedance-based fault location.

3.4.1 Event 1: Lightning Strike on a 161-kV Transmission Line - Successful Fault Location from One-ended Methods

On 12 June 2011, a lightning strike caused a line-to-line fault between phases B and C of a 161-kV transmission line at 1:33 pm. The transmission line is radial and has a total length of 12.58 miles. The positive- and zero-sequence line impedances are $Z_{L1} = 1.38 + j9.32\,\Omega$ and $Z_{L0} = 5.88 + j25.86\,\Omega$, respectively. According to the utility, the fault is located 7.54 miles from Station 1 as shown in Fig. 3.22. A digital fault recorder at Station 1 captures the three-phase line-to-ground voltages and currents during the fault at 100 samples per cycle as shown in Fig. 3.23. Before the fault, Station 1 supports a load current of 110 A. During the fault, the current magnitude increases to 3.5 kA in the faulted phases. The fault lasts for three cycles, after which the fault current is interrupted by the operation of a circuit breaker at Station 1.

To estimate the distance to fault, one-ended fault location algorithms were applied to the voltage and current waveforms captured at Station 1. Notice that the fault currents have a significant DC offset. Therefore, to minimize the effect of DC offset, the third cycle after fault inception was selected for computing the distance to fault as illustrated in Fig. 3.23. Because the transmission line is radial in nature, Novosel *et al.* method was used instead of the Eriksson method. The positive-sequence source impedance (Z_{G1}), required as an additional input to the Novosel *et al.* method, was

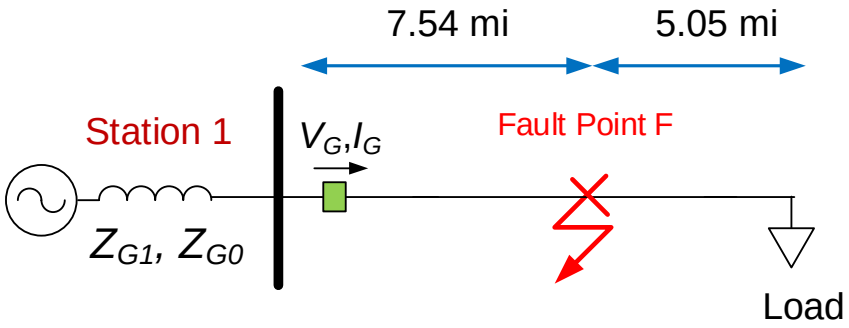

Figure 3.22: Event 1 is a BC fault at 7.54 miles from Station 1.

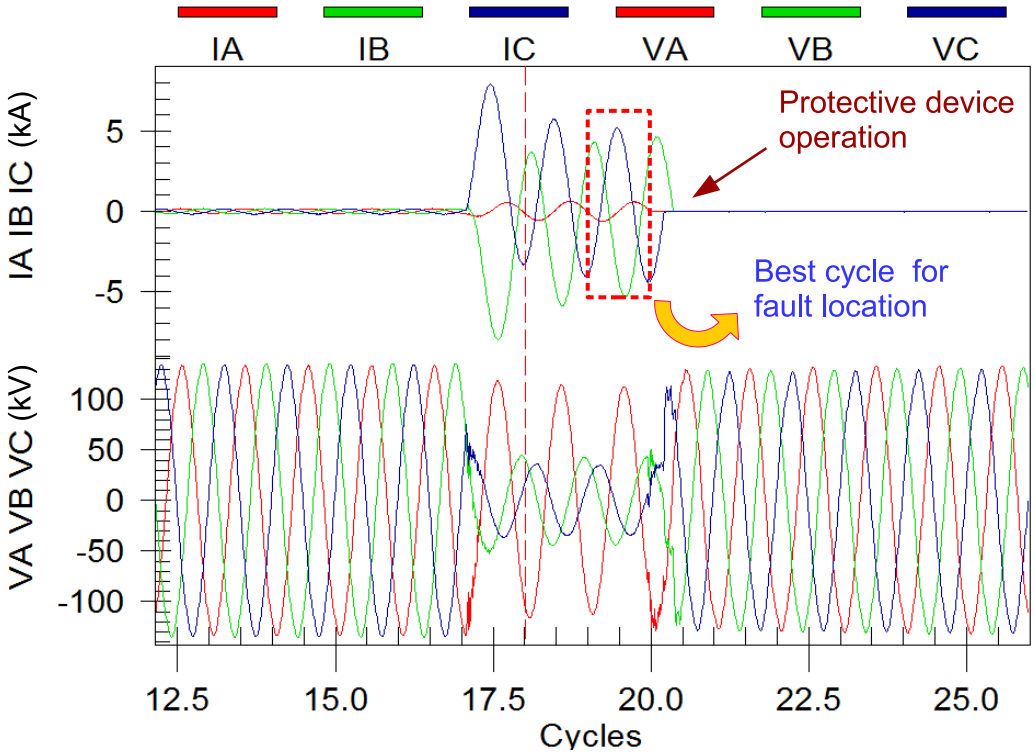

Figure 3.23: Event 1 waveforms captured by the DFR at Station 1.

computed using (8.44) to be $4.03 + j20.22\,\Omega$. As seen from Table 3.9, location estimates from one-ended algorithms are in agreement with that estimated by the DFR and are close to the actual location of the fault. In summary, this event demonstrates the success of one-ended algorithms in tracking down the exact location of a fault.

Table 3.9: Event 1 Fault Location Estimates from One-ended Methods

Station	Actual Location (mi)	DFR Estimate (mi)	Estimated Location (mi)		
			Simple Reactance	Takagi	Novosel *et al.*
1	7.54	7.60	7.34	7.38	7.35

3.4.2 Event 2: Bird Contact with a 161-kV Transmission Line - Superior Performance of Two-ended Methods over One-ended Methods

Event 2 is a single line-to-ground fault event on phase A that occurred on 29 March 2012 at 7:28 pm. The fault was caused by birds coming in contact with a 161-kV transmission line that connects Station 1 with Station 2 as shown in Fig. 3.24. The transmission line is 31.30 miles long and has a total positive- and zero-sequence line impedance of $Z_{L1} = 5.00 + j25.27\ \Omega$ and $Z_{L0} = 23.67 + j79.40\ \Omega$, respectively. The actual distance to the fault is known to be 30.86 miles from Station 1 or 0.44 miles from Station 2 as shown in Fig. 3.24.

Digital fault recorders at Station 1 and Station 2 record the voltage and current waveforms at 96 samples per cycle. Before the fault, load currents at Station 1 and Station 2 are 89 A and 70 A, respectively. During the fault, the circuit breaker at Station 2 measures a fault current magnitude of 5.86 kA and trips in 2.5 cycles as seen from

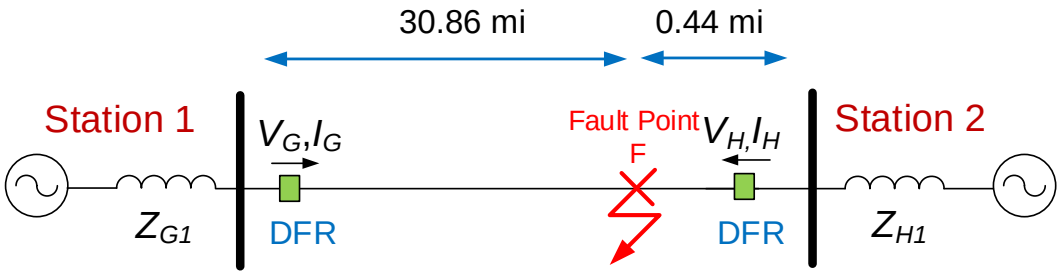

Figure 3.24: Event 2 is a A-G fault 30.86 miles from Station 1 or 0.44 miles from Station 2.

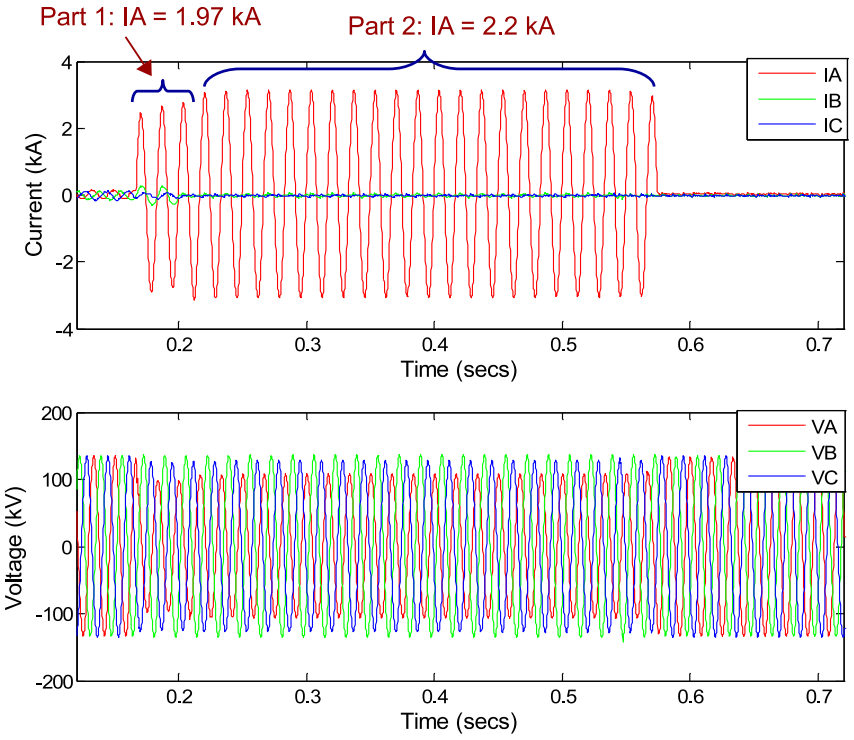

(a) DFR measurements at Station 1.

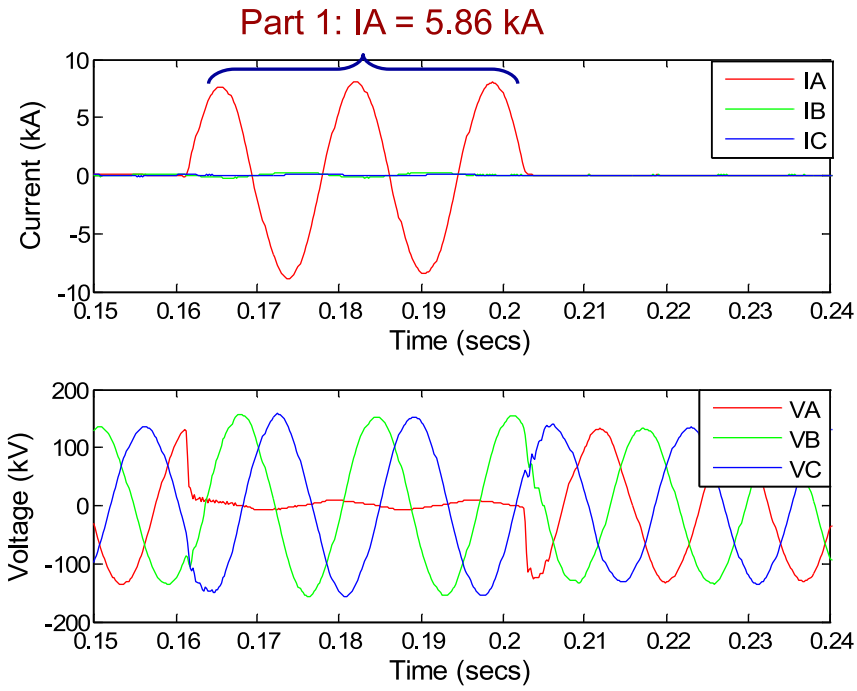

(b) DFR measurements at Station 2.

Figure 3.25: Event 2 waveforms captured at both line ends.

Fig. 3.25(b). Station 1, on the other hand, continues to contribute fault current for 22.5 cycles. During the first 2.5 cycles, when both stations are feeding the fault, the DFR at Station 1 records a fault current of 1.97 kA as indicated by "Part 1" in Fig. 3.25(a). After 2.5 cycles, when Station 2 trips offline due to the operation of a circuit breaker, fault current contributed by Station 1 increases to 2.2 kA as illustrated by "Part 2" in Fig. 3.25(a).

To compute the location of the fault from Station 1, impedance-based fault locating algorithms were applied to "Part 2" of the waveform data. This is because in "Part 2", only Station 1 contributes current to the fault without remote infeed from Station 2. As a result, location estimates are expected to be accurate. Unfortunately, as observed from Table 3.10, the distance to fault estimates are offset from the actual fault location by 7 miles. In addition to the one-ended methods, the DFR present at Station 1 also underestimates the location of the fault by 5 miles. Although the source of error is not apparent, an erroneous estimate from the Eriksson method rules out fault resistance, non-homogeneous system, and load current as possible sources of error. It is possible that the zero-sequence line impedance parameter is incorrect and may have offset the accuracy of location estimates. Distance to fault computed from Station 2 waveforms, on the other hand, are close to the actual location of the fault. Note that the source impedance parameters, required as an input to the Eriksson method, were estimated using (8.44) to be $Z_{G1} = j11.71\,\Omega$ and $Z_{H1} = 0.11 + j11.73\,\Omega$.

To investigate whether two-ended methods can improve the accuracy of location estimates, the unsynchronized current-only two-ended method was chosen since the DFRs at Station 1 and Station 2 have different fault trigger times. The waveforms are, therefore, unsynchronized. The two-ended method was applied to that part of the fault wherein both stations are contributing to the fault, i.e.,"Part 1" of Station 1 and Station 2 waveforms. As seen from Table 3.11, the location estimate from the two-ended method

shows a significant improvement over the one-ended methods. Recall that two-ended methods do not require zero-sequence line impedance in their fault location calculation. In summary, this event highlights the superior performance of two-ended methods over one-ended methods in computing the distance to a fault.

Table 3.10: Event 2 Location Estimates from One-ended Methods

Station	Actual Location (mi)	DFR Estimate (mi)	Estimated Location (mi)		
			Simple Reactance	Takagi	Eriksson
1	30.86	25.70	23.80	23.79	23.87
2	0.44	0.50	0.50	0.48	0.47

Table 3.11: Event 2 Location Estimate from Two-ended Methods

Station	Actual Location (mi)	Estimated Location (mi)
1 and 2	30.86	29.34

3.4.3 Event 3: Lightning Strike on a 161-kV Transmission Line - Incorrect Application or Inaccurate Input Causes Two-ended Methods to Fail

On 14 September 2011, a double line-to-ground fault occurred between phases A and B of a 161-kV transmission line at 6:23 pm. The fault was caused by a lightning strike during stormy weather conditions. The transmission line experiencing fault is 46.25 miles long and connects Station 1 with Station 2 as shown in Fig. 3.26. The positive- and zero-sequence impedances of the transmission line are $Z_{L1} = 7.26 + j36.70\,\Omega$ and $Z_{L0} = 29.34 + j108.24\,\Omega$, respectively. The actual location of the fault was reported by the utility to be 29.49 miles from Station 1 or 16.76 miles from Station 2.

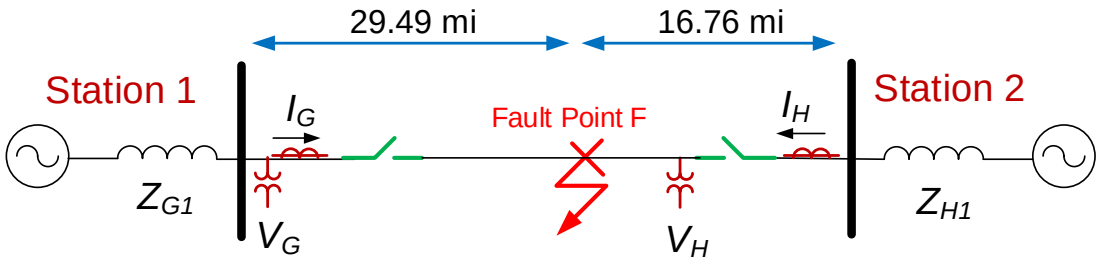

Figure 3.26: Event 3 is a AB-G fault 29.49 miles from Station 1.

Table 3.12: Event 3 Location Estimates from One-ended Methods

Station	Actual Location (mi)	DFR Estimate (mi)	Estimated Location (mi)		
			Simple Reactance	Takagi	Eriksson
1	29.49	49.10	49.27	49.43	49.65
2	16.76	16.60	16.68	16.66	16.65

A digital fault recorder (DFR), present at Station 1, records the voltage and current waveforms during the fault at 100 samples per cycle as shown in Fig. 3.27(a). A DFR at Station 2 also records the voltage and current waveforms at 96 samples per cycle as shown in Fig. 3.27(b). Prefault currents from Station 1 and 2 are 120 A and 70 A, respectively. During the fault, Station 1 records a current magnitude of 1.9 kA in phases A and B, and Station 2 records a current magnitude of 3.2 kA in the faulted phases. After 2.5 cycles, the fault is cleared by the operation of a circuit breaker at either line end. Since this is a short-duration fault, the FFT operation was performed on the second cycle after fault inception to minimize the effect of DC offset. Also observe that the voltage at Station 2 goes to zero once the fault is cleared from the circuit, indicating that the voltage measurements are captured by a line PT downstream from the breaker as illustrated in Fig. 3.26.

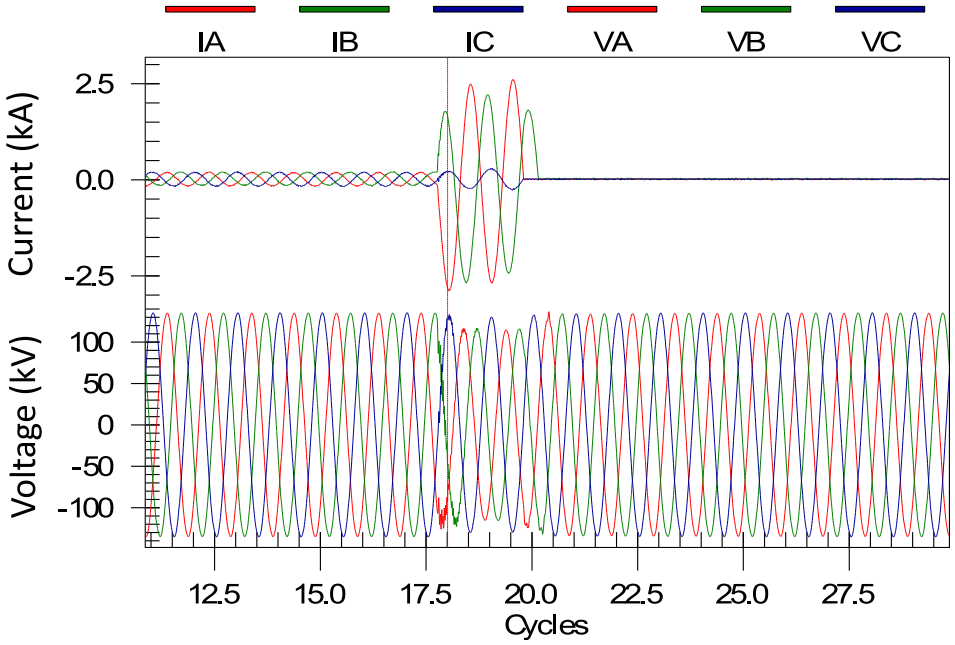

(a) DFR measurements at Station 1, IA = IB = 1.9 kA.

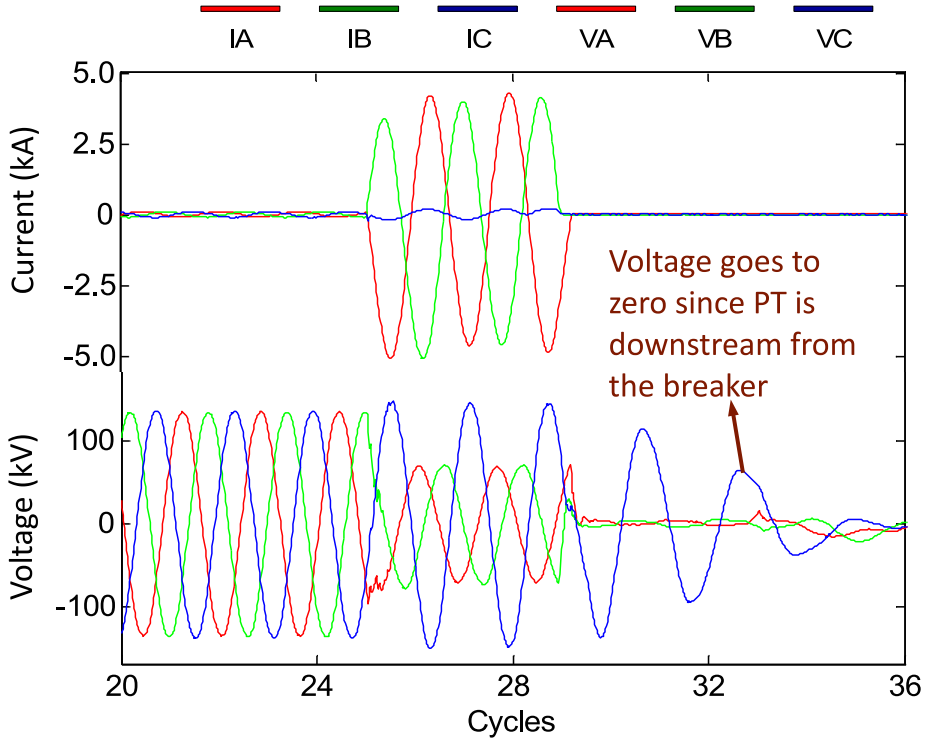

(b) DFR measurements at Station 2, IA = IB = 3.2 kA.

Figure 3.27: Event 3 waveforms captured at both line ends.

Table 3.13: Event 3 Location Estimate from Two-ended Methods

Station	Actual Location (mi)	Estimated Location (mi)
1 and 2	29.49	37.41

Table 3.12 lists the distance to fault estimates from one-ended fault location algorithms. Source impedances at Stations 1 and 2, required as an input to the Eriksson method, were estimated using (8.44) to be $Z_{G1} = 0.67 + j9.58\,\Omega$ and $Z_{H1} = 1.26 + j14.44\,\Omega$, respectively. As shown in Table 3.12, one-ended fault location techniques are successful in pinpointing the exact location of the fault from Station 2. The same fault-locating algorithms, however, overestimate the location of the fault from Station 1. The actual location of the fault is 29.49 miles from Station 1 while one-ended methods estimate the distance to be around 49.65 miles. The location estimate from the DFR at Station 1 also show a considerable error of 19.6 miles.

In an effort to improve the accuracy of location estimates, two-ended fault location techniques were implemented using measurements from both ends of the transmission line. Since the DFRs at Station 1 and Station 2 have different sampling rates, measurements are not synchronized. Therefore, the unsynchronized two-ended method was used. Surprisingly, the location estimate from the two-ended method also show a considerable fault-location error of 8 miles as shown in Table 3.13.

To explain the error in fault location from Station 1, recall that two-ended methods are robust to fault resistance, load current, non-homogeneous system, zero-sequence mutual coupling, and an uncertain value of zero-sequence line impedance. Therefore, the above sources of fault-locating error were ruled out. Furthermore, since the one-

ended location estimates from Station 2 are accurate, it is reasonable to assume that the positive-sequence line impedance is also accurate. The fact that the distance to fault from Station 1 was overestimated indicates a strong possibility of a third generating station between Station 1 and the fault as illustrated in Fig. 3.28. The fault current from Station 3, I_T, increases the apparent impedance measured at Station 1. As a result, one- and two-ended algorithms overestimate the location of the fault from Station 1. One-ended fault location estimates computed from only one of the three terminals, Station 2 in this case, was accurate as discussed in Section 3.3.4. In summary, this event highlights the importance of the user being aware of the fault-locating application scenario. The two-ended algorithm failed not because of limitations in the algorithm but because it was not meant for use in a three-terminal line. Another possibility that can explain the fault location error from Station 1 is inaccurate CT ratio or other scaling issues in the digital fault recorder settings at Station 1.

3.4.4 Event 4: A-G Fault Location on a 34.5-kV Distribution Feeder with Line-to-Line Voltages

On 21 June 2010, a 34.5-kV distribution feeder experienced a single line-to-ground fault on phase A at 22:03 hours as shown in Fig. 3.29. The circuit model of the distri-

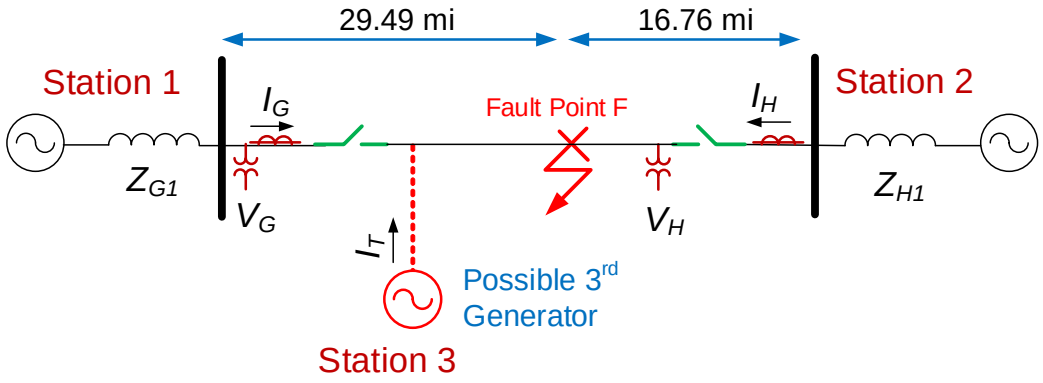

Figure 3.28: A third station is suspected to be present between Station 1 and the fault.

bution feeder is available in APEN OneLiner software and is shown in Fig. 3.30. The distribution feeder has a positive- and zero-sequence line impedance of $z_{L1} = 0.11 + j0.60$ Ω/mile and $z_{L0} = 0.39 + j2.62$ Ω/mile, respectively. A SEL-251D relay [66], present at the substation for overcurrent protection, records the three-phase line currents and the line-to-line voltages at four samples per cycle as shown in Fig. 3.31. The relay measures 180 A before the fault and 2212 A during the fault. The root-cause and the actual location of the fault are unknown.

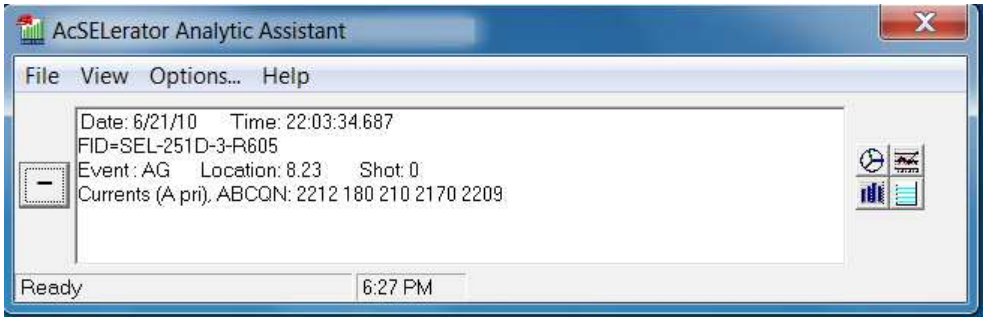

Figure 3.29: Event 4 fault event log from the SEL-251D relay.

One-ended impedance-based fault location algorithms require the input of line-to-ground voltages when calculating the distance to a single line-to-ground fault. In this event, because line-to-line voltages are available instead of the line-to-ground voltages, the line-to-ground voltage of the faulted phase was calculated using (3.1) to be 17.53 kV. Note that the zero-sequence source impedance, required for calculating the line-to-ground voltage in (3.1), was obtained from the circuit model as $Z_{G0} = 0.02 + 2.97$ Ω. The fault-distance estimates are shown in Table 3.14.

Although the actual fault location is not known, the circuit model can be used to ascertain the accuracy of the distance-to-fault estimates in Table 3.14. For example, the SEL relay estimates the fault location to be 8.23 miles. To test the accuracy of this location

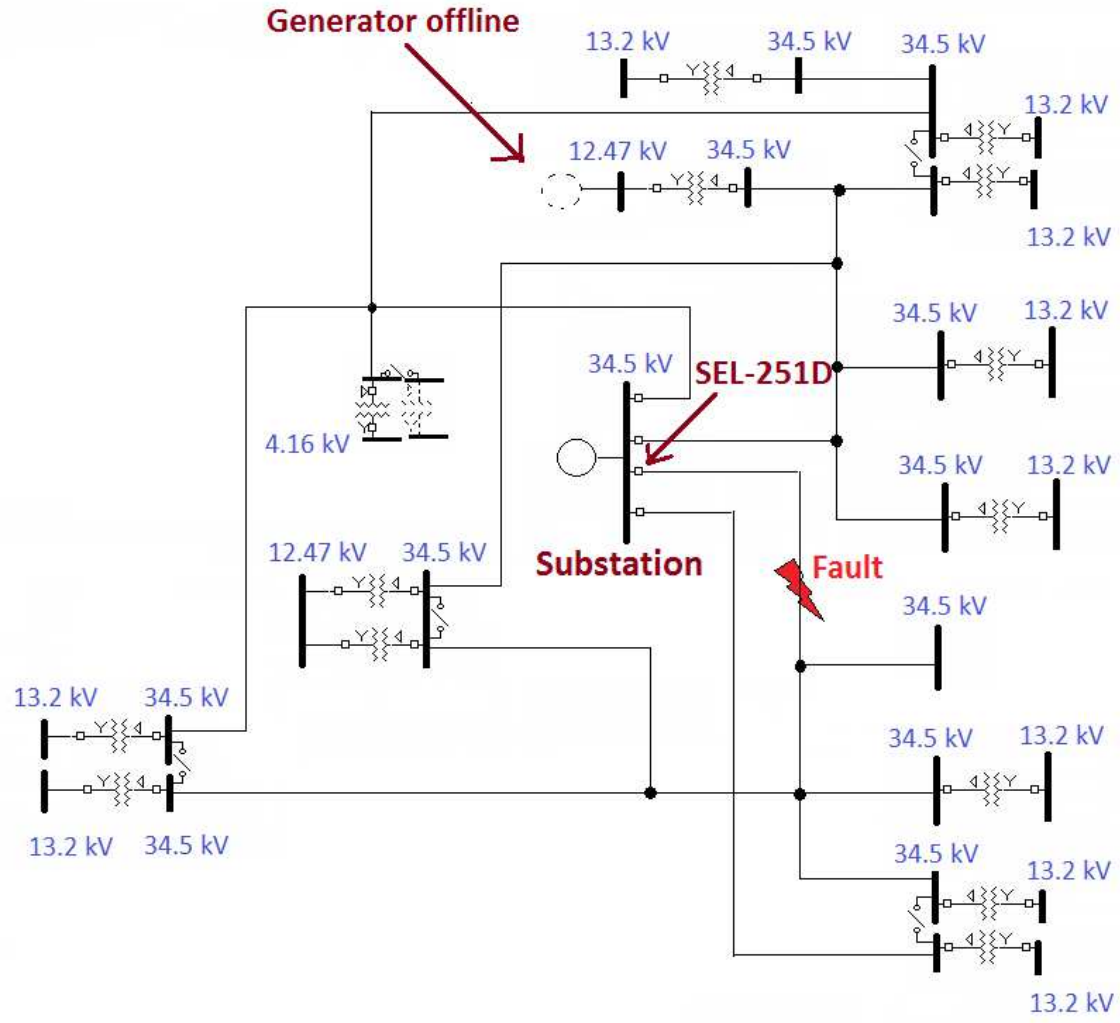

Figure 3.30: Event 4 utility circuit model in ASPEN OneLiner.

Table 3.14: Event 4 Location Estimates from One-ended Methods

	Distance Estimate (mi)	Model Short-circuit Current (kA)	Actual Fault Current (kA)
SEL Relay	8.23	1.59	
Takagi	5.65	2.29	2.21
Simple Reactance	5.59	2.33	

estimate, a phase A-to-ground fault was simulated in the ASPEN circuit model at 8.23 miles from the substation with zero fault resistance. The bolted fault assumption is rea-

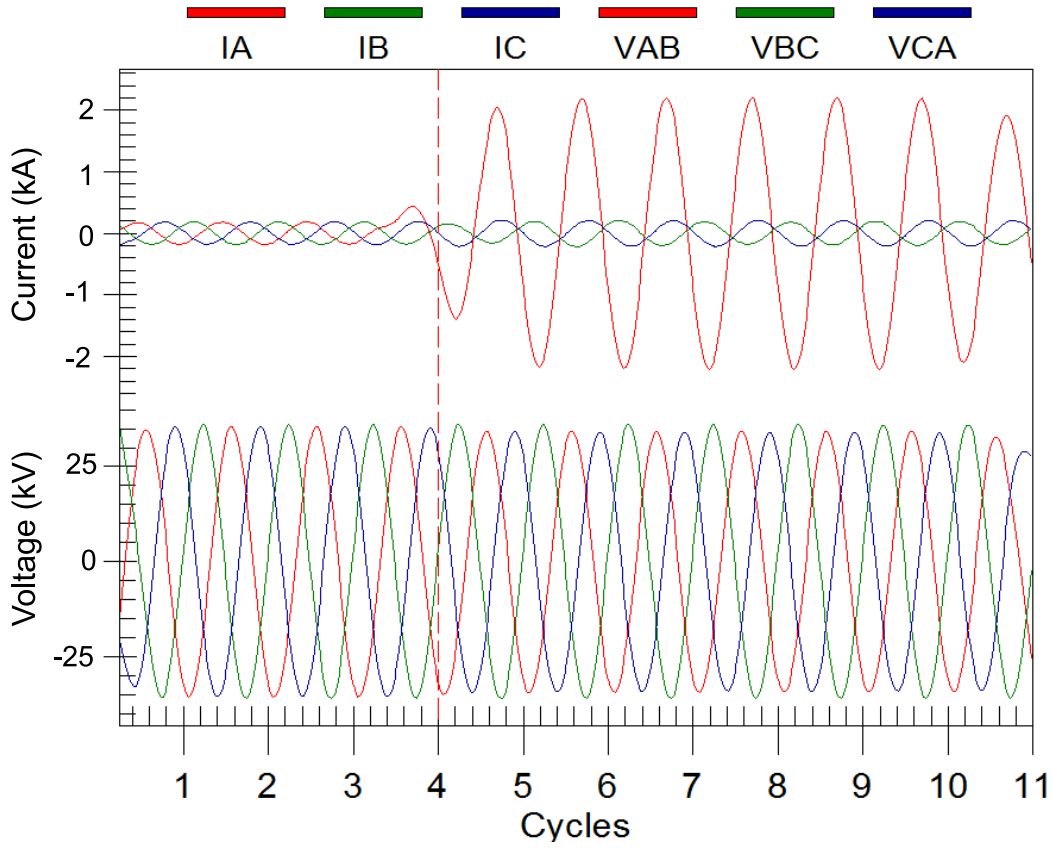

Figure 3.31: Event 4 line currents and line-to-line voltages recorded by the SEL-251D relay.

sonable since the Takagi method did not show a significant improvement over the simple reactance method in Table 3.14, indicating that the simple reactance did not suffer from a reactance error. The location estimate of 8.23 miles corresponds to a short-circuit current of 1.59 kA in the circuit model. A lower short-circuit current than the actual fault current suggests that the SEL relay has overestimated the location of the fault. Perhaps the line impedance and source impedance relay settings were incorrect. Estimates from the simple reactance and Takagi methods are close to the actual fault location since the model short-circuit currents match well with that recorded by the relay. In summary, this event illustrates the procedure for locating single line-to-ground faults when the relay records line-to-line voltages.

3.4.5 Event 5: Tree Contact Fault with a 34.5-kV Distribution Feeder - Challenging Fault with a Variable Fault Resistance

Event 5 is a line-to-line fault that occurred between phases B and C of a 34.5-kV distribution feeder on 27 June 2010 at 4:01 am as shown by the fault event log in Fig. 3.32. The distribution feeder is 2.42 miles long and has a positive- and zero-sequence line impedance of $Z_{L1} = 0.88 + j1.21\,\Omega$ and $Z_{L0} = 2.00 + j2.96\,\Omega$, respectively. A SEL-351A relay [67] at the substation records the three-phase line currents and line-to-ground voltages at four samples per cycle as shown in Fig. 3.33. The relay estimates the fault location to be 1.55 miles while the distribution utility reports the actual fault location to be 0.95 miles from the substation. The fault was caused by two large trees which fell on the primary feeder. After trimming the trees, maintenance personnel were able to restore power back to the customers.

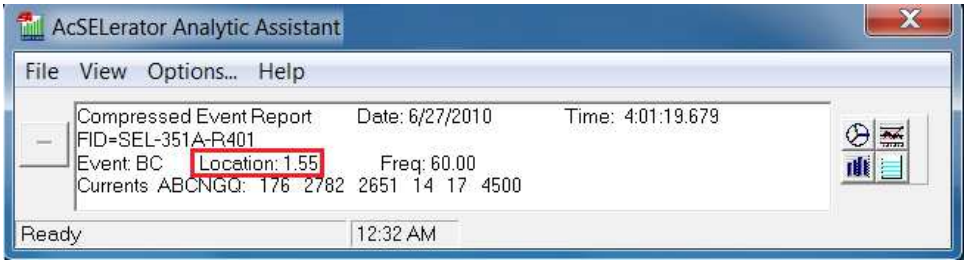

Figure 3.32: Event 5 fault event log from the SEL-351A relay.

Initially, the fault has a high fault resistance and the SEL relay records a fault current magnitude of 1.8 kA in phases B and C. After 7.5 cycles, the fault resistance decreases and the fault current magnitude increases to 2.7 kA. Therefore, in order to avoid any fault location error due to fault resistance, the thirteenth cycle was selected for fault location purposes. The simple reactance method estimates the distance to fault to be 1.18 miles from the substation which is close to the actual fault location. None of the other one-ended fault location methods could be used due to absence of prefault data.

Now, we must explain the fault location error of 0.6 miles from the SEL relay.

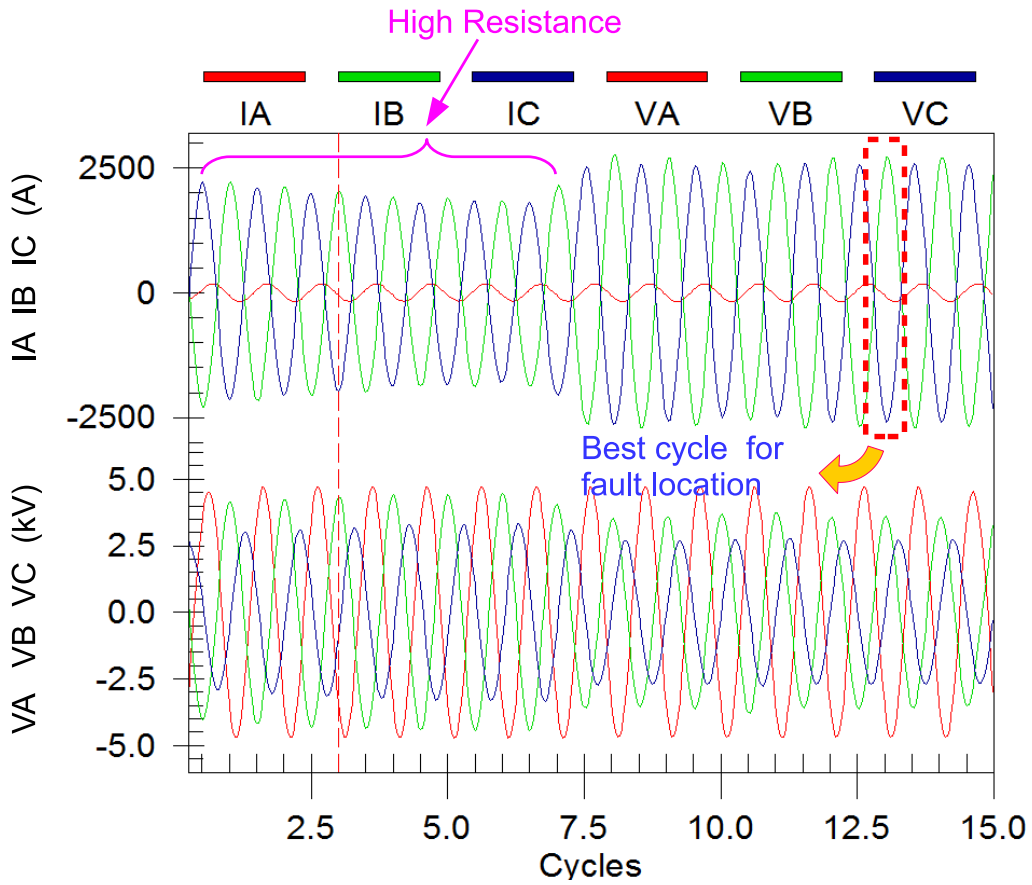

Figure 3.33: Event 5 waveforms recorded by the SEL-351A relay. Initially IB = IC = 1.8 kA. After 7.5 cycles, IB = IC = 2.7 kA.

Typically, SEL relays choose a cycle in the center of the fault window to estimate the distance to a fault. Note that the fault window starts from the onset of a fault and extends up to the cycle when the fault clears. Unfortunately, in this event, the center cycle coincides with the time when the fault resistance dramatically changes from a high to a low value. Since fault location algorithms assume a constant fault resistance, the changing fault resistance and timing of the fault resistance change leads to an error in the location estimate. To summarize, this event demonstrates the challenge faced by automated fault location systems in locating faults having a variable fault resistance. An offline analysis is necessary to choose the best cycle for determining the fault location.

3.4.6 Event 6: Transformer Inrush Mistaken as a Fault on a 4.16-kV Distribution Feeder - Filtered vs. Unfiltered Events

On 15 December 2012, a SEL-351S distribution relay [68] recorded a three-phase fault event at 2:07 am as shown by the fault event log in Fig. 3.34. The distribution feeder has a rated voltage of 4.16 kV, and a positive and zero-sequence line impedance of $z_{L1} = 0.15 + j0.13\ \Omega$/mile and $z_{L0} = 0.15 + j0.13\ \Omega$/mile, respectively. The relay allows utility operators to retrieve two types of event reports: filtered and unfiltered (raw) events as illustrated in Fig. 3.35. The unfiltered waveform is the digitized version of the analog waveform recorded by a current transformer and contains the power frequency, harmonic frequencies, CT saturation, and DC offset. The filtered waveform is a mathematically generated waveform, processed by a cosine filter which rejects all other frequencies except the 60 Hz frequency. The filtered currents waveforms are shown in Fig. 3.36. Although the relay has characterized the fault as an ABC event, the fault does not look to be balanced. Notice how the phase C current starts off with a very high magnitude of 0.9 kA and then decays to 0.3 kA. Currents in the other two phases also have a small magnitude of 0.2 kA. Applying one-ended impedance-based fault-locating algorithms to the third cycle yields a distance estimate of 40.21 miles which seems unlikely.

To find out what the relay actually "saw" during the time of the event, let's take a look at the unfiltered waveform in Fig. 3.37. The unfiltered current has unipolar peaks that decay with time which is a signature characteristic of a transformer inrush event. In other words, this was not a fault event and hence, incorrect application of impedance-based fault location algorithms resulted in the fault location error.

In summary, this event highlights the importance of downloading both filtered and unfiltered event reports from the relay for fault location analysis. Although filtered events are useful for fault calculations, important information may be lost. Unfiltered

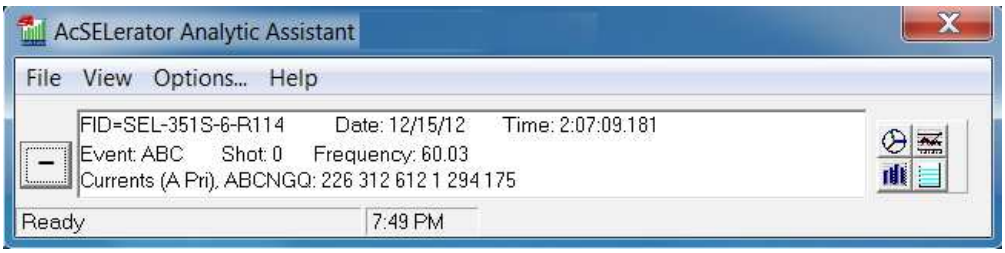

Figure 3.34: Event 6 fault event log from the SEL-351S relay.

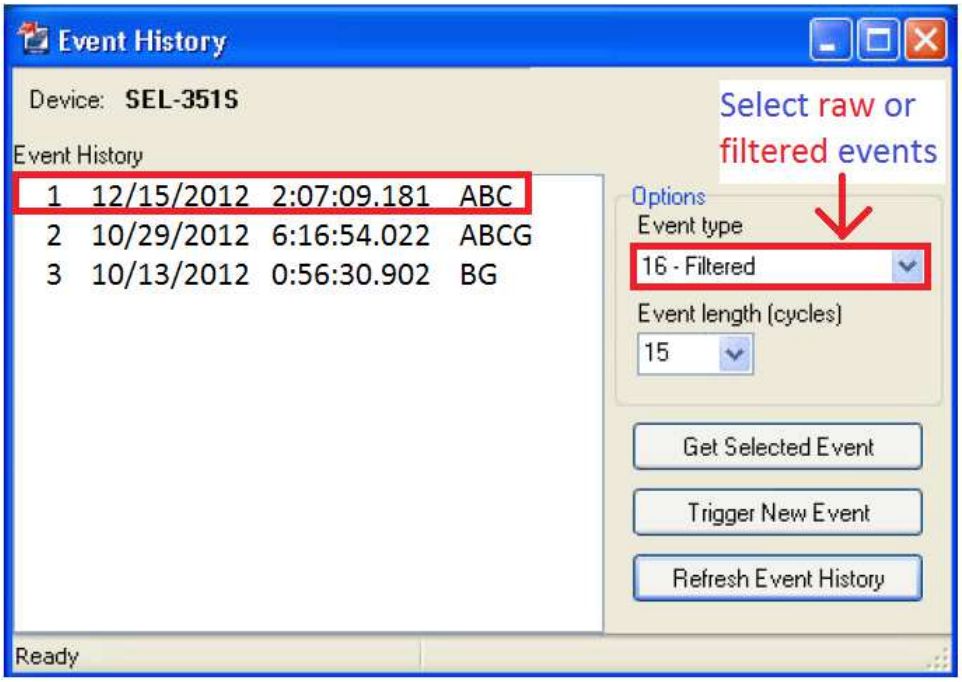

Figure 3.35: Window which allows users to download filtered or unfiltered events from SEL relays.

events, on the other hand, give an accurate account of what happened during a fault.

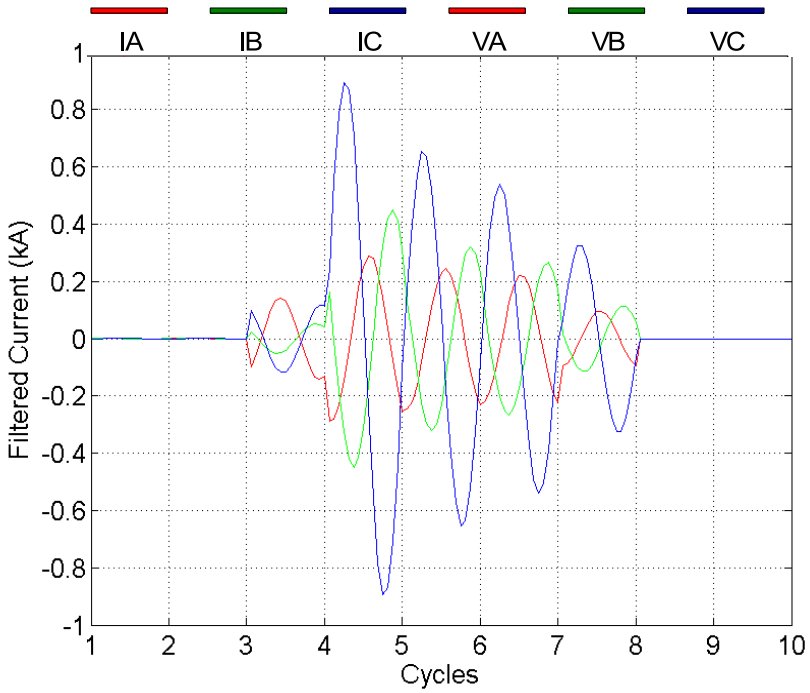

Figure 3.36: Event 6 filtered current waveforms.

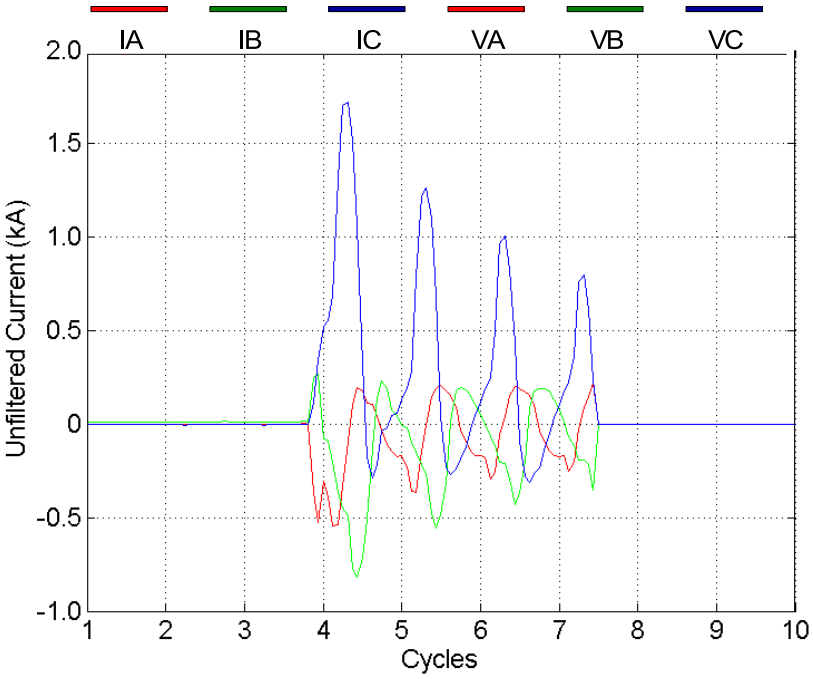

Figure 3.37: Event 6 unfiltered current waveforms.

3.5 Summary

Table 3.15 summarizes the sources of fault location error evaluated in this Chapter and their corresponding impact on impedance-based fault location algorithms.

Table 3.15: Summary of Fault-locating Error Sources that Affect Impedance-based Fault Location Algorithms

Input Data	Simple Reactance	Takagi	Modified Takagi	Eriksson	Novosel *et al.*	Synchronized Two-ended	Unsynchronized Two-ended	Unsynchronized Current-only Two-ended
Inaccurate Input Data								
DC Offset	✓	✓	✓	✓	✓	✓	✓	✓
CT Saturation	✓	✓	✓	✓	✓	✓	✓	✓
Delta-connected[1] PT	✓	✓	✓	✓	✓	✓	✓	
Untransposed Lines	✓	✓	✓	✓	✓	✓	✓	✓
Earth Resistivity[2]	✓	✓	✓	✓	✓			
Tower Footing Resistance	✓	✓	✓	✓	✓			
Earth Current Return Model	No Impact							
Non-homogeneous Lines	✓	✓	✓	✓	✓	✓	✓	✓
Application Related Challenges								
System Load	✓							
Non-homogeneous System	✓	✓						
Parallel Lines[3]	✓	✓	✓	✓	✓			✓
Tapped Radial[4] Lines	✓	✓	✓	✓	✓	✓	✓	✓
Three-Terminal[4] Lines	✓	✓	✓	✓	✓	✓	✓	✓

[1] Delta-connected PTs pose a problem in locating single line-to-ground faults only. If the zero-sequence impedance of the local source is available, estimate the corresponding line-to-ground voltages.
[2] Earth resistivity affects the accuracy of locating single line-to-ground faults only.
[3] Mutual coupling affects the accuracy of one-ended algorithms in locating single line-to-ground faults only. If transmission lines are parallel for the entire line length, then the residual current from the parallel line can improve the accuracy of one-ended methods. The unsynchronized current-only two-ended method is not affected by mutual coupling but requires the negative-sequence currents at both ends of the parallel line.
[4] It is possible to modify two-ended methods for application to tapped lines and three-terminal lines.

Chapter 4

Fault Location Algorithms using Current Only

Impedance-based fault location algorithms described in Chapter 2 require both voltage and current measurements to give reasonable fault location estimates. Unfortunately, most relays in distribution networks are of the overcurrent type and record only the current. Voltage measurements are, thus, simply not recorded. SEL-551 [8] shown in Fig. 4.1 is an example of such an overcurrent distribution relay. Voltage measurements can also be missing when a fuse protecting the voltage transformer blows and results in a loss-of-potential [22]. In such scenarios, existing impedance-based algorithms cannot be used to estimate the distance to a fault.

To overcome the above limitation, the ***objective*** of this Chapter is to develop fault location algorithms that use current data as the only input for estimating the distance to a fault. Depending on data availability, the algorithms are developed in two parts: fault location using current phasor (magnitude and phase angle) and fault location using current magnitude only. The approach consists of using the source impedance parameters and Kirchhoff's circuit laws to estimate the missing fault voltage at the monitoring location. Once the fault voltage is available, impedance-based fault location principles can be applied from the monitoring location to estimate the distance to the fault. Another approach searches for the fault location by matching the short-circuit in the circuit model with the measured fault current. The ***contribution*** of this Chapter lies in developing current-only algorithms that complement existing algorithms and will allow system operators to perform fault location even in the absence of voltage data. The proposed algorithms are non-iterative and straightforward to implement. Analysis

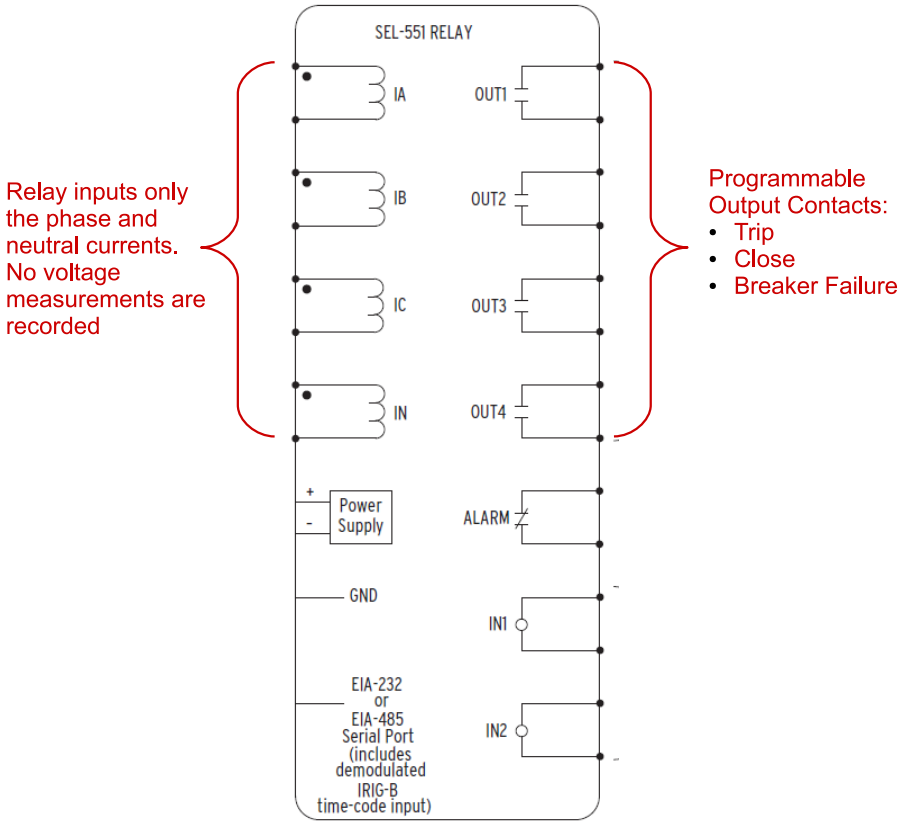

Figure 4.1: The SEL-551 relay inputs only the current measurements [8].

conducted on simulation and field data reveal that the fault location approach using current phasors is accurate within 0.31 miles of the actual fault location and is capable of locating single line-to-ground, line-to-line, double line-to-ground, and three-phase faults. The fault location approach using only the fault current magnitude is accurate within 0.71 miles of the actual fault location and is capable of locating single line-to-ground, line-to-line, and three-phase faults. The approach that uses the circuit model is valid for locating single line-to-ground, line-to-line, double line-to-ground, and three-phase faults.

Publications:

– S. Das, N. Karnik, and S. Santoso, "Distribution fault location using current only," *IEEE Trans. Power Del.*, vol. 27, no. 3, pp. 1144-1153, Jul. 2012.

– S. Das, S. Kulkarni, N. Karnik, and S. Santoso, "Distribution fault location using short-circuit fault current profile approach," in *Proc. IEEE Power Energy Soc. General Meeting*, San Diego, CA, Jul. 2011, pp. 1-7.

4.1 Fault Location using Current Phasors

This Section presents a step-by-step derivation of the algorithm that utilizes current phasors as the only input for computing the distance to a fault. Figure 2.5 shows the one-line diagram of a distribution feeder whose upstream transmission network is represented by a Thevenin impedance, Z_G, in series with an ideal voltage source. The distribution feeder is homogeneous with positive- and zero-sequence impedances of Z_{L1} and Z_{L0} ohms, respectively. All loads served by the distribution feeder are lumped at the end of the feeder and represented by an impedance of Z_{Load} ohms. When a single line-to-ground fault occurs at m per unit distance from terminal G, a power quality monitor at the terminal records only the current phasors before and during the fault. The procedure to estimate the fault location from the current phasors is outlined below.

Step 1: Estimate the sequence components of the fault voltage at the monitor

This step estimates the sequence components of the missing fault voltage at the monitoring location. For this purpose, the sequence network during a single line-to-ground fault is used as shown in Fig. 4.2. In the figure, V_{G0}, V_{G1} and V_{G2} are the sequence fault voltages at terminal G, I_{G0}, I_{G1} and I_{G2} are the sequence fault currents at terminal G, V_{F0}, V_{F1} and V_{F2} are the sequence fault voltages at the fault point F, Z_{L0}, Z_{L1} and Z_{L2} are the sequence line impedances, Z_{G0}, Z_{G1} and Z_{G2} are the sequence source impedances at terminal G, and $Z_{Load,0}$, $Z_{Load,1}$ and $Z_{Load,2}$ are the sequence load impedances. Voltage V_{G2} can be estimated using Kirchhoff's circuit laws as

$$V_{G2} = -\left(Z_{G2} \times I_{G2}\right) \tag{4.1}$$

In a similar manner, V_{G0} can be estimated as

$$V_{G0} = -\left(Z_{G0} \times I_{G0}\right) \tag{4.2}$$

The calculation of V_{G1}, on the other hand, is complicated by the presence of the internal generator voltage source, E_G. To develop a workaround, the superposition principle is used to decompose the network during fault into a prefault and "pure fault" network as shown in Fig. 4.3. The concept of a "pure fault" network is described in Section 2.1.2. Voltage V_{G1} is given as

$$V_{G1} = V_{preflt} + \Delta V_{G1} \tag{4.3}$$

where V_{preflt} is the prefault voltage and ΔV_{G1} is the "pure fault" voltage at terminal G. Now, the magnitude of V_{preflt} is close to 1 per unit in any practical power system. The phase angle of V_{preflt} (θ_v) can be obtained from the power factor (pf) of the circuit as

$$\theta_v = \cos^{-1}(pf) + \theta_i \tag{4.4}$$

where θ_i is the phase angle of the prefault current, I_{preflt}. Note that the power factor can be determined by carrying out a load flow analysis on the circuit model of the distribution feeder. The "pure fault" voltage can be estimated from the "pure fault" network as

$$\Delta V_{G1} = -\left[Z_{G1} \times \left(I_{G1} - I_{preflt}\right)\right] \tag{4.5}$$

Step 2: Transform the sequence components into fault voltage phasors

Impedance-based algorithms require the line-to-ground phase voltages to estimate the distance to a fault as shown in Table 2.1. For this purpose, this step transforms the estimated fault voltages at the monitoring location from the sequence to the phasor domain. As an example, the transformation for a A-G fault is shown below:

$$\begin{bmatrix} V_{AF,estimated} \\ V_{BF,estimated} \\ V_{CF,estimated} \end{bmatrix} = \begin{bmatrix} 1 & 1 & 1 \\ 1 & a^2 & a \\ 1 & a & a^2 \end{bmatrix} \times \begin{bmatrix} V_{G0} \\ V_{G1} \\ V_{G2} \end{bmatrix}; \quad a = 1\angle 120^\circ \tag{4.6}$$

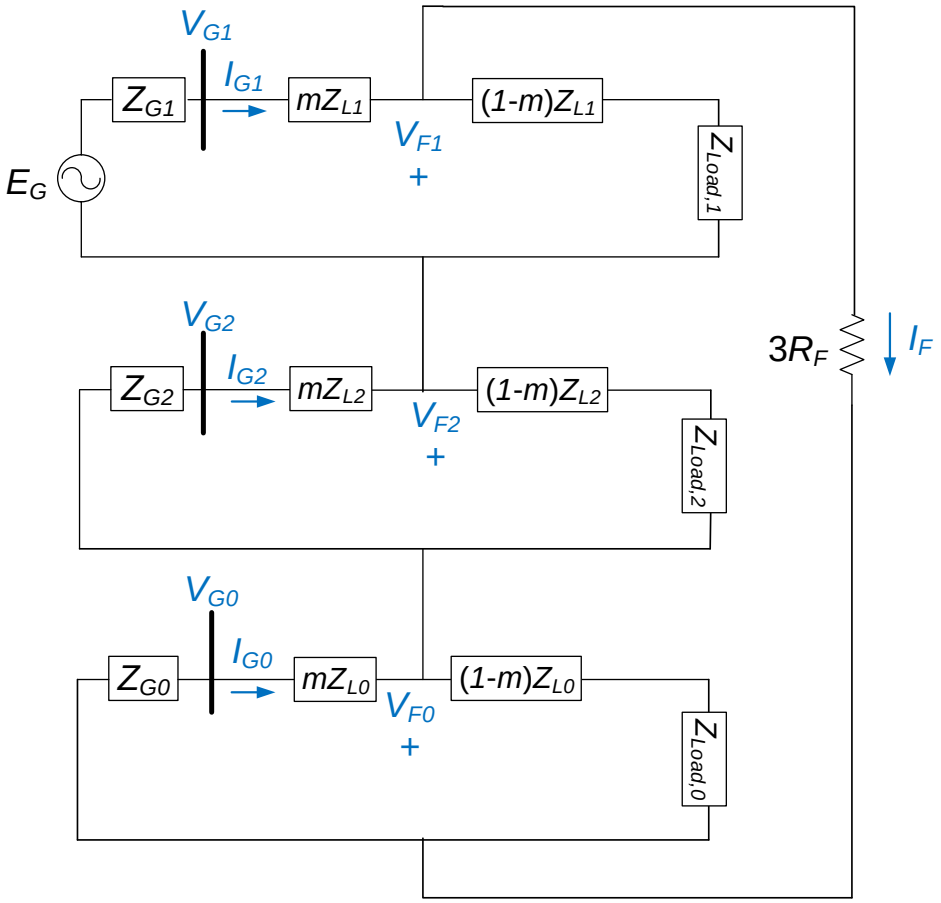

Figure 4.2: Sequence network during a single line-to-ground fault.

where $V_{AF,estimated}$, $V_{BF,estimated}$, and $V_{CF,estimated}$ are the estimated fault voltages in phases A, B, and C.

Step 3: Estimate the distance to a fault

Once the missing phase fault voltages are available, existing impedance-based fault location algorithms can be applied to estimate the fault location. For example, the simple reactance method can be used to estimate the distance to a A-G fault as

$$m = \frac{\text{imag}\left(\dfrac{V_{AF,estimated}}{I_G}\right)}{\text{imag}\left(Z_{L1}\right)} \tag{4.7}$$

where the form taken by I_G during a A-G fault is defined in Table 2.1.

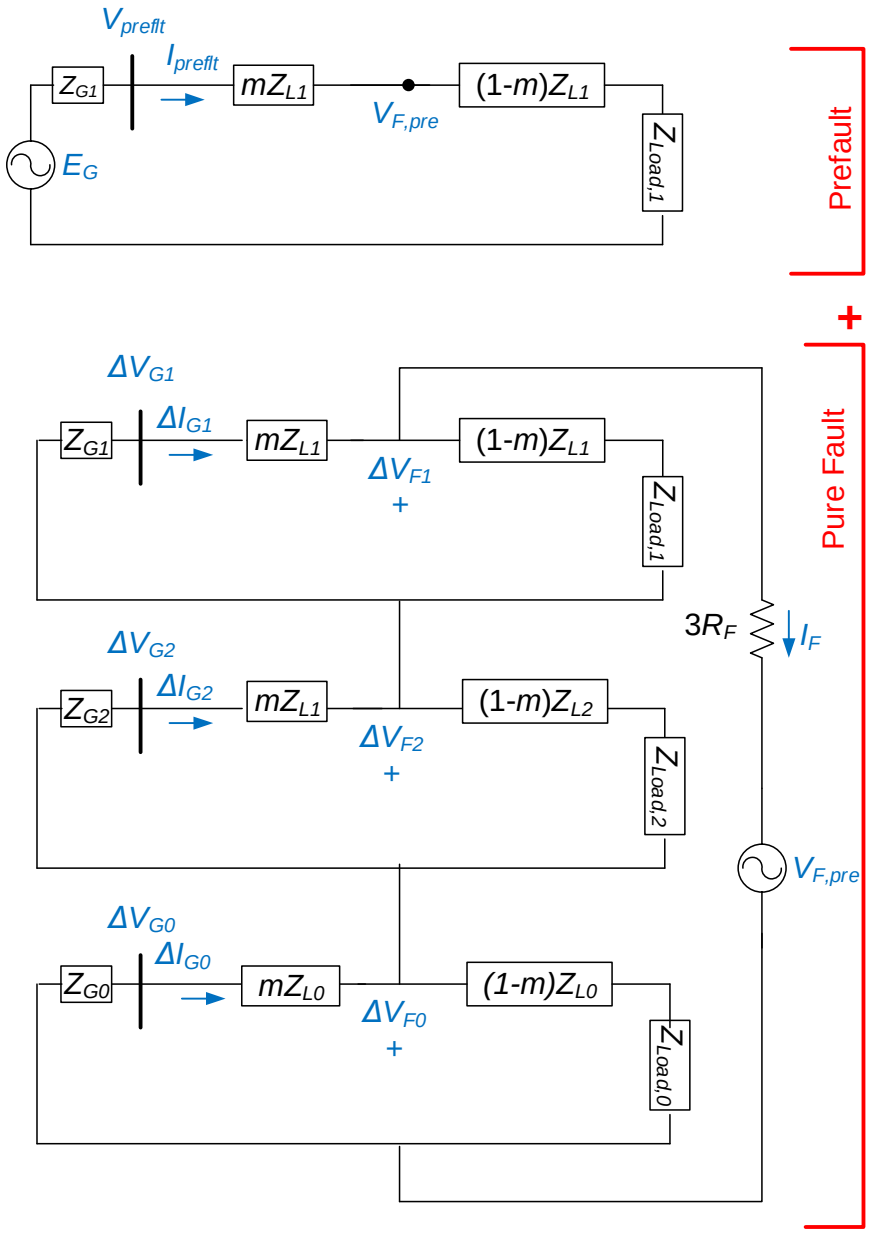

Figure 4.3: Superposition principle used to decompose the distribution network into a prefault and "pure fault" network during a single line-to-ground fault.

The steps above describe fault location using current phasors for a single line-to-ground fault. However, the same approach can be extended for locating three-phase, line-to-line, and double line-to-ground faults.

4.2 Fault Location using Current Magnitude

This Section presents simple yet powerful algorithms that utilize current magnitude as the only input for computing the distance to a fault. To illustrate the application scenario, consider the distribution feeder shown in Fig. 2.5. When a fault occurs on the feeder, the power quality monitor at the substation records only the fault current magnitudes in phases A, B, and C as $|I_{AF}|$, $|I_{BF}|$, and $|I_{CF}|$. The procedure to locate three-phase, line-to-line, and single line-to-ground faults are outlined below:

(a) Three-phase Fault

The first step is to estimate the magnitude of the positive-sequence fault voltage at the monitoring location, V_{G1}. From Section 4.1, V_{G1} is given by

$$V_{G1} = V_{preflt} - [Z_{G1} \times (I_{G1} - I_{preflt})] \tag{4.8}$$

Because three-phase faults are balanced faults, the positive-sequence fault current, I_{G1}, in (4.8) is equal to one of the three phase currents. In addition, since $I_{G1} \gg I_{preflt}$, a simplifying assumption is made to neglect the prefault current. As a result, (4.8) simplifies to

$$V_{G1} = V_{preflt} - [Z_{G1} \times I_{AF}] \tag{4.9}$$

Rewriting (4.9) in polar form, the following is obtained:

$$|V_{G1}|\angle\theta_v = |V_{preflt}|\angle\theta_{vpre} - |Z_{G1}| \times |I_{AF}|\angle(\theta_z + \theta_{ia}) \tag{4.10}$$

where θ_v is the phase angle of V_{G1}, θ_{vpre} is the phase angle of prefault voltage, θ_z is the phase angle of Z_{G1}, and θ_{ia} is the phase angle of I_{AF}. From the reverse triangular inequality theorem [69], the magnitude of V_{G1} can be calculated as follows:

$$|V_{G1}| \geq ||V_{preflt}| - (|Z_{G1}| \times |I_{AF}|)| \qquad \because |u - v| \geq ||u| - |v|| \tag{4.11}$$

The equality condition will be valid only when $\theta_{vpre} = \theta_z + \theta_{ia}$. Assuming this condition to hold true, $|V_{G1}|$ can be estimated as

$$|V_{G1}| = ||V_{preflt}| - (|Z_{G1}| \times |I_{AF}|)| \tag{4.12}$$

Next, to estimate the fault distance, consider the positive-sequence network during a three-phase fault as shown in Fig. 2.3. Writing the voltage drop from terminal G as

$$V_{G1} - mZ_{L1}I_{G1} = I_F R_F \tag{4.13}$$

Because most faults in distribution feeders have negligible fault resistance values [14], assume a bolted fault and express the distance to fault as

$$m = \frac{V_{G1}}{Z_{L1} \times I_{G1}} \tag{4.14}$$

Rewriting (4.14) in polar form and substituting $I_{G1} = I_{AF}$

$$m = \frac{|V_{G1}|}{|Z_{L1}| \times |I_{AF}|} \angle (\theta_v - \theta_{zl} - \theta_{ia}) \tag{4.15}$$

where θ_{zl} is the phase angle of the positive-sequence line impedance. Since m is a real number, it can be calculated from only the magnitude terms as

$$m = \frac{|V_{G1}|}{|Z_{L1}| \times |I_{AF}|} \tag{4.16}$$

It should be noted that the calculation of $|V_{G1}|$ in (4.12) assumes that θ_{vpre} is equal to $(\theta_z + \theta_{ia})$. When this condition is not fulfilled, the estimated value of $|V_{G1}|$ will be less than it's actual value. As a result, (4.16) will underestimate the location of the fault. Put another way, the distance estimate using (4.16) can be regarded as a lower bound for the actual fault location. However, as demonstrated in Section 4.3 and Section 4.4, the error due to this angle mismatch is not substantial and the estimate using (4.16) is close to the actual fault location.

(b) Line-to-line Fault

Suppose that a line-to-line fault occurs between phases A and B of a distribution feeder. The first step in the fault location process is to reconstruct the fault current phasors from the fault current magnitudes. For this purpose, assign a phase angle value to I_{AF}, 50 degrees in this example. Now, according to the property of a line-to-line fault, I_{BF} must be equal and opposite to I_{AF}. A simplifying assumption is made to ignore the load current in the healthy phase, I_{CF}, since $|I_{AF}|$ and $|I_{BF}| \gg |I_{CF}|$. The reconstructed fault current phasors during a AB fault are given by

$$\begin{aligned} I_{AF} &= |I_{AF}| \times (\cos 50^\circ + j\sin 50^\circ) \\ I_{BF} &= -I_{AF} \\ I_{CF} &= 0 \end{aligned} \tag{4.17}$$

The second step is to estimate the sequence current phasors as

$$\begin{bmatrix} I_{G0} \\ I_{G1} \\ I_{G2} \end{bmatrix} = \begin{bmatrix} 1 & 1 & 1 \\ 1 & a^2 & a \\ 1 & a & a^2 \end{bmatrix}^{-1} \times \begin{bmatrix} I_{CF} \\ I_{AF} \\ I_{BF} \end{bmatrix}; \quad a = 1\angle 120^\circ \tag{4.18}$$

The third step is to estimate the magnitude of the difference between the positive- and the negative-sequence fault voltage phasors at the monitoring location, $|V_{G1} - V_{G2}|$. From (4.9) and (4.1), the voltage difference can be expressed as

$$V_{G1} - V_{G2} = V_{preflt} - Z_{G1} \times (I_{G1} - I_{G2}) \tag{4.19}$$

Rewriting (4.19) in polar form, the following is obtained:

$$|V_{G1} - V_{G2}|\angle\theta_{v12} = |V_{preflt}|\angle\theta_{vpre} - [|Z_{G1}| \times |I_{G1} - I_{G2}|\angle(\theta_z + \theta_{i12})] \tag{4.20}$$

where θ_{v12} is the phase angle of $(V_{G1} - V_{G2})$ and θ_{i12} is the phase angle of $(I_{G1} - I_{G2})$. Invoking the reverse triangular inequality theorem and assuming θ_{vpre} to be equal to $(\theta_z + \theta_{i12})$, $|V_{G1} - V_{G2}|$ can be estimated as

$$|V_{G1} - V_{G2}| = ||V_{preflt}| - |Z_{G1}| \times |I_{G1} - I_{G2}|| \tag{4.21}$$

The final step is to estimate the distance to a line-to-line fault. For this purpose, recall that the positive- and negative-sequence fault voltages at the fault point during a line-to-line fault are related as

$$V_{F1} - V_{F2} = I_F R_F \tag{4.22}$$

Substituting the expressions of V_{F1} and V_{F2} and assuming a zero fault resistance, the expression for fault distance can be written as

$$m = \frac{V_{G1} - V_{G2}}{Z_{L1} \times (I_{G1} - I_{G2})} \tag{4.23}$$

Writing (4.23) in polar form,

$$m = \frac{|V_{G1} - V_{G2}|}{|Z_{L1}| \times |I_{G1} - I_{G2}|} \angle (\theta_{v12} - \theta_{zl} - \theta_{i12}) \tag{4.24}$$

Since m is a real number, it can be estimated from only the magnitude terms as

$$m = \frac{|V_{G1} - V_{G2}|}{|Z_{L1}| \times |I_{G1} - I_{G2}|} \tag{4.25}$$

Note that the calculation of $|V_{G1} - V_{G2}|$ in (4.21) assumes θ_{vpre} to be equal to $(\theta_z + \theta_{i12})$. When this condition is not fulfilled, the estimated value of $|V_{G1} - V_{G2}|$ will be less than it's actual value. As a result, the distance estimate using (4.25) will underestimate the fault location and can be regarded as a lower bound for the actual fault location. However, as demonstrated in Section 4.3 and Section 4.4, the error due to this angle mismatch is not significant and (4.25) can accurately track down the location of a line-to-line fault.

(c) Single Line-to-ground Fault

Suppose that a single line-to-ground fault occurs on phase A of a distribution feeder. The first step in the fault location process is to estimate the sequence current phasors at the monitoring location. Because $|I_{BF}|$ and $|I_{CF}| \ll |I_{AF}|$, a simplifying assumption is made to ignore the load currents in the unfaulted phases. As a result, the

sequence current calculation simplifies down to

$$\begin{bmatrix} I_{G0} \\ I_{G1} \\ I_{G2} \end{bmatrix} = \begin{bmatrix} 1 & 1 & 1 \\ 1 & a^2 & a \\ 1 & a & a^2 \end{bmatrix}^{-1} \times \begin{bmatrix} I_{AF} \\ 0 \\ 0 \end{bmatrix}; \quad a = 1\angle 120^\circ \tag{4.26}$$

The magnitude of the sequence current phasors are

$$|I_{G0}| = |I_{G1}| = |I_{G2}| = \frac{|I_{AF}|}{3} \tag{4.27}$$

The next step is to estimate the fault location. For this purpose, the loop impedance to the fault, Z_n, is calculated from the "pure fault" network in Fig. 4.3 as

$$Z_n = \frac{V_{F,pre}}{I_{G0}} - (2Z_{G1} + Z_{G0}) \tag{4.28}$$

Writing (4.28) in polar form, the following is obtained:

$$|Z_n|\angle\theta_{zn} = \frac{|V_{F,pre}|}{|I_{G0}|}\angle(\theta_{vf} - \theta_{ig0}) - |2Z_{G1} + Z_{G0}|\angle\theta_{zg} \tag{4.29}$$

where θ_{zn} is the phase angle of the loop impedance, θ_{vf} is the phase angle of the prefault voltage, θ_{ig0} is the phase angle of I_{G0}, and θ_{zg} is the phase angle of $(2Z_{G1} + Z_{G0})$. Calculate $|Z_n|$ by applying the reverse triangular inequality theorem as

$$|Z_n| = \left| \frac{|V_{F,pre}|}{|I_{G0}|} - |2Z_{G1} + Z_{G0}| \right| \qquad \because \angle(\theta_{vf} - \theta_{ig0}) = \angle\theta_{zg} \tag{4.30}$$

Alternatively, the loop impedance can be calculated as

$$Z_n = (2m \times Z_{L1}) + (m \times Z_{L0}) = m(r_s + jx_s) \tag{4.31}$$

where r_s and x_s are the loop resistance and reactance in Ω/mile. The magnitude of Z_n can be calculated from (4.31) as

$$|Z_n| = m\sqrt{(r_s^2 + x_s^2)} \tag{4.32}$$

Equating (4.30) and (4.32), the distance to the fault can be solved as

$$m = \frac{\left| \frac{|V_{F,pre}|}{|I_{G0}|} - |2Z_{G1} + Z_{G0}| \right|}{\sqrt{(r_s^2 + x_s^2)}} \tag{4.33}$$

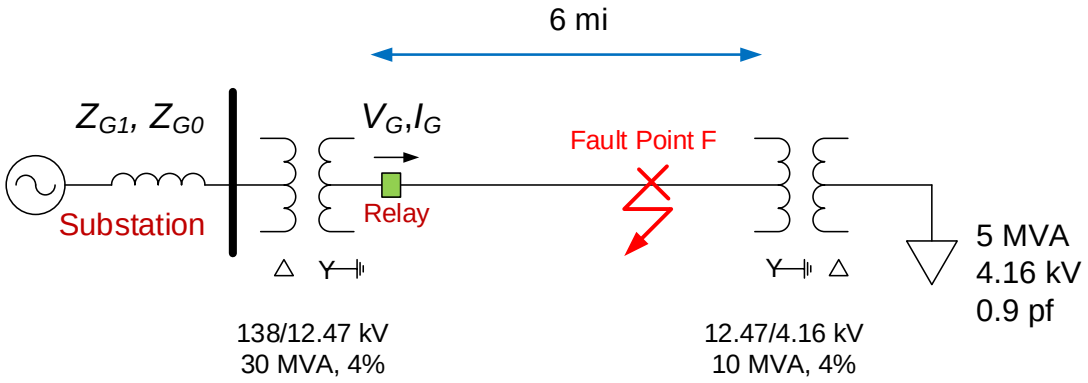

Figure 4.4: One-line diagram of the test case.

4.3 Demonstration using a Benchmark Test Case

The efficacy of the proposed current-only algorithms was demonstrated using a radial distribution feeder modeled in PSCAD simulation software. The one-line diagram of the test feeder is shown in Fig. 4.4. A 12.47-kV distribution feeder is fed by a 138-kV transmission system via a 30 MVA 138/12.47 kV transformer with a leakage impedance of 4%. The distribution feeder is six miles long and has the following positive- and zero-sequence impedances, $Z_{L1} = 0.9180 + j1.8810\,\Omega$ and $Z_{L0} = 2.3202 + j5.8122\,\Omega$. A 5-MVA constant impedance load with 0.9 lagging power factor is served by a 10 MVA 12.47/4.16 kV transformer with a 4% leakage impedance. A relay at the substation captures the voltage and current waveforms at 128 samples per cycle. The upstream transmission network has the following positive- and zero-sequence Thevenin impedances, $Z_{G1} = j0.20733\,\Omega$ and $Z_{G0} = j0.2384\,\Omega$. The test feeder has been intentionally designed to be simple and homogeneous. In such a scenario, the error in fault location estimates is strictly proportional to the assumptions made by the current-only algorithms and will give an accurate measure of how those assumptions affect fault location accuracy.

Faults with different fault types are staged along the entire length of the feeder. For fault location using current phasors only, the relay is assumed to record only the current waveform. As described in Section 4.1, the first step is to estimate the missing

fault voltage at the monitoring location. The estimated fault voltages are an exact match with the actual fault voltages recorded by the relay as shown in Table 4.1. The estimated fault voltages are then used by the Takagi method to successfully estimate the fault locations.

Table 4.1: Actual vs. Estimated Fault Location using the Current Phasor Approach

Fault Type	Actual Location (mi)	Faulted Phase Voltage (kV)		Estimated Location (mi)
		Actual	Estimated	
ABC	2.00	5.47	5.47	2.00
BC	3.00	6.53	6.53	3.00
AB-G	4.00	6.44	6.44	4.00
A-G	1.50	7.04	7.04	1.50

For fault location with current magnitude only, assume that the relay records only the current magnitude of the faulted phase. For locating the ABC fault, the approach starts by estimating $|V_{G1}|$. As seen from Table 4.2, the estimated $|V_{G1}|$ is lower than it's actual magnitude. The error can be attributed to the phase angle mismatch when applying the reverse triangular inequality theorem to (4.12). This error, however, is not substantial since the distance estimate using (4.16) has a fault location error of only 0.05 miles. The location of the BC fault proceeds by estimating $|V_{G1} - V_{G2}|$. As seen from the table, the phase angle mismatch when applying the reverse triangular inequality theorem to (4.21) results in $|V_{G1} - V_{G2}|$ having a lower magnitude than it's actual magnitude. This error is not observed to have a significant impact on fault location accuracy since the distance estimate using (4.25) is close to the actual fault location. The current magnitude approach cannot be applied to locate double line-to-ground faults. For the next case of locating a single line-to-ground fault, the current

magnitude algorithm does not directly estimate the fault voltage. Instead, the distance to fault is estimated from the loop impedance to fault. As seen from the table, the estimated fault location underestimates the actual fault location due to the phase angle mismatch when applying the reverse triangular inequality theorem in (4.30). The fault location error is not substantial, around 0.13 miles.

Table 4.2: Actual vs. Estimated Fault Location using the Current Magnitude Approach

Fault Type	Actual Location (mi)	Faulted Phase Voltage (kV)		Estimated Location (mi)
		Actual	Estimated	
ABC	2.00	5.47	5.33	1.95
BC	3.00	5.96	5.84	2.94
AB-G	4.00	Cannot be applied		
A-G	1.50	–	–	1.37

Overall, the Section demonstrates the success of current-only algorithms in tracking down the exact location of a fault. Because of more data availability, the algorithm using current phasors makes no assumptions when estimating the distance to a fault and hence, has a superior performance. The algorithm using current magnitude, on the other hand, estimates the fault location with limited data. Although several assumptions are necessary to obtain a location estimate, the method is powerful and accurate.

4.4 Application to Field Data

This Section demonstrates the application of current-only fault locating algorithms on ten fault events collected from utility distribution networks. Fault location on two of the events is explained in details followed by a summary of the remaining events.

4.4.1 Event 1: Recloser Failure on a 34.5-kV Distribution Feeder

On 2 August 2010, a 34.5-kV distribution feeder experienced a single line-to-ground fault on phase C at 3:09 pm. The fault occurred on a feeder recloser at a distance of 3.07 miles from the substation as shown in Fig. 4.5. The distribution feeder is 5.79 miles long and is constructed using five different line configurations. The line configuration used to construct the majority of the feeder length has a positive- and zero-sequence line impedances of $z_{L1} = 0.1308 + j0.5546\,\Omega$/mile and $z_{L0} = 0.4029 + j1.8619\,\Omega$/mile, respectively. These sequence impedances are utilized for fault location purposes. The positive- and zero-sequence Thevenin impedances of the upstream transmission network are $Z_{G1} = 0.1480 + j3.0820\,\Omega$ and $Z_{G0} = 0.0028 + j0.0610\,\Omega$, respectively. Figure 4.6 illustrates the voltage and current waveforms captured by a SEL-651R relay during the fault at 32 samples per cycle. From the waveforms, it is evident that the voltage transformer has malfunctioned, and that the voltage data cannot be used for fault location purposes. As a result, this event is the perfect example that demonstrates the need for developing current-only fault location algorithms.

(a) Fault Location using Current Phasors

This event is a short-duration fault that lasts for only two cycles. As a result, the Fast Fourier transform is applied to the second cycle after fault inception to extract the phase C fault current phasor as 3.15$\angle$-170° kA. The prefault current phasor is 129$\angle$-110° A. Towards determining the fault location using current phasors only, the first step is to estimate the prefault voltage at the monitoring location. For this purpose, the magnitude of the prefault voltage is assumed to be 1 per unit. A load flow analysis in the circuit model indicates that the distribution feeder is operating at 0.998 lagging power factor. Since the prefault current has a phase angle of -110 degrees, the prefault voltage is calculated to have a phase angle of -106 degrees. Next, using (4.3) to (4.6), the

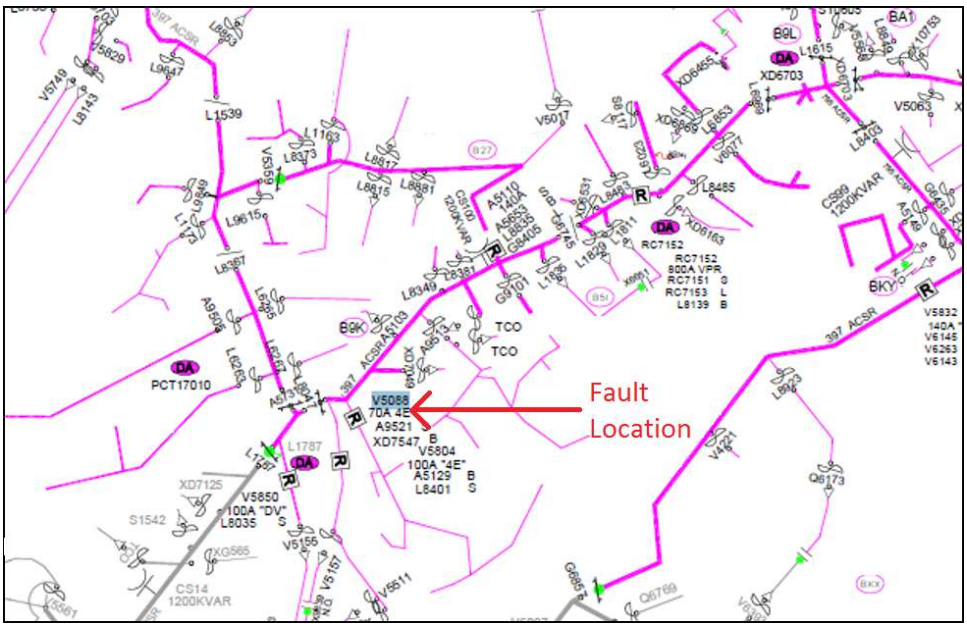

Figure 4.5: Event 1 is a C-G fault on a feeder recloser at 3.07 miles from the substation.

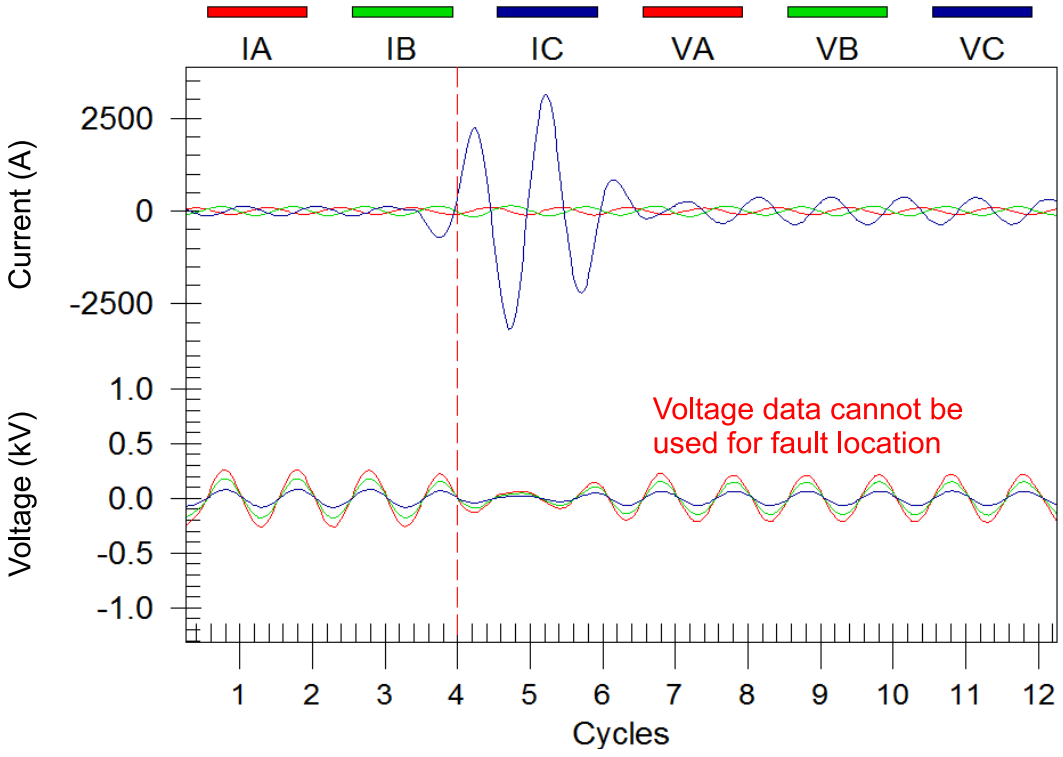

Figure 4.6: Voltage and current waveforms recorded by the SEL-651R relay.

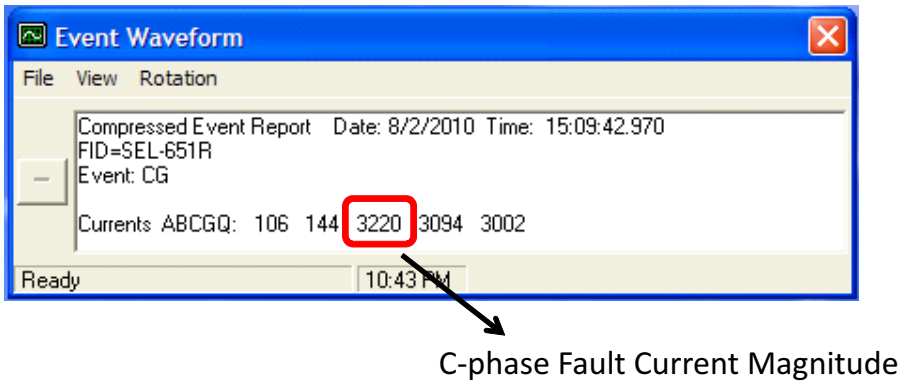

Figure 4.7: Relay at the substation records only the fault current magnitude.

fault voltage at the monitoring location, $V_{CF,estimated}$, is estimated to be 12.89∠-124° kV. This estimated voltage is then used by the Takagi method to compute the distance to the fault to be 3.07 miles. The estimate matches exactly with the actual fault location with no loss in accuracy.

(b) Fault Location using Current Magnitude

This approach assumes that only the current magnitude of the faulted phase, 3220 A, is available for fault location purposes as shown in Fig. 4.7. Ignoring the currents in the unfaulted phases, the sequence fault currents are determined by (4.27) as

$$|I_{G0}| = |I_{G1}| = |I_{G2}| = \frac{|I_{CF}|}{3} = \frac{3220}{3} = 1073.3 \text{ A}$$

The actual sequence fault currents are:

$$\begin{aligned} |I_{G0,actual}| &= 1012.3 \text{ A} \\ |I_{G1,actual}| &= 1109.8 \text{ A} \\ |I_{G2,actual}| &= 1025.6 \text{ A} \end{aligned}$$

Although the healthy phase currents were ignored in the sequence fault current calculation, the estimated sequence currents are observed to be close to the actual sequence

currents. Next, assuming a prefault voltage magnitude of 1 per unit, the distance to fault is computed using (4.33) to be 3.32 miles from the substation. The actual fault location is 3.07 miles.

4.4.2 Event 2: Tree Contact Fault with a 8.32-kV Distribution Feeder

This event is a line-to-line fault that occurred between phase A and phase B of a 8.32-kV distribution feeder on 27 June 2010 at 02:37 am. The fault was caused by a tree falling on the overhead feeder at a distance of 0.96 miles from the substation. The feeder has a positive- and zero-sequence line impedance of $z_{L1} = 0.8817 + j1.2135\,\Omega$/mile and $z_{L0} = 1.9945 + j2.9569\,\Omega$/mile, respectively. A SEL-351A relay at the substation, present as a backup relay, records the voltage and current waveforms during the fault at 4 samples per cycle as shown in Fig. 4.8. However, for the purpose of evaluating the efficacy of the current-only fault location algorithms, pretend that the voltage waveforms are missing or not available.

(a) Fault Location using Current Phasors

From the fault current waveform recorded by the relay, the Fast Fourier transform calculates the fault current phasors in phases B and C to be 2.86$\angle$64° kA and 2.73$\angle$-112° kA, respectively. The prefault current phasor in phase A is 157$\angle$-167° A. Since the circuit model of the distribution feeder is not available, (8.44) is used to estimate the positive-sequence source impedance as $Z_{G1} = 0.1091 + j0.8633\,\Omega$. From the phase angles of the voltage and current waveforms, the distribution feeder was found to operate with a 0.87 lagging power factor. It is also necessary to determine the prefault voltage phasor, V_{preflt}, for calculating the distance to fault using current phasors. The magnitude of V_{preflt} is assumed to be 1 per unit while the phase angle is calculated to be -137° using (4.4). Next, using using (4.3) to (4.6), the fault voltages at the monitoring location are

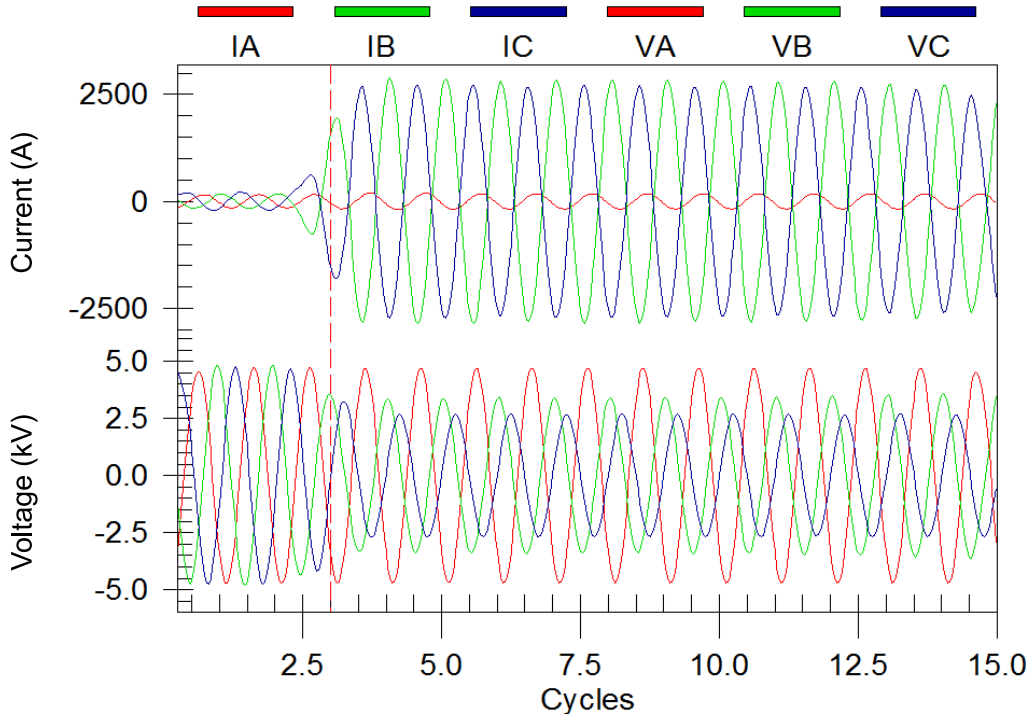

Figure 4.8: Voltage and current waveforms recorded by the SEL-351A relay at the substation. Pretend that the voltage waveforms are missing.

estimated as follows:

$$V_{BF,estimated} = 3.51\angle 75^\circ \text{ kV}$$

$$V_{CF,estimated} = 2.64\angle -3^\circ \text{ kV}$$

The actual fault voltages are as follows:

$$V_{BF,actual} = 3.40\angle 78^\circ \text{ kV}$$

$$V_{CF,actual} = 2.67\angle 1^\circ \text{ kV}$$

The estimated fault voltages are observed to be close to the actual fault voltage phasors recorded by the relay in phases B and C. Next, the estimated voltages are used by the Takagi method to compute the distance to the fault to be 1.09 miles. The actual location is 0.95 miles.

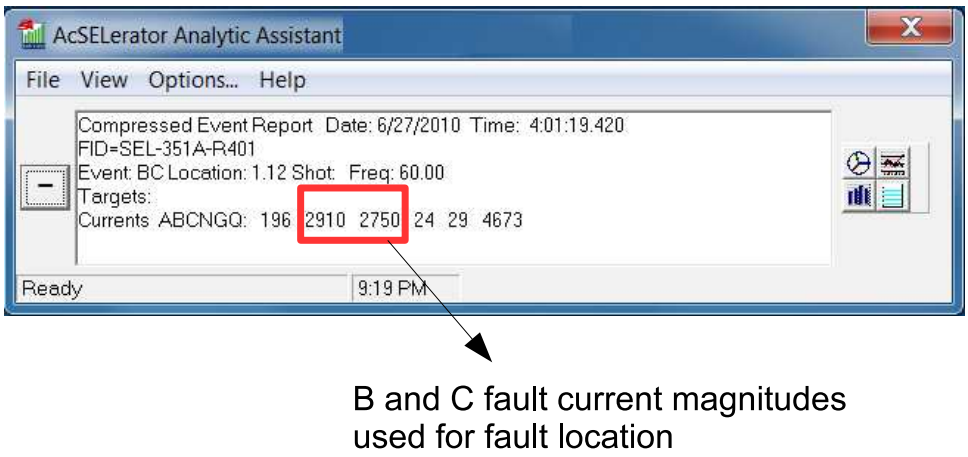

Figure 4.9: Relay at the substation records only the fault current magnitudes in phases B and C.

(b) Fault Location using Current Magnitude

This fault-locating approach proceeds with the assumption that only the fault current magnitudes in phases B and C are available for fault location purposes. From Fig. 4.9, $|I_{BF}| = 2910$ A and $|I_{CF}| = 2750$ A, respectively. Suppose I_{BF} has a phase angle of 50°. Since $I_{CF} = -I_{BF}$, I_{CF} has a phase angle equal to -130°. Next using (4.18), the positive- and negative-sequence fault current phasors are calculated to be

$$\begin{aligned} |I_{G1,estimated}| &= 1.68\angle 140^\circ \text{ kA} \\ |I_{G2,estimated}| &= 1.68\angle -40^\circ \text{ kA} \end{aligned}$$

The actual sequence fault current phasors are close to the estimated phasors as shown below:

$$\begin{aligned} |I_{G1,actual}| &= 1.69\angle 157^\circ \text{ kA} \\ |I_{G2,actual}| &= 1.54\angle -27^\circ \text{ kA} \end{aligned}$$

Next, the difference between negative- and positive-sequence fault voltage phasors, $|V_{G2} - V_{G1}|$, is calculated using (4.21) to be 1.84 kV. The distance to fault is then estimated to

be 0.88 miles. The actual location is 0.95 miles.

4.4.3 Fault Location Analysis of the Remaining Events

Fault location analysis on all the remaining events are summarized in Table 4.3. Event 3 is a single fault at 1.42 miles from the substation. The sub-events correspond to the fast and slow operation of a downstream recloser. In certain sub-events, the fault location using current phasor approach cannot be applied due to the absence of prefault data. In Event 6, the fault evolves from a line-to-line to a three-phase fault and back to a line-to-line fault in a matter of few seconds. In Event 8, the utility reports a possible fault location of 2.50 miles. However, as per the analysis conducted using existing impedance-based fault location algorithms, the fault is suspected to be located at 0.33 miles from the substation. Estimates from the current-only algorithms support this conclusion as well. The analysis in Event 9 reveals that the distribution feeder had, in fact, experienced two faults: a A-G fault that evolved into a ABC fault at 4.27 miles, and another AB fault at 0.55 miles. This reasoning is further supported by the dramatic increase in fault current from 3.4 kA to 6.8 kA in Event 9g.

Overall, the analysis of field data proves that the proposed current-only algorithms are successful in tracking down the exact location of a fault with no significant loss in accuracy. For this dataset, the fault location approach using only the current phasor is accurate within 0.37 miles while the fault location approach using only the current magnitude is accurate within 0.81 miles of the actual fault location.

Table 4.3: Actual vs. Estimated Location using Current Phasors and Current Magnitude

Event	Fault Type	Actual Location (mi)	Estimated Fault Location (mi)		
			Voltage and Current Phasors	Current Phasor	Current Magnitude
3a	AB	1.42	1.49	1.30	1.35
3b	AB	1.42	1.47	1.53	1.43
3c	AB	1.42	1.47	Prefault data absent	1.41
3d	AB	1.42	1.45	1.14	1.40
3e	AB	1.42	1.44	Prefault data absent	1.32
4a	BG	1.70	1.62	1.81	1.93
4b	BG	1.70	1.68	Prefault data absent	2.39
5	AG	10.70	10.72	10.68	11.41
6a	AB	1.51	1.70	1.65	1.59
6b	AB	1.51	1.68	Prefault data	1.59
6c	AB	1.51	1.65	absent	1.57
6d	ABC	1.51	1.54	⋮	1.72
6e	ABC	1.51	1.47	⋮	1.78
6f	AB	1.51	1.69	⋮	1.61
6g	AB	1.51	1.71	⋮	1.72
7	CG	5.33	4.82	4.96	4.52
8	BG	2.50	0.33	0.32	0.36
9a	AG	4.27	4.24	4.27	4.14
9b	ABC	4.27	3.97	3.94	3.76
9c	ABC	4.27	4.00	Prefault data absent	3.87
9d	ABC	4.27	3.96	4.18	3.66
9e	ABC	4.27	4.03	Prefault data absent	3.89
9f	AB	4.27	0.55	0.44	0.23
9g	AB	4.27	0.58	Prefault data	0.49
9h	AB	4.27	0.16	absent	0.03
9i	ABC	4.27	3.98	4.14	3.64
9j	ABC	4.27	4.01	Prefault data absent	3.91
10a	AG	0.28	0.24	0.24	0.28
10b	BC	0.28	0.20	Prefault data absent	0.14

4.5 Short-circuit Fault Current Profile Method

The short-circuit fault current profile method uses the circuit model of the distribution feeder to determine the location of a fault. The approach is to simulate the same fault in the circuit model along the entire length of the feeder. The location at which the short-circuit current matches with the measures fault current magnitude is selected as the actual fault location. The method does not require voltage measurements and has a high level of accuracy as demonstrated in [57, 70].

4.6 Summary

This Chapter proposes practical fault location algorithms that use only the current data recorded by a relay to estimate the distance to a fault. Two fault locating approaches using current phasors and current magnitude are developed. Both approaches work by estimating fault voltage at the monitoring location and then invoking impedance-based fault-locating principles. Analysis on simulation and field data showed promise. The fault location approach using only the current phasors is accurate within 0.31 miles while the fault location approach using only the current magnitude is accurate within 0.71 miles of the actual fault location. The Chapter also presents another approach that uses the fault current phasor or fault current magnitude and the system circuit model for fault location purposes.

Chapter 5

Effects of Distributed Generators on Fault Location

One-ended impedance-based fault location algorithms such as the simple reactance, Takagi, and Novosel *et al.* methods are commonly used to locate faults in distribution networks. These algorithms assume a radial distribution feeder with a unidirectional flow of power from the substation to the end users as discussed in Chapter 2. With the integration of distributed generators to the distribution circuit, however, distribution feeders are no longer radial. Short-circuit current to a fault comes from two sources, the utility substation and distributed generators. Since the level of penetration of DGs is expected to increase over the next few years, ignoring the latter term will certainly compromise the accuracy of location estimates.

Based on the aforementioned background, the ***objective*** of this Chapter is to evaluate the effect of distributed generators on the accuracy of existing impedance-based fault-locating algorithms. The focus is on faults that occur downstream from DGs. This is because when faults are located upstream from distributed generators, fault current contributed by DGs act as a source of remote infeed and will not have a significant impact on fault location accuracy [71]. Authors in [72] investigate the impact of DG technology on impedance-based fault location algorithms. They conclude that synchronous generators have the worst impact on fault location algorithms since the short-circuit current from these generators is five to ten times the rated current. Authors in [30] conduct simulation studies to demonstrate the impact of other factors such as MVA capacity of the DG unit, tapped loads, and location of the fault from DG

on fault location estimates. Simulation studies are, however, not helpful in understanding how these factors act as a source of error. The ***contribution*** of this Chapter is that it provides a detailed insight into how each of the factors mentioned above affect impedance-based fault location algorithms in the presence of DGs and how to interpret the results. A detailed understanding of error sources is useful for developing improved fault locating solutions. Furthermore, this Chapter investigates additional factors that may influence fault location downstream from DGs. They are fault resistance and configuration of the DG interconnect transformer.

The analysis in this Chapter concludes that higher the MVA capacity of the DG unit, greater is the error in fault location. If faults occur very close to DGs, the error in fault location is marginal. As the fault moves further downstream from DGs, the error increases significantly. Although tapped loads counter the effect of DGs, the improvement in fault location accuracy is not significant. Reactance error due to fault resistance can cancel out the effect of DGs or further magnify the error in location estimates. Under such circumstances, an improved fault locating algorithm proposed in Chapter 6 is recommended. Only if DG interconnect transformers have a delta configuration on the utility side, DGs will not contribute any current during a single line-to-ground fault. In such cases, existing impedance-based fault locating methods may still be used.

The Chapter is organized as follows: Section 5.1 presents a discussion on how distributed generators act as a source of short-circuit current and compromise the accuracy of locating faults that occur downstream from DGs, Section 5.2 develops a time-domain model of a distribution feeder, Section 5.3 uses this model to evaluate the critical factors that affect impedance-based fault locating algorithms when DGs are interconnected to the distribution feeder, and Section 5.4 summarizes the key findings of the Chapter.

Publications:

– S. Das, S. Santoso, and A. Maitra, "Effects of distributed generators on impedance-based fault location algorithms," in *Proc. IEEE PES General Meeting Conf. Expo.*, Jul. 2014, pp. 1-5.

5.1 Impact of DGs on Impedance-based Fault Location

As seen in Chapter 2, impedance-based fault location algorithms assume a radial distribution feeder where power flows unidirectionally from the substation to the end users. However, with increased penetration of distributed generators (DGs) to the distribution circuit, distribution feeders are no longer radial. When a fault occurs downstream from the DG unit, DGs contribute to the total fault current and will modify the apparent impedance seen from the substation. To illustrate this concept, consider the distribution feeder shown in Fig. 5.1. The feeder has a total positive-sequence line impedance of Z_{L1} ohms. The DG is interconnected to the feeder (referred to as the point of interconnection or POI) at a distance d per unit from the substation. When a three-phase fault with a fault resistance R_F occurs at a distance of m per unit from the substation, the substation and DG operate in parallel to feed the fault.

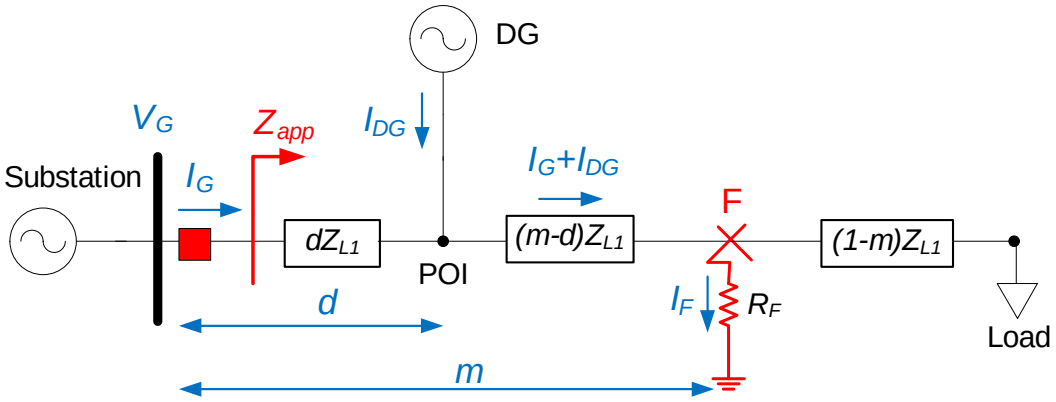

Figure 5.1: Distribution feeder with a fault located downstream from the DG.

Voltage drop from the substation can be written as,

$$V_G = dZ_{L1}I_G + (m-d)Z_{L1}\left(I_G + I_{DG}\right) + R_F I_F \tag{5.1}$$

where V_G and I_G are the voltage and current phasors recorded at the substation during the fault, I_{DG} is the fault current from the DG unit, and I_F is the current at the fault point. Dividing throughout by I_G and simplifying, the apparent impedance (Z_{app}) seen from the substation is

$$Z_{app} = \frac{V_G}{I_G} = mZ_{L1} + (m-d)Z_{L1}\frac{I_{DG}}{I_G} + R_F\left(\frac{I_F}{I_G}\right) \tag{5.2}$$

As evident from (5.2), when the fault is located downstream from the DG unit, the apparent impedance seen from the substation is proportional to the impedance to the fault (mZ_{L1}) as well as two additional terms: $(m-d)Z_{L1}\left(I_{DG}/I_G\right)$ and $R_F\left(I_F/I_G\right)$. Since one-ended fault locating methods make use of only V_G and I_G at the substation, neglecting I_{DG} in (5.2) will certainly compromise the accuracy of the location estimates.

For a bolted fault, the term $(m-d)Z_{L1}\left(I_{DG}/I_G\right)$ increases Z_{app} as shown in Fig. 5.2 (a). As a result, impedance-based fault location algorithms will overestimate the location of the fault. When the fault has a significant R_F, impedance-based fault location algorithms are affected by an additional reactance error. Since short-circuit current at the fault point (I_F) comes from the utility substation (I_G) and the distributed generator (I_{DG}), phase angles of I_F and I_G are not equal to each other. When I_F leads I_G, the term $R_F\left(I_F/I_G\right)$ is inductive, and together with $(m-d)Z_{L1}\left(I_{DG}/I_G\right)$ increases the apparent impedance to the fault as shown in Fig. 5.2 (b). This is the worst case scenario and fault location algorithms will significantly overestimate the fault location. When I_F lags I_G, on the other hand, $R_F\left(I_F/I_G\right)$ is capacitive and will attempt to cancel out the effect of $(m-d)Z_{L1}\left(I_{DG}/I_G\right)$ as illustrated in Fig. 5.2 (c).

In summary, when a fault occurs downstream from DGs, fault location error from the one-ended algorithms will depend on the magnitude of $(m-d)Z_{L1}\left(I_{DG}/I_G\right)$

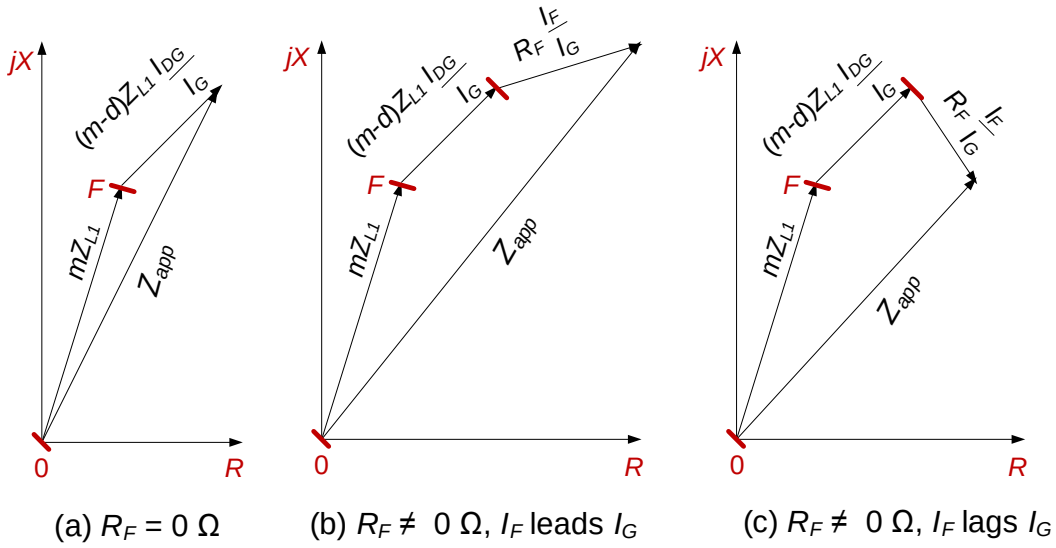

Figure 5.2: Apparent impedance Z_{app} from the substation

and $R_F\,(I_F/I_G)$. Several factors can affect the magnitude of these terms and hence, the accuracy of location estimates. These factors are investigated in Section 5.3.

5.2 Distribution Test Case Feeder

This Section describes a distribution feeder which will serve as a test bed for evaluating the different factors that affect fault location downstream from DGs. The test feeder was modeled in PSCAD simulation software [47] and is capable of replicating actual faults occurring in a distribution feeder. Fig. 5.3 shows the single line diagram of the test feeder. The transmission network upstream from the distribution feeder is represented by an ideal voltage series behind an equivalent positive- and zero-sequence Thevenin impedance of $Z_1^{eq} = j3.81\ \Omega$ and $Z_0^{eq} = j11.43\ \Omega$, respectively. A 10-MVA, delta/wye-grounded transformer with a leakage impedance of 4% is used to step down the voltage from 138 to 13.8 kV. A power quality monitor at the substation records the three-phase line-to-ground voltages and line currents at 128 samples per cycle. The main distribution feeder is 6 miles long and has a line configuration shown in Fig. 5.4. The

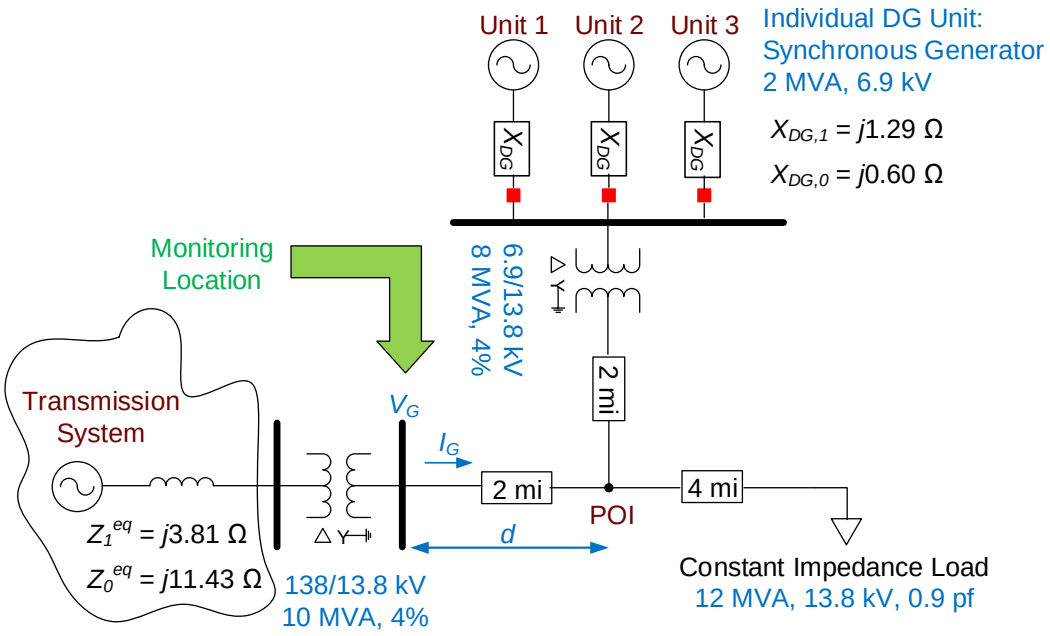

Figure 5.3: One-line diagram of the distribution test case feeder.

phase and neutral conductors are built using an all-aluminum conductor (AAC) of size 336 AWG. Using Carson's equations [3], the positive- and zero-sequence line impedances were calculated to be $Z_{L1,1} = 0.2780 + j0.6584\ \Omega/\text{mi}$ and $Z_{L1,0} = 0.5474 + j1.9720\ \Omega/\text{mi}$, respectively. These line impedances will be used for fault location in Section 5.3.

The distribution feeder serves a 12-MVA constant impedance load with a 0.9 lagging power factor. Part of this load is supported by the substation, limited only by the size of the 10-MVA transformer. The remaining load is served by three diesel generator units that are interconnected to the POI via a 2-mile long feeder. Each unit, rated at 2 MVA, consists of a diesel engine acting as a prime mover to a synchronous generator. In this analysis, synchronous generators were chosen since fault current contributed by these generators have the worst impact on fault location algorithms [72]. The generator was modeled as a voltage source behind a sub-transient reactance, X_d". This simple model is sufficient for performing short-circuit studies [2]. Machine constants of a Caterpillar diesel generator were used [2] and are listed in Table 5.1. Notations $X_{DG,2}$ and $X_{DG,0}$

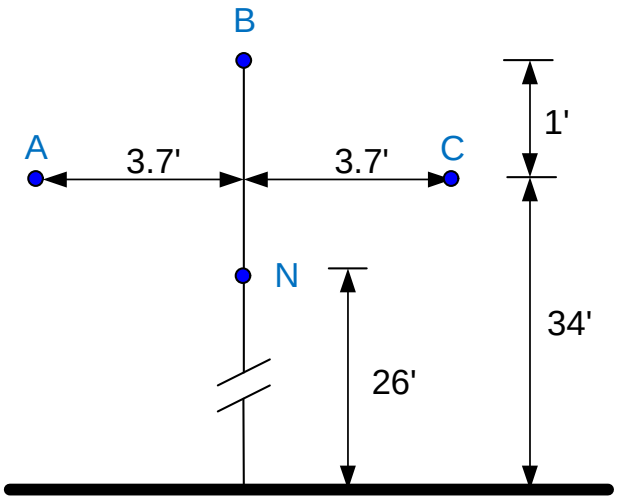

Figure 5.4: Line geometry of the 13.8-kV overhead distribution feeder.

refer to the negative- and zero-sequence generator reactance while the positive-sequence reactance of the generator ($X_{DG,1}$) is equal to X_d". An 8-MVA, delta/wye-grounded transformer with a leakage impedance of 4% interfaces the DG units to the feeder. The DG units appear to be "effectively grounded" since [33]

$$\frac{R_0}{X_1} = 0 \ < 1 \text{ and } \frac{X_0}{X_1} = 0.36 \ < 3$$

where R_0 is the zero-sequence resistance, X_0 and X_1 are the zero- and positive-sequence reactances, respectively at the high voltage side of the DG interconnect transformer.

Note that the test feeder has been intentionally designed to be simple, homogeneous, and compliant with the other assumptions [13] made by impedance-based fault locating algorithms. In such a scenario, the error in fault location estimates will be strictly proportional to the fault current contributed by DGs and will give an accurate measure of how DGs affect fault location accuracy.

Table 5.1: CAT SR4-HV Synchronous Generator Data [2]

Parameter	Data
Gen Manufacturer	Cat SR4-HV
Type of DG	Diesel
MVA-Continuous	2
Voltage (kV)	6.9
X_d" (pu)	0.162
$X_{DG,0}$ (pu)	0.0752
$X_{DG,2}$ (pu)	0.162

5.3 Factors that Affect Fault Location Downstream from DGs

5.3.1 DG Technology

The magnitude and duration of the fault current contributed by distributed generators (I_{DG}) depends on the electrical converter that DGs use to interconnect to the distribution feeder. According to the IEEE Standard 1547 [73], there are three types of electrical converters: synchronous machines, induction machines, and inverter-based DGs. Synchronous machines used by diesel generators, gas turbines and hydro generators provide a sustained fault current and have the worst impact on impedance-based fault locating algorithms [71]. Fault current is 5 to 10 times the rated current during the sub-transient period and then decays to 2 to 4 times the rated current [33]. Induction generators, used in fixed-speed and wide-slip wind turbines, can also contribute to a fault so long as the residual voltage on the healthy phase can establish a rotating magnetic field. Although the initial magnitude of the fault current is 5 to 10 times the rated current, the current decays at a rate which depends on the fault type [34]. As a result, the error in fault location depends on the fault type and also on the cycle chosen for fault location. Inverter-based DGs such as fuel cells, photovoltaic generators, double-fed induction generator (DFIG), and permanent magnet wind turbines contribute fault current for less than half a cycle [33]. In the worst case, if inverter-based DGs continue to

feed a fault, the fault current is only 1 to 2 times the rated current. The corresponding error in fault location estimates is, therefore, lower than other DG technologies [71].

5.3.2 DG Interconnect Transformer

Configuration of the step-up transformer that interfaces the distributed generator to the distribution feeder is an important consideration when applying impedance-based fault location algorithms. If the transformer is connected as a delta on the utility side, then DGs will not contribute any zero-sequence current during a single line-to-ground fault. As a result, the fault location error will be lower than when the transformer is wye-connected. Recall that single line-to-ground faults are the most common amongst all other types of fault.

5.3.3 Size of the DG Unit

The magnitude of I_{DG} in terms $(m-d)Z_{L1}\,(I_{DG}/I_G)$ and $R_F\,(I_F/I_G)$ of (5.2) depends on the MVA capacity of the installed distributed generators. Single DG units with a small MVA capacity do not contribute a significant fault current. However, when the MVA capacity is increased by aggregating a number of small or a few large DG units, the equivalent generator impedance decreases [33]. As a result, the total fault current from DGs increase and can significantly offset the accuracy of fault location algorithms.

To demonstrate how the MVA capacity of the DG unit affects fault locating algorithms, consider the test feeder developed in Section 5.2. At a particular instant of time, suppose that only Unit 1 DG is in operation while the remaining generators are switched off. When a single line-to-ground fault on phase A ($R_F = 0\ \Omega$) occurs at a distance of 4 miles from the substation, Unit 1 DG contributes a fault current of 0.47 kA. Using V_G and I_G recorded at the substation, location estimates from the impedance-based methods are shown in Table 5.2. Now, when Unit 2 DG is brought online along with Unit

1, then for the same fault, the total fault current at the DG terminal (I_{DG}) is 0.62 kA. This is because both the generators are in parallel and the equivalent impedance reduces to 0.08 pu. Since I_{DG} increases, the error in fault location also increases. Similarly, if a fault occurs when all the three DG units are in operation, the magnitude of I_{DG} is even higher, and the error in fault location increases proportionally.

Table 5.2: Impact of DG MVA Size on Fault Location Algorithms

DG Size (MVA)	X_d" (pu)	I_{DG} (kA)	Actual Location (mi)	Estimated Location (mi)		
				Simple Reactance	Takagi	Novosel *et al.*
2	0.16	0.47	4	4.84	4.86	4.84
4	0.08	0.62		5.01	5.04	5.01
6	0.05	0.73		5.14	5.17	5.14

5.3.4 Fault Distance from the DG Unit

As discussed in Section 5.1, when a bolted fault occurs downstream from the DG, the error in fault location primarily stems from the term $(m-d)Z_{L1}\,(I_{DG}/I_G)$. Location of the fault m affects the magnitude of this term in two ways: factors $(m-d)$ and the current ratio I_{DG}/I_G. When a fault occurs at the POI, the fault is very close to the distributed generator. Current I_{DG} and, therefore, I_{DG}/I_G is maximum. However, because m is equal to d, the term $(m-d)Z_{L1}\,(I_{DG}/I_G)$ becomes zero and DG will not affect the accuracy of location estimates.

The impact of how the distance to fault from the DG unit affects impedance-based fault location algorithm is illustrated by using the test case developed in Section 5.2. A single line-to-ground fault ($R_F = 0\ \Omega$) on phase A is simulated at a distance of 2 miles from the substation. Since the DG is also interconnected to the feeder at 2 miles, the term $(m-d)Z_{L1}\,(I_{DG}/I_G)$ becomes zero and DG has no impact on impedance-based fault

Table 5.3: Effect of Distance of the Fault from the DG Unit on Fault Location Algorithms

Actual Location (mi)	$m-d$ (mi)	$\frac{I_{DG}}{I_G}$	$\text{imag}\left[(m-d)Z_{L1}\frac{I_{DG}}{I_G}\right]$ (Ω)	Estimated Location (mi)		
				Simple Reactance	Takagi	Novosel *et al.*
2	0	$0.60\angle -3.7°$	$j0.0000$	2.00	2.00	2.00
3	1	$0.59\angle -5.4°$	$j0.3697$	3.56	3.57	3.56
4	2	$0.57\angle -7.2°$	$j0.7096$	5.08	5.10	5.08
5	3	$0.56\angle -9.2°$	$j1.0192$	6.55	6.60	6.55

location algorithms as shown in Table 5.3. When the same fault is simulated further downstream from DGs, $(m-d)$ increases. The current ratio I_{DG}/I_G, on the other hand, decreases since impedance to the fault increases. As seen in Table 5.3, this decrease in the current ratio is small. The increase in $(m-d)$ is the dominating factor. As a result, the corresponding error in the fault location estimates increase significantly.

5.3.5 Fault Resistance

To investigate how fault resistance affects fault location algorithms in the presence of distributed generators, a single line-to-ground fault on phase A is simulated in the test feeder at a distance of 4 miles from the substation. The fault resistance was varied from 0 to 10 Ω. As seen in Table 5.4, when $R_F = 0\ \Omega$, the reactance error due to $\text{imag}(R_F\,(I_F/I_G))$ is zero. Because of the fault current contributed by DGs, the term $(m-d)Z_{L1}\,(I_{DG}/I_G)$ in (5.2) increases the apparent impedance seen from the substation (Z_{app}). As a result, fault location algorithms overestimate the location of the fault. When the same fault is simulated with a fault resistance of 4 Ω, the reactance error is capacitive as seen in Table 5.4. In this case, the reactance error decreases Z_{app} while the term $(m-d)Z_{L1}\,(I_{DG}/I_G)$ tends to increase Z_{app}. As a result, location estimates from the simple reactance method improve as shown in Table 5.4. For $R_F = 8\,\Omega$, however, the reactance error is inductive. This is the worst case scenario since both the reactance

Table 5.4: Impact of R_F on Impedance-based Fault Locating Algorithms when the Fault is Downstream from DGs

R_F (Ω)	Actual Location (mi)	imag$\left[(m-d)Z_{L1}\frac{I_{DG}}{I_G}\right]$ (Ω)	imag$\left[R_F \times \frac{I_F}{I_G}\right]$ (Ω)	Estimated Location (mi)		
				Simple Reactance	Takagi	Novosel *et al.*
0		$j0.7096$	$j0.0000$	5.08	5.10	5.08
4	4	$j0.6569$	-$j0.1398$ (Capacitive)	5.05	5.52	4.79
8		$j0.6150$	$j0.0937$ (Inductive)	5.54	5.86	4.58

error and $(m-d)Z_{L1}\,(I_{DG}/I_G)$ increase Z_{app}. As a result, simple reactance and Takagi methods overestimate the location of the fault. It is interesting to observe that for non-zero values of R_F, accuracy of estimates from the Novosel *et al.* method improve as seen in Table 5.4. This does not indicate a good estimate. Rather, the error due to fault resistance is canceling out the effect of DG.

5.3.6 Tapped Load

Impedance-based fault locating algorithms assume that loads served by a distribution feeder are lumped at the end of the feeder [13]. In practice, loads are tapped along the entire length of the feeder as shown in Fig. 5.5. When a bolted fault ($R_F = 0\,\Omega$) occurs at point F as shown in Fig. 5.5, the actual impedance between the substation and the fault point F, Z_{GF}, is

$$Z_{GF} = Z_{GT} + Z_{TF} \tag{5.3}$$

where Z_{GT} is the positive-sequence impedance of the line segment between the substation and the tap point, and Z_{TF} is the positive-sequence line impedance between the tap point and the fault. However, due to tapped loads, relay G uses V_G and I_G to measure the

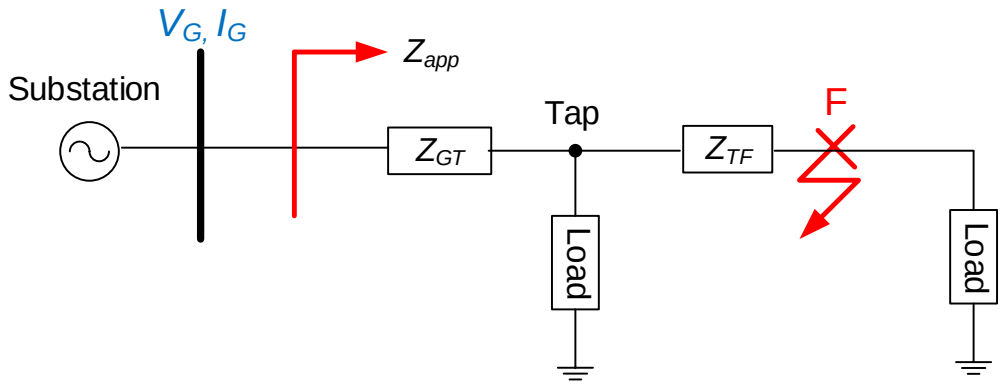

Figure 5.5: Loads tapped along the entire length of the distribution feeder.

apparent impedance to be

$$Z_{app} = \frac{V_G}{I_G} = Z_{GT} + \frac{Z_{TF} \times Z_{Load}}{Z_{TF} + Z_{Load}} < Z_{GF}. \tag{5.4}$$

Since Z_{Load} has a much higher impedance than Z_{TF}, the resultant value of $\left(\frac{Z_{TF} \times Z_{Load}}{Z_{TF} + Z_{Load}}\right)$ in (5.4) is closer to but slightly smaller than Z_{TF} [30]. In other words, tapped loads act as a negative impedance and Z_{app} is smaller than the actual impedance to the fault, Z_{GF}. In contrast, fault current contribution from DGs (I_{DG}) increase Z_{app} seen from the substation. Therefore, the two error factors, tapped load and I_{DG}, tend to cancel out each other and can help improve the accuracy of impedance-based fault locating algorithms.

The positive effect of tapped loads in locating faults that occur downstream from DGs is illustrated using the test feeder in Section 5.2. A single line-to-ground fault on phase A ($R_F = 0\,\Omega$) is simulated at a distance of 4 miles from the substation. In the first case, the load is lumped at the end of the feeder. As expected, using V_G and I_G at the substation, impedance-based algorithms overestimate the location of the fault as shown in Table 5.5. In the second case, the 12-MVA load is tapped at the POI. The tapped load, acting as a negative impedance, counters the effect of I_{DG} in increasing Z_{app}. As a result, fault location accuracy improves, albeit marginally.

Table 5.5: Impact of Load Taps on Fault Locating Algorithms

Load Tap	Actual Location (mi)	Estimated Location (mi)		
		Simple Reactance	Takagi	Novosel *et al.*
No	4	5.08	5.10	5.08
Yes		4.97	5.01	4.98

5.4 Summary

This Chapter concludes that the accuracy of impedance-based fault locating algorithms are compromised when faults occur downstream from distributed generators. The Chapter also identifies a number of factors which influence the magnitude of the fault location error. Synchronous DGs result in a higher fault location error as compared to inverter-based DGs while the fault location error due to induction generators depends on the fault type. The error in fault location also depends on the installed MVA capacity of the DG unit. Higher the MVA capacity, greater will be the error in fault location. DG interconnect transformers with a delta configuration on the utility side prevents the flow of zero-sequence currents during a ground fault. As a result, there will be no error in locating single line-to-ground faults. Tapped loads may counter the negative effect of DGs and help improve the accuracy of location estimates. Reactance error due to fault resistance may aid or further decrease the accuracy of location estimates. Finally, if a fault is located very close to the DG unit, the error in location estimates is negligible. As the fault moves further downstream from the DG unit, the fault location error increases significantly.

Chapter 6

An Impedance-based Fault-Locating Technique for Distribution Networks with Distributed Generators

As discussed in Chapter 5, the accuracy of existing impedance-based fault location algorithms deteriorate when locating faults downstream from distributed generators (DGs) in a distribution feeder. Short-circuit current to a fault comes from two sources, the utility substation and the distributed generators. Neglecting the latter term in the fault location calculation severely compromises the accuracy of impedance-based algorithms. Algorithms proposed by [26–28] aim to improve fault location accuracy in the presence of DGs. Unfortunately, these algorithms require additional measurements at the DG terminal that may not be available. Authors in [29] present an interesting, but iterative approach that utilize measurements captured at the substation only. Algorithms in [30] and [31] also make use of substation measurements; however, their application is limited to line-to-line and three-phase faults, respectively.

Based on the background mentioned above, the ***objective*** of this Chapter is to present a methodology that improves the accuracy of locating faults downstream from distributed generators. The ***contribution*** is based on the fact that the proposed algorithm uses only the voltage and current at the substation and the distributed generator impedance to estimate the missing fault current at the DG terminal. The estimated current is then included in the fault location calculation to improve the fault location accuracy. The proposed algorithm is non-iterative, straightforward to implement, and capable of locating single line-to-ground, line-to-line, double line-to-ground, and three-phase faults. When validated against an actual 34.5-kV distribution feeder, the distance

estimates from the proposed approach are within 0.5 miles of the actual fault location. The improvement in fault location accuracy over conventional algorithms is 0.56 miles.

6.1 Overview of the Proposed Approach

Chapter 5 demonstrates that the fault location error of existing impedance-based fault location algorithms is proportional to the magnitude of the following terms: $(m-d)Z_{L1}\,(I_{DG}/I_G)$ and $R_F\,(I_F/I_G)$. The approach proposed in this Chapter focuses on addressing each of those error terms to improve the accuracy of location estimates. For example, consider the scenario shown in Fig. 5.1. To eliminate the fault location error due to $(m-d)Z_{L1}\,(I_{DG}/I_G)$, the approach is to estimate the fault current contributed by the distributed generator, I_{DG}. Data required consists of voltage and current at the substation and the distributed generator impedance. The generator impedance can be obtained from manufacturer specifications, an example of which is shown in Table 5.1. The estimated I_{DG} is then incorporated into the fault location calculation to negate the error due to $(m-d)Z_{L1}\,(I_{DG}/I_G)$. The next step is to minimize the reactance error due to $R_F\,(I_F/I_G)$. For this purpose, observe that the distribution feeder in Fig. 5.1 is radial at the POI and that the current at the fault point, I_F, has a phase angle close to the current at the POI, I_{POI}. As a result, the reactance error can be minimized by using the voltage and current measurements at the POI for fault location. This step is equivalent to moving the monitoring location "electrically" from the substation to the POI as illustrated in Fig. 6.1.

6.2 Step-by-Step Derivation of the Proposed Approach

This Section presents a step-by-step derivation of the proposed approach for locating a single line-to-ground fault. The same principle can be extended for locating line-to-line, double line-to-ground, and three-phase faults.

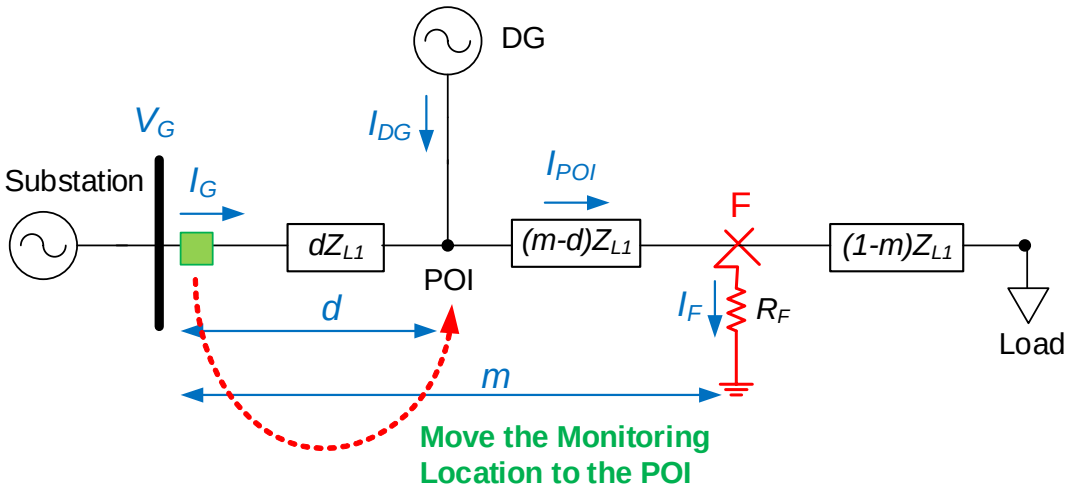

Figure 6.1: Move the monitoring location "electrically" from the substation to the POI.

Step 1: Estimate the Fault Current Contributed by DGs

The sequence network during a single line-to-ground fault is shown in Fig. 6.2. When a fault occurs downstream from the point of interconnection (POI), the substation and DGs operate parallel to each other while feeding the fault. As a result, the negative-sequence fault voltage at the POI, V_{POI2}, is the same when calculated from the substation or the DG terminal as shown below:

$$\text{Substation:} \quad V_{POI2} = V_{G2} - dZ_{L2}I_{G2} \tag{6.1}$$

$$\text{DG terminal:} \quad V_{POI2} = -Z_{DG2}I_{DG2} \tag{6.2}$$

where V_{G2} and I_{G2} are the negative-sequence fault voltage and current at the substation, I_{DG2} is the negative-sequence fault current from the DG terminal, d is the distance between the POI and the substation, Z_{DG2} is the equivalent negative-sequence Thevenin impedance between the DG and POI, and Z_{L2} is the negative-sequence line impedances. Equating (6.1) with (6.2), I_{DG2} can be estimated as

$$I_{DG2} = \frac{dZ_{L2}I_{G2} - V_{G2}}{Z_{DG2}} \tag{6.3}$$

Using the same principle, the zero-sequence fault current from the DG terminal, I_{DG0}, can be estimated as

$$I_{DG0} = \frac{dZ_{L0}I_{G0} - V_{G0}}{Z_{DG0}} \tag{6.4}$$

where V_{G0} and I_{G0} are the zero-sequence fault voltage and current at the substation, Z_{DG0} is the equivalent zero-sequence Thevenin impedance between the DG and POI, and Z_{L0} is the zero-sequence line impedances.

The calculation of the positive-sequence fault current from the DG terminal, I_{DG1}, on the other hand, is complicated by the presence of the internal source voltages. For this purpose, the superposition theorem is used to decompose the network during fault into a prefault and "pure fault" network as shown in Fig. 6.3. Fault current I_{DG1} is, therefore, the summation of the prefault and the "pure fault" current, I_{DGpre} and ΔI_{DG1}, respectively. The estimation of ΔI_{DG1} is straightforward and is given by

$$\Delta I_{DG1} = \frac{dZ_{L1}\Delta I_{G1} - \Delta V_{G1}}{Z_{DG1}} \tag{6.5}$$

where $\Delta V_{G1} = V_{G1} - V_{Gpre}$, $\Delta I_{G1} = I_{G1} - I_{Gpre}$, V_{G1} and I_{G1} are the positive-sequence fault voltage and current at the substation, V_{Gpre} and I_{Gpre} are the prefault voltage and current at the substation, and Z_{DG1} is the equivalent positive-sequence impedance between the DG and POI. The prefault current, I_{DGpre}, can be estimated as

$$|I_{DGpre}| = \frac{S_{DG}}{\sqrt{3} \times |V_{DGpre}|} \tag{6.6}$$

where S_{DG} is the rated power output of the DG unit and $|V_{DGpre}|$ is 1 per unit. The phase angle of I_{DGpre} can be obtained by assuming that I_{DGpre} lags V_{POIpre} by the power factor of the load. The calculation of V_{POIpre} is given by (6.7).

Step 2: Move the Monitoring Location "Electrically" to the POI

To minimize the reactance error due to fault resistance R_F, the monitoring location is moved "electrically" to the POI as illustrated in Fig. 6.1. The new set of voltage

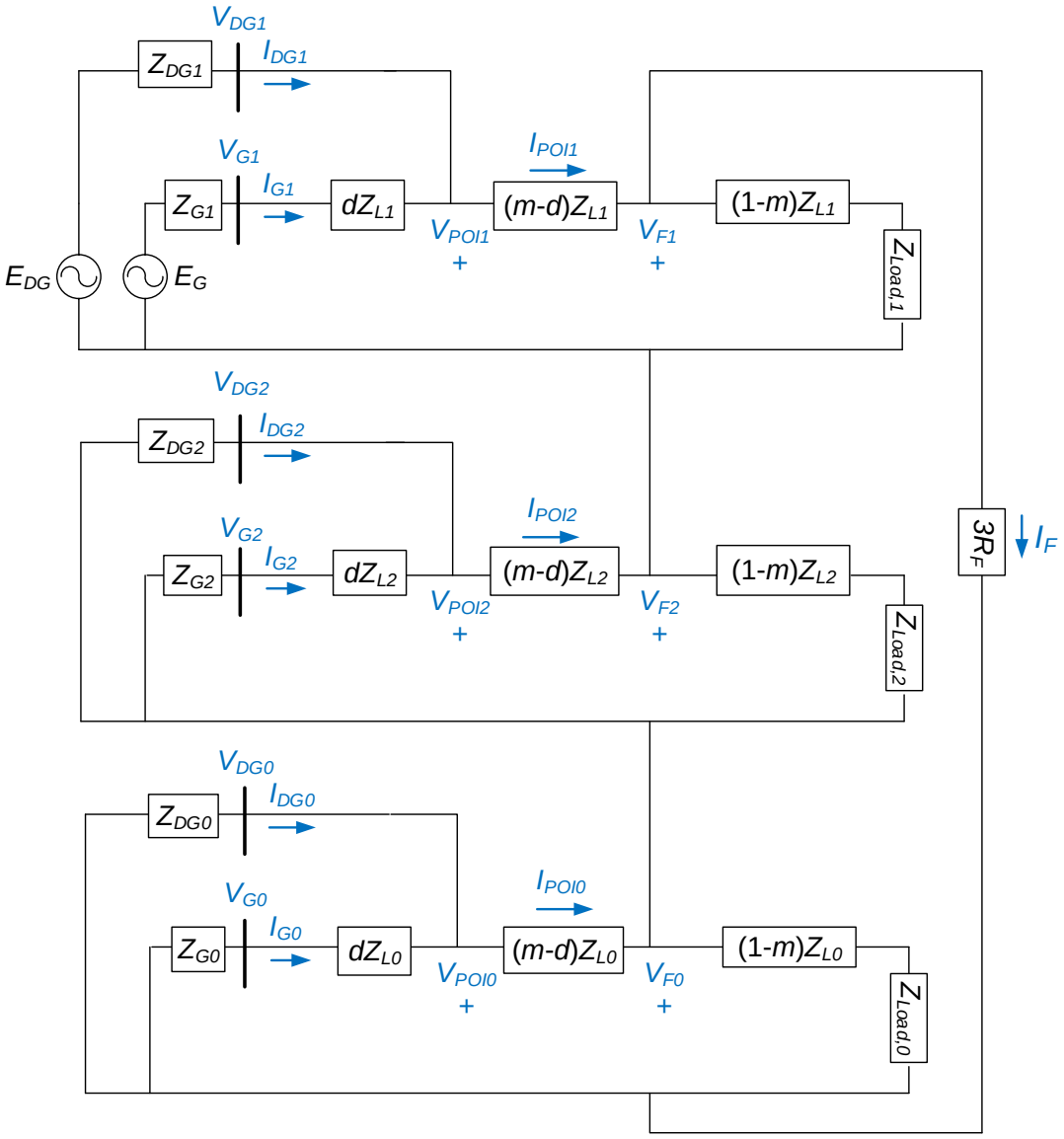

Figure 6.2: Sequence network during a single line-to-ground fault.

and current measurements at the POI can be computed from the substation measurements and will be used to solve for the distance to fault. For example, the prefault voltage and current phasors at the POI, V_{POIpre} and I_{POIpre}, can be calculated as:

$$\begin{aligned} V_{POIpre} &= V_{Gpre} - dZ_{L1} I_{Gpre} \\ I_{POIpre} &= I_{Gpre} + I_{DGpre} \end{aligned} \tag{6.7}$$

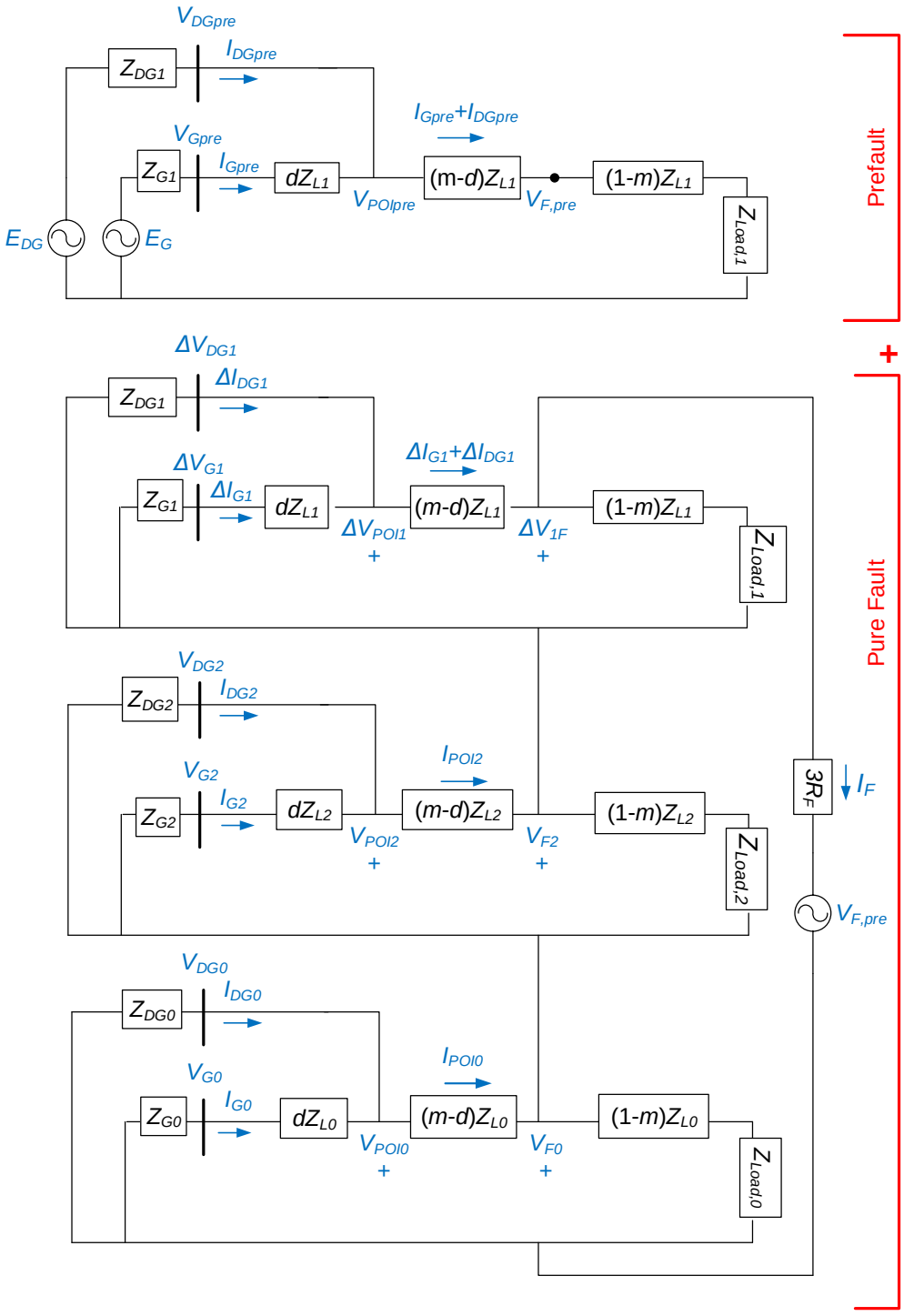

Figure 6.3: Superposition principle used to decompose the network into a prefault and "pure fault" network.

The positive-, negative-, and zero-sequence fault voltage phasors at the POI, V_{POI1}, V_{POI2}, and V_{POI0} are:

$$\begin{aligned} V_{POI1} &= V_{G1} - dZ_{L1}I_{G1} \\ V_{POI2} &= V_{G2} - dZ_{L2}I_{G2} \\ V_{POI0} &= V_{G0} - dZ_{L0}I_{G0} \\ \therefore V_{POI} &= V_{POI1} + V_{POI2} + V_{POI0} \end{aligned} \tag{6.8}$$

The positive-, negative-, and zero-sequence fault current phasors at the POI, I_{POI1}, I_{POI2}, and I_{POI0} are:

$$\begin{aligned} I_{POI1} &= I_{G1} + I_{DG1} \\ I_{POI2} &= I_{G2} + I_{DG2} \\ I_{POI0} &= I_{G0} + I_{DG0} \\ \therefore I_{POI} &= I_{POI1} + I_{POI2} + I_{POI0} \end{aligned} \tag{6.9}$$

Step 3: Apply Impedance-based Methods from the POI

The voltage and current phasors at the POI can be used in existing impedance-based fault location algorithms to estimate the distance to the fault. As an example, the simple reactance method computes the distance to fault as

$$m = \frac{\text{imag}\left(\dfrac{V_{POI}}{I_{POI} + kI_{POI0}}\right)}{\text{imag}\left[(1-d) \times Z_{L1}\right]} + d \tag{6.10}$$

6.3 Description of the Test Distribution Feeder

An actual 34.5-kV distribution feeder serving utility customers in rural New York was used to demonstrate the efficacy of the proposed approach. Customers on this feeder experience power outages longer than 10 hours. The high restoration time can be attributed to the fact that the distribution feeder is fed by a single radial transmission or sub-transmission supply line. Furthermore, maintenance crew need time to travel to the remote area and patrol the entire line length to find the fault location. Therefore, to reduce downtime and achieve the state Customer Average Interruption Duration Index (CAIDI) target of 2.5 hours, one part of the proposed solution was to develop a micro-grid. For this purpose, a 416-kW biomass diesel generator and a 6.6-MW wind farm were interconnected to the distribution feeder as shown in Fig. 6.4. Under normal operating conditions, the distributed generators would deliver power to the distribution circuit. Following a permanent fault, the micro-grid would disconnect itself from the faulted supply line and restore power to as many customers as possible until the fault is repaired. To reduce downtime, another part of the proposed solution was to employ fault location algorithms to narrow the search radius for the maintenance crew. Unfortunately, the presence of distributed generators challenge the accuracy of conventional fault location algorithms and provide the motivation for developing the improved solution presented in this Chapter. No field data is available since the system is being redesigned, and the objective was to demonstrate the feasibility of equipping the feeder with fault location capabilities in an interconnected grid condition. For this reason, a detailed time-domain model that emulates the distribution feeder was developed in PSCAD simulation software.

The rated voltage at the substation 34.5 kV. The line section between the substation and the POI is 7.42 miles long. The line section between the biomass diesel generator and the POI is 4 miles long while the line section between the POI and the wind farm is 6.3 miles long. The positive- and zero-sequence impedances of each line

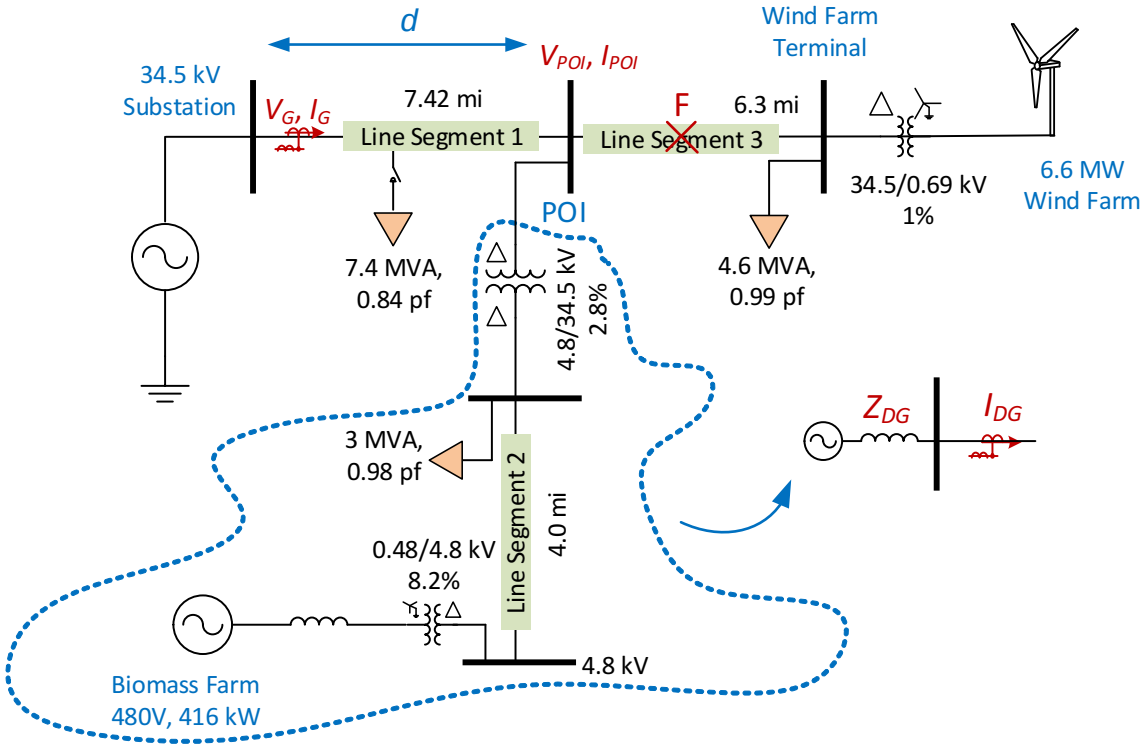

Figure 6.4: One-line diagram of the 34.5-kV distribution feeder. Transformer impedances are specified on a 100-MVA base.

segment are listed in Table 6.1. The 416-kW biomass diesel generator has a positive- and zero-sequence source impedance of $Z_{Biomass1} = Z_{Biomass0} = 0.0484\,\Omega$. The 6.6-MW wind farm consists of ten identical wind turbines connected in parallel. The specifications of each single wind turbine is shown in Table 6.2. For simulation purposes, all ten wind turbines are modeled as a single coherent machine. The impedances of a single wind turbine are divided by ten.

Table 6.1: Line Impedance Parameters of the 34.5-kV Distribution Feeder

	Line Length (mi)	Positive-sequence Line Impedance (Ω/mi)	Zero-sequence Line Impedance (Ω/mi)
Line Segment 1	1.12	$0.4379 + j0.6621$	$0.7216 + j3.1595$
	6.30	$0.8001 + j0.8119$	$1.0600 + j2.9353$
Line Segment 2	4.00	$0.9927 + j1.1478$	$0.9927 + j1.1478$
Line Segment 2	6.30	$0.8826 + j0.8676$	$1.1562 + j3.1030$

Table 6.2: 6.6-MW Wind Turbine Data

Specification	Single Wind Turbine
Rated Power Output (MW)	0.66
Rated Voltage (kV)	0.69
Rated Slip (%)	5
Rated Generator Speed (rpm)	1890
Power Factor at Full Load	0.89
Stator Resistance (Ω)	0.0034
Rotor Resistance (Ω)	0.0045
Stator Reactance (Ω)	0.068
Rotor Reactance (Ω)	0.078
Magnetizing Reactance (Ω)	2.58
External Resistance at Rated Slip (Ω)	0.0285
Blades and Generator Inertia Referred to the Generator Side (kgm^2)	118.99

6.4 Application of the Proposed Method

This Section demonstrates the efficacy of the proposed approach using the distribution feeder described in Section 6.3. Distance estimates from conventional algorithms and the proposed approach are compared.

6.4.1 Case 1: Estimating the Distance to a ABC Fault at 13.08 miles

In the first case, a single line-to-ground fault is simulated on Line Segment 3 at a distance of 13.08 miles from the substation. Both the substation and the biomass diesel generator operate in parallel to feed the fault. As a result, neglecting the fault current from the biomass generator will affect the accuracy of existing impedance-based fault location algorithms. The 6.6-MW wind farm also contributes current to the fault. However, because the fault is located upstream from the wind farm, the fault current appears as a remote infeed and will not have a significant impact on location estimates.

The first step towards determining the location of the fault is to estimate the fault current contributed by the biomass diesel generator. For this purpose, (6.5) is used to estimate the "pure fault" current, ΔI_{DG1}, as 0.03 kA. The actual ΔI_{DG1} is 0.03 kA. Next, knowing S_{DG} to be equal to 0.48 kW, I_{DGpre} is estimated using (6.6) to be 0.01 kA. The actual value of I_{DGpre} is 0.01 kA. The negative- and zero-sequence fault currents are zero during a three-phase fault. Next, impedance-based fault locating algorithms are applied from the POI to estimate the distance to fault to be 12.67 miles. The estimate from conventional fault location algorithms is 12.11 miles. As a result, the proposed approach is successful in improving the fault location accuracy by 0.56 miles.

6.4.2 Case 2: Estimating the Distance to a AB Fault at 12.46 miles

In the second case, a line-to-line fault involving phases A and B is simulated on Line Segment 3 at a distance of 12.46 miles from the substation. The simulated

fault resistance is 5Ω. Again, both the substation and the biomass generator operate in parallel to feed the fault. Using (6.5), the "pure fault" current, ΔI_{DG1}, is estimated to be 0.02 kA. The actual ΔI_{DG1} is 0.02 kA. The negative-sequence fault current from the DG terminal, I_{DG2} is estimated using (6.3) to be 0.01 kA. The actual value of I_{DG2} is 0.01 kA. Next, impedance-based fault locating algorithms are applied from the POI to estimate the distance to fault to be 12.04 miles. The estimate from conventional fault location algorithms is 11.53 miles. As a result, the proposed approach is successful in improving the fault location accuracy by 0.51 miles.

6.5 Summary

In summary, this Chapter develops a fault location algorithm that improves fault location accuracy in the presence of distributed generators. The proposed approach uses only the voltage and current at the substation and the distributed generator impedance to estimate the missing fault current at the DG terminal. The estimated current is then included in the fault location calculation to improve the accuracy of location estimates. The proposed algorithm is non-iterative, straightforward to implement, and capable of locating single line-to-ground, line-to-line, double line-to-ground, and three-phase faults. When validated against an actual 34.5-kV distribution feeder, the distance estimates from the proposed approach are within 0.5 miles of the actual fault location. The improvement in fault location accuracy over conventional algorithms is observed to be 0.56 miles.

Chapter 7

Effects of Distributed Generators on Relay Settings

For a successful operation of the power system, system operators are required to solve for the minimum and maximum fault currents. The minimum fault current is used for selecting fuses and specifying the relay pickup current while the maximum fault current is used for determining the rating of power system equipment. In traditional power systems, both the minimum and maximum fault currents are calculated by assuming a radial distribution feeder where electrical power flows unidirectionally from the substation to the load. With the integration of distributed generators (DGs) to the grid, however, DGs also contribute short-circuit current to the fault. For example, synchronous DGs (diesel generators, gas turbines, and hydro generators) and induction DGs (fixed-speed and wide-slip wind turbines) contribute a significant fault current as discussed in Chapter 5. Inverter-based DGs (photovoltaic generators, double-fed induction generator, and permanent magnet wind turbines), on the other hand, contribute a fault current which is only one or two times the rated current for less than half a cycle. Therefore, depending on the type of DG, it is essential to adjust the minimum and maximum fault currents to ensure that the system protection is well coordinated and that the maximum ratings of power system equipment are not exceeded.

It is a standard practice to use the IEC 60909-0 Standard for calculating the minimum and maximum fault currents in networks interconnected with DGs [32, 35]. The Chapter is motivated by the fact that the Standard has been developed for a traditional power system with conventional generators. However, fixed-speed and wide-slip wind turbines have specific features that distinguish them from conventional generators, the

fundamental difference being that the primary drive source, i.e., the wind speed is variable and intermittent in nature. In addition to this stochastic variation in wind speed, tower shadow and wind shear also cause periodic fluctuations in wind speed [36, 59]. Tower shadow is the obstruction of the tower to the wind and wind shear is the variation of wind speed with height. During a fault, the fault current from wind turbines is a function of the generator internal voltage at the instant of fault and the impedance to fault, the latter being a constant quantity. The generator internal voltage increases with increasing wind speed. For stochastic variations in wind speed, this increase in generator voltage is negligible and will not affect the fault current magnitude [74]. However, if the wind turbine is connected to a weak grid, the periodic fluctuations in wind due to tower shadow and wind shear can cause the generator internal voltage to fluctuate with a frequency between 0.5-2 Hz [75]. The voltage fluctuations are further pronounced in a wind farm where all the wind turbines are synchronized with each other. Therefore, depending on whether the generator internal voltage is maximum or minimum at the time of fault, the maximum and minimum fault current levels will also vary. Authors in [37,38] conclude that under heavily loaded conditions, the periodic variations in wind speed may have a substantial effect on short-circuit currents. However, they provide no guidelines on how such wind speed variations affect the relay pickup current and equipment ratings.

The ***objective*** of this Chapter is to illustrate how wind speed variation (stochastic and periodic) affects the fault current levels of a wind turbine and the system protection settings. The focus is on fixed-speed wind turbines since they contribute the maximum fault current, 6 or more times the rated current [76]. Section 7.1 presents the approach outlined in the IEC 60909-0 Standard to calculate the short-circuit current. The Section also presents an alternative approach for calculating the short-circuit current, which is more intuitive in understanding how wind speed variation can affect the maximum and minimum fault currents from a wind turbine. Section 7.2 discusses the

development of a detailed time-domain model of a fixed-speed wind turbine in PSCAD simulation software [47] that includes the tower shadow and wind shear effects. Section 7.3 presents five case studies of a fixed-speed wind turbine connected to the distribution grid in PSCAD. The first three case studies study the impact of the stochastic variation in wind speed on fault current levels while the remaining case studies investigate the impact of periodic fluctuations in wind due to tower shadow and wind shear on the short-circuit current contribution of a wind turbine. For each case study, the approach consists of comparing the fault current obtained via simulation at different wind speeds with the theoretical limits calculated using the IEC 60909-0 Standard. Section 7.4 summarizes the key findings of this Chapter.

The ***contributions*** of this Chapter are identified as follows: (a) Developed a detailed time-domain model of a fixed-speed wind turbine with tower shadow and wind shear effects, (b) Illustrated how the variation in wind speed can affect the generator internal voltage and hence, the magnitude of the short-circuit fault current, and (c) Verified the suitability of using the IEC 60909-0 Standard in calculating the maximum and minimum fault currents for networks interconnected with DG.

Publications:

- S. Das, N. Karnik, and S. Santoso,"Time-domain modeling of tower shadow and wind shear in wind turbines," *ISRN Renewable Energy*, vol. 2011, no. 890582, Jul. 2011 [59].
- S. Das and S. Santoso, "Effect of wind speed variation on the short-circuit contribution of a wind turbine," in *Proc. IEEE Power Energy Soc. General Meeting*, Jul. 2012, pp. 1-8 [60].

7.1 Maximum and Minimum Fault Currents from a Fixed-speed Wind Turbine

This Section outlines the approach recommended by the IEC 60909-0 Standard for calculating the maximum and minimum fault currents from a wind turbine. It also presents an alternative approach which provides an insight into how the variation in wind speed can affect the fault current contribution from a wind turbine.

7.1.1 IEC 60909-0 Standard

The IEC 60909-0 Standard uses an equivalent voltage source method to calculate the maximum and minimum fault currents from a wind turbine [32, 35]. An equivalent voltage source $cU_n/\sqrt{3}$ is applied at the fault point, and all other generation sources are neglected. Distribution feeders and rotating machines are replaced by their internal impedances while non-rotating loads are ignored. For a symmetrical three-phase fault, the initial symmetrical short-circuit current, $I_k^{''}$, is calculated as

$$I_k^{''} = \frac{cU_n}{\sqrt{3} \times Z_k} \tag{7.1}$$

where Z_k is the equivalent short-circuit impedance at the fault point, U_n is the nominal system voltage at the fault point, and c is a voltage factor that accounts for any variation of the actual voltage from the nominal value. The Standard recommends calculating the maximum and minimum fault currents as follows:

(a) Maximum Short-circuit Current

The maximum short-circuit current will be used to determine the rating of power system equipment, and can be calculated under the following conditions:

- Use a voltage factor $c = c_{max}$. For MV/HV networks, c_{max}=1.1.
- Calculate the line resistance, R_L, at 20°C.

- Include motors according to the guidelines in the IEC Standard.
- Choose the maximum current contribution from power plants and network feeders.

(b) Minimum Short-circuit Current

The minimum short-circuit current will be used to select fuses and determine the settings of protective relays, and can be calculated under the following conditions:

- Use a voltage factor $c = c_{min}$. For MV/HV networks, c_{min}=1.
- Calculate the line resistance, R_L, at a higher temperature as

$$R_L = [1 + \alpha(\theta_e - 20°\text{C})] \times R_{L20} \tag{7.2}$$

  where R_{L20} is the line resistance at 20°C, θ_e is the conductor temperature in °C at the end of a fault, and α is the temperature co-efficient resistance of the material.
- Neglect motors.
- Choose the minimum current contribution from power plants and network feeders.

7.1.2 Alternative Approach

To understand how the variation in wind speed affects the fault current contribution from a wind turbine, this subsection describes an alternative approach for calculating the initial symmetrical short-circuit current. Consider a wind turbine generator operating at full voltage and supplying a load current of I_{Load}. When a symmetrical three-phase fault occurs at the generator terminals, $I_k^{''}$ can be calculated as [77, 78]

$$I_k^{''} = \frac{E^{''}}{X_{gen}^{''}} \tag{7.3}$$

where $E^{''}$ is the subtransient internal voltage of the generator at the moment of short-circuit and $X_{gen}^{''}$ is the subtransient reactance of the generator. Note that the armature

resistance is negligible and is hence, neglected. Equation (7.3) is more intuitive in understanding how wind speed variation may impact the fault current magnitude. The fault current, $I_k^{''}$, depends on $E^{''}$ and $X_{gen}^{''}$, the latter being a constant quantity. The internal voltage of the generator is given as

$$E^{''} = V_{terminal} + I_{Load} X_{gen}^{''} \tag{7.4}$$

Substituting the expression for $E^{''}$ in (7.3):

$$I_k^{''} = \frac{V_{terminal} + I_{Load} X_{gen}^{''}}{X_{gen}^{''}} \tag{7.5}$$

As seen from (7.4) and (7.5), the magnitude of fault current, $I_k^{''}$, is directly proportional to the generator internal voltage, $E^{''}$ [37, 38]. Since $E^{''}$, in turn, depends on $V_{terminal}$ and I_{Load}, the impact of those two factors on $E^{''}$ and hence, on $I_k^{''}$ is explained below:

(a) Variation in Load Current, I_{Load}

The load current contribution of a fixed-speed wind turbine is directly proportional to the wind speed. The maximum load current ($I_{Load} = I_{rated}$) is supplied at the rated wind speed as shown in Fig. 7.1. For all other wind speeds, the load current decreases. Therefore, the maximum internal voltage of the generator, $E_{max}^{''}$, is

$$E_{max}^{''} = V_{terminal} + I_{rated} X_{gen}^{''} \tag{7.6}$$

Since $E^{''} < E_{max}^{''}$ at all other wind speeds, the fault current contributed by the wind turbine is expected to be maximum at the rated wind speed. However, this variation in $E^{''}$ due to I_{Load} is small and will not have a significant impact on $I_k^{''}$. This is because the subtransient generator reactance, $X_{gen}^{''}$, is a small number. As a result, any change of the voltage drop term $I_{Load} X_{gen}^{''}$ in (7.5) will have a minor impact on $I_k^{''}$.

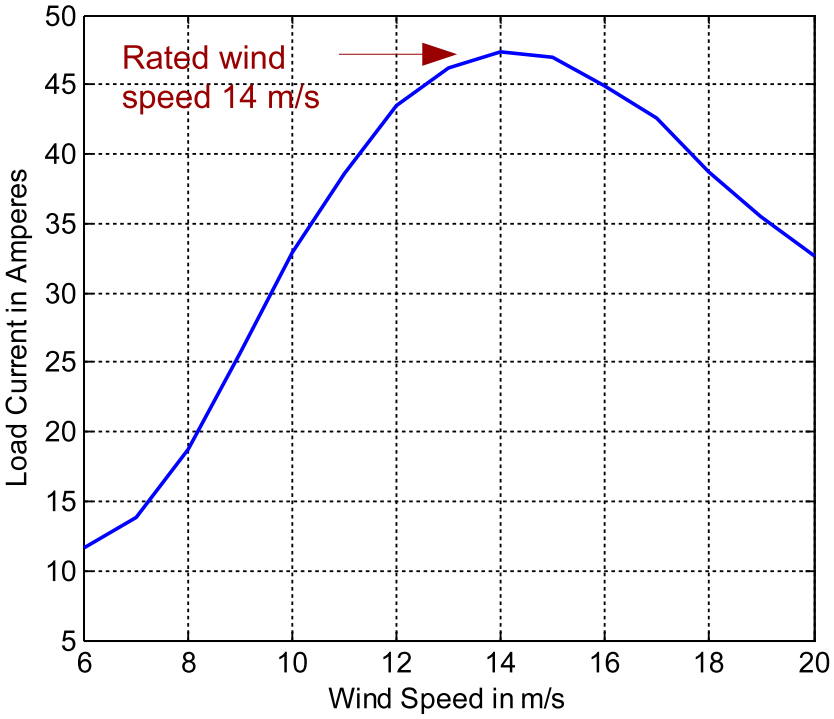

Figure 7.1: Load current from a fixed-speed wind turbine is maximum at rated wind speed.

(b) Variation in Terminal Voltage, $V_{terminal}$

Fixed-speed wind turbines are characterized by having a fixed rotational speed and being directly interconnected to the grid. As a result, when the output power from the wind turbine fluctuate due to the variation in wind speed, the reactive power consumed by the induction generator and hence, the generator terminal voltage also fluctuate [79]. A strong grid forces the terminal voltage to be relatively constant. However, when the wind turbine is connected to a weak grid, the terminal voltage will oscillate. These oscillations in terminal voltage are further pronounced when the effects of tower shadow and wind shear are included in the wind turbine model. For a three-bladed wind turbine, tower shadow and wind shear cause the output power to fluctuate with a $3p$ frequency where p is the rotational frequency of the blades. Consequently, $V_{terminal}$ also fluctuates at a $3p$ frequency which is in the range of 0.5 - 2 Hz. As an example, Fig. 7.2

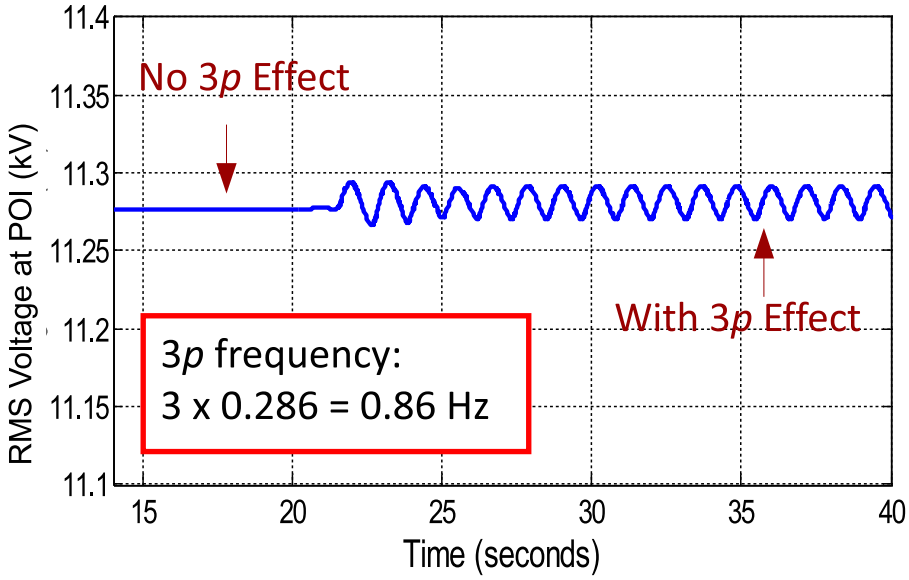

Figure 7.2: Terminal voltage fluctuating at a $3p$ frequency.

shows the variation in the wind turbine terminal voltage at a $3p$ frequency. In a wind farm, where all the wind turbines are synchronized with each other, the $3p$ effect will be further amplified, resulting in severe fluctuations in $V_{terminal}$. Since E'' depends on $V_{terminal}$, E'' will also fluctuate. When a fault occurs at the instant E'' is maximum, the fault current will be greater than when the fault occurs at the instant E'' is minimum.

It should be noted that the magnitude of voltage fluctuations due to $3p$ depends on wind speed. The magnitude of fluctuations increase almost linearly with increase in wind speed and is maximum at the rated wind speed. For a wind speed greater than the rated wind speed, the fluctuation decreases as demonstrated in [59, 75]. Therefore, the maximum variation in fault current levels will be obtained at the rated wind speed.

7.2 Time-domain Modeling of a Fixed-speed Wind Turbine

A wind turbine extracts the kinetic energy available in winds and converts it into electrical energy [59]. This energy conversion requires an interaction between the

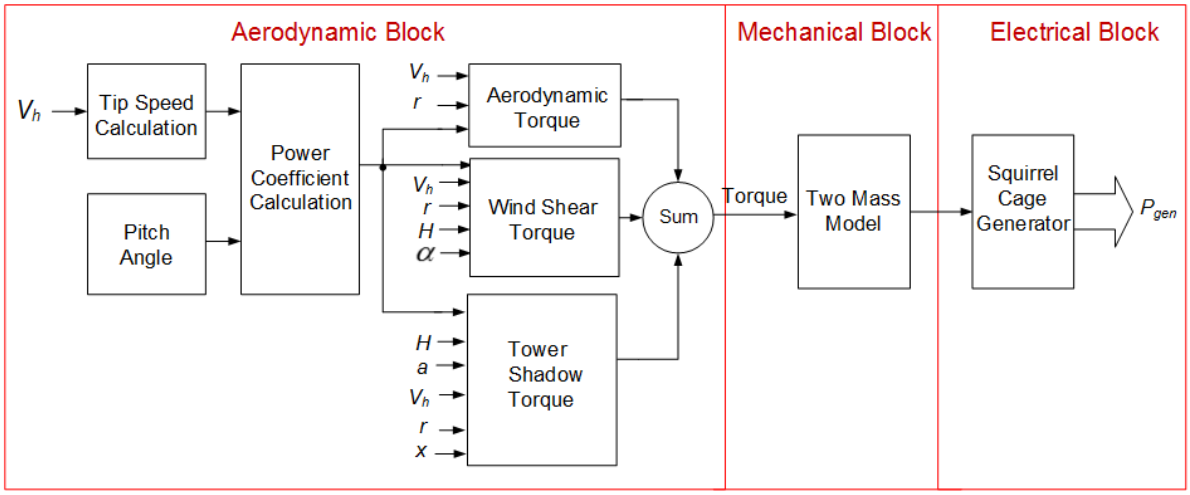

Figure 7.3: Block diagram of a fixed-speed wind turbine with tower shadow and wind shear.

aerodynamic, mechanical, and electrical components as illustrated in Fig. 7.3. The building blocks are briefly described below:

(a) Aerodynamic Block

The aerodynamic block inputs the wind speed (V_h) and computes the total aerodynamic torque that rotates the wind turbine rotor. The module titled "tip speed calculation" calculates the tip speed ratio which is defined as the ratio of the blade tip speed to the wind speed. The tip speed ratio together with the blade pitch angle is used to determine the power coefficient. This coefficient is then used to solve for the aerodynamic torque due to the kinetic energy in the wind. Two separate modules are used to simulate the fluctuations in torque due to tower shadow and wind shear.

Wind shear is the variation of wind speed with height. The wind turbine blades experience maximum wind when facing directly upwards and minimum when facing downwards as illustrated in Fig. 7.4. For three-bladed wind turbines, each of the three blades experiences minimum wind speed in one complete rotation. As a result, the torque due to wind shear fluctuates at $3p$ frequency. Wind shear is expressed by the

power law as

$$V(z) = V_h \left(\frac{z}{H}\right)^{\alpha} \tag{7.7}$$

where $V(z)$ is the disturbance in wind speed due to wind shear, z is the elevation above ground, H is the hub height, and α is the empirical wind shear component.

Tower shadow is the reduction in wind speed due to the presence of the tower. When the blade is in front of the tower of an upwind turbine, each of the three blades experiences minimum wind speed in one complete rotation as illustrated in Fig. 7.4. As a result, the torque due to tower shadow also fluctuates at $3p$ frequency. The disturbance in wind speed due to tower shadow, $V(r, \theta, x)$, can be expressed as

$$V(r, \theta, x) = V_h \times \frac{a^2 \left(r^2 sin^2\theta - x^2\right)}{\left(r^2 sin^2\theta + x^2\right)} \tag{7.8}$$

where a is the tower radius, x is the distance of the blade origin from the tower midline, r is the radial distance from the rotor axis, and θ is the blade azimuthal angle. The total torque is the summation of the aerodynamic, wind shear, and tower shadow torques. Equations governing each block are detailed in [59, 80].

(b) Mechanical Block

The mechanical block consists of the wind turbine shaft, generator shaft, and gearbox. These components have been modeled using a two-mass model since this model is simple and shows the dynamic response of the wind turbine generator.

(c) Electrical Block

The main component of the electrical block in a fixed-speed wind turbine is a squirrel-cage induction generator.

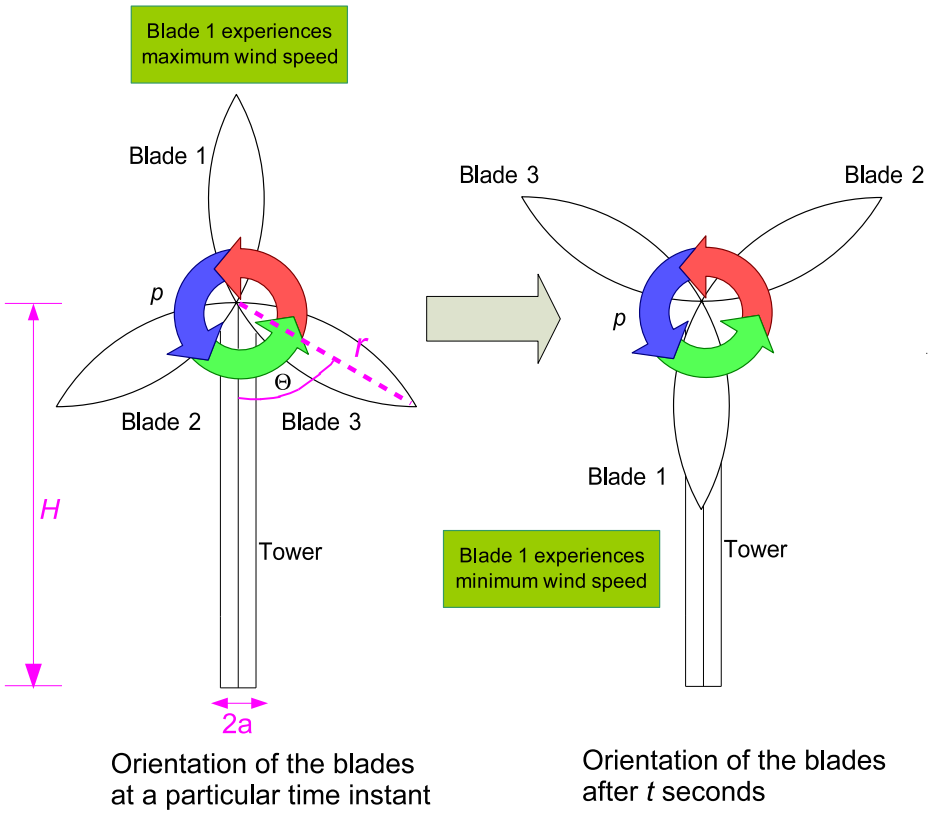

Figure 7.4: Illustrating the tower shadow and wind shear effect in wind turbines.

7.3 Analysis of Wind Speed Variation on Fault Currents

This Section presents a comprehensive analysis of the effects of wind speed variation on the fault current contribution from a fixed-speed wind turbine. It begins by describing the approach adopted for analysis. Next, the Section presents five case studies in PSCAD simulation software. The first three case studies explore the impact of stochastic variations in wind speed on fault current levels while the remaining case studies examine the effect of periodic pulsations in wind speed due to tower shadow and wind shear.

7.3.1 Approach for Analysis

The time-domain model of a fixed-speed wind turbine developed in Section 7.2 was used to analyze the impact of wind speed variation on the fault current contribution

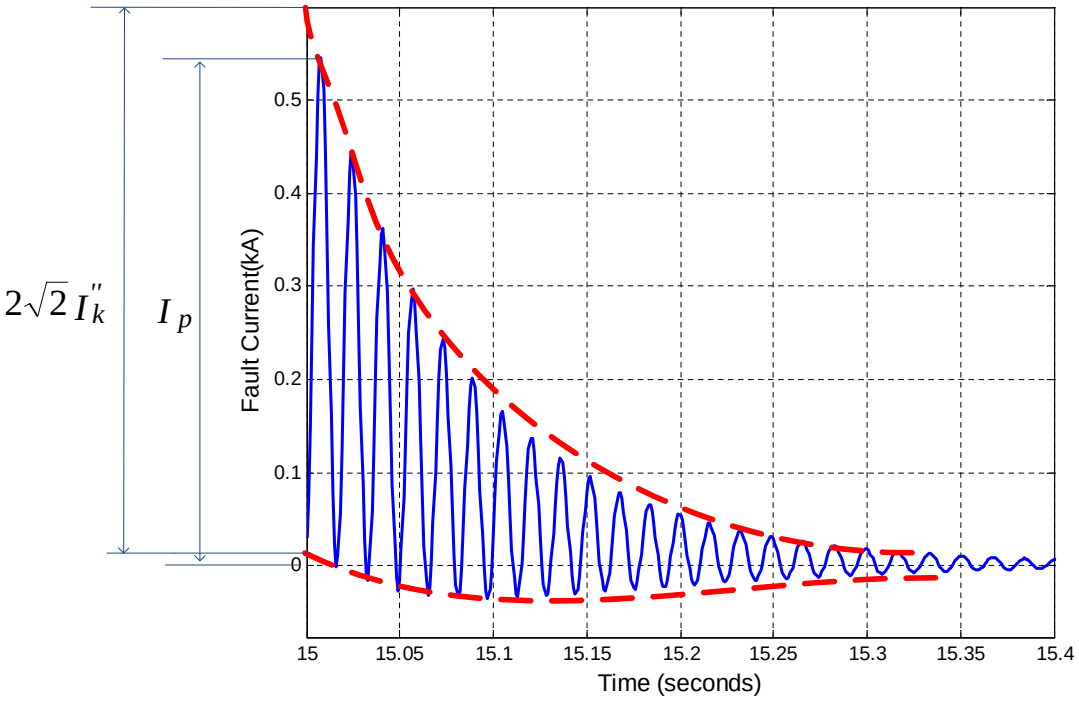

Figure 7.5: Three-phase fault current from a fixed-speed wind turbine.

from a wind turbine. The approach consists of using the IEC 60909-0 Standard for calculating the maximum and minimum symmetrical fault currents during a three-phase fault in the system. The same fault is then simulated in the wind turbine model under different wind speeds in order to compare the theoretical magnitudes of fault current with those obtained from simulation. Fig. 7.5 shows a typical fault current waveform from a fixed-speed wind turbine. As expected, the fault current decays as the magnetic flux required to maintain the internal voltage of an induction generator collapses in a few cycles [76]. Because the AC component of the current is not constant, determining the magnitude of the symmetrical current, I_k'', from such a waveform is difficult. Therefore, this analysis compares the peak currents instead of the symmetrical currents.

The peak current in the first half cycle has a decaying DC offset and is a function of the fault instant. The DC offset is maximum when the fault occurs at the zero cross-

ing of the internal voltage and minimum when the fault occurs at peak voltage. Since the fault inception time is not exactly known, the peak current calculated theoretically and that obtained from simulation will be different. Therefore, instead of matching the theoretical and simulated peak currents, the Chapter calculates a theoretical range of the peak current and evaluates whether the peak current obtained from simulation is within that range. The procedure for calculating the range is as follows:

Step 1: Calculate the maximum short-circuit current, $I''_{k,max}$, using (7.1). The corresponding peak current is $i_p = \kappa\sqrt{2}I''_{k,max}$. For maximum DC offset, κ is

$$\kappa = 1.02 + 0.98e^{-3R/X}$$

Using the above value of κ yields the maximum possible peak current. For zero DC offset, the peak current is $i_p = \sqrt{2}I''_{k,max}$. Therefore, for a maximum fault current of $I''_{k,max}$, the peak current, $I_{p,max}$, lies within the following range:

$$\sqrt{2}I''_{k,max} \leq I_{p,max} \leq \kappa\sqrt{2}I''_{k,max} \tag{7.9}$$

Step 2: Calculate the minimum short-circuit current, $I''_{k,min}$, using (7.1). The corresponding peak current is $I_{p,min}$ and it's range is:

$$\sqrt{2}I''_{k,min} \leq I_{p,min} \leq \kappa\sqrt{2}I''_{k,min} \tag{7.10}$$

Step 3: Combine the range obtained in Step 1 and Step 2. The peak fault current from simulation studies is expected to fall within the following theoretical range:

$$\sqrt{2}I''_{k,min} \leq I_{p,simulation} \leq \kappa\sqrt{2}I''_{k,max} \tag{7.11}$$

The range given in (7.11) takes into account the minimum pick-up current of relays as well as the maximum rating of circuit breakers.

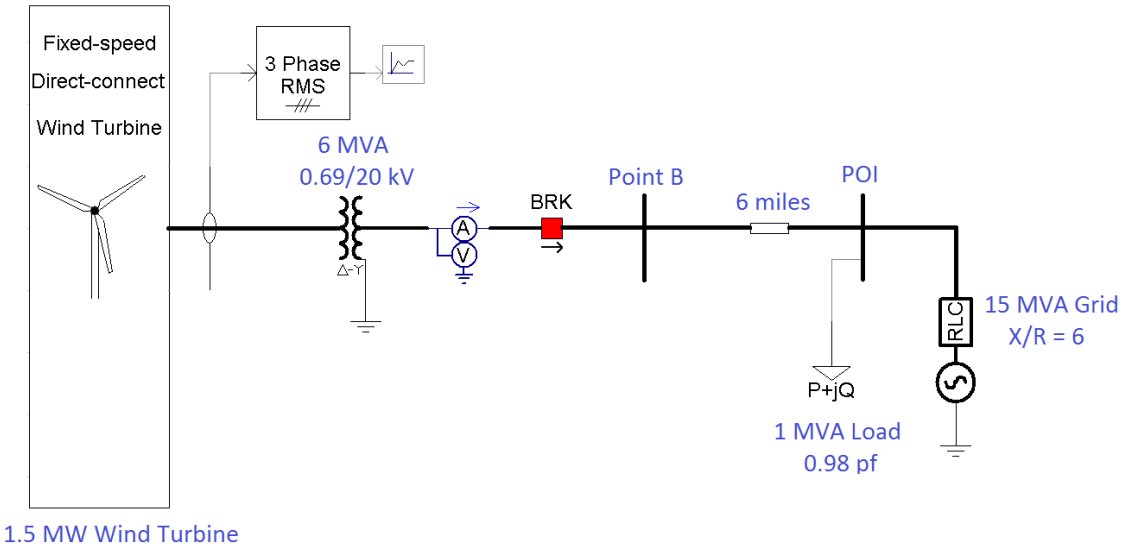

Figure 7.6: A 1.5-MW fixed-speed wind turbine connected to the distribution grid in PSCAD simulation software.

7.3.2 Case Study: Fixed-speed Wind Turbine and a Weak Grid

In this case study, the wind turbine components described in Section 7.2 were integrated to build a 1.5-MW fixed-speed wind turbine in PSCAD simulation software. The wind turbine was then connected to a 15-MVA grid via a 6-MVA, 0.69/20-kV delta-wye grounded transformer and a 6-mile medium voltage cable as illustrated in Fig. 7.6. A 1-MVA, 0.98-pf load was connected at the point of interconnection (POI). Data used for developing the network are listed in Table 7.1. The objectives of this case study are twofold: (a) investigate the impact of stochastic wind speed variation on the fault current contribution of the wind turbine, and (b) identify the part of the network which is most susceptible to the wind speed variation.

(a) Symmetrical Fault at the POI

A three-phase fault with a zero fault resistance was simulated at the POI in Fig. 7.6. The per unit equivalent circuit with a 20-kV, 6-MVA base is shown in Fig. 7.7. The load at the POI is a non-rotating load and was ignored for short-circuit calculations.

Table 7.1: Network Data

Parameter	Value
Blade radius, r	36 m
Hub height, H	80 m
Tower radius, a	36 m
Blade origin from tower midline, x	56 m
Wind shear component, α	0.3
Gear ratio	70
Rotor moment of inertia	1000 kgmm
Generator moment of inertia	80 kgmm
Generator rated power	1.7 MW
Generator pole pairs	3
Generator impedance, X''_{gen}	$j0.209$ pu
Transformer impedance	$0.011 + j0.0595$ pu
Transmission line, Z_{line}	$1.3778 + j0.8412\ \Omega$ (maximum I''_K) $2.4268 + j0.8412\ \Omega$ (minimum I''_K)
Grid impedance, Z_{grid}	$4.3839 + j26.304\ \Omega$

Using the equivalent circuit, the maximum fault current from the wind turbine can be calculated as

$$I''_{k,WT,max} = \frac{1.1 \times 20}{\sqrt{3}\,(0.1342 + j0.8728) \times 66.67} = 215.8\angle -81.26^\circ \text{ A}$$

Similarly, the minimum fault current from the wind turbine is calculated as

$$I''_{k,WT,min} = \frac{1.0 \times 20}{\sqrt{3}\,(0.2295 + j0.8728) \times 66.67} = 191.9\angle -75.27^\circ \text{ A}$$

Using (7.11) and $\kappa = 1.6379$, the peak current from the wind turbine is expected to fall within the following theoretical range:

$$271.4 \leq I_p \leq 499.8 \text{ A} \tag{7.12}$$

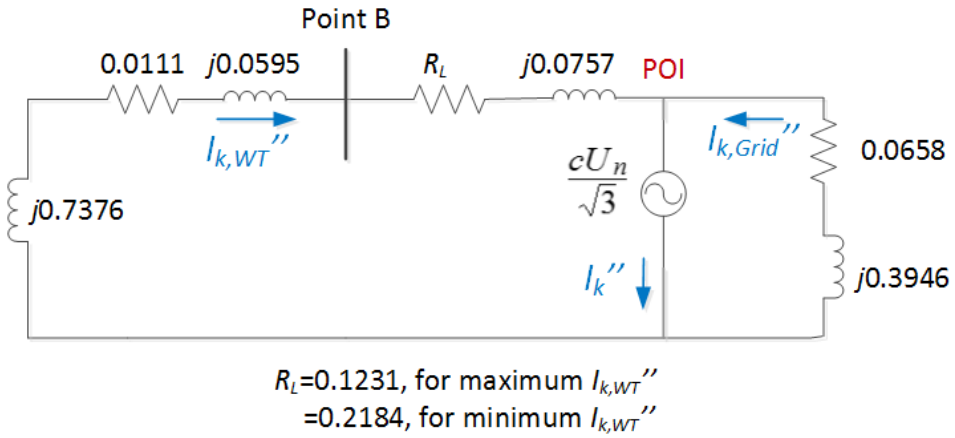

Figure 7.7: The per unit equivalent of the system in Fig. 7.6 on a 20-kV, 6-MVA base.

Next, the wind turbine model in PSCAD was subjected to wind speeds ranging from 6 m/s to 20 m/s. At each wind speed, the peak fault current measured at the wind turbine terminal was tabulated in Table 7.2. Because the aim is to study the stochastic variation of wind speed on the fault current contribution from a wind turbine, the tower shadow and wind shear modules were switched off. Table 7.2 shows that the load current supported by the wind turbine increases with increase in wind speed and is maximum at the rated wind speed of 14 m/s. However, the corresponding fluctuation in peak current is only in the range of a few amperes and within the theoretical range given by (7.12). The reason can be attributed to the small value of X''_{gen} as discussed in Section 7.1.2.

Another interesting observation is that with the increase in wind speed from 6 m/s, the peak fault current also increases. However, at the rated wind speed, there is a small drop in the peak fault current. For wind speeds greater than the rated wind speed, the peak fault current again increases. This is unexpected since the maximum peak current must be at the rated wind speed (maximum power output). Note that it is possible to compare the peak current at different time instants since the fault at each wind speed has been simulated at the same time instant, i.e., at the same time instant of the instantaneous voltage. This discrepancy in the behavior of the wind turbine can

Table 7.2: Fault Current Contribution from the Wind Turbine at Different Wind Speeds

Wind Speed (m/s)	Peak Fault Current (A)	Wind Turbine Terminal Voltage (kV)	Load Current (A)	Reactive Power Demand (VAR)
6	383	0.669	12	384.82
10	391	0.680	33	551.97
14	388	0.677	48	745.72
20	390	0.680	39	626.90

be explained by taking into account the short-circuit capacity (SCC) of the grid. The 15-MVA grid with no external reactive power support is electrically weak since

$$\frac{SCC}{P_{gen}} = \frac{15}{1.5} = 10 < 20$$

where P_{gen} is the power output from the wind turbine. When the wind speed increases, the reactive power demand of the wind turbine also increases and is maximum at the rated wind speed as shown in Table 7.2. Because the grid is electrically weak, it cannot support the reactive power demand of the wind turbine at the rated wind speed. As a result, the terminal voltage drops as shown in Table 7.2. Recall that E'' decreases when $V_{terminal}$ decreases in (7.4). Therefore, the magnitude of fault currents also decrease. At a wind speed of 18 m/s, the reactive power demand of the wind turbine decreases. The terminal voltage recovers and the peak fault current increases to 390 A.

(b) Symmetrical Fault at the High Voltage side of the Transformer

To identify the part of the network most susceptible to the variation in wind speed, a three-phase fault was simulated at the high voltage side of the transformer as indicated by point B in Fig. 7.6. Because the fault is so close to the wind turbine terminal, the wind turbine will contribute the maximum fault current. Using the IEC Standard, the maximum and minimum possible fault currents from the wind turbine are

$$\begin{aligned} I''_{k,WT,max} &= 239.0\angle -89.2^\circ \text{ A} \\ I''_{k,WT,min} &= 217.3\angle -89.2^\circ \text{ A} \end{aligned}$$

Table 7.3: Fault Current Contribution from the Wind Turbine at Different Wind Speeds

Wind Speed (m/s)	Peak Fault Current (A)	Wind Turbine Terminal Voltage (kV)	Load Current (A)
6	527.5	0.668	12
10	536.9	0.680	33
14	532.4	0.677	48
20	535.9	0.680	39

Using (7.4), the theoretical limits for the peak current is:

$$307.3 \leq I_p \leq 662.4 \text{ A} \tag{7.13}$$

Next, the same fault is simulated in the PSCAD model at different wind speeds and is shown in Table 7.3. The peak currents at each wind speed are within the theoretical limits given in (7.13). An interesting observation is that although the wind turbine contributes a much higher fault current, the fluctuation in peak current due to wind speed variation is still in the range of a few amperes. In other words, the fluctuations in peak current are independent of the fault location. This can be understood from the following expression:

$$\Delta E^{''} = \Delta V_{terminal} + \Delta I_{Load} X^{''}_{gen} \tag{7.14}$$

Fluctuations in internal voltage $\Delta E^{''}$ and hence, the peak current are a function of the change in terminal voltage, $\Delta V_{terminal}$, and the change in load current, ΔI_{Load}. Both factors are measured before fault and are not influenced by the location of the fault.

In summary, this case study concludes that the stochastic variations in wind speed does not affect the fault current contribution from a fixed-speed wind turbine. The fluctuations in fault current are within the maximum and minimum limits set by the IEC 60909-0 Standard. The fault current is expected to be maximum at the rated wind speed. However, when connected to a weak grid, the fault current at the rated wind speed may decrease due to insufficient reactive power support. Furthermore, the fluctuations in fault current are independent of the fault location.

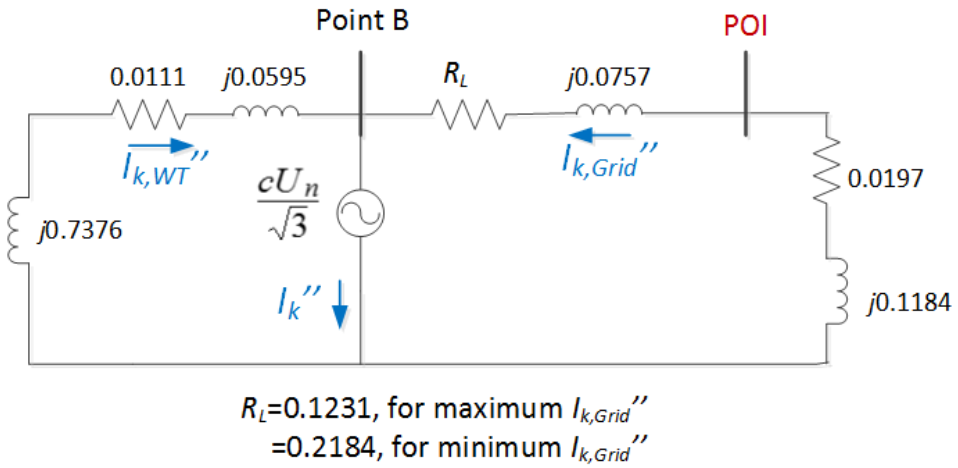

Figure 7.8: Equivalent circuit of the system in Fig. 7.6 interconnected to a 50-MVA distribution grid.

7.3.3 Case Study: Fixed-speed Wind Turbine and a Strong Grid

This case study investigates the impact of grid strength on the fault current levels of a wind turbine. For this purpose, the 1.5-MW wind turbine in Section 7.6 was connected to a 50-MVA grid. This is an electrically strong grid since

$$\frac{SCC}{P_{gen}} = \frac{50}{1.5} = 33 > 20$$

A symmetrical fault was then simulated on the HV side of the transformer as indicated by point B in Fig. 7.6. The equivalent circuit of the system is shown in Fig. 7.8. Since all other network parameters remain the same as the case study in Section 7.3.2, the theoretical limits for the peak current (I_p) are the same as (7.13), i.e.,

$$307.3 \leq I_p \leq 662.4 \text{ A}$$

As seen from Table 7.4, the fault current levels from the wind turbine under different wind speeds is within the theoretically calculated minimum and maximum limits. Also note that the wind turbine now contributes the maximum fault current at the rated wind speed. This is because the short-circuit strength of the grid is sufficient to support

Table 7.4: Fault Current from a 1.5-MW Wind Turbine Connected to a Strong Grid at Different Wind Speeds

Wind Speed (m/s)	Peak Fault Current (A)	Wind Turbine Terminal Voltage (kV)	Load Current (A)
6	536.5	0.680	12
10	548.4	0.695	33
14	550.5	0.699	48
20	549.7	0.697	39

the reactive power demand of the wind turbine at the rated wind speed. There is no drop in $V_{terminal}$ as seen in Table 7.4. Therefore, this case study concludes that in the presence of a strong grid, the fault current contribution from a fixed speed wind turbine is maximum at rated wind speed. Furthermore, the fault currents levels at different wind speeds are within the limits calculated using the IEC 60909-0 Standard.

7.3.4 Case Study: Fixed-speed Wind Farm and a Strong Grid

This case study investigates whether the fluctuations in fault currents due to wind speed variation are more significant in a wind farm. To that end, a 4.5-MW wind farm was connected to a 500-MVA grid via a 10-MVA 0.69/20-kV transformer and a 1-mile long transmission line. The aggregate wind farm model described in [80] was used to model the wind farm. In an aggregate model, all wind turbines encounter the same wind speed and all induction generators experience the same aerodynamic torque. In other words, in an aggregate wind farm model, all the wind turbines are synchronized with each other. Since the case study aimed to study the impact of stochastic variations in wind speed, the tower shadow and wind shear modules were switched off.

The equivalent circuit is shown in Fig. 7.9. A symmetrical fault was placed at the HV side of the transformer as indicated by point B in Fig. 7.9. The maximum and

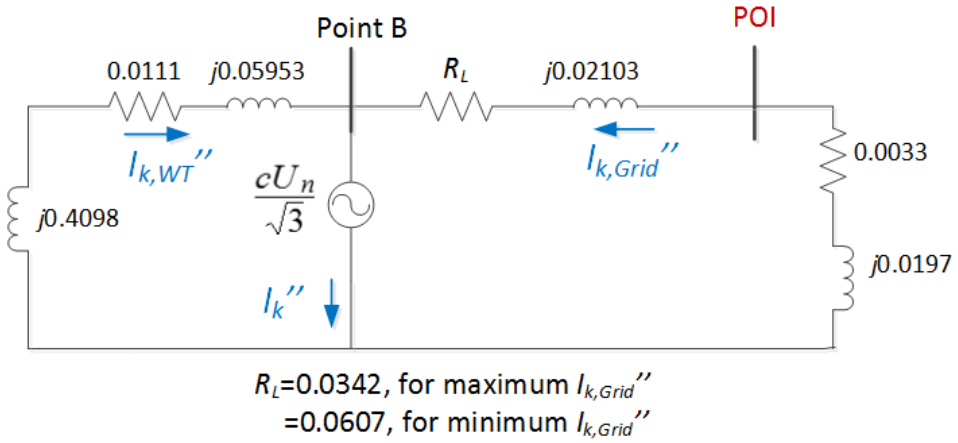

Figure 7.9: Equivalent circuit of a 4.5-MW wind farm connected to a 500-MVA strong grid.

minimum possible symmetrical currents are:

$$I''_{k,WT,max} = 676.4\angle -88.65° \text{ A}$$
$$I''_{k,WT,min} = 614.9\angle -88.65° \text{ A}$$

Therefore, the theoretical range for the peak current (I_p) is,

$$869.6 \leq I_p \leq 1849 \text{ A} \tag{7.15}$$

The simulation results at different wind speeds are tabulated in Table 7.5. As expected, the fault current magnitude from the wind farm is higher, but the variation of the peak current is still in the range of a few amperes. The theoretical limits specified by (7.15) are not violated. In a wind farm, the change in load current with variation in wind speed, ΔI_{Load}, is high. However, because all the wind turbines are are operating in parallel, the equivalent generator impedance, X''_{gen}, is small. As a result, the term $\Delta I_{Load} X''_{gen}$ in (7.14) has a minor impact on I''_k. Therefore, this case study concludes that the fault current levels of a wind farm are not significantly affected by the variation in wind speed.

Table 7.5: Fault Currents from a 4.5-MW Wind Farm Connected to a Strong Grid at Different Wind Speeds

Wind Speed (m/s)	Peak Fault Current (A)	Wind Farm Terminal Voltage (kV)
6	1502	0.683
10	1516	0.691
14	1515	0.693
20	1513	0.692

7.3.5 Case Study: Fixed-speed Wind Turbine with $3p$ and a Weak Grid

This case study investigates how the periodic fluctuations in $V_{terminal}$ due to tower shadow and wind shear affect the peak fault current contribution from a fixed-speed wind turbine. The network model in Section 7.6 was used. After initializing the PSCAD model for 20 seconds, the tower shadow and wind shear modules were switched on. Because the 1.5-MW fixed-speed wind turbine is connected to a 15-MVA weak grid, the rms voltage at the wind turbine terminals, $V_{terminal}$, immediately starts fluctuating at $3p$ frequency. The fluctuations in $V_{terminal}$ at the rated wind speed are shown in Fig. 7.10. The percent voltage modulation can be calculated as

$$\% \text{ Voltage Modulation} = \frac{V_{max} - V_{min}}{V_0} \tag{7.16}$$

where V_{max} and V_{min} are the maximum and minimum values of voltage, and V_0 is the average value of the normal operating voltage. Using (7.16), the percent voltage modulation is 0.05%. Next, the wind turbine model was subjected to different wind speeds. At each wind speed, a three-phase fault was simulated at two different time instants as shown in Fig. 7.10. The fault at time instant A was simulated when the terminal voltage was maximum while the fault at time instant B was simulated when the terminal voltage was minimum. The results are shown in Table 7.6. Note that the peak current is expected to fall within the same theoretical limits calculated in Case

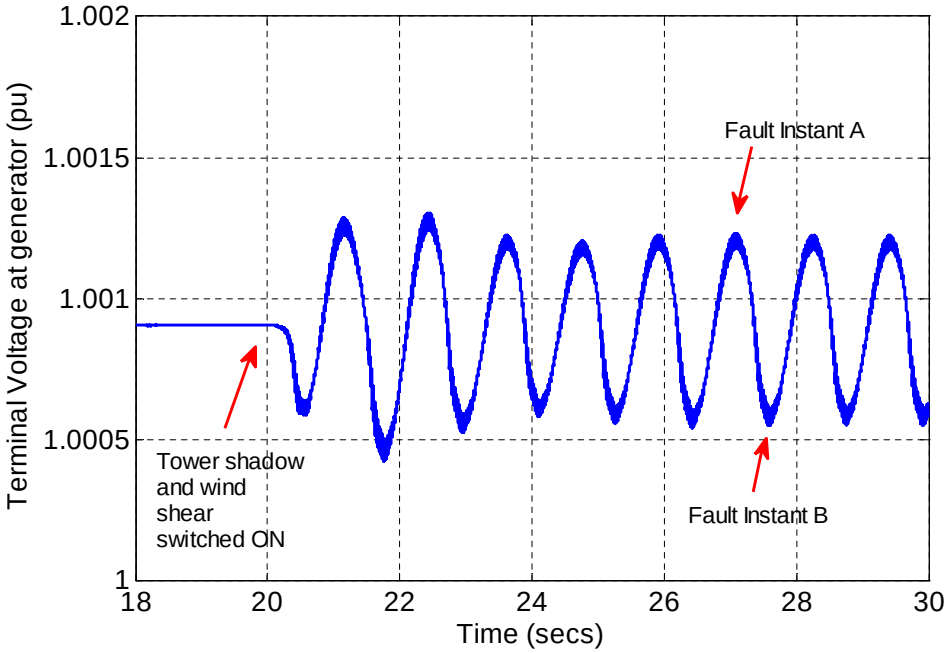

Figure 7.10: Fluctuations in the wind turbine terminal voltage are maximum at the rated wind speed.

Study presented in Section 7.3.2, i.e.,

$$307.3 \leq I_p \leq 662.4 \text{ A} \tag{7.17}$$

As seen from Table 7.6, peak fault currents contributed by the wind turbine under periodic fluctuations in wind speed are within the theoretical limits specified by the IEC Standard. It is possible that the percent voltage modulation of 0.05% was infinitesimal and hence, no significant difference in the fault current levels were observed. Note that the magnitude of fault currents at different wind speeds should not be compared with each other since the DC component is no longer constant (fault simulated at different time instants). Therefore, this case study concludes that the periodic fluctuations in wind speed do not affect the fault current contribution of a single fixed-speed wind turbine. The fault levels are within the limits of the IEC 60909-0 Standard.

Table 7.6: Fault Currents from a 1.5-MW Wind Turbine, Including $3p$

Wind Speed (m/s)	Peak Fault Current at Time Instant A (A)	Peak Fault Current at Time Instant B (A)
6	534.1	353.7
10	542.4	542.7
14	367.8	542.7
18	340.1	341.3

7.3.6 Case Study: Fixed-speed Wind Farm with $3p$ and a Weak Grid

In the previous case study, the $3p$ effect in a single fixed-speed 1.5-MW wind turbine did not cause a significant variation in the wind turbine terminal voltage, $V_{terminal}$. As a result, the fault current levels did not deviate from the limits set by the IEC 60909-0 Standard. Since the $3p$ effect is amplified in a wind farm and may cause a severe fluctuation in $V_{terminal}$, this case study investigates the impact of wind speed variation due to $3p$ on the fault current contribution of a wind farm. For this purpose, a 4.5-MW wind farm was interconnected with a weak grid in PSCAD simulation software. The wind farm model was initialized for 20 seconds, after which the tower shadow and wind shear modules were switched on. An aggregate wind farm model was used which represents the worst case scenario since all wind turbines experience the same reduction in wind speed due to the $3p$ effect. As a result, the fluctuations in $V_{terminal}$ are severe as shown in Fig. 7.11. In terms of percent voltage modulation, the voltage fluctuation was calculated to be 0.27%, which is a significant increase over the previous case study. Next, the wind farm was subjected to different wind speeds and faults were simulated at two time instants (A and B). The time instants A and B correspond to the maximum and minimum wind farm terminal voltage, respectively. The simulation results are tabulated in Table 7.7. The theoretical range for the peak current is the same as that

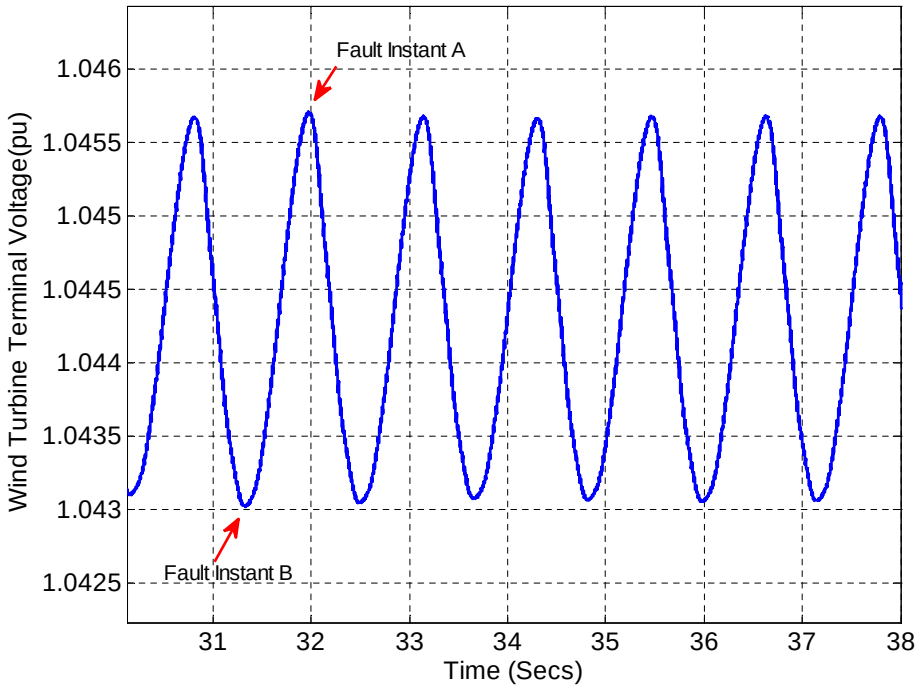

Figure 7.11: Fluctuations in the wind farm terminal voltage at the rated wind speed.

Table 7.7: Fault Currents from a 4.5-MW Wind Farm, Including $3p$

Wind Speed (m/s)	Peak Fault Current at Time Instant A (A)	Peak Fault Current at Time Instant B (A)
6	970.3	970.4
10	960.3	962.3
14	928.5	938.2
18	1580.0	955.5

calculated in Case Study presented in Section 7.3.4, i.e.,

$$869.6 \leq I_{p,windturbine} \leq 1849 \text{ A}$$

As observed from the table, the peak fault currents do not violate the maximum and minimum fault current limits, even though the fluctuation in terminal voltage was significant.

7.4 Summary

In summary, this Chapter develops a comprehensive time-domain model of a fixed-speed wind turbine with a detailed representation of tower shadow and wind shear effects. The model was then used to investigate the impacts of wind speed variation (stochastic and periodic) on the short-circuit fault current levels of a fixed-speed wind turbine and protective device settings. A comprehensive analysis reveals that the variation in wind speed affects the voltage at the fault point which, in turn, affects the fault current contributed by the fixed-speed wind turbine. The IEC Standard accounts for these variations in the actual voltage from the nominal voltage by using the voltage factor c when calculating the minimum and maximum fault currents. As a result, the limits set by the IEC Standard are conservative and not violated by the variation in wind speed.

Chapter 8

Analysis of Intelligent Electronic Device Data

Event reporting is a powerful functionality of digital relays, digital fault recorders, and other intelligent electronic devices (IEDs). Data are available in the form of voltage and current waveforms, and provide a snapshot of the power system at the time of fault. Knowledge gained from analyzing event reports can help system operators understand what happened during an event, why it happened, and how to prevent it from happening again [39–41]. Momentary faults can be detected and repaired before they evolve into a system-wide blackout. A study by North Electric Reliability Corporation (NERC) [42] identifies relay setting error as one of the major causes of relay misoperations. Therefore, assessing relay performance is one of the major benefits of event report analysis. Any undesired operation due to incorrect settings can be identified and corrected. Even if the subject relay did not misoperate, routine analysis of events is a good practice to ensure that the relay operated with due consideration to selectivity, dependability, and security.

Event report analysis can also be used to validate the zero-sequence impedance of transmission and distribution feeders. This parameter plays an important role in distance and directional protection [43, 44], and fault location calculations. Unfortunately, as discussed in Chapter 3, the accuracy of the zero-sequence line impedance is subject to much uncertainty since it depends on earth resistivity. Although utilities use a typical value of 100 Ω-m, the earth resistivity is difficult to measure and changes with soil type, temperature, and moisture content in soils. As a result, to avoid relay misoperations and incorrect fault location, efforts must be made to validate the zero-sequence line impedance using fault event data. Authors in [15] attempt to validate the zero-sequence

line impedance using IED data captured at one end of the line. However, they assume a known fault location and a zero fault resistance. To avoid making such assumptions, authors in [43] use synchronized IED data from both ends of a transmission line to verify the zero-sequence impedance. Because IEDs can have different sampling rates, or detect the fault at slightly different time instants, waveforms captured by IED devices at both ends of a transmission line may not be synchronized with each other. Furthermore, three-terminal transmission lines are frequently being used by utilities to increase operational support and meet system demand [45]. Very little work, if any, has been conducted on validating the zero-sequence line impedance of three-terminal transmission lines. Therefore, it is necessary to devise a methodology that can use unsynchronized measurements to confirm the zero-sequence impedance of two and three-terminal transmission lines.

Voltage and current waveforms captured during a fault can also be used to estimate the fault resistance and gain insight into the root cause of a fault. Analysis of 148 fault events in utility circuits reveals that trees with a larger diameter present a fault resistance greater than 20 ohms when they fall on overhead lines [46]. Animals like squirrel, birds, or snakes coming in contact with the transmission line have the least resistance while lightning induced faults have a resistance equal to the tower footing resistance. In addition to identifying the root cause of the fault, fault resistance also plays an important role in replicating the fault in the system circuit model and confirming it's accuracy. The circuit model in PSCAD [47], CAPE [48], OpenDSS [49], and other power system software is used by system operators to conduct short-circuit studies, determine protective relay settings, and choose the maximum rating of circuit breakers and other power system equipment. Incorrect short-circuit model parameters can lead to erroneous relay settings and relay misoperations, an example of which is described in [50]. As a result, it is vital to ensure that the system model is accurate and continually updated to reflect any system additions, repair, or modifications.

Based on the aforementioned background, the ***objective*** of this Chapter is to assess what additional information can be gleaned from waveform data captured by intelligent electronic devices during a fault. The goals are to improve power system performance and reliability. The ***contribution*** lies in developing algorithms that validate the zero-sequence line impedance of two- and three-terminal lines with unsynchronized IED data. Other ***contributions*** include using the IED data to successfully reconstruct the sequence of events, assess the performance of relays, estimate the fault resistance, estimate the short-circuit impedance, and verify the accuracy of the system short-circuit model. All potential applications described above are demonstrated with field data in Chapter 9.

Publications:

- S. Das, S. Santoso, A. Gaikwad, and M. Patel, "Impedance-based fault location in transmission networks: theory and application," *IEEE Access*, vol. 2, pp. 537-557, 2014.

8.1 Assess Relay Performance

Event reports recorded by digital relays, digital fault recorders, and other intelligent electronic devices document the voltage and current waveforms at the time of a fault and the response of the power system to the fault. As a result, event reports are an invaluable resource for assessing the performance of relays. Any undesired operation due to incorrect settings can be identified and corrected. Even if the subject relay did not misoperate, routine analysis of events is a good practice to ensure that the relay operated with due consideration to selectivity, dependability, and security. The application to assess relay performance is demonstrated using actual fault event data in Section 9.1 and Section 9.4. This Section outlines the steps to evaluate the relay performance.

Step 1: Review relay settings and understand it's expected behavior

The first step is to review relay settings and understand its expected behavior during a fault. Pay close attention to the trip equation since this equation governs the trip and close operations of the relay. The trip equation is typically composed of internal relay variables as shown in Fig. 9.8. Trace the function of each of those relay variables by referring to the instruction manual provided by the relay manufacturer.

Step 2: Reconstruct the sequence of events

The next step is to establish a timeline of the sequence of events. For this purpose, it is necessary to understand what triggers an IED to generate an event report. As an example, Schweitzer relays automatically record an event report following a trip equation. In addition to a trip operation, these relays allow system operators to monitor specific relay variables via an event report (ER) equation. If one of the relay variables in the ER equation assert, the relay records an event report.

Step 3: Compare the actual vs. expected relay operation

After reconstructing the sequence of events, the final step is to check whether the actual relay response times match with the expected behavior during the fault. Any discrepancy in the operate times must be thoroughly investigated.

8.2 Validate the Zero-sequence Impedance of Two-terminal Lines

The zero-sequence impedance of an overhead line is a user-defined setting in relays as shown in Fig. 8.1 and plays an important role in system protection. For example, the zero-sequence line impedance is used by distance relays to monitor the apparent impedance seen by the relay. An apparent impedance lower than the zone reach setting indicates a fault and the relay operates to clear the fault from the transmission

network [43]. Furthermore, directional elements are often used in multi-terminal transmission lines to determine the forward or the reverse direction of a fault, and supervise the trip operation of an overcurrent relay. The fault direction is identified by comparing the apparent impedance with threshold values, which are calculated using the zero-sequence line impedance [44]. As a result, an accurate zero-sequence line impedance is essential to prevent any relay misoperation. In addition to system protection, the zero-sequence line impedance is also required by impedance-based fault location algorithms to pinpoint the exact location of single line-to-ground faults.

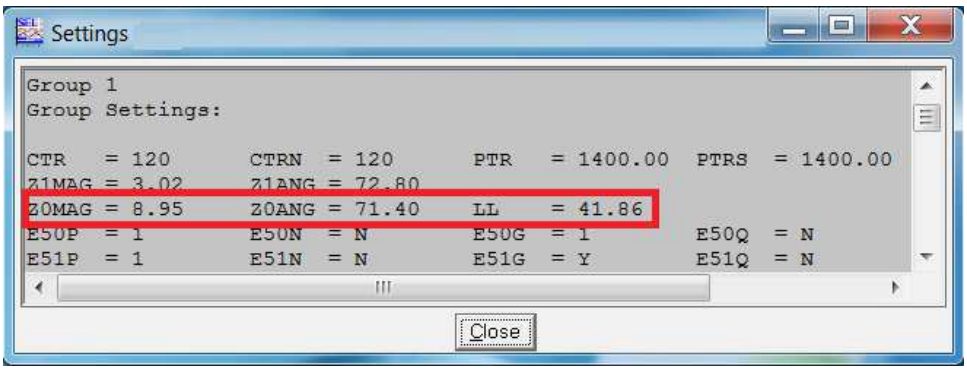

Figure 8.1: Zero-sequence line impedance setting in SEL relays. Here, Z0MAG and Z0ANG are the magnitude and phase angle of the zero-sequence line impedance.

Although line constants at power frequency are popularly solved using modified Carson's equations, the accuracy of the zero-sequence line impedance is subject to much uncertainty. The reason can be attributed to the dependency of the zero-sequence line impedance on accurately knowing the earth resistivity. Unfortunately, the earth resistivity is difficult to measure and varies with soil type, moisture content in soils, and temperature as discussed in Section 3.2.4. Typically, utilities use an earth resistivity value of 100 Ω-m. However, any change in earth resistivity will cause a significant variation in the zero-sequence line impedance as shown in Table 3.3. This variation can have a detrimental effect on system protection and fault location and hence, efforts must be taken to validate the zero-sequence line impedance setting in relays.

This Section presents two approaches for validating the zero-sequence line impedance using waveform data recorded by IEDs during a fault. The first approach uses IED data from one end of the line while the second approach uses IED data from both line ends. Note that the zero-sequence line impedance can be validated only when the fault has a return through the ground, i.e., during a single or a double line-to-ground fault.

8.2.1 Approach 1: Data from One Terminal

This approach estimates the zero-sequence impedance of the transmission or distribution feeder using voltage and current waveforms at only one end of the line. The expression for estimating the zero-sequence line impedance depends on the fault type.

(a) Single Line-to-ground Fault

Consider a single line-to-ground fault at a distance m per unit from terminal G on the two-terminal line shown in Fig. 2.1. The sequence network is shown in Fig. 8.2. Notations in the figure are defined as follows:

E_G, E_H	are the internal generator voltages at terminal G and terminal H (kV)
V_{G0}, V_{G1}, V_{G2}	are the sequence components of the fault voltage at terminal G (kV)
V_{H0}, V_{H1}, V_{H2}	are the sequence components of the fault voltage at terminal H (kV)
I_{G0}, I_{G1}, I_{G2}	are the sequence components of the fault current at terminal G (kA)
I_{H0}, I_{H1}, I_{H2}	are the sequence components of the fault current at terminal H (kA)
V_{F0}, V_{F1}, V_{F2}	are the sequence components of the fault voltage at the fault point (kV)
Z_{L0}, Z_{L1}, Z_{L2}	are the sequence components of the line impedance (Ω)
Z_{G0}, Z_{G1}, Z_{G2}	are the sequence source impedances at terminal G (Ω)
Z_{H0}, Z_{H1}, Z_{H2}	are the sequence source impedances at terminal H (Ω)

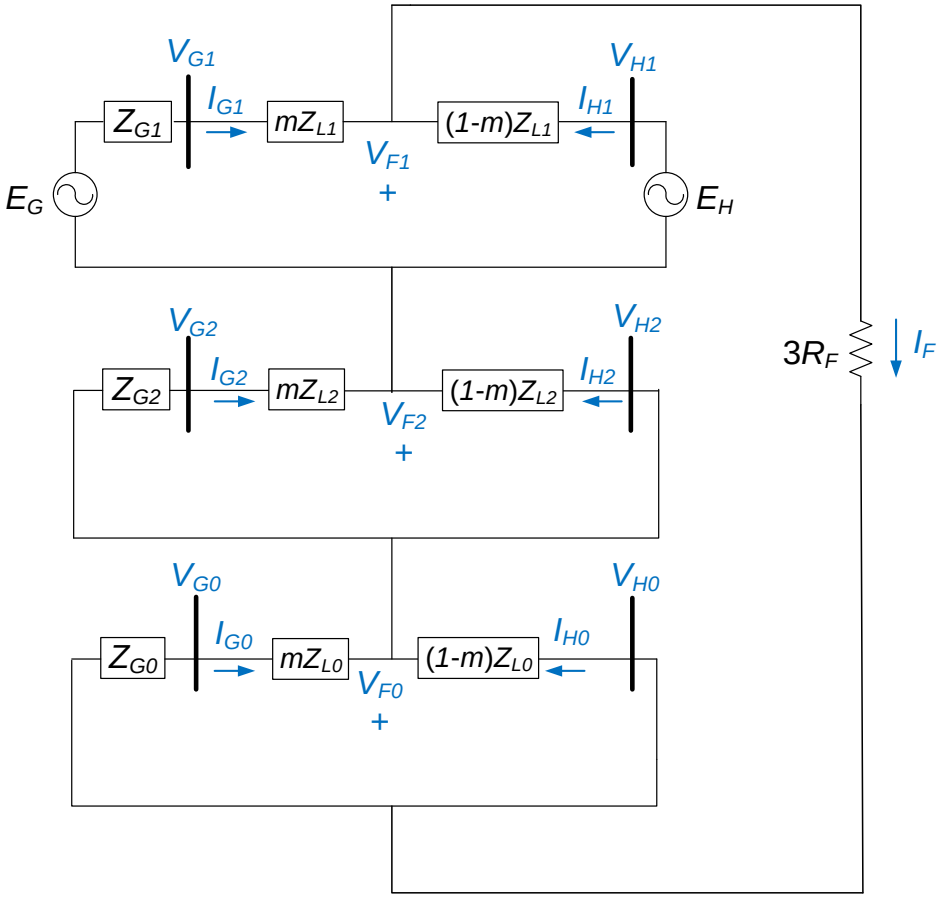

Figure 8.2: Sequence network during a single line-to-ground fault.

Using Kirchhoff's circuit laws, the voltage drop from terminal G can be written as:

$$V_{F1} = V_{G1} - mZ_{L1}I_{G1} \tag{8.1}$$

$$V_{F2} = V_{G2} - mZ_{L2}I_{G2} \tag{8.2}$$

$$V_{F0} = V_{G0} - mZ_{L0}I_{G0} \tag{8.3}$$

The voltage at the fault point can be obtained by summing the sequence components as

$$V_F = V_G - mZ_{L1}\left(I_{G1} + I_{G2}\right) - mZ_{L0}I_{G0} \tag{8.4}$$

where V_G is the voltage of the faulted phase at terminal G. If the fault is assumed to occur with a zero fault resistance, V_F can be set equal to zero. The zero-sequence line

impedance can then be estimated as

$$Z_{L0} = \frac{V_G - mZ_{L1}\left(I_{G1} + I_{G2}\right)}{mI_{G0}} \tag{8.5}$$

The actual location of the fault, m, must be available. Furthermore, the positive-sequence line impedance in (8.5) is assumed to be known precisely since it's calculation depends on the arrangement of phase and neutral conductors, and conductor data.

(b) Double Line-to-ground Fault

Suppose that a double line-to-ground fault occurs at a distance m per unit from terminal G in Fig. 2.1. The sequence network is shown in Fig. 8.3. If the fault resistance is assumed to be zero, then all the sequence networks are parallel to each other at the fault point F. As a result, the negative-sequence voltage at the fault point, V_{F2}, is equal to the zero-sequence voltage at the fault point, V_{F0}, as shown below:

$$V_{G2} - mZ_{L2}I_{G2} = V_{G0} - mZ_{L0}I_{G0} \tag{8.6}$$

The zero-sequence line impedance can then be estimated as follows:

$$Z_{L0} = \frac{V_{G0} - V_{G2} + mZ_{L2}I_{G2}}{mI_{G0}} \tag{8.7}$$

Again, the fault location and the positive-sequence line impedance ($Z_{L2} = Z_{L1}$) are assumed to be precisely known.

Assumptions:

Assumptions made by Approach 1 when estimating the zero-sequence line impedance are summarized below:

1. Fault resistance is zero
2. Fault type is known

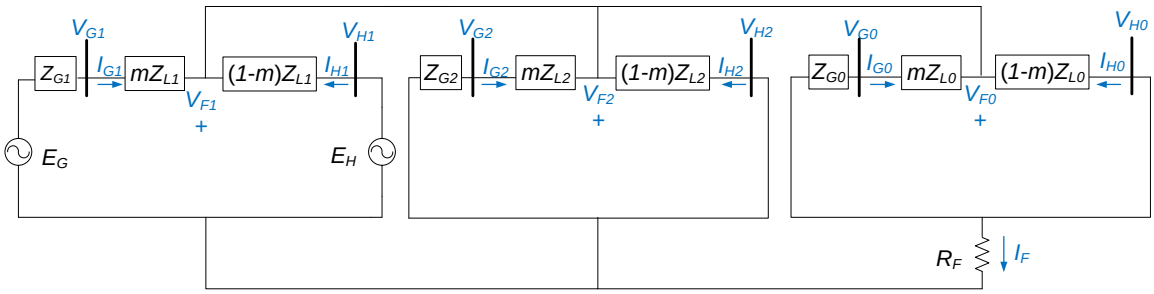

Figure 8.3: Sequence network during a double line-to-ground fault.

3. Fault location is known
4. Line is homogeneous
5. Zero-sequence mutual coupling is absent

8.2.2 Approach 2: Data from Two Terminals

This approach validates the zero-sequence line impedance using the voltage and current phasors at both terminals of a transmission line. The phasors are desired to be synchronized to a common time reference via a global positioning system (GPS). Unfortunately, phasors at both line ends are not always time synchronized with each other [4]. The GPS device may be absent or not functioning correctly. Alternatively, IEDs can have different sampling rates or they may detect the fault at slightly different time instants. The communication channel, which transfers data from one IED to the other, can also introduce a phase shift as shown in Fig. 8.4. Therefore, the first step is to align the voltage and current phasors at terminal G with those at terminal H. The negative-sequence network shown in Fig. 8.2 is used for this purpose. Let δ represent the synchronization error between the phasors at terminal G and those at terminal H. The approach is to use the voltage and current phasors at terminal H as reference quantities and adjust the phasors at terminal G by $e^{j\delta}$. Consequently, the new set of synchronized negative-sequence voltage and current phasors at terminal G are $V_{G2}e^{j\delta}$ and $I_{G2}e^{j\delta}$. To

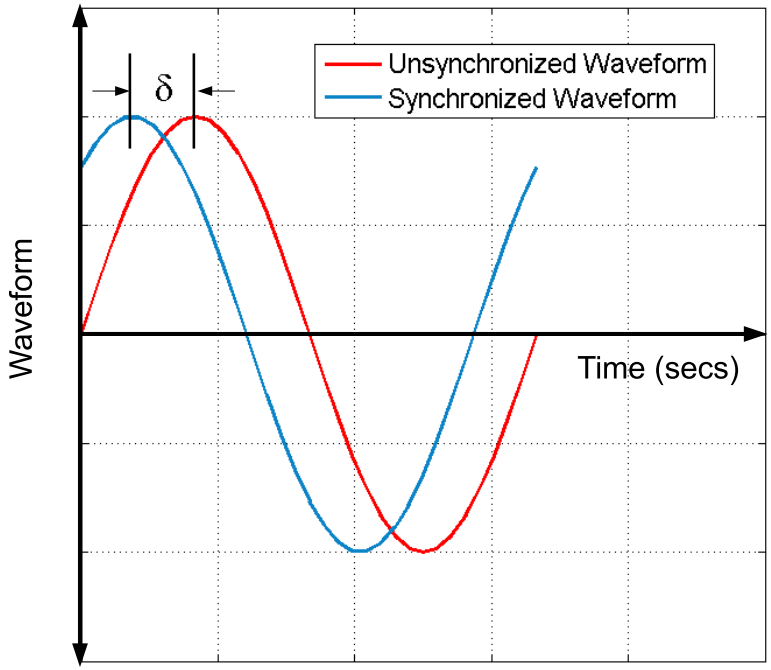

Figure 8.4: Unsynchronized waveform phase-shifted with respect to the synchronized waveform.

solve for the value of $e^{j\delta}$, calculate V_{F2} from either line end as

$$\text{Terminal G:} \quad V_{F2} = V_{G2}e^{j\delta} - mZ_{L2}I_{G2}e^{j\delta} \tag{8.8}$$

$$\text{Terminal H:} \quad V_{F2} = V_{H2} - (1-m)Z_{L2}I_{H2} \tag{8.9}$$

If terminal G and terminal H measurements are synchronized with each other, V_{F2} is the same when calculated from either terminal. Therefore, the value of $e^{j\delta}$ that forces V_{F2} from terminal G to be equal to that from terminal H is

$$e^{j\delta} = \frac{V_{H2} - (1-m)Z_{L2}I_{H2}}{V_{G2} - mZ_{L2}I_{G2}} \tag{8.10}$$

If the actual fault location, m, is unknown, estimate it using the synchronized two-ended method described in Chapter 2. The next step is to estimate the zero-sequence line impedance from the zero-sequence network shown in Fig. 8.4. Calculate V_{F0} from

terminals G and H as

$$\text{Terminal G:} \quad V_{F0} = V_{G0}e^{j\delta} - mZ_{L0}I_{G0}e^{j\delta} \tag{8.11}$$

$$\text{Terminal H:} \quad V_{F0} = V_{H0} - (1-m)Z_{L0}I_{H0} \tag{8.12}$$

Since V_{F0} remains the same when calculated from either line terminal, equate (8.11) with (8.12) to solve for Z_{L0} as

$$Z_{L0} = \frac{V_{G0}e^{j\delta} - V_{H0}}{mI_{G0}e^{j\delta} - (1-m)I_{H0}} \tag{8.13}$$

Approach 2 makes no assumptions about the fault resistance and hence, has a superior performance over Approach 1. In addition, there is no need to know the exact fault location and fault type. The presence or absence of zero-sequence currents indicates whether the fault involves the ground or not.

Assumptions:

Assumptions made by Approach 2 when estimating the zero-sequence line impedance are summarized below:

1. Line is homogeneous
2. Zero-sequence mutual coupling is absent

8.2.3 Demonstration using a Benchmark Test Case

This Section demonstrates the efficacy of Approach 1 and Approach 2 in estimating the zero-sequence line impedance during a single or a double line-to-ground fault. Two case studies were conducted using the 69-kV test case in Section 3.1 and are described below.

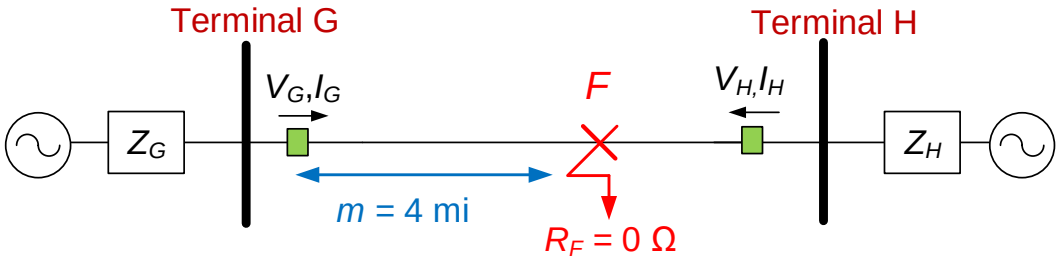

Figure 8.5: Case study 1 is a AB-G fault, 4 miles from terminal G with $R_F = 0\,\Omega$.

(a) Case Study 1: AB-G Fault with $R_F = 0\,\Omega$

This case study demonstrates the success of Approach 1 and Approach 2 in estimating the zero-sequence line impedance for a bolted ground fault. To this end, a double line-to-ground fault on phases A and B was simulated at a distance of 4 miles from terminal G with a zero fault resistance as shown in Fig. 8.5. Monitors at terminals G and H capture the voltage and current waveforms at 32 and 64 samples per cycle, respectively. Because the monitors have different sampling rates, this case study is a perfect example wherein the measurements at both line ends are not synchronized with each other. Before the fault, both terminals support a load current of 220 A. During the fault, the currents at terminals G and H increase to 5.1 kA and 1.5 kA, respectively. Next, assuming Z_{L1} to be accurate, Approach 1 and Approach 2 developed in Section 8.2.1 and Section 8.2.1 were used to estimate the zero-sequence line impedance. As seen from Table 8.1, both approaches are successful in estimating the zero-sequence line impedance. The magnitude and phase angle error were calculated as follows [43]:

$$\begin{aligned} \text{Magnitude Error } \% &= \frac{||\text{Actual } Z_{L0}| - |\text{Estimated } Z_{L0}||}{|\text{Actual } Z_{L0}|} \times 100 \\ \text{Phase Angle Error} &= |\angle\text{Actual } Z_{L0} - \angle\text{Estimated } Z_{L0}| \end{aligned} \tag{8.14}$$

Table 8.1: Case Study 1: Estimated vs. Actual Zero-sequence Line Impedance

Approach	Zero-sequence Line Impedance (Ω)		Magnitude Error (%)	Phase Angle Error (degrees)
	Actual	Estimated		
Approach 1	14.56+j30.36	14.63+j30.28	0.12	0.16
Approach 2		14.71+j30.68	1.05	0.01

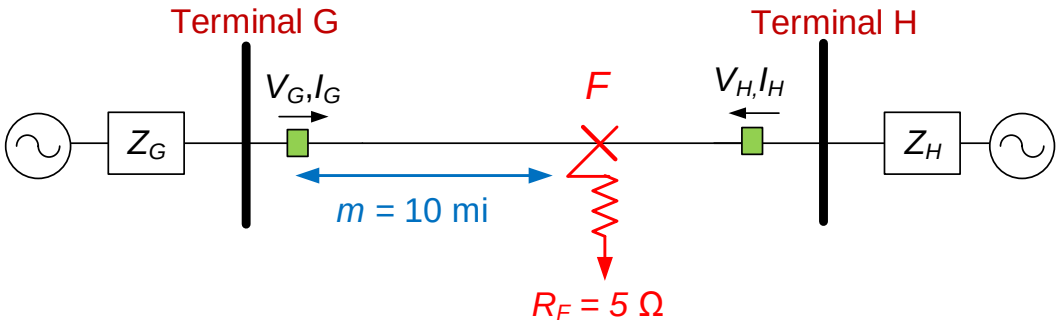

Figure 8.6: Case study 2 is a A-G fault, 10 miles from terminal G with $R_F = 5\,\Omega$.

(b) Case Study 2: A-G Fault with $R_F = 5\,\Omega$

This case study highlights the superior performance of Approach 2 in estimating the zero-sequence line impedance when the fault occurs with a significant fault resistance. For this purpose, a single line-to-ground fault on phase A was simulated at a distance of 10 miles from terminal G with a fault resistance of 5 Ω as shown in Fig. 8.6. A monitor at terminal G measures the voltage and current waveforms at 32 samples per cycle. The load current at the time of the fault is 220 A while the fault current is 1.9 kA. A monitor at terminal H also records the voltage and current waveforms, but at 64 samples per cycle. The load current is 220 A while the fault current is 1.1 kA. Next, Approach 1 and Approach 2 are used to estimate the zero-sequence impedance of the transmission line. As seen from Table 8.2, the impedance estimate from Approach 1 show a significant deviation from the zero-sequence line impedance used in the simulation model. The error stems from the fact that Approach 1 assumes a zero fault resistance which does not hold true in this particular case. Since Approach 2 does not make any assumptions

about the fault resistance, the estimated zero-sequence line impedance is accurate.

Table 8.2: Case Study 2: Estimated vs. Actual Zero-sequence Line Impedance

Approach	Zero-sequence Line Impedance (Ω)		Magnitude Error (%)	Phase Angle Error (degrees)
	Actual	Estimated		
Approach 1	14.56+j30.36	59.66+j30.14	98.51	37.57
Approach 2		14.67+j30.19	0.33	0.28

8.3 Validate the Zero-sequence Impedance of Three-terminal Lines

Three-terminal transmission lines are frequently used by utilities to transfer bulk electrical power and support loads from three generating sources [45]. Often, utilities upgrade an existing two-terminal line to a three-terminal line by simply connecting a line with a generating source to it. Building three-terminal lines has several advantages. There are no costs associated with constructing a new substation and procuring new circuit breakers and other power system equipment. No right-of-way and regulatory approvals are required. As a result, three-terminal lines are expeditious in increasing the operational support necessary to meet system demands. However, such lines do pose a significant challenge to the task of validating the zero-sequence line impedance. The third terminal contributes to the total fault current and changes the impedance equations developed in Section 8.2. Furthermore, with the introduction of a third terminal, there are, now, two lines whose zero-sequence line impedances have to be validated from a single fault event. Based on this aforementioned background, this Section presents two approaches for validating the zero-sequence line impedance in three-terminal lines. Approach 1 requires the availability of voltage and current waveforms at all the three terminals while Approach 2 uses waveforms captured at two terminals.

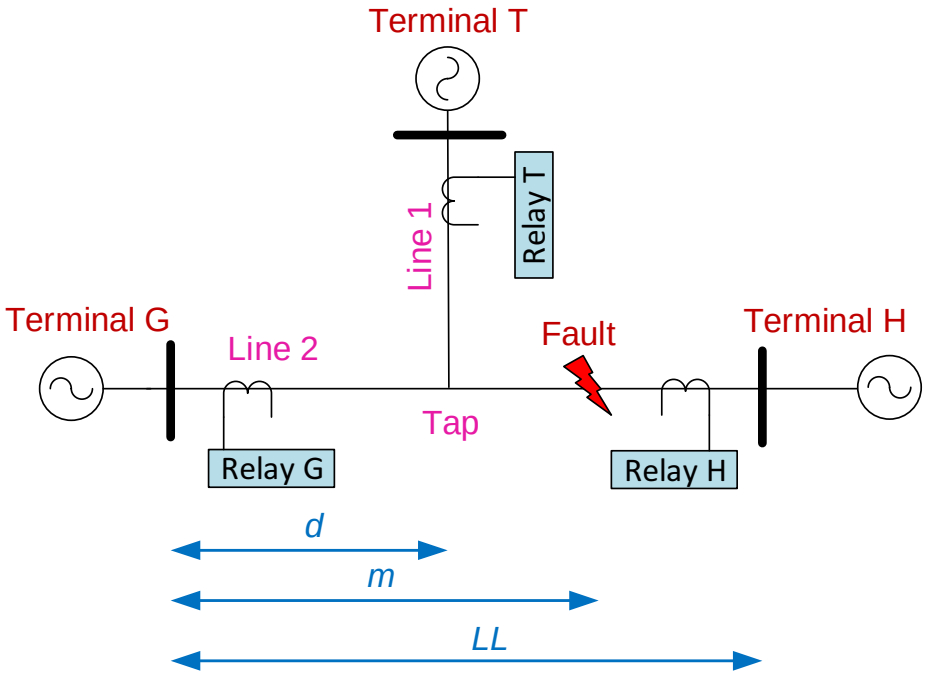

Figure 8.7: Three-terminal transmission line.

8.3.1 Approach 1: Data from Three Terminals

This approach requires the availability of voltage and current phasors at all the three terminals during a fault and is illustrated using the three-terminal transmission line shown in Fig. 8.7. Line 2 is homogeneous and connects terminal G with terminal H. Line 1 is also homogeneous and connects terminal T with Line 2 at a distance of d per unit from terminal G. When a single or double line-to-ground fault occurs on Line 2 at m per unit distance from terminal G, all three sources contribute to the fault. Digital relays at each terminal capture the voltage and current phasors during the fault. The phasors need not be synchronized with each other. The steps to validate the zero-sequence impedance of Line 1 and Line 2 are outlined below.

Step 1: Synchronize Terminal T with Terminal G

Consider the negative-sequence network of a three-terminal line during a single or a double line-to-ground fault as shown in Fig. 8.8. Let $\delta 1$ represent the synchronization error between the measurements at terminal T and terminal G. Therefore, to align the voltage and current phasors at terminal T with respect to terminal G, a synchronization operator, $e^{j\delta 1}$, is applied to the terminal T measurements. The value of $e^{j\delta 1}$ can be determined by calculating V_{Tap2} from both terminals as

$$\text{Terminal G:} \quad V_{Tap2} = V_{G2} - (d \times Z2L2 \times I_{G2}) \tag{8.15}$$

$$\text{Terminal T:} \quad V_{Tap2} = V_{T2}e^{j\delta 1} - \left(Z2L1 \times I_{T2}e^{j\delta 1}\right) \tag{8.16}$$

where V_{Tap2} is the negative-sequence voltage at the tap point, V_{G2} and V_{T2} are the negative-sequence fault voltages at terminals G and T, I_{G2} and I_{T2} are the negative-sequence fault currents at terminals G and T, $Z2L1$ is the negative-sequence impedance of Line 1, and $Z2L2$ is the negative-sequence impedance of Line 2. Since terminals G and T operate in parallel to feed the fault, V_{Tap2} should be equal when calculated from either terminal. From this principle, $e^{j\delta 1}$ can be solved as

$$e^{j\delta 1} = \frac{V_{G2} - (d \times Z2L2 \times I_{G2})}{V_{T2} - (Z2L1 \times I_{T2})} \tag{8.17}$$

In effect, this step calculates the phase angle mismatch between terminal G and terminal T measurements, and accordingly adjusts the phasors at terminal T by $e^{j\delta 1}$.

Step 2: Synchronize terminal H with terminals T and G

After the synchronization process in Step 1, the new negative-sequence voltage and current phasors at terminal T are $V_{T2}e^{j\delta 1}$ and $I_{T2}e^{j\delta 1}$, respectively, and at terminal G are V_{G2} and I_{G2}, respectively. This step synchronizes the phasors at terminal H with the phasors at terminals G and T. For this purpose, a second synchronizing operator,

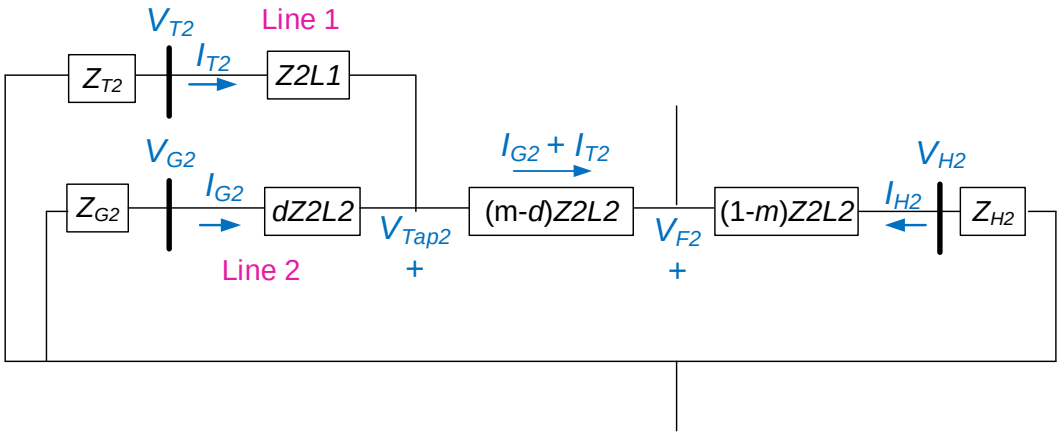

Figure 8.8: Negative-sequence network of the three-terminal line in Fig. 8.7 during a single or double line-to-ground fault.

$e^{j\delta 2}$, is applied to the measurements at terminal H. The value of $e^{j\delta 2}$ can be calculated from the fact that the negative-sequence voltage at the fault point, V_{F2}, must be the same when calculated from either terminal G or H as

$$\text{Terminal G: } V_{F2} = V_{G2} - [mZ2L2 \times I_{G2}] - \left[(m-d)\, Z2L2 \times I_{T2}e^{j\delta 1}\right] \quad (8.18)$$

$$\text{Terminal H: } V_{F2} = V_{H2}e^{j\delta 2} - \left[(1-m)Z2L2 \times I_{H2}e^{j\delta 2}\right] \quad (8.19)$$

Therefore, $e^{j\delta 2}$ is given by

$$e^{j\delta 2} = \frac{V_{G2} - [mZ2L2 \times I_{G2}] - \left[(m-d)\, Z2L2 \times I_{T2}e^{j\delta 1}\right]}{V_{H2} - [(1-m)Z2L2 \times I_{H2}]} \quad (8.20)$$

At the end of this step, the voltage and current measurements at terminals T and H are synchronized with respect to those at terminal G.

Step 3: Validate the zero-sequence impedance of Line 2

To estimate the zero-sequence impedance of Line 2, the zero-sequence network during a single or double line-to-ground fault is shown in Fig. 8.9. The zero-sequence

voltage at the fault point, V_{F0}, can be calculated from terminal G and H as

$$\text{Terminal G: } V_{F0} = V_{G0} - (mZ0L2 \times I_{G0}) - \left[(m-d)\, Z0L2 \times I_{T0}e^{j\delta 1}\right] \quad (8.21)$$

$$\text{Terminal H: } V_{F0} = V_{H0}e^{j\delta 2} - \left[(1-m)Z0L2 \times I_{H0}e^{j\delta 2}\right] \quad (8.22)$$

where V_{G0} and V_{H0} are the zero-sequence fault voltages at terminals G and H, I_{G0}, I_{H0} and I_{T0} are the zero-sequence fault currents at terminals G, H and T, and $Z0L2$ is the zero-sequence impedance of Line 2. Since V_{F0} is equal when calculated from either line terminal, equate (8.21) and (8.22) to solve for $Z0L2$ as

$$Z0L2 = \frac{V_{G0} - V_{H0}e^{j\delta 2}}{mI_{G0} + (m-d)\, I_{T0}e^{j\delta 1} - (1-m)\, I_{H0}e^{j\delta 2}} \quad (8.23)$$

Step 4: Validate the zero-sequence impedance of Line 1

To validate the zero-sequence impedance of Line 1, $Z0L1$, calculate the zero-sequence voltage at the tap point, V_{Tap0}, from terminals G and T as

$$\text{Terminal G: } V_{Tap0} = V_{G0} - (dZ0L2 \times I_{G0}) \quad (8.24)$$

$$\text{Terminal T: } V_{Tap0} = V_{T0}e^{j\delta 1} - \left(Z0L1 \times I_{T0}e^{j\delta 1}\right) \quad (8.25)$$

where V_{T0} is the zero-sequence fault voltages at terminal T. Because V_{Tap0} from terminal G is equal to that from terminal T, equate (8.24) and (8.25) to solve for $Z0L1$ as

$$Z0L1 = \frac{V_{T0}e^{j\delta 1} - V_{G0} + (dZ0L2 \times I_{G0})}{I_{T0}e^{j\delta 1}} \quad (8.26)$$

In this way, Approach 1 is successful in validating the zero-sequence impedance of Line 1 and Line 2. If the actual fault location is not available, then an additional step (Step 0) must be performed to track down the exact fault location before applying the steps described above.

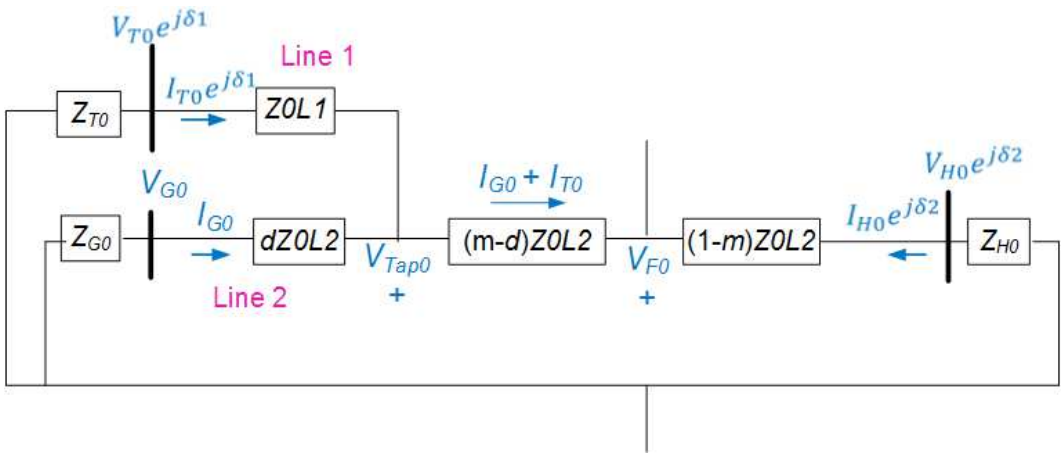

Figure 8.9: Zero-sequence network of the three-terminal line in Fig. 8.7 during a single or double line-to-ground fault.

Step 0: Identify the fault location

Before computing the distance to the fault, it is necessary to identify whether the fault is on Line 1 or on Line 2. The negative-sequence network shown in Fig. 8.8 is used for this purpose. When the fault is between terminal H and the tap point, V_{Tap2} from the other two terminals are equal. Therefore, to identify the faulted section of the feeder, the approach consists of calculating V_{Tap2} from each terminal as

$$\begin{aligned} \text{Terminal G:} \quad & |V_{Tap2}| = |V_{G2} - (d \times Z2L2 \times I_{G2})| \\ \text{Terminal H:} \quad & |V_{Tap2}| = |V_{H2} - ((LL - d) \times Z2L2 \times I_{H2})| \\ \text{Terminal T:} \quad & |V_{Tap2}| = |V_{T2} - (Z2L1 \times I_{T2})| \end{aligned} \tag{8.27}$$

The estimated $|V_{Tap2}|$ from two of the terminals will be an exact match while $|V_{Tap2}|$ from the third terminal will be different. The fault is expected to lie between that third terminal and the tap point. Next, apply one-ended algorithms to the voltage and current waveforms at the third terminal and estimate the distance to the fault.

Assumptions:

Assumptions made by Approach 1 when estimating the zero-sequence impedances of Line 1 and Line 2 are summarized below:

1. Line 1 and Line 2 are homogeneous
2. Zero-sequence mutual coupling is absent

8.3.2 Approach 2: Data from Two Terminals

Although Approach 1 can successfully validate the zero-sequence impedance of three-terminal transmission lines, voltage and current phasors from all the three terminals may not be available. For this reason, this Section develops a methodology that can use data from only two terminals to validate the zero-sequence impedance of three-terminal lines. To illustrate the approach, consider the scenario shown in Fig. 8.7. Suppose that the measurements captured by digital relays at terminals G and H are available while measurements from terminal T are missing. The procedure to validate the zero-sequence impedance of Line 1 and Line 2 in such a scenario are outlined below:

Step 1: Estimate the negative-sequence current from terminal T

To estimate the negative-sequence fault current from terminal T, I_{T2}, the negative-sequence network shown in Fig. 8.8 is used. The approach consists of calculating V_{Tap2} from terminal G and terminal T as

$$\text{Terminal G:} \quad V_{Tap2} = V_{G2} - (d \times Z2L2 \times I_{G2}) \tag{8.28}$$

$$\text{Terminal T:} \quad V_{Tap2} = -(Z_{T2} + Z2L1)\, I_{T2} \tag{8.29}$$

where Z_{T2} is the negative-sequence source impedance of terminal T. Since V_{Tap2} is equal when calculated from either terminal, I_{T2} can be estimated as

$$I_{T2} = \frac{(d \times Z2L2 \times I_{G2}) - V_{G2}}{Z_{T2} + Z2L1} \tag{8.30}$$

Note that since terminal G measurements are being used to estimate the fault current from terminal T, measurements of these two terminals are automatically synchronized.

Step 2: Synchronize terminal H with terminals G and T

This step applies a synchronization operator, $e^{j\delta}$, to the terminal H measurements so as to align the measurements at this terminal with those at terminals G and T. The fact that V_{F2} is the same when calculated from terminals G and H is used to calculate the synchronization operator as

$$e^{j\delta} = \frac{V_{G2} - (mZ2L2 \times I_{G2}) - [(m-d) \times Z2L2 \times I_{T2}]}{V_{H2} - [(1-m)Z2L2 \times I_{H2}]} \tag{8.31}$$

The new set of sequence voltage phasors at terminal H are $V_{H1}e^{j\delta}$, $V_{H2}e^{j\delta}$, and $V_{H0}e^{j\delta}$. Similarly, the new set of current phasors at terminal H are $I_{H1}e^{j\delta}$, $I_{H2}e^{j\delta}$, and $I_{H0}e^{j\delta}$

Step 3: Estimate the zero-sequence impedance of Line 2

Using Approach 1 described in Section 8.2.1, estimate the zero-sequence line impedance of Line 2 from terminal H measurements.

Step 4: Estimate the zero-sequence current from terminal T

The zero-sequence voltage at the fault point, V_{F0}, is the same when calculated from terminal G or terminal H. This principle is used to the zero-sequence fault current contributed by terminal T, I_{T0}, as

$$I_{T0} = \frac{V_{G0} - V_{H0}e^{j\delta} + Z0L2\left[(1-m)\, I_{H0}e^{j\delta} - mI_{G0}\right]}{Z0L2\,(m-d)} \tag{8.32}$$

Step 5: Estimate the zero-sequence impedance of Line 1

The fact that V_{Tap0} is the same when calculated from terminal G or terminal T is used to estimate the zero-sequence impedance of Line 1 as

$$Z0L1 = \frac{(d \times Z0L2 \times I_{G0}) - V_{G0}}{I_{T0}} - Z_{T0} \tag{8.33}$$

Assumptions:

Assumptions made by Approach 2 when estimating the zero-sequence line impedance are summarized below:

1. Line 1 and Line 2 are homogeneous
2. Fault location is known
3. Fault resistance is zero
4. Zero-sequence mutual coupling is absent

8.3.3 Demonstration using a Benchmark Test Case

To demonstrate the efficacy of Approach 1 and Approach 2 in validating the zero-sequence line impedances, the three-terminal network shown in Fig. 8.7 was modeled in PSCAD simulation software. The positive- and zero-sequence source impedances at terminal G are $Z_{G1} = 3.75\angle 86^\circ\,\Omega$ and $Z_{G0} = 11.25\angle 86^\circ\,\Omega$, respectively. The positive- and zero-sequence source impedances at terminal H are $Z_{H1} = 12\angle 80^\circ\,\Omega$ and $Z_{H0} = 36\angle 80^\circ\,\Omega$, respectively. The positive- and zero-sequence source impedances at terminal T are $Z_{T1} = 5\angle 83^\circ\,\Omega$ and $Z_{T0} = 12\angle 83^\circ\,\Omega$, respectively. The distance between terminal G and the tap point is 6.21 miles. Line 2 is 18.64 miles long and has the same configuration as shown in Fig. 3.1. The positive- and zero-sequence line impedances at an earth resistivity value of 100 Ω-m are $Z1L2 = 5.38\angle 70^\circ\,\Omega$ and $Z0L2 = 11.55\angle 65^\circ\,\Omega$, respectively. Line 1 is 6.21 miles long and also has the same configuration as Fig. 3.1. However, the

earth resistivity is changed to 80 Ω-m. The positive- and zero-sequence line impedances are $Z1L1 = 16.15\angle 70^\circ\,\Omega$ and $Z0L1 = 34.87\angle 64^\circ\,\Omega$, respectively. When a bolted phase A-to-ground fault occurs at a distance of 13 miles from terminal G, monitors at terminals G, H, and T capture the voltage and current waveforms at 32, 64, and 128 samples per cycle, respectively. The waveforms are, therefore, not synchronized with each other.

To assess the effectiveness of Approach 1, the fault location is assumed to be unknown. Following Step 0, the negative-sequence voltage magnitude at the tap point, $|V_{Tap2}|$, is calculated to be 4.05 kV from terminal G, 261.78 kV from terminal H, and 4.05 kV from terminal T. Since $|V_{Tap2}|$ from terminals G and T are equal, the fault is expected to lie between terminal H and the tap point. Next, the simple reactance method is applied to the measurements at terminal H to estimate the distance to fault to be 13 miles. The next step is to synchronize the measurements at terminals T and H with those at terminal G, and estimate the zero-sequence impedances of Line 1 and Line 2. As seen from Table 8.3, the estimated line impedances match with those used in the simulation test case.

Approach 2, on the other hand, uses the voltage and current waveforms captured at terminal G and terminal H, and assumes that the fault location is available. As seen from Table 8.3, the estimated line impedances are close to those used in the simulation.

Table 8.3: Case Study: Estimated vs. Actual Zero-sequence Line Impedance

Approach	$Z0L1$ (Ω)		$Z0L2$ (Ω)	
	Actual	Estimated	Actual	Estimated
Approach 1	$4.98+j10.42$	$4.99+j10.39$	$15.08+j31.44$	$15.13+j31.33$
Approach 2		$4.95+j10.46$		$15.12+j31.38$

8.4 Estimate the Fault Resistance

Voltage and current waveforms captured by IEDs during a fault can be used to estimate the magnitude of fault resistance and gain insight into the root cause of a fault. In addition to identifying the root cause of the fault, fault resistance also plays an important role in replicating the exact fault scenario in the circuit model and confirming the accuracy of the circuit model. Therefore, depending on whether the voltage and current waveforms are available from one or both ends of the line, this Section presents two approaches to estimate the fault resistance.

8.4.1 Approach 1: Data from One Terminal

Eriksson and Novosel *et al.* algorithms described in Chapter 2 can be used to estimate the fault resistance from the waveform data captured at one end of the line as

$$R_F = \frac{d - mb}{f} \tag{8.34}$$

The form taken by constants b, d, and f depends on the fault type and the number of terminals in a transmission line. For example, if a fault occurs on a one-terminal transmission line, constants b, d, and f are the same as those defined for the Novosel *et al.* algorithm in Section 2.1.5. For a fault on a two-terminal transmission line, constants b, d, and f are the same as those defined for the Eriksson algorithm in Section 2.1.4. It should be noted that the fault resistance is assumed to remain constant during the cycle used for calculating the voltage and current phasors.

8.4.2 Approach 2: Data from Two Terminals

Although Approach 1 can successfully estimate the value of fault resistance, it requires prefault data that may not be always available. Therefore, to avoid using the prefault data, the approach described in this Section uses the voltage and current

waveforms at both terminals of the transmission line. The waveforms at either line end need not be synchronized with each other.

(a) Single Line-to-ground Fault

During a single line-to-ground fault, the voltage at the fault point can be calculated from terminal G by (8.4). Since V_F, in turn, is given by $V_F = 3I_F R_F$ and I_F is the summation of the zero-sequence fault currents contributed by terminals G and H, the fault resistance can be estimated as

$$R_F = \frac{V_G - mZ_{L2}\left(I_{G1} + I_{G2}\right) - mZ_{L0}I_{G0}}{3\left(I_{G0}e^{j\delta} + I_{H0}\right)} \times e^{j\delta} \tag{8.35}$$

Here $e^{j\delta}$ is the synchronization operator calculated in (8.10).

(b) Line-to-line Fault

During a line-to-line fault, the positive- and negative-sequence voltages at the fault point, V_{F1} and V_{F2}, are related to the fault resistance as

$$V_{F1} - V_{F2} = I_F R_F \tag{8.36}$$

where V_{F1} and V_{F2} are given by (8.2) and (8.3), respectively. Since the fault current, I_F, is the summation of I_{G1} and I_{H1}, the fault resistance can be solved as

$$R_F = \frac{V_{G1} - V_{G2} - mZ_{L1}\left(I_{G1} - I_{G2}\right)}{\left(I_{G1}e^{j\delta} \times + I_{H1}\right)} \times e^{j\delta} \tag{8.37}$$

(c) Double Line-to-ground Fault

During a double line-to-ground fault, the negative- and zero-sequence voltages at the fault point are related to the fault resistance as

$$V_{F2} - V_{F0} = I_F R_F \tag{8.38}$$

where V_{F2} and V_{F0} are given by (8.3) and (8.3), respectively. Expressing the fault current, I_F, as the summation of I_{G0} and I_{H0}, the fault resistance can be solved as

$$R_F = \frac{V_{G2} - V_{G0} + m\left(Z_{L0}I_{G0} - Z_{L2}I_{G2}\right)}{\left(I_{G0}e^{j\delta} + I_{H0}\right)} \times e^{j\delta} \tag{8.39}$$

(d) Three-phase Fault

During a three-phase fault, the positive-sequence voltage at the fault point, V_{F1}, can be calculated from terminal G by (8.2). Since V_{F1}, in turn, is given by $V_{F1} = I_F R_F$ and I_F is the summation of the positive-sequence currents contributed by terminals G and H, the fault resistance can be estimated as

$$R_F = \frac{V_{G1} - mZ_{G1}I_{G1}}{I_{G1}e^{j\delta} + I_{H1}} \times e^{j\delta} \tag{8.40}$$

Note that the synchronization operator in a three-phase fault must be calculated with positive-sequence components in (2.21).

8.4.3 Demonstration using a Benchmark Test Case

The 69-kV test case described in Section 3.1 was used to demonstrate the application of Approach 1 and Approach 2 in estimating the fault resistance. Several faults, each having a different fault type and fault resistance, were simulated in the test case. Because the voltage and current waveforms at terminal G and terminal H were measured at different sampling rates of 32 and 64 samples per cycle, respectively, the waveforms at both line ends are unsynchronized. Table 8.4 compares the fault resistance estimated by Approach 1 and Approach 2 with the actual fault resistance used in the simulation study. The error % is calculated as follows:

$$\text{Error } \% = \frac{\text{Estimated } R_F - \text{Actual } R_F}{\text{Actual } R_F} \times 100 \tag{8.41}$$

As seen from the table, both approaches are successful in estimating the fault resistance.

Table 8.4: Case Study: Actual vs. Estimated R_F

Fault Type	Fault Location (mi)	Approach	Fault Resistance (Ω)		Error (%)
			Actual	Estimated	
A-G	6	Approach 1	5	5.04	0.80
		Approach 2		5.00	0.00
AB	8	Approach 1	3	3.00	0.00
		Approach 2		3.00	0.00
ABC	12	Approach 1	1	1.00	0.00
		Approach 2		1.00	0.00

8.5 Estimate the Thevenin Impedance

Voltage and current waveforms captured by IEDs during a fault can be used to estimate the Thevenin impedance of the transmission network upstream from the monitoring location as illustrated in Fig. 8.10. The Thevenin impedance, often referred to as the short-circuit impedance, plays an important role when calculating the currents during a balanced or an unbalanced fault [11]. System operators obtain the Thevenin impedance by performing a short-circuit analysis on the circuit model. However, to avoid any erroneous fault current calculations due to an inaccurate circuit model, it is a good practice to validate the short-circuit impedance from the circuit model with that calculated from the fault data. The Thevenin impedance is also required by the Eriksson, Novosel *et al.*, and other fault-locating algorithms to track down the location of a fault. Furthermore, the Thevenin impedance calculated at regular intervals during a long duration fault can provide insight into the state of the transmission network upstream from the fault. As an example, if the Thevenin impedance is observed to decrease during the duration of the fault, it indicates that critical loads upstream from the monitoring location may have switched offline as demonstrated in Section 9.2.

The negative-sequence Thevenin impedance, Z_{G2}, can be calculated from the

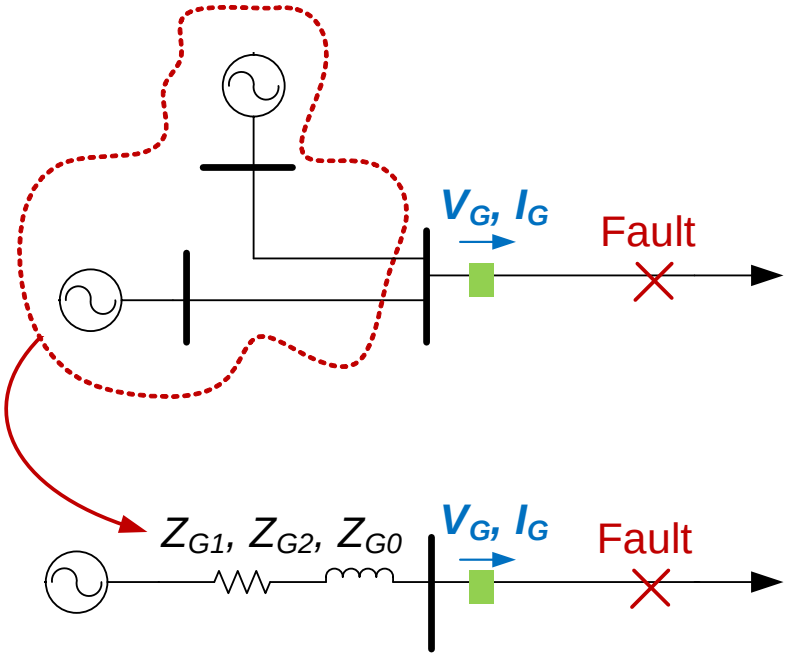

Figure 8.10: Waveforms during a fault can be used to estimate the Thevenin impedance.

negative-sequence network shown in Fig. 2.6 during an unbalanced fault as

$$Z_{G2} = -\frac{V_{G2}}{I_{G2}} \tag{8.42}$$

In a similar manner, the zero-sequence source impedance, Z_{G0}, can be calculated from the zero-sequence network in Fig. 2.4 during a ground fault as

$$Z_{G0} = -\frac{V_{G0}}{I_{G0}} \tag{8.43}$$

The calculation of the positive-sequence source impedance, Z_{G1}, on the other hand, is complicated by the presence of an internal generator voltage, E_G, as shown in Fig. 2.3. As a workaround, the superposition principle is used to decompose the network into a prefault and "pure fault" network. Impedance Z_{G1} can be estimated from the "pure fault" network as

$$Z_{G1} = -\frac{\Delta V_G}{\Delta I_G} = -\frac{V_{G1} - V_{G1pre}}{I_{G1} - I_{G1pre}} \tag{8.44}$$

It should be noted that Z_{G1} is not assumed to be equal to Z_{G2} and is calculated separately using (8.44). This is because the positive-sequence impedance equals the negative-sequence impedance in static electrical components such as lines and transformers. However, the sequence impedances are not equal to each other in rotating machines.

To demonstrate the efficacy of the above approach in estimating the Thevenin impedance, the 69-kV test case described in Section 3.1 was used. A single line-to-ground fault on phase A was simulated at a distance of 7.5 miles from terminal G. The sequence voltage and current phasors recorded by the relay at terminal G before and during the fault are as follows:

$V_{G1} = 36.36\angle 102^\circ$ kV $\quad V_{G2} = 3.25\angle$-$78^\circ$ kV $\quad V_{G0} = 9.59\angle$-$85^\circ$ kV

$I_{G1} = 1.02\angle 56^\circ$ kA $\quad I_{G2} = 0.87\angle 31^\circ$ kA $\quad I_{G0} = 0.85\angle 31^\circ$ kA

$V_{G1pre} = 39.60\angle 102^\circ$ kV $\quad I_{G1pre} = 0.44\angle 114^\circ$ kA

Next, the above phasors were used to calculate the Thevenin impedances using (8.42) - (8.44). As seen from Table 8.5, the estimated negative- and zero-sequence short-circuit impedances matched well with the actual impedances used in the simulation model. The positive-sequence impedance, however, show a small deviation from the actual value. Most likely, the error stems from the constant current load model assumption in (8.44).

Table 8.5: Actual vs. Estimated Thevenin Impedances at Terminal G

Z_{G1} (Ω)		Z_{G2} (Ω)		Z_{G0} (Ω)	
Actual	Estimated	Actual	Estimated	Actual	Estimated
$1.22+j3.55$	$1.11+j3.57$	$1.22+j3.55$	$1.22+j3.55$	$4.76+j10.20$	$4.76+j10.20$

8.6 Verify the Power System Model

System operators usually have detailed circuit models of transmission and distribution networks in PSCAD [47], CAPE [48], OpenDSS [49], and other power system

software. The circuit model is useful for conducting short-circuit studies, determining protective relay settings, and choosing the maximum rating of circuit breakers and other power system equipment. Incorrect short-circuit model parameters can lead to erroneous relay settings and relay misoperations, an example of which is described in [50]. As a result, it is essential that the system model be accurate and continually updated to reflect any system additions, repair, or modifications.

Voltage and current waveforms captured by IEDs during a fault can be used to verify the accuracy of the system model and ensure that the model is representative of the real world feeder. Knowing the actual fault location and estimating the fault resistance in Section 8.4, the same fault can be replicated in the short-circuit model. A good match between the current predicted by the short-circuit model and the actual fault current measurement confirms the accuracy of the circuit model. This approach is demonstrated using field event data in Section 9.4.

8.7 Summary

This Chapter presents the theory of potential applications of intelligent electronic device data in improving power system performance and reliability. Potential applications include assessing the performance of relays, validating the zero-sequence impedance of two- and three-terminal transmission lines, estimating the fault resistance, estimating the Thevenin impedance, and verifying the accuracy of the short-circuit model. The next Chapter demonstrates the above applications with actual fault event data collected from utility transmission and distribution networks.

Chapter 9

Demonstration of the Benefits of Analyzing Intelligent Electronic Device Data using Field Data

Chapter 8 presents the theory of potential applications of IED data to improve power system reliability. The ***objective*** of this Chapter is to demonstrate those potential applications using field data collected from utility transmission and distribution networks. The ***contribution*** of this Chapter lies in analyzing five case studies in details, sharing lessons learned, and illustrating the following applications of IED data: (a) event reconstruction, (b) zero-sequence line impedance validation, (c) relay and circuit breaker performance evaluation, (d) detection of incorrect power system equipment installation, (e) fault resistance and root-cause identification, and (f) circuit model verification.

Publications:

- S. Das, S. Santoso, A. Gaikwad, and M. Patel, "Impedance-based fault location in transmission networks: theory and application," *IEEE Access*, vol. 2, pp. 537-557, 2014.

9.1 Case Study 1: Distribution Fault Analysis Reveals Incorrect Line Impedance Setting

On 22 July 2010, a 24.9-kV utility distribution feeder serving 743 customers experienced a series of complex power system faults at 9:18 pm. A digital relay [81] at the substation reclosed twice to allow the temporary fault to clear out from the feeder.

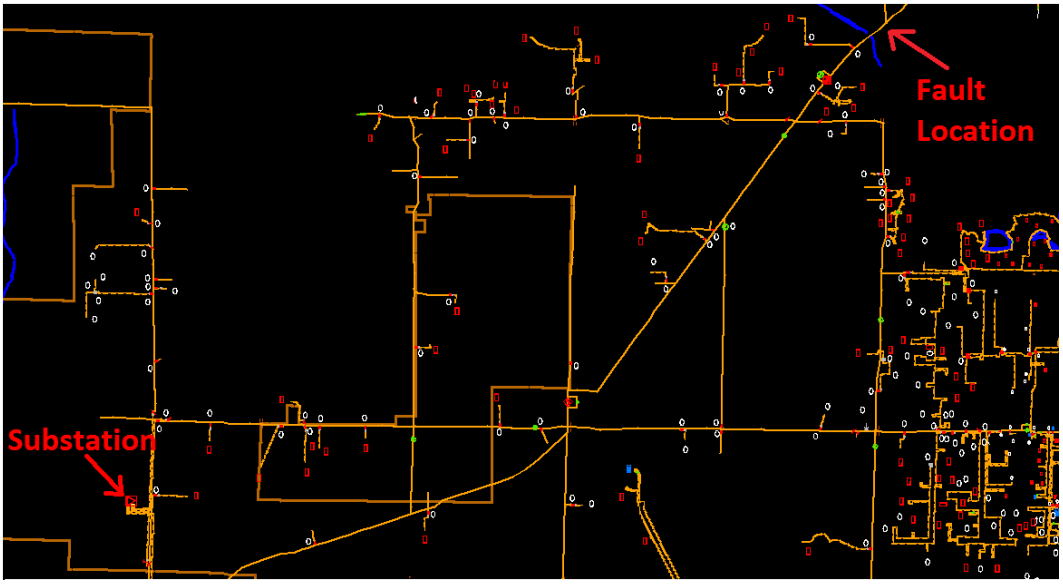

Figure 9.1: Utility network diagram showing the fault location.

The reclose attempts, however, failed to clear the fault and the relay locked out, causing all 743 customers to experience a sustained interruption for 176 minutes. During line inspection, maintenance crew found a jumper burned open on a distribution pole at a distance of 4.43 miles from the substation as shown in Fig. 9.1. This distance was, therefore, reported as the actual fault location. Figure 9.2 shows the event log from the relay. From the date and time stamp, it is evident that the relay recorded Events 3 to 7 during the fault, with Event 7 being the oldest entry. Voltage and current waveforms of each event are shown in Figures 9.3 - 9.7. Notice how the fault type is different for each event. Furthermore, location estimates computed by the relay during the B-G fault match well with the reported fault location. However, the estimated and reported fault location show a significant discrepancy for other fault types. After replacing the jumper, the distribution feeder was re-energized by manually closing the breaker at the substation. Unfortunately, replacing the jumper did not fix the root cause of the fault and the feeder experienced another fault close to the previous location of 4.43 miles on 9 August 2010 as seen from Events 1 and 2 in Fig. 9.2. This Case Study reconstructs

EVENT	DATE	TIME STAMP	FAULT TYPE	FAULT LOCATION	SHOT	MAX PHASE CURRENT	
1	8/9/10	04:02:11.995	ABC T*	4.52	0	3389	Fault reappears 3 weeks later
2	8/9/10	04:02:11.375	ABC	4.18	0	3466	
3	7/22/10	21:19:32.495	BCG T*	5.34	2	2820	Relay recorded 5 events on 7/22/10
4	7/22/10	21:19:31.458	BG	4.51	2	2190	
5	7/22/10	21:19:02.945	BC T*	5.22	1	2670	
6	7/22/10	21:19:02.000	BG	4.48	1	2210	
7 (oldest)	7/22/10	21:18:58.629	BC T*	5.46	0	2600	

* T indicates that the relay has tripped in that event, SHOT indicates the number of reclosures

Figure 9.2: Fault event log from the digital relay.

the perplexing sequence of events and solves the discrepancy in location estimates.

9.1.1 System Protection Description

The first step when reconstructing the sequence of events is to review relay settings and understand its expected behavior during a fault. Figure 9.8 shows the settings of the digital relay. Because most faults on overhead distribution lines are temporary in nature, the relay has been programmed to allow two reclosing shots. The first reclose open interval (79IO1) is 2.5 secs, while the second reclose open interval (79I02) is 27.5 secs. The relay resets itself when the fault disappears from the distribution feeder for more than 70 secs. All trip operations are governed by the trip (TR) equation. As seen from Fig. 9.8, trip occurs when the phase time-overcurrent (51T), the phase definite-time overcurrent (50LT), the ground time-overcurrent (51NT), or the ground definite-time overcurrent (50NLT) elements assert. Element 50LT asserts when the relay measures a phase current greater than 7200 A primary and the relay trips with no intentional time delay. If the phase current is greater than 842.4 A primary but less than 7200 A primary, the phase time-overcurrent pickup element, 51P, asserts first and starts timing on the U3 curve, whose equation is given as [81]:

$$t_{op} = TD \times \left[0.0963 + \frac{3.88}{M^2 - 1}\right] \tag{9.1}$$

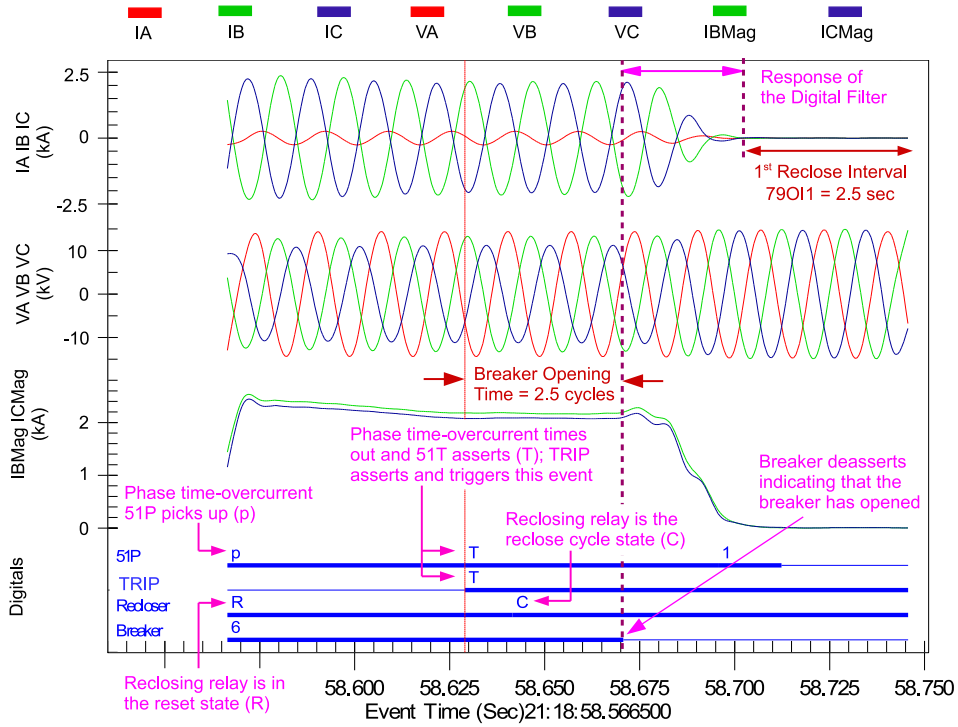

Figure 9.3: Event 7 is a BC fault at an estimated location of 5.46 miles.

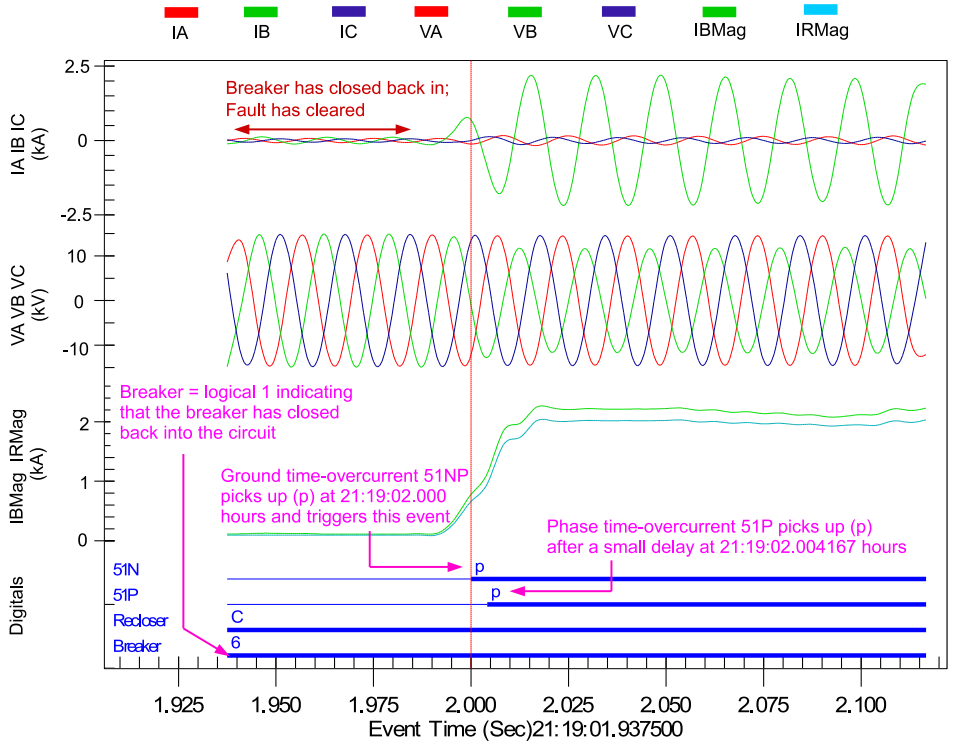

Figure 9.4: Event 6 is a B-G fault at an estimated location of 4.48 miles.

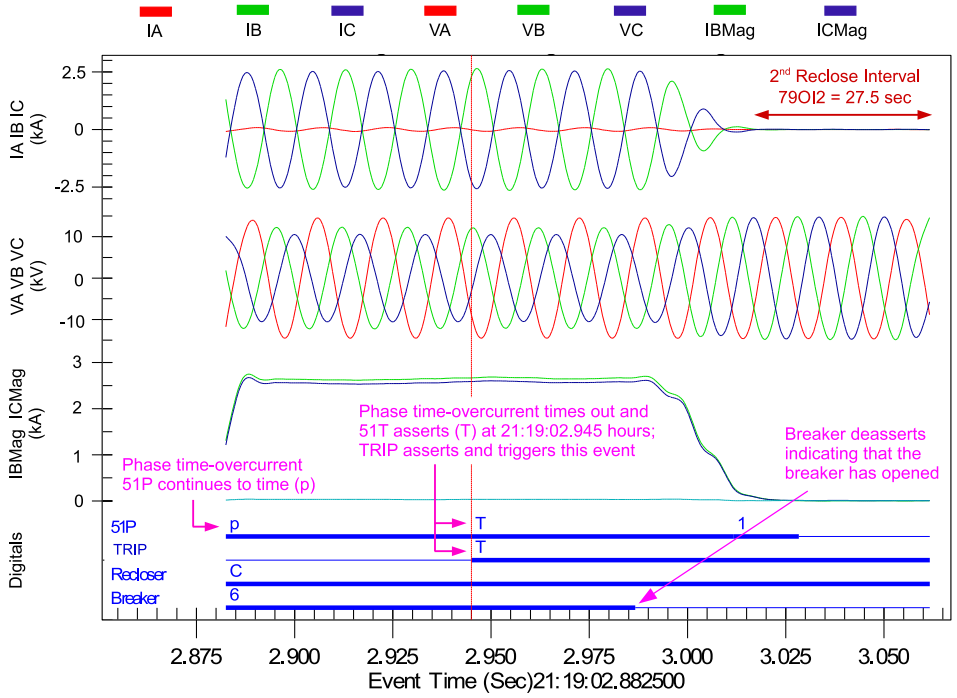

Figure 9.5: Event 5 is a BC fault at an estimated location of 5.22 miles.

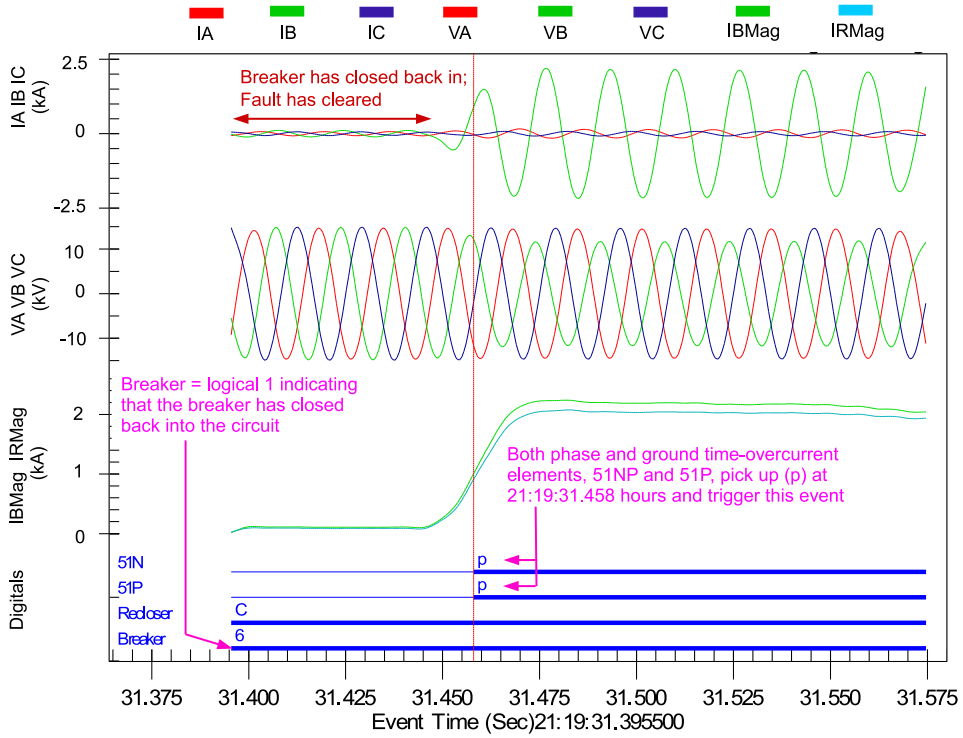

Figure 9.6: Event 4 is a B-G fault at an estimated location of 4.51 miles.

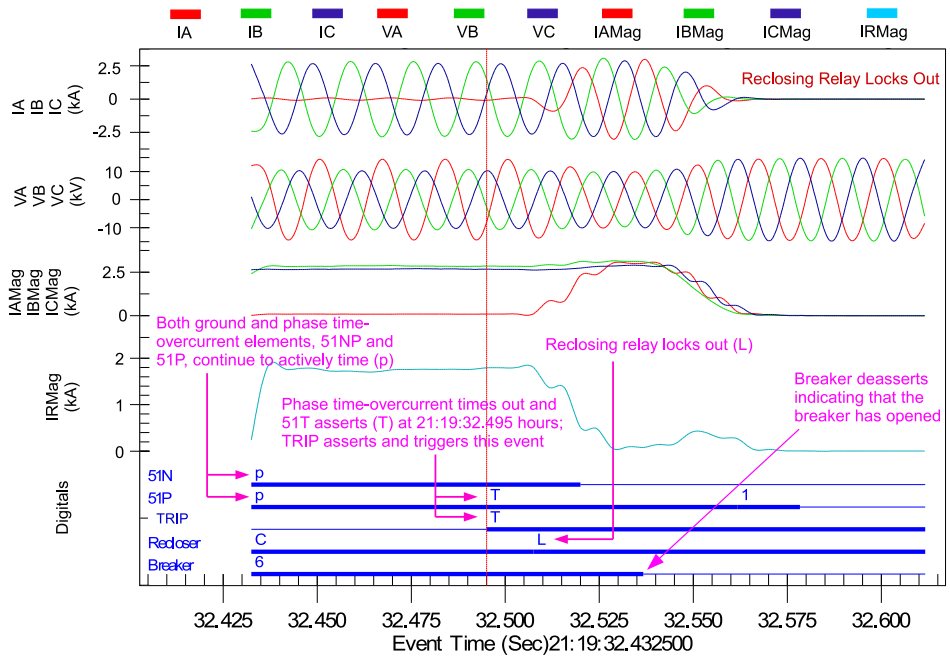

Figure 9.7: Event 3 is a BC-G fault at an estimated location of 5.34 miles.

where t_{op} is the relay trip time in seconds, M is a multiple of pickup and is calculated as the ratio of the fault current to the pickup setting, and TD is the time dial setting. After a lapse of t seconds, 51P times out and 51T asserts, causing the relay to initiate a trip. During a ground fault, if the relay detects a residual current greater than 6408 A primary, 50NLT asserts and the relay trips instantaneously. When the residual current is greater than 597.6 A primary but less than 6408 A primary, the ground time-overcurrent pickup element, 51NP, asserts and starts timing on the U3 curve. Once 51NP times out, 51NT asserts and trips the relay.

9.1.2 Event Report Trigger Criteria

Another important step when reconstructing the sequence of events is to understand what triggers IEDs to generate event reports. The relay automatically records an event report when the trip equation (TR) asserts [81]. The 11-cycle long event report contains voltage and current waveforms during prefault, fault, and post-fault conditions

General Settings:

Current Transformer Ratio (CTR) = 240
Positive-sequence Line Impedance (z_1) = 0.28 + j0.54 Ω/mi
Zero-sequence Line Impedance (z_0) = 0.61 + j2.07 Ω/mi

Reclosing Relay Data:

Relay Open Interval Time 1 (79OI1) = 150 cycles = 2.5 sec
Relay Open Interval Time 2 (79OI2) = 1650 cycles = 27.5 sec
Relay Reset Interval Time (79RST) = 4200 cycles = 70 sec

Phase Definite-Time Overcurrent Element (50LT):

Pickup (50L) = (30 A secondary)*(CTR = 240) = 7200 A primary, Time Delay = 0 cycle

Phase Time-Overcurrent Element (51T):

Pickup (51P) = (3.51 A secondary)*(CTR = 240) = 842.40 A primary
Curve Type = U3 (Very Inverse), Time Dial = 1.72, Reset Time = 1 cycle

Ground/Residual Definite-Time Overcurrent Element (50NLT):

Pickup (50NL) = (26.7 A secondary)*(CTR = 240) = 6408 A primary, Time Delay = 0 cycle

Ground/Residual Time-Overcurrent Element (51NT):

Pickup (51NP) = (2.49 A secondary)*(CTR = 240) = 597.60 A primary
Curve Type = U3 (Very Inverse), Time Dial = 2.06, Reset Time = 1 cycle

Trip (TR) and Event Report (ER) Equations:

TR = 51T + 50LT + 51NT + 50NLT; ER = 51P + 51NP + 27

Figure 9.8: Settings in the digital relay.

at 4 samples per cycle. A cosine filter processes the waveform data to remove DC offset and other harmonic frequencies. Apart from the TR equation, digital relays also allow system operators to monitor specific relay variables via the event report (ER) setting. An event report is triggered when the monitored variables change state. For example, according to the ER setting in Fig. 9.8, event reports will be triggered when the phase time-overcurrent pickup (51P), the ground time-overcurrent pickup (51NP), or the phase undervoltage (27) elements assert. To ensure that multiple event reports are not generated for the same fault, relay elements responsible for triggering an event report must deassert for four cycles before they can trigger another event report.

9.1.3 Event Reconstruction

To reconstruct an accurate account of events, start with the oldest event (Event 7) recorded by the relay. Keep in mind that the waveforms record what the relay "saw" during a fault while the digitals document the relay response during the fault. A digital

having a solid thick line indicates logical 1. Now, according to Fig. 9.3, the relay sees a BC fault and a fault current magnitude of 2600 A primary, which exceeds the 51P pickup setting of 842.4 A in Fig. 9.8. As a result, 51P starts timing on the U3 curve and times out at 21:18:58.629 hours. 51T asserts and trips the relay, which prompts the relay to record this event. Note that an earlier event showing the fault inception is missing. After receiving the trip signal from the relay, the circuit breaker takes 2.5 cycles to interrupt the fault current (Breaker = logical 0). This additional time, known as the breaker operating time, can be compared against manufacturer specifications to evaluate the breaker performance. Observe that the fault current is visible for another 1.5 cycles after the circuit breaker has opened and is the response of a cosine filter to an abrupt change in current from 2200 A to 0 A. At the start of the event, the relay is in the reset state (Recloser = R). However, after issuing a trip command, the relay enters the reclose cycle state (Recloser = C) and starts timing on the first open interval, 79OI1.

The relay starts recording Event 6 from 21:19:01.9375 hours as shown in Fig. 9.4. By this time, 79OI1 has timed out, the relay has closed back into the circuit, and the shot counter has increased to 1. The fault appears to have cleared out from the distribution feeder. However, before the relay can reset itself (79RST = 70 secs), the feeder experiences a B-G fault. The phase B current is 2210 A primary and the residual current is 2020 A primary. Both currents are greater than the pickup settings of phase and ground time-overcurrent elements, 51P and 51NP. The more sensitive 51NP picks up first and triggers this event, followed by 51P as illustrated in Fig. 9.4.

When the relay starts recording Event 5, the B-G fault has developed into a BC fault as shown in Fig. 9.5. The residual current is insignificant which causes 51NP to drop out. 51P continues to actively time on the U3 curve and times out at 21:19:02.945 hours. The resulting trip initiates this event, and the relay enters the second open interval, 79OI2. Since the relay has not reclosed yet, the shot count stays equal to 1.

The relay starts recording Event 4 after 29.28 secs as shown in Fig. 9.6. Since 79IO2 is 27.5 secs, the relay has already closed back into the circuit, and the shot counter increases to 2. The fault appears to have cleared out from the distribution feeder. However, before the relay can reset itself, the fault resurfaces as a B-G fault. The phase current is 2190 A primary while the residual current is 1937 A primary. Both 51P and 51NP assert simultaneously and start timing on the U3 curve at 21:19:31.458 hours.

By Event 3, the fault has developed into a BC-G fault as shown in Fig. 9.7. The primary phase and residual current magnitudes are 2820 A ($M = 3.35$) and 1793 A ($M = 3$), respectively. Relay variables 51P and 51NP continue to actively time on the U3 curve. According to (9.1), the operating time of the phase and ground time-overcurrent elements are 0.809 and 1.197 secs, respectively as shown in Fig. 9.9. As a result, 51T asserts before 51NP has a chance to time out and triggers the relay to record the event. As mentioned earlier, the circuit breaker takes an additional 2.5 cycles to open and isolate the fault. Within this time, the fault has evolved into a three-phase fault. Since all reclose attempts fail to clear the fault, the relay locks out (Recloser = L).

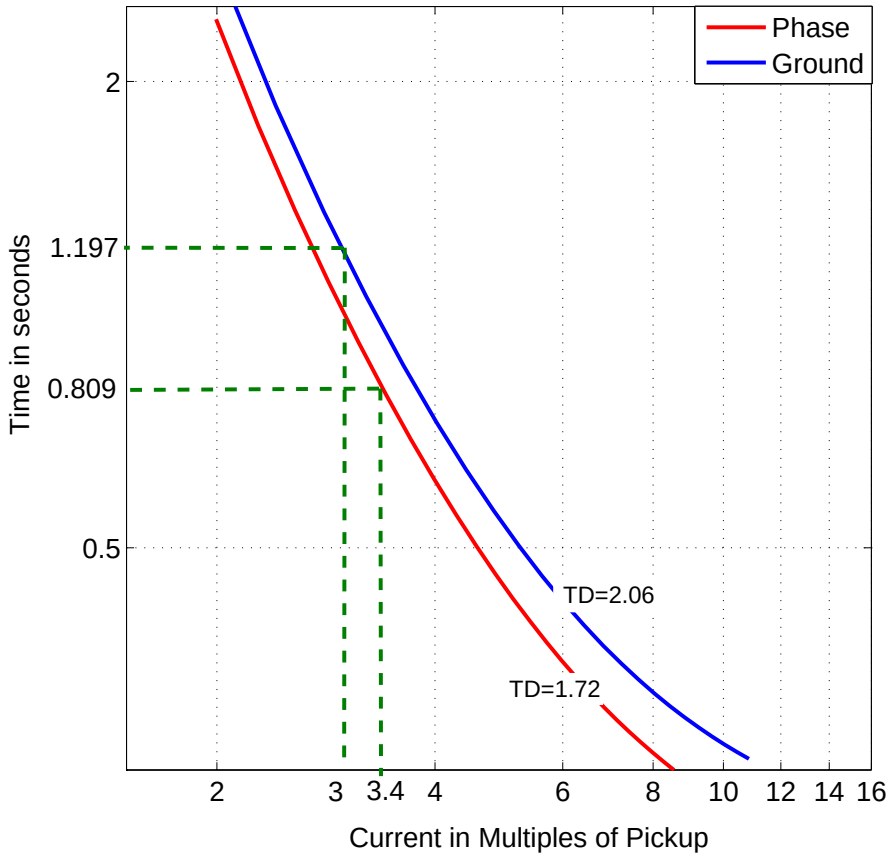

Figure 9.9: U3 very inverse time-overcurrent curve. TD = 1.72 for the phase and TD = 2.06 for the ground time-overcurrent element.

9.1.4 Fault Location Discrepancy Analysis

The first step towards investigating the discrepancy in fault location estimates is to confirm the accuracy of the positive- and zero-sequence line impedance relay settings in Fig. 9.8. The phase conductor is constructed using a 336 ACSR conductor, and the neutral conductor is constructed using a 500 aluminum conductor. The characteristics of the conductor material are listed in Table 9.1. Since the actual spacings between the phase and neutral conductors are not available, a typical line configuration of a 24.9-kV distribution feeder shown in Fig. 9.10 is used. The positive- and zero-sequence line

Table 9.1: Conductor Data [3]

	Material	Resistance (Ω/mi)	GMR (feet)
Phase	336 ACSR	0.306	0.0244
Neutral	500 AAC	0.206	0.0260

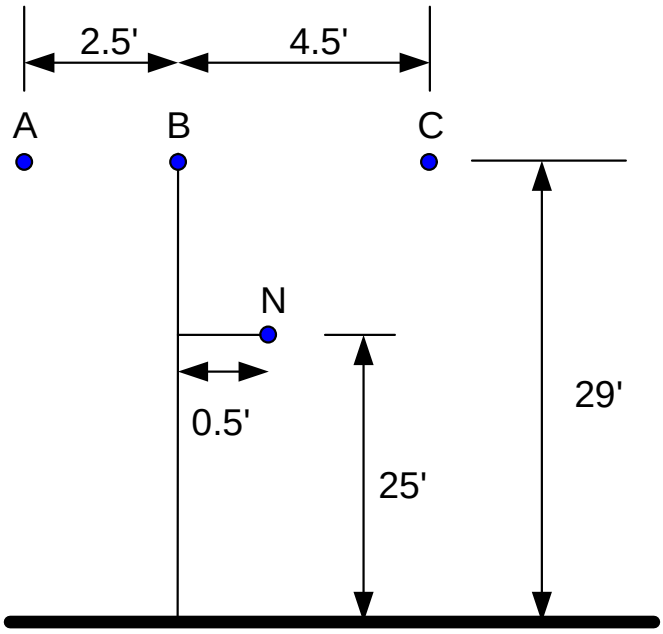

Figure 9.10: Line Configuration of a Typical 24.9-kV Distribution Feeder [3, 9].

impedances are calculated using Carson's equations to be $z_{1new} = 0.31 + j0.63\,\Omega$/mi and $z_{0new} = 0.55 + j1.73\,\Omega$/mi, respectively. Notice that these line impedance parameters are different than those used by the digital relay for fault location calculations.

Next, the typical line impedance parameters of a 24.9-kV distribution feeder, z_{1new} and z_{0new}, are used to estimate the distances to the fault. As seen in Table 9.2, location estimates from all events are now close to the actual fault location. Therefore, these findings strongly suggest that the disparity in location estimates was due to inaccurate line impedance settings. It is recommended that the utility recalculate the line impedance parameters and make changes as necessary.

Table 9.2: Location Estimates using Line Impedance Parameters of a Typical 24.9-kV Distribution Feeder having a 336 ACSR Phase and a 500 AAC Neutral Conductor is close to the Actual Fault Location

Event	Fault Type	Actual Location (mi)	Estimated Location (mi)
7	BC	4.43	4.72
6	B-G		4.58
5	BC		4.54
4	B-G		4.58
3	BC-G		4.57

9.1.5 Evolving Fault Analysis

Now, in addition to solving the disparity in fault location estimates, we must also explain why the fault evolves from a BC to a B-G fault. Also, after every reclose operation, why does the fault disappear for a few cycles and then reappear? To find a suitable explanation, let's take a look at the weather conditions on the day of the event. Severe thunderstorms accompanied by rain and wind gust speeds of 40 miles per hour were reported in the area as shown in Fig. 9.11. Most likely, high wind speeds pushed a tree into the phase B and phase C conductors, causing conductor slapping and a BC fault. Because of the fault, the jumper cable at 4.43 miles burned open. The high wind speeds caused the burned open jumper cable to swing around and touch the phase and ground conductors, resulting in a series of B-G, BC, and BC-G faults. The theory of the tree contact fault is further supported by the recurrence of another fault on 9 August 2010 at the same location of 4.51 miles as seen from Events 2 and 1 in Fig. 9.2. Stormy weather was reported on that day as well. The recurring fault also proves that the burned jumper cable was the failure effect and not the root cause of the fault on 22 July 2010.

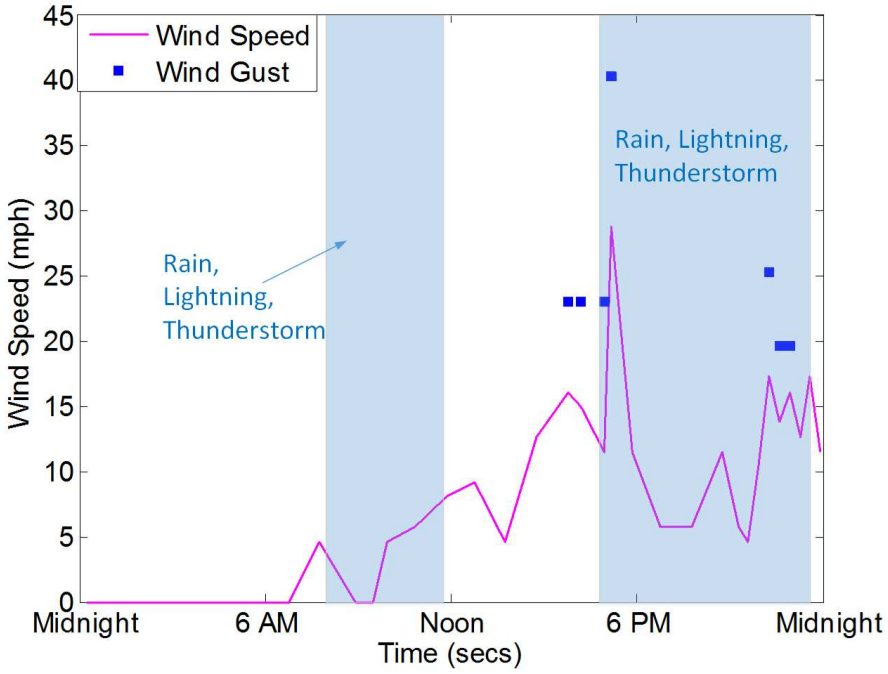

Figure 9.11: Stormy weather on 22 July 2010.

9.1.6 Lessons Learned

1. Any discrepancy between the reported fault location and location estimates computed by the relay must be thoroughly investigated. For example, the analysis in this case study strongly suggest that the disparity in location estimates is due to inaccurate line impedance settings. It is recommended that the utility recalculate the line impedance parameters and revise relay settings as needed.

2. Analysis of faults can provide insights into the root causes of faults. In this case study, the BC fault was, most likely, caused by a tree pushing together two phase conductors during high wind speeds. The utility is advised to trim trees near 4.43 miles to prevent future recurrence of such faults.

3. Event reports must be downloaded before being overwritten by more recent events. For instance, an event before Event 7, which should have recorded the fault inception

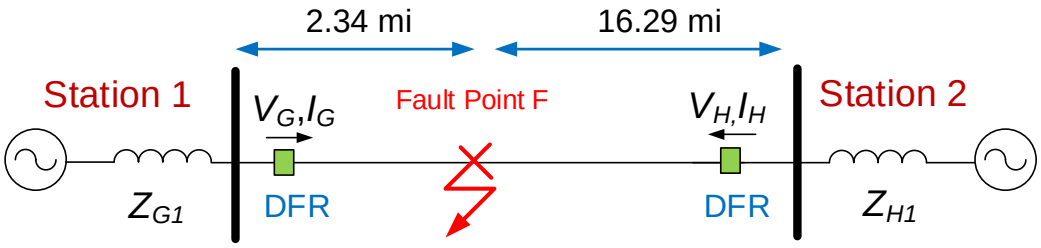

Figure 9.12: Case study 2 is a AB fault at 2.34 miles from Station 1 or 16.29 miles from Station 2.

time, is missing. Furthermore, event reports must be thoroughly analyzed before re-energizing the system. If event reports on 22 July 2010 were reviewed in details, the fault on 9 August 2010 could have been prevented.

4. Events described in this case study take a longer time to unfold than the standard event report length of eleven cycles. To visualize entire events such as these in the future and ensure that no valuable data is lost, the utility is advised to use timers for triggering consecutive events as described in [39].

9.2 Case Study 2: Tree Contact with a 161-kV Transmission Line Reveals the Upstream Network Response to a Fault

This event is a line-to-line fault that occurred between phases A and B of a 161-kV transmission line on 25 March 2012 at 03:56 pm. The transmission line is 18.63 miles long and connects Station 1 with Station 2 as shown in Fig. 9.12. The positive- and zero-sequence impedances of the line are $Z_{L1} = 2.39 + j12.81\,\Omega$ and $Z_{L0} = 9.95 + j40.70\,\Omega$, respectively. The fault was caused by a tree falling on the transmission line 2.34 miles from Station 1 or 16.29 miles from Station 2.

9.2.1 Event Reconstruction

The sequence of events can be reconstructed from the voltage and current waveforms captured by digital fault recorders (DFRs) at both ends of the transmission line. The waveforms at Station 1 and Station 2 are shown in Fig. 9.13 and Fig. 9.14, respectively. Both DFRs have a sampling rate of 100 samples per cycles. Before the fault, Station 1 and Station 2 support a load current of 47 A and 55 A, respectively. When a fault occurs 2.34 miles from Station 1, the DFR at Station 1 measures a fault current of 4.8 kA in phases A and B. After 3.5 cycles, a protective relay at Station 1 initiates a fast trip operation.

Station 2, on the other hand, continues to feed the fault for 34.5 cycles. During the first 3.5 cycles, when both stations are feeding the fault, the DFR at Station 2 records a current of 3.2 kA in the faulted phases. This is marked as "Part 1" in Fig. 9.14. When Station 1 trips offline after 3.5 cycles, the fault current from Station 2 increases to 4 kA as indicated by "Part 2" in Fig. 9.14. After 34.5 cycles, the recloser at Station 2 operates to allow the fault to clear out on its own. The reclose interval is 2.07 seconds. The fault is, however, permanent and the DFR measures a fault current magnitude of 4 kA when the recloser closes back into the transmission line. This is illustrated by "Part 3" in Fig. 9.14. The recloser eventually locks out after 3.5 cycles.

9.2.2 Fault Location

To track down the location of the permanent fault, one-ended impedance-based fault location algorithms were applied from Station 1. Location estimates are, however, not accurate and exceed the actual location of the fault by 1.4 miles as shown in Table 9.3. One-ended fault location algorithms were then applied to "Part 2" and "Part 3" of the waveforms captured at Station 2. This is because in "Part 2" and "Part 3", only Station 2 contributes current to the fault. There is no remote infeed from Station 1 and hence,

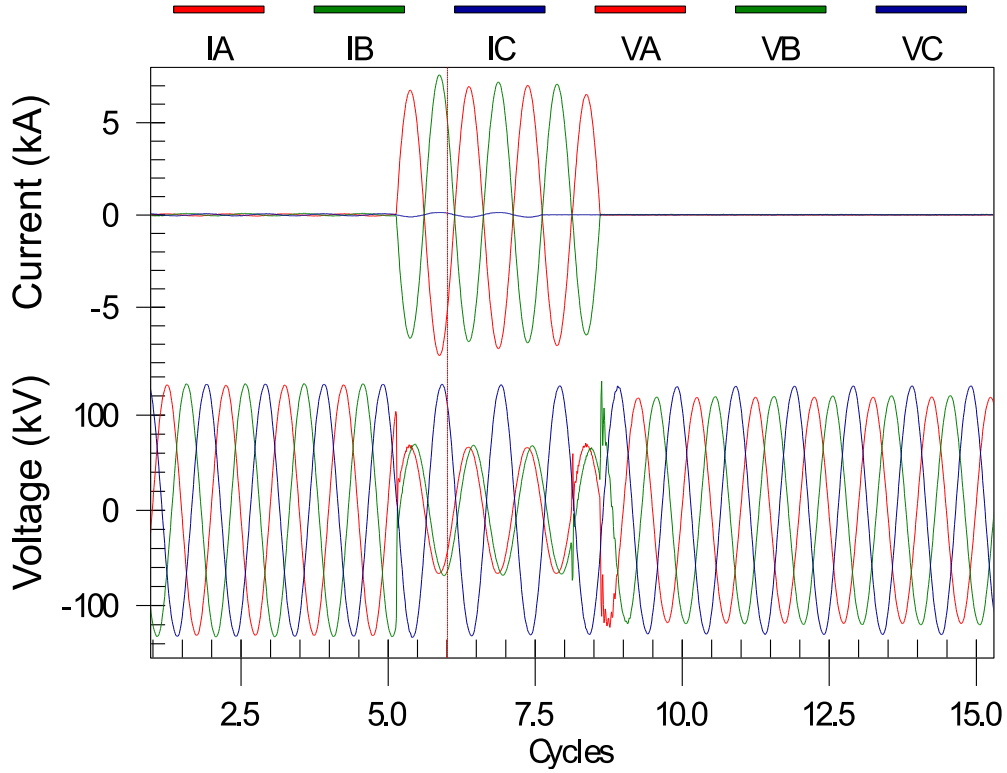

Figure 9.13: Case study 2 DFR measurements at Station 1, $I_{AF} = I_{BF}$ =4.8 kA.

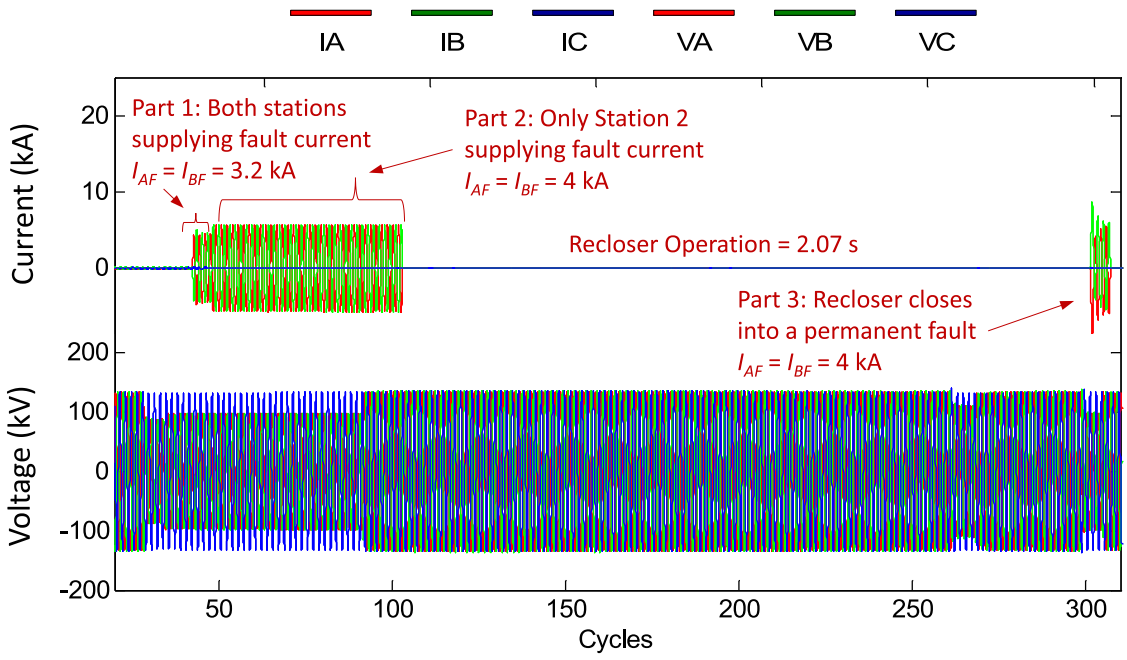

Figure 9.14: Case study 2 DFR measurements at Station 2.

location estimates are expected to have a high degree of accuracy. Unfortunately, as seen in Table 9.3, one-ended methods from Station 2 also overestimate the location of the fault by 1.9 miles. It should be noted that in addition to the one-ended methods, the DFRs at Station 1 and Station 2 also incorrectly identify the location of the fault.

To explain the fault location error, recall that the Eriksson method is robust to fault resistance, load, and a non-homogeneous system. Erroneous estimates from the Eriksson method, therefore, rules out the above sources of fault-locating error. Moreover, since the fault does not involve the ground, zero-sequence mutual coupling and uncertainty in zero-sequence line impedance can also be eliminated as potential error sources. Additional information regarding the transmission network is required to identify the factor responsible for the error in fault location.

Table 9.3: Case Study 2 Location Estimates from One-ended Methods

Station	Actual Location (mi)	DFR Estimate (mi)	Estimated Location (mi)		
			Simple Reactance	Takagi	Eriksson
1	2.34	3.90	3.77	3.77	3.78
2, Part 2	16.29	18.00	18.08	18.08	18.04
2, Part 3			18.18	18.18	18.16

Among the two-ended methods, the unsynchronized two-ended algorithm was chosen since the DFRs at Station 1 and Station 2 have different fault trigger times. The algorithm was applied to that part of the waveform wherein both stations are contributing to the fault, i.e., Station 1 and "Part 1" of Station 2 waveform. As seen from Table 9.4, the location estimate from the two-ended method show a significant improvement over one-ended methods and is within 0.15 miles of the actual fault location.

9.2.3 Fault Resistance Estimation

The fault resistance was estimated by applying (8.37) to Station 1 and "Part 1" of Station 2 waveforms to be 0.88 Ω. The accuracy of the estimated fault resistance can be ascertained from the fact that the location estimates from the simple reactance and Takagi methods in Table 9.3 are identical. In other words, the simple reactance method did not suffer from any reactance error due to load current, thereby confirming that the fault resistance in this event is indeed negligible.

9.2.4 Thevenin Impedance Estimation

Voltage and current waveforms captured during Event 2 were used to estimate the Thevenin impedance of the transmission networks upstream from Station 1 and Station 2. The results are tabulated in Table 9.5. Because the event is a line-to-line fault, only the positive- and negative-sequence Thevenin impedances could be estimated. Observe the sudden change in the positive- and negative-sequence Thevenin impedances at Station 2 from "Part 1" to "Part 2". Since Station 2 contributes fault current for a long time frame, 34.5 cycles, several generators and loads upstream from Station 2 must have switched offline, resulting in a sharp decrease in the source impedance.

Table 9.4: Case Study 2 Location Estimate from the Unsynchronized Two-ended Method

Station	Actual Location (mi)	Estimated Location (mi)
1 and 2	2.34	2.46

Table 9.5: Case Study 2 Estimated Thevenin Impedance

Station	Positive-sequence Impedance (Ω)	Negative-sequence Impedance (Ω)
1	$1.85 + j14.46$	$3.04 + j13.66$
2, Part 1	$4.25 + j12.80$	$2.83 + j12.28$
2, Part 2	$6.46 + j6.29$	$1.72 + j7.39$
2, Part 3	$3.19 + j7.22$	$1.67 + j7.37$

9.2.5 Lessons Learned

Analysis of faults can provide system operators with valuable clues about the response of the upstream transmission network during a fault. For example, this case study reveals that several critical loads upstream from the DFR at Station 2 must have tripped offline during the fault that lasts for 34.5 cycles. In addition, the fault data is also useful in estimating the fault resistance. Finally, the case study highlights the superior performance of two-ended methods in estimating the fault location.

9.3 Case Study 3: Failed Line Arrestor on a 161-kV Transmission Line Validates the Zero-sequence Line Impedance

On 27 April 2012, a single line-to-ground fault occurred on phase A of a 161-kV transmission line at 00:48 am. The transmission line experiencing fault is 21.15 miles long and connects Station 1 with Station 2 as shown in Fig. 9.15. The positive- and zero-sequence impedances of the line are $Z_{L1} = 3.18 + j16.68\,\Omega$ and $Z_{L0} = 15.21 + j52.45\,\Omega$, respectively. The fault was caused by a failed line arrestor located 14.90 miles from Station 1 or 6.25 miles from Station 2. Digital fault recorders (DFRs) at both stations record the three-phase line-to-ground voltage and current waveforms at 100 samples per cycle as shown in Fig. 9.16 and Fig. 9.17. Before the fault, Station 1 supports a load current of 150 A and Station 2 supports a load current of 130 A. During the fault, the

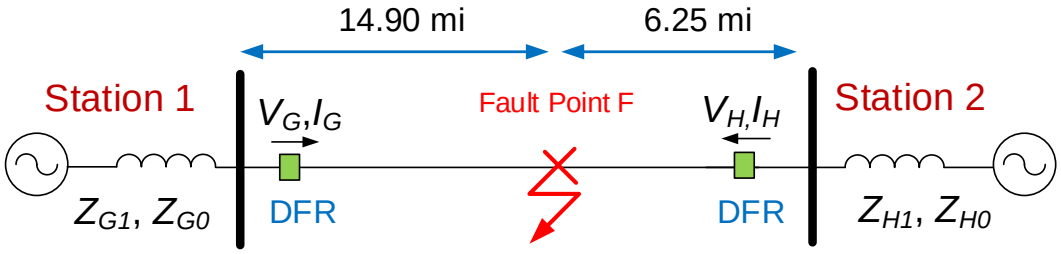

Figure 9.15: Case study 3 is a A-G fault located 14.90 miles from Station 1 or 6.25 miles from Station 2.

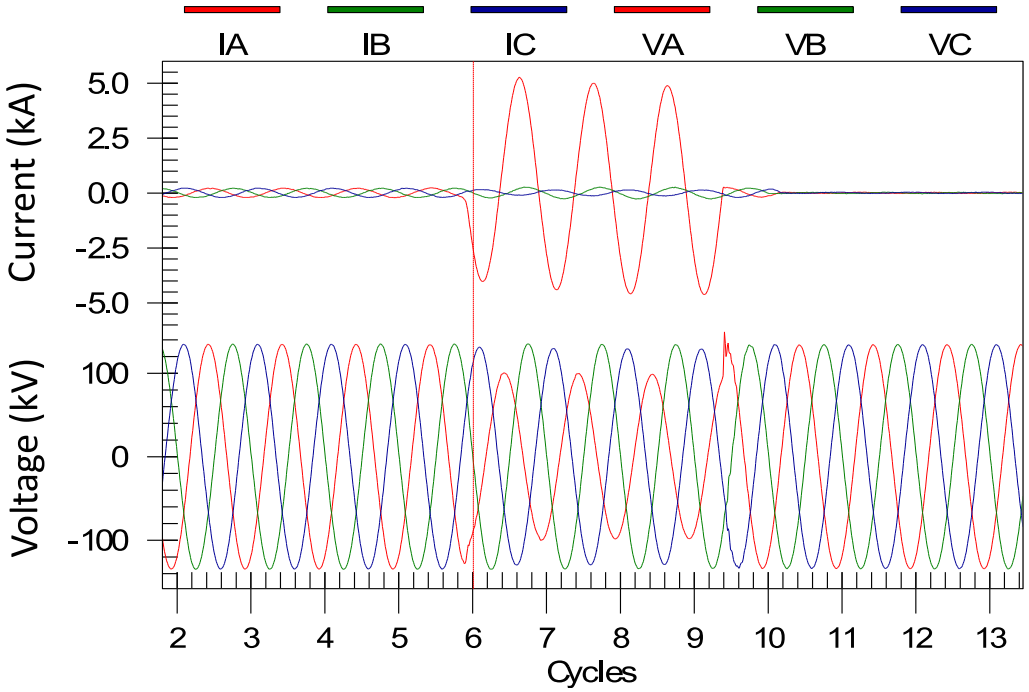

Figure 9.16: Case study 3 DFR measurements at Station 1, $I_{AF} = 3.4\,\text{kA}$.

current magnitude in the faulted phase increases to 3.4 kA at Station 1 and to 6.1 kA at Station 2. Note that to calculate the fault current at Stations 1 and 2, the third cycle after fault was chosen for calculating fault current phasors.

9.3.1 Fault Location

One-ended impedance-based fault location algorithms were applied from Station 1 and Station 2 to estimate the distance to fault. As shown in Table 9.6, the location

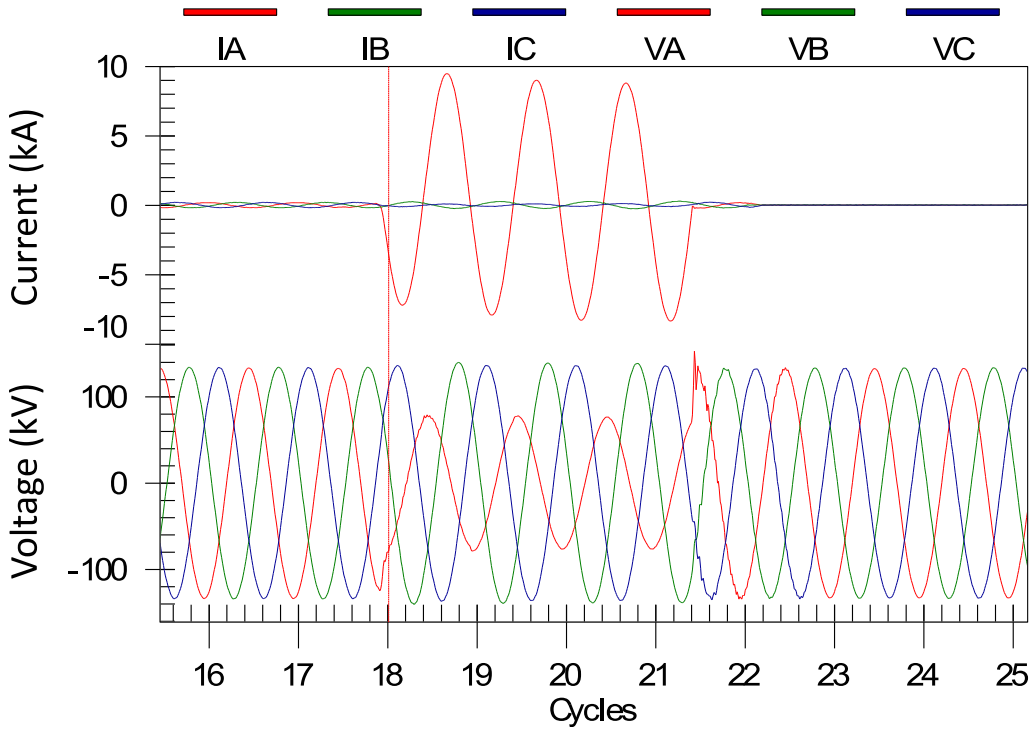

Figure 9.17: Case study 3 DFR measurements at Station 2, $I_{AF} = 6.1\,\text{kA}$.

estimates are in agreement with those estimated by the DFRs and close to the actual location of the fault. In addition to one-ended methods, two-ended fault location methods were also used to estimate the distance to fault. Since the measurements from both ends of the transmission line are unsynchronized due to a difference in the fault trigger time, the unsynchronized two-ended method was used. Distance to fault was computed to be 14.76 miles from Station 1 as shown in Table 9.7.

Table 9.6: Case Study 3 Location Estimates from One-ended Methods

Station	Actual Location (mi)	DFR Estimate (mi)	Estimated Location (mi)			
			Simple Reactance	Takagi	Modified Takagi	Eriksson
1	14.90	14.40	14.78	14.77	14.77	14.77
2	6.25	6.40	6.38	6.36	6.36	6.36

Table 9.7: Case Study 3 Location Estimate from the Unsynchronized Two-ended Method

Station	Actual Location (mi)	Estimated Location (mi)
1 and 2	14.90	14.76

9.3.2 Fault Resistance Estimation

Voltage and current waveforms at both ends of the line were used by (8.35) to estimate the fault resistance to be $0.19\,\Omega$. Accurate location estimates from the simple reactance method confirms that the fault resistance in this event was indeed negligible.

9.3.3 Thevenin Impedance Estimation

Since this case study is a ground fault, it is possible to estimate the positive-, negative-, and zero-sequence short-circuit impedances at Station 1 and Station 2. The estimates are listed in Table 9.8. Observe that Station 1 has a higher short-circuit impedance and is hence, electrically weaker than Station 2. The magnitude of fault currents contributed by each station supports this observation.

9.3.4 Zero-sequence Line Impedance Validation

Approach 1 and Approach 2 developed in Section 8.2 were used to validate the zero-sequence line impedance. Recall that Approach 1 uses waveform data from one

Table 9.8: Case Study 3 Estimated Short-circuit Impedances

Station	Positive-sequence Source Impedance (Ω)	Negative-sequence Source Impedance (Ω)	Zero-sequence Source Impedance (Ω)
1	$0.13 + j9.40$	$1.38 + j8.05$	$0.00 + j6.13$
2	$0.00 + j5.93$	$1.05 + j5.32$	$1.31 + j8.68$

Table 9.9: Case Study 3 Setting vs. Estimated Zero-sequence Line Impedance

Approach	Zero-sequence Line Impedance		Error	
	Setting (Ω)	Estimated (Ω)	Magnitude (%)	Phase Angle (degrees)
Approach 1 (Station 1)	$15.21 + j52.45$	$17.35 + j51.70$	0.14	2.38
Approach 1 (Station 2)		$18.12 + j53.97$	4.24	2.38
Approach 2 (Station 1, 2)		$16.93 + j53.45$	2.65	1.41

end of the line and assumes a zero value of fault resistance. However, as seen in Section 9.3.2, the fault resistance in this case study is not exactly zero. Furthermore, since the measurements from both ends of the line are not aligned due to a difference in the fault trigger time, this case study highlights the necessity of developing Approach 2. As seen from Table 9.9, the estimated zero-sequence line impedance matched well with that used by the utility as protection settings.

9.3.5 Lessons Learned

This case study confirms the accuracy of the zero-sequence line impedance that was being used as a protective device setting. The fault was also found to have encountered the least resistance path to the ground. Furthermore, Station 1 was learned to be electrically weak than Station 2.

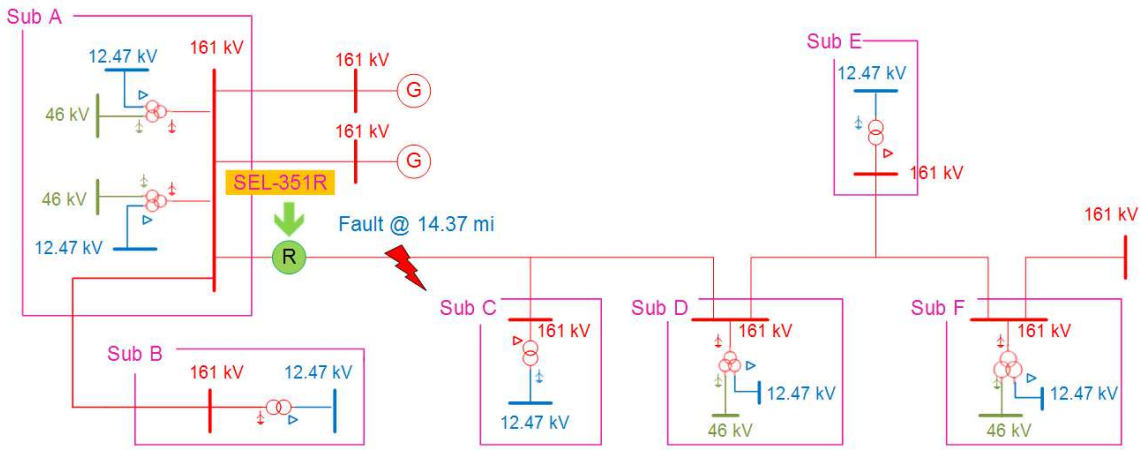

Figure 9.18: Case study 4 utility circuit model in CAPE software.

9.4 Case Study 4: B-G Fault Verifies Relay Performance, Validates the Zero-sequence Line Impedance, and Authenticates the System Model

In this case study, the circuit model of the utility transmission network is available in CAPE software [48] as shown in Fig. 9.18. The rated voltage at Substation A is 161 kV. A SEL-351R relay [10] is responsible for protecting the 23.6-mile long transmission line that connects Substation A with Substation C. The line geometry is shown in Fig. 9.19 and the conductor data are provided in Table 9.10. This line data is used in Carson's equations to calculate the positive- and zero-sequence line impedances as $Z_{L1} = 6.01 + j19.00\,\Omega$ and $Z_{L0} = 19.72 + j56.23\,\Omega$, respectively. On 10 January 2012, a single line-to-ground fault on phase B occurred at a distance of 14.37 miles from Substation A as illustrated in Fig. 9.18. The root cause of the fault is not known. The fault, being momentary in nature, is cleared by the first shot of the SEL-351R relay. However, the same fault reappears in the circuit after 15 minutes as seen from the event log in Fig. 9.20. The SEL relay operates again to allow the temporary fault to clear from the circuit. During the entire duration, the relay records four events, whose voltage and current waveforms are shown in Figures 9.22 - 9.25. This Section uses the waveform

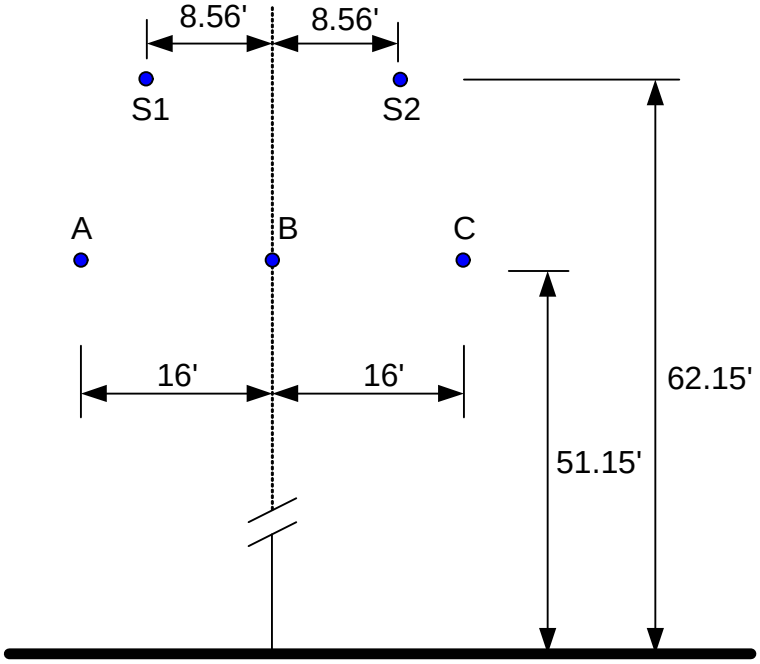

Figure 9.19: Overhead transmission line spacing in feet.

Table 9.10: Conductor Data

	Material	Resistance (Ω/mi)	Diameter (inch)	GMR (feet)
Phase Conductor	397,500 26/7 ACSR	0.2537	0.7836	0.0265
Shield Wire	3/8 A HSS	5.6500	0.3600	0.0120

data to reconstruct the sequence of events, estimate the fault location, assess relay performance, estimate the fault resistance, validate the zero-sequence line impedance, and verify the accuracy of the system model.

9.4.1 System Protection Description

The settings of the SEL-351R relay are shown in Fig. 9.21. The relay is programmed to perform three automatic reclosures. The first reclose open interval (79IO1) is 10 cycles, the second reclose open interval (79I02) is 1800 cycles, and the third reclose open interval (79IO3) is 3600 cycles. The relay resets itself when the fault disappears

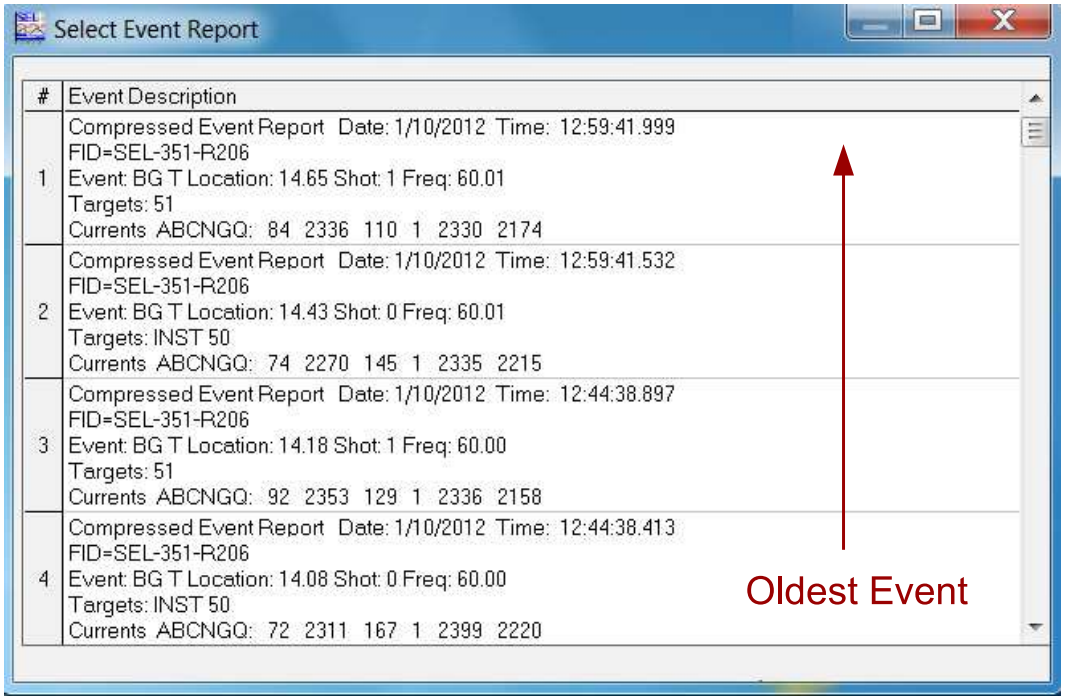

Figure 9.20: SEL-351R fault event history.

from the transmission feeder for more than 900 cycles. A trip occurs when the phase instantaneous element with directional control (67P1T), the phase time-overcurrent (51PT) element, the ground instantaneous element with directional control (67G1T), or the ground time-overcurrent (51NT) element asserts as evident from the TR equation in Fig. 9.21. Now, 67P1T asserts when the phase current is greater than 1048.80 A primary and the relay trips with no intentional time delay. On the other hand, if the phase current is between 540 A primary and 1048.80 A primary, the phase time-overcurrent pickup element, 51P, picks up and starts to time on the U3 curve given by (9.1). When 51P times out, 51T asserts and causes the relay to initiate a trip. During a ground fault, if the relay detects a ground current greater than 560.40 A primary, element 67G1T asserts and the relay trips instantaneously. When the ground current is greater than 288 A primary but less than 560.40 A primary, the ground time-overcurrent pickup element, 51GP, asserts and starts timing on the U3 curve. Once 51GP times out, 51GT asserts

General Settings:

```
Current Transformer Ratio (CTR) = 120
Positive-sequence Line Impedance (Z1) = 6.01 + j19.00 Ω
Zero-sequence Line Impedance (Z0) = 19.72 + j56.23 Ω
Line Length (LL) = 23.6 mi
```

Reclosing Relay Data:

```
Relay Open Interval Time 1 (79OI1) = 10 cycles  = 0.17 sec
Relay Open Interval Time 2 (79OI2) = 1800 cycles = 30 sec
Relay Open Interval Time 3 (79OI3) = 3600 cycles = 60 sec
Relay Reset Interval Time  (79RST) = 900 cycles = 15 sec
```

Phase Instantaneous Overcurrent Element with Directional Control (67P1T):

```
Pickup (50P1P) = (8.74 A secondary)*(CTR = 120) = 1048.80 A primary
```

Phase Time-Overcurrent Element (51PT):

```
Pickup (51P) = (4.50 A secondary)*(CTR = 120) = 540 A primary
Curve Type = U3 (Very Inverse), Time Dial = 1.29
```

Ground Instantaneous Overcurrent Element with Directional Control (67G1T):

```
Pickup (50G1P) = (4.67 A secondary)*(CTR = 120) = 560.40 A primary
```

Ground Time-Overcurrent Element (51GT):

```
Pickup (51G) = (2.40 A secondary)*(CTR = 240) = 288 A primary
Curve Type = U3 (Very Inverse), Time Dial = 1.48
```

Trip (TR) and Event Report (ER) Equations:

```
TR = (67P1T*!SH1) + 51PT + (67G1T*!SH1) + 51GT
ER = /51P + /51G + /TR
```

Figure 9.21: Settings in the SEL-351R relay.

and trips the relay. It is important to note that 67P1T and 67G1T are disabled for shot 1 as specified by the trip equation in Fig. 9.21. Logical operator ! indicates a NOT function, operator * indicates a AND function, and SH1 = 1 when the relay is at shot = 1. In other words, during shot 1, the relay will trip only for 51P1T and 51G1T elements.

9.4.2 Event Report Trigger Criteria

According to the ER setting in Fig. 9.21, the SEL-351R relay records an event report when the trip equation (TR) asserts or when the phase and ground time-overcurrent

elements, 51P and 51G, pick up. The operator / indicates the rising edge of the element. The 16-cycle long event report contains voltage and current waveforms during prefault, fault, and post-fault conditions at 16 samples per cycle.

9.4.3 Event Reconstruction

To build an accurate account of the sequence of events, start with the oldest event recorded by the relay in Fig. 9.22. The load current supported by the substation is 116 A. During the phase B-to-ground fault, the phase and the ground fault current magnitudes increase to 2360 A and 2300 A, respectively. As a result, both 67P1T and 67G1T assert simultaneously at 12:44:38.413 hours and the relay send a trips signal to the circuit breaker. Observe that the circuit breaker takes an additional three cycles to interrupt the current as shown in Fig. 9.22. This breaker operate time can be compared against manufacturer specifications to verify the breaker performance. After receipt of the circuit breaker open status, the relay starts timing on the first open interval, 79OI1.

When 79OI1 times out, the shot counter increases to 1 and the circuit breaker closes back into the circuit at 12:44:38.885 hours as shown by Event 3 in Fig. 9.23. The fault, however, is still present in the circuit and the relay measures a phase and ground current of 2860 A and 2811 A, respectively. Since the operation of the 67P1T and 67G1T elements are suspended in shot 1, the ground time-overcurrent element picks up at 12:44:38.893 hours and starts timing on the U3 curve. The phase time-overcurrent element also picks up at 12:44:38.897 hours and triggers this event. According to (9.1), the operating time of the phase and ground time-overcurrent elements are 0.316 and 0.203 secs, respectively. As a result, 51GT asserts before 51P has a chance to time out and issues a trip signal to the circuit breaker. Because the SEL relay records only 16 cycles of waveform data, the opening of the circuit breaker is not shown.

By the time the SEL-351R relay starts recording Event 2 at 12:59:41.476 hours,

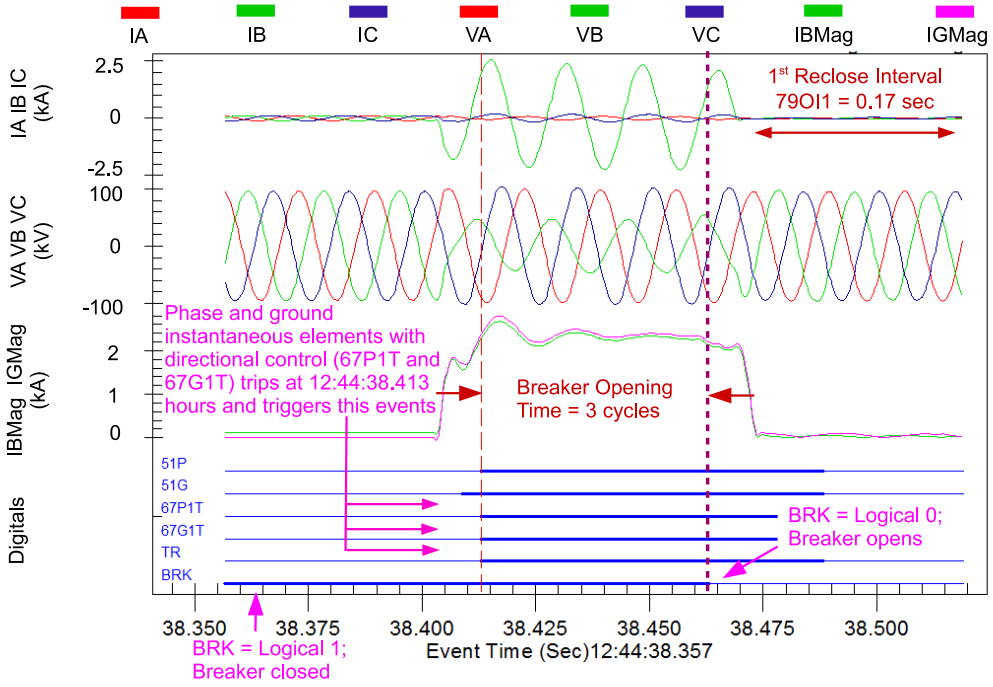

Figure 9.22: Event 4 voltage and current waveforms at shot = 0.

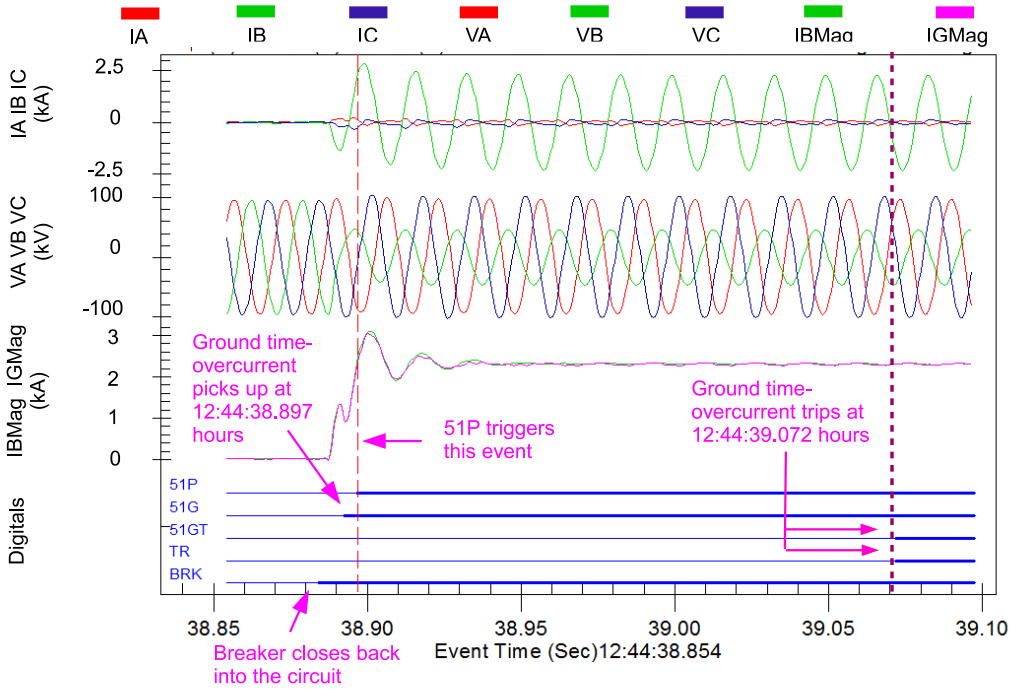

Figure 9.23: Event 3 voltage and current waveforms at shot = 1.

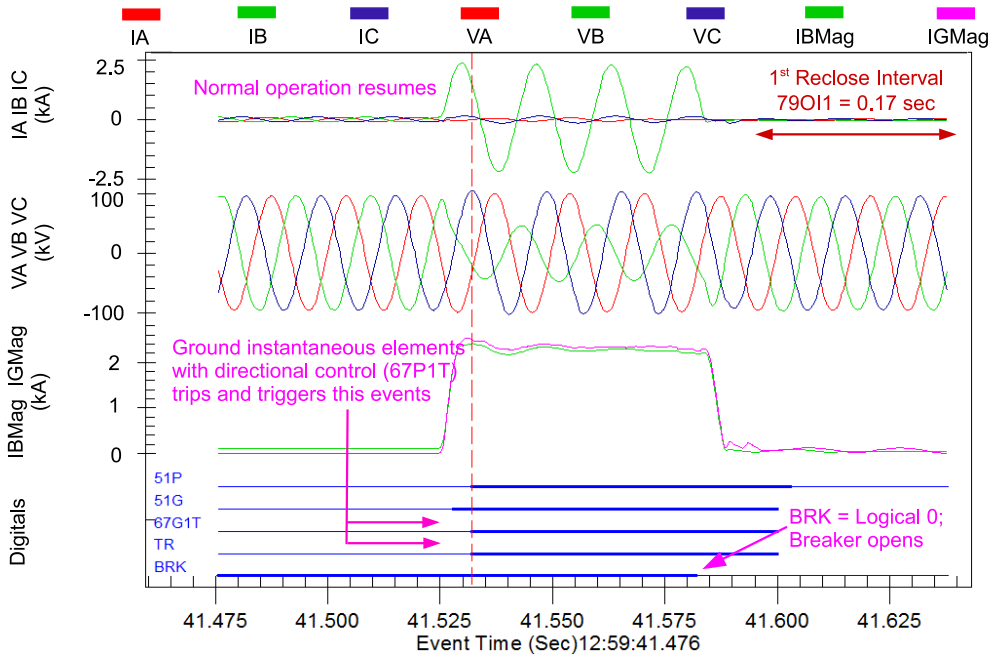

Figure 9.24: Event 2 voltage and current waveforms at shot = 0.

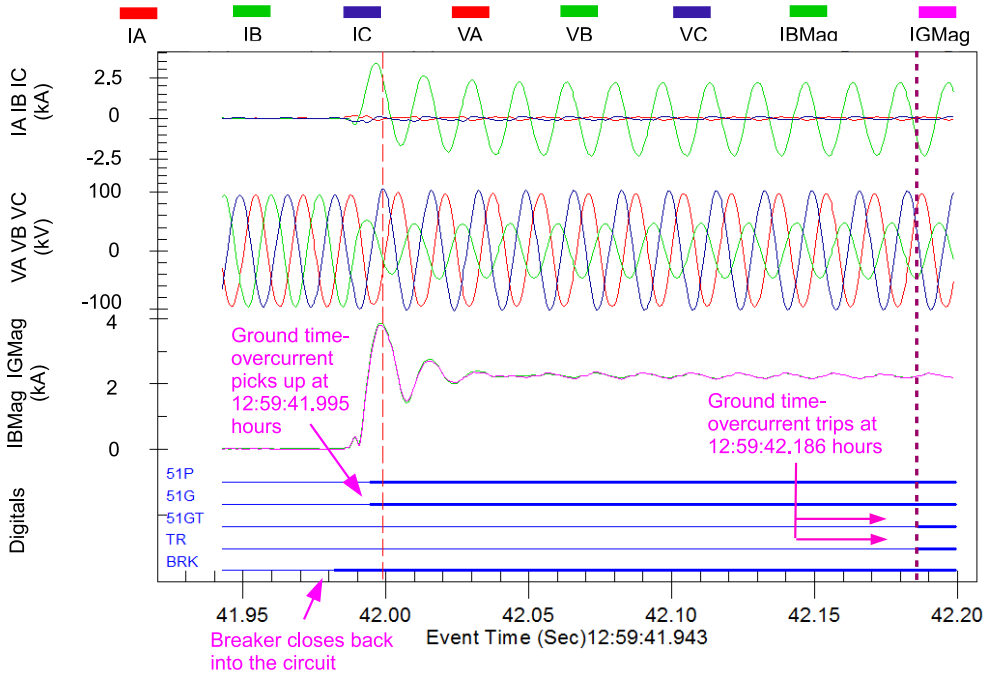

Figure 9.25: Event 1 voltage and current waveforms at shot = 1.

the circuit breaker has already closed back into the circuit. The fault has cleared and the phase B current has returned back to normal load current levels as shown in Fig. 9.24. The relay has also reset itself since the fault was absent from the transmission network for more than 900 cycles. Unfortunately, the fault reappears on phase B at 12:59:41.526 hours. Element 67G1T asserts immediately and trips the circuit breaker. The relay starts timing on the first open interval, 79OI1.

When 79OI1 times out, the circuit breaker closes back into the circuit, and the shot counter increases to 1. The fault, however, persists, and the relay measures a phase and a ground current of 3380 A and 3340 A, respectively. Since the operation of the 67P1T and 67G1T elements are suspended for shot 1, both the phase and the ground time-overcurrent elements pick up at 12:59:41.995 hours and start timing on the U3 curve. The more sensitive ground time-overcurrent, 51GT, times out before its phase counterpart, 51PT, and trips the circuit breaker at 12:59:42.186 hours. No other event reports are available. Therefore, it is not clear whether this shot of the relay removed the fault or whether the relay eventually locked out to isolate the permanent fault.

9.4.4 Relay Performance Assessment

The Section aims to assess the performance of the SEL-351R relay and to determine whether relay operating times are within set time limits. The goal is to compare the expected time of operation with the actual relay operating time.

(a) Assessment of Trip Time during Shot 1 in Event 3

During this shot, the relay measures a ground fault current magnitude of 2811 A primary (2811/CTR = 23.43 A secondary). The actual operating time is the time difference between assertion of 51GP at 12:44:38.893 hours and assertion of 51GT at 12:44:39.072 hours, and is calculated to be 0.179 secs.

Pickup Range:	0.50–16.00 A, 0.01 A steps (5 A nominal) 0.10–3.20 A, 0.01 A steps (1 A nominal) 0.005–0.160 A, 0.001 A steps (0.05 A nominal channel IN current input)
Steady-State Pickup Accuracy:	±0.05 A and ±3% of setting (5 A nominal) ±0.01 A and ±3% of setting (1 A nominal)
Curve Timing Accuracy:	±1.50 cycles and ±4% of curve time for current between 2 and 30 multiples of pickup

Figure 9.26: Functional specifications of the SEL-351R relay [10].

Next, when calculating the expected operating time of the relay, the functional specifications of the relay must be taken into consideration. According to Fig. 9.26, 51G has a pickup accuracy of $\pm 3\%$ of setting ± 0.05 A. Therefore, for a pickup setting of 2.40 A secondary, the pickup accuracy equals ± 0.12 A. This means that when the actual fault current is 23.43 A secondary, 51GT can assert when the current is between 23.31 A and 23.55 A secondary (23.43 ± 0.12 A).

Suppose the relay picks up at 23.31 A secondary ($M = 9.71$). Using (9.1), the operating time of the relay is 0.204 secs. As per Fig. 9.26, 51G has a curve timing accuracy of $\pm 4\%$ of the operating time and ± 1.5 cycles. For an operate time of 0.204 secs, the curve timing accuracy equals 0.0332 secs ($4\% \times 0.204 \pm 0.025$ secs). Therefore, the relay is expected to operate within 0.1708 and 0.2372 secs ($t_1 = 0.204 \pm 0.0332$ secs).

Alternatively, suppose the relay picks up when the fault current is 23.55 A secondary ($M = 9.81$). From (9.1), the operating time of the relay is solved to be 0.203 secs. The curve timing accuracy for this operate time is calculated to be 0.0331 secs ($4\% \times 0.203 \pm 0.025$ secs). Therefore, the relay will operate within 0.1699 and 0.2361 secs ($t_2 = 0.203 \pm 0.0331$ secs).

The final time window, t_{final}, that accounts for both pickup and curve timing accuracy can be calculated as $\text{Min}(t_2) < t_{final} < \text{Max}(t_1)$ or $0.1699 < t_{final} < 0.2372$ secs.

The actual trip time of 0.179 secs falls within the expected window of operation, thereby validating the relay first shot.

(b) Assessment of Trip Time during Shot 1 in Event 1

During shot 1 in Event 1, the relay measures a ground fault current magnitude of 3340 A primary (3340/CTR = 27.83 A secondary). Following the procedure outlined in the previous section, the relay is expected to operate within 0.1528 and 0.2184 secs. From Fig. 9.25, 51GP asserts at 12:59:41.995 hours while 51GT asserts at 12:59:42.186 hours. Therefore, the actual operating time of 0.191 secs lies within the expected window of operation and hence, the relay performs as expected.

9.4.5 Fault Location

Distance to the fault was computed by applying one-ended fault location algorithms such as the simple reactance, Takagi, and Novosel *et al.* methods to all the four events. Notice that Event 4 and Event 2 are short-duration faults with a significant DC offset. Therefore, the third cycle after fault inception was chosen to compute the fault current phasors and minimize any error due to DC offset. Results tabulated in Table 9.11 indicate that the fault location estimates from the one-ended algorithms are in good agreement with those estimated by the SEL 351-R relay and are close to the actual fault location.

Table 9.11: Case Study 4 Location Estimates from One-ended Methods

Event	Actual Location (mi)	SEL-351R Estimate (mi)	Estimated Location (mi)		
			Simple Reactance	Takagi	Novosel *et al.*
4	14.37	14.08	14.18	14.20	14.17
3		14.18	14.08	14.07	14.07
2		14.43	14.45	14.46	14.45
1		14.65	14.65	14.63	14.62

Table 9.12: Estimated Values of Fault Resistance in Case Study 4

Event	Fault Resistance (Ω)
4	0.02
3	0.06
2	0.90
1	1.70

9.4.6 Fault Resistance Estimation

Using voltage and current waveforms from one end of the line and the known fault location, Approach 1 described in Section 8.4 was used to estimate the fault resistance. As seen from Table 9.12, the fault resistance is expected to lie between 0.02 and 1.7 Ω.

9.4.7 Thevenin Impedance Estimation

Since Events 4 through 1 describe an unbalanced fault with a return path to the ground, the waveforms captured in those events can be used to estimate the positive-, negative-, and zero-sequence Thevenin impedances upstream from the SEL-351R relay. The estimated Thevenin impedances were then compared with the circuit model in CAPE to gauge the accuracy of estimation. As seen in Table 9.13 and Table 9.14, the reactance component of the Thevenin impedances are a good fit with those obtained

from the circuit model. The resistive component, on the other hand, absorbs the error and hence, show greater variations.

9.4.8 Zero-sequence Line Impedance Validation

Since the fault described in Events 4 through 1 involve a return path through the ground, it is possible to use the event data captured by the SEL-351R relay to verify the zero-sequence line impedance. Because data from only one end of the line is available, Approach 1 described in Section 8.2 was used and the results are shown in Table 9.15. The magnitude and phase angle errors were calculated using (8.14). From Table 9.15, it can be concluded that the estimated zero-sequence line impedance matched well with that used as relay setting.

9.4.9 Short-circuit Model Verification

Event reports captured by the SEL 351-R recloser can be used to confirm the accuracy of the circuit model in CAPE. As described in Section 8.6, the approach is to replicate the actual fault in the circuit model and compare the resulting short-circuit current with actual field measurements. As an example, Event 1 was recreated by simulating a B-G fault in the CAPE circuit model at the known location of the fault, i.e., 14.37 miles from the substation as shown in Fig. 9.18. The fault resistance estimated in Table 9.12, $R_F = 0.02\,\Omega$, was used. Comparison between the short-circuit current in CAPE and the fault current measured by the SEL relay in Event 1 is shown in Fig. 9.27. The currents match well once the DC offset decays out after the third cycle. Comparison between short-circuit currents in CAPE and SEL relay measurements for all the remaining events are presented in Table 9.16. Results indicate that the circuit model in CAPE is representative of the actual transmission network.

Table 9.13: Actual vs. Estimated Positive- and Negative-sequence Thevenin Impedances

Event	Positive-sequence Impedance (Ω)		Negative-sequence Impedance (Ω)	
	Circuit Model	Estimated	Circuit Model	Estimated
4	$2.82 + j17.90$	$3.62 + j17.35$	$2.91 + j18.03$	$2.94 + j17.09$
3		$1.90 + j18.36$		$3.18 + j16.84$
2		$4.12 + j17.31$		$3.13 + j17.08$
1		$1.43 + j18.77$		$3.71 + j17.11$

Table 9.14: Actual vs. Estimated Zero-sequence Thevenin Impedance

Event	Zero-sequence Thevenin Impedance (Ω)	
	Circuit Model	Estimated
4	$5.29 + j30.72$	$4.88 + j29.75$
3		$5.20 + j29.59$
2		$5.17 + j29.70$
1		$5.89 + j29.78$

Table 9.15: Setting vs. Estimated Zero-sequence Line Impedance

Event	Zero-sequence Line Impedance (Ω)		Error	
	Relay Setting	Estimated	Magnitude (%)	Phase Angle (degrees)
4	$19.72+j56.22$	$24.06+j55.03$	0.79	4.29
3		$23.60+j54.30$	0.63	4.16
2		$21.84+j56.75$	2.05	1.72
1		$26.12+j57.37$	5.79	5.15

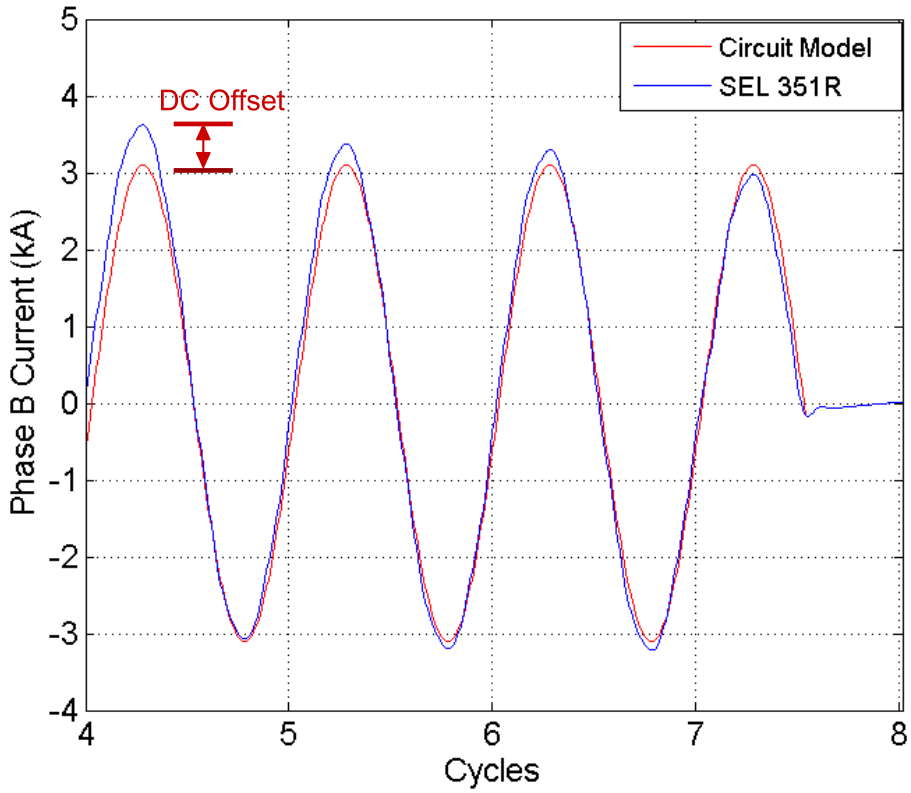

Figure 9.27: Fault current in the circuit model matches well with that measured by the SEL-351R relay in Event 1.

Table 9.16: Short-circuit Current in CAPE vs. Actual Measurements from SEL-351R

Event	Actual Location (mi)	Estimated Location (mi)	Fault Current (kA)	
			SEL-351R	CAPE
1	14.37	14.18	2.36	2.19
2		14.08	2.30	2.19
3		14.45	2.34	2.18
4		14.65	2.33	2.17

9.4.10 Lessons Learned

Analysis of this event successfully reconstruct the sequence of events and verifies the performance of the relay. In addition, the fault data was used to validate the zero-sequence line impedance setting in the SEL-351R relay. Furthermore, the fault event data was used to estimate the fault resistance and confirm that the circuit model is representative of the actual transmission network.

9.5 Case Study 5: Lightning Strike on a 161-kV Transmission Line Reveals Incorrect CT Polarity and Missing Phase CT

On 21 January 2012, a 161-kV transmission line experienced a three-phase fault due to a lightning strike at 5.86 miles from Station 1 or 17.53 miles from Station 2 as shown in Fig. 9.28. The transmission line is 23.39 miles long and has a positive- and zero-sequence impedance of $Z_{L1} = 2.85 + j18.22\ \Omega$ and $Z_{L0} = 16.80 + j60.89\ \Omega$, respectively. A digital fault recorder at Station 1 captures the voltage and current waveforms at 100 samples per cycle as shown in Fig. 9.29. Notice that the phase A current waveform is missing. The prefault current at Station 1 is 150 A while the fault current is 11 kA. The three-phase voltage and current waveforms at Station 2 are recorded by a DFR having a sampling rate of 96 samples per cycle and are shown in Fig. 9.30. The prefault current is 200 A while the fault current magnitude is 3.6 kA.

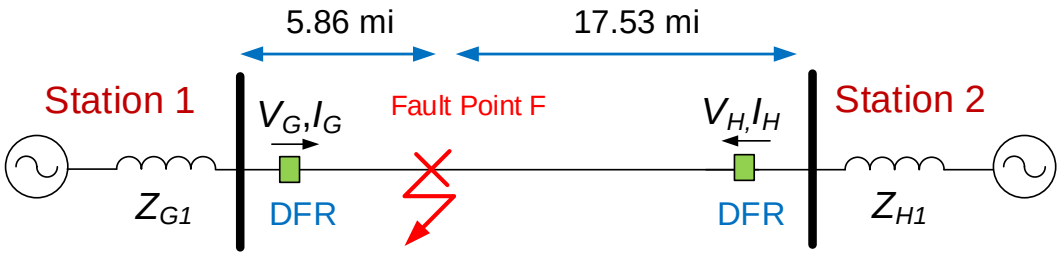

Figure 9.28: Case study 5 is a ABC fault at 5.86 miles from Station 1 or 17.53 miles from Station 2.

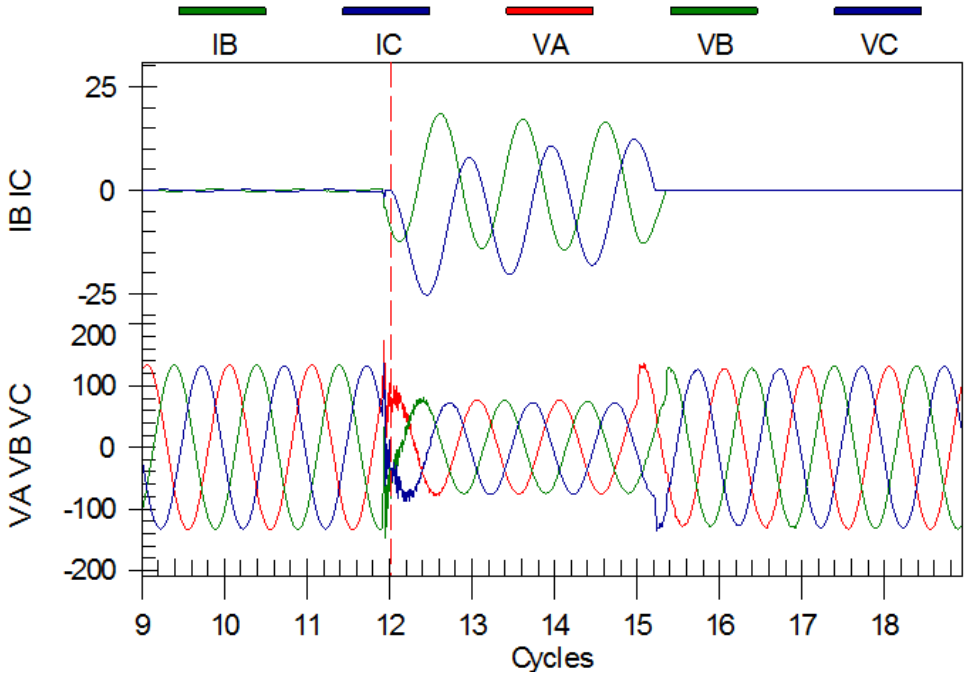

Figure 9.29: Case study 5 voltage and current waveforms at Station 1. Phase A current is missing.

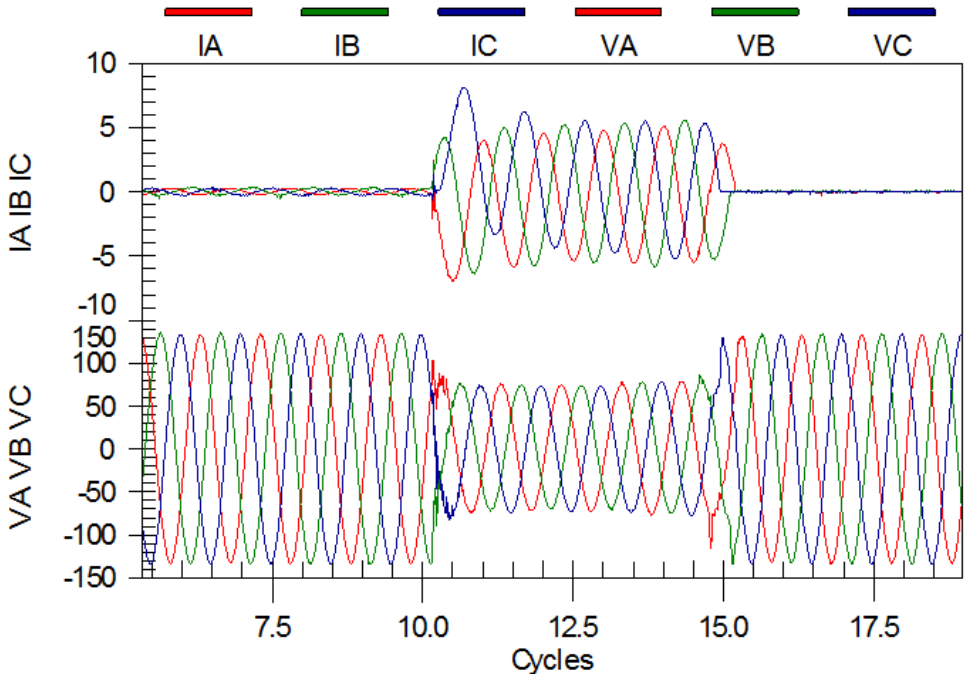

Figure 9.30: Case study 5 voltage and current waveforms at Station 2.

9.5.1 Fault Location

When one-ended fault-locating algorithms are applied to Station 1 data, distance-to-fault estimates are close to the actual location of the fault as seen in Table 9.17. Estimates from one-ended algorithms applied to Station 2 data are also close to the actual fault location. However, it is puzzling to observe that the distance estimates are negative. Most likely, the CT has been installed with a reverse polarity and hence, measures current in a direction opposite to the fault as illustrated in Fig. 9.31. The reverse CT polarity is further evident if one looks closely at the positive- and negative peak of the voltage and current waveforms recorded at Station 2. As shown in Fig. 9.30, when current in a particular phase has a positive peak, the corresponding voltage has a negative peak, i.e., a 180-degree phase shift. Therefore, the negative location estimate can be interpreted as 17.80 miles upstream with respect to the Station 2 DFR direction shown in Fig. 9.31. It is also interesting to observe that the DFR at Station 2 underestimated the fault location by a mile. It is possible that the incorrect CT polarity or inaccurate line parameters contributed to the fault location error.

Table 9.17: Location Estimates from One-ended Methods

Station	Actual Location (mi)	DFR Estimate (mi)	Estimated Location (mi)		
			Simple Reactance	Takagi	Eriksson
1	5.86	5.90	5.96	5.96	5.96
2	17.53	16.60	-17.70	-17.80	-17.60

Because the sampling rate of the DFRs at Station 1 and Station 2 are not equal, the unsynchronized two-ended method described in Section 2.2.2 was chosen to estimate the fault location. The missing phase A current at Station 1 did not allow for the

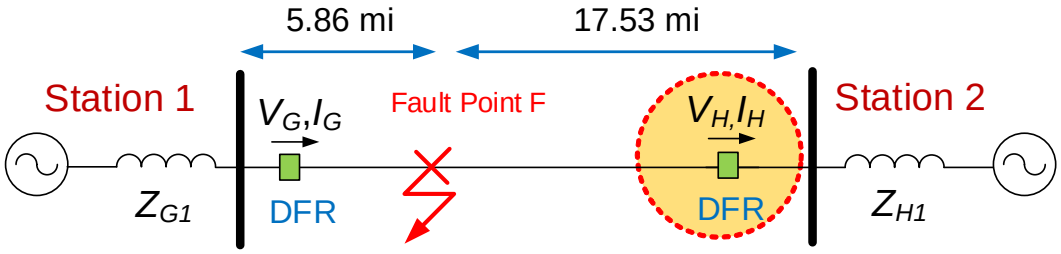

Figure 9.31: Negative distance estimate from Station 2 indicates that the meter direction is reversed.

calculation of sequence components. However, since the event is a balanced three-phase fault, it was possible to use phase components instead of symmetrical components. The reverse polarity of the CT at Station 2 was also taken into account. As seen from Table 9.18, the location estimate from the two-ended method is close to the actual fault location.

Table 9.18: Case Study 5 Location Estimate from Two-ended Methods

Station	Actual Location (mi)	Estimated Location (mi)
1 and 2	5.86	5.71

9.5.2 Fault Resistance Estimation

Voltage and current waveforms at both ends of the line were used in (8.40) to estimate the fault resistance as 0.26 Ω. The accuracy of the estimated fault resistance can be ascertained from the fact that the simple reactance method in Table 9.17 did not suffer from a reactance error due to load current. The absence of the reactance error suggests that the fault resistance in this event is indeed negligible.

9.5.3 Thevenin Impedance Estimation

Since Event 4 is a balanced three-phase fault, only the positive-sequence Thevenin impedance could be estimated from the fault data as shown in Table 9.19. Results indicate that Station 2 is electrically weaker than Station 1. Although the circuit model is not available, judging from the fault currents contributed by each station, impedance estimates are likely to be accurate.

Table 9.19: Estimated Positive-sequence Source Impedances

Station	Source Impedance (Ω)
1	$0.46 + j3.66$
2	$2.25 + j11.38$

9.5.4 Lessons Learned

Analysis of fault data can reveal incorrect setup of power system equipment or incorrect field wiring that was missed during field commissioning tests. Results of the analysis can be used to take corrective action and avoid future misoperations. For example, this event shows that the CT at Station 2 was installed with an incorrect polarity. As a result, the direction of the current was reversed and can affect the reliability and performance of directional relays. Furthermore, the phase A current at Station 1 was missing. It is possible that the phase CT has not been connected to the DFR and can result in loss of valuable information. The fault was observed to have encountered the least resistance path to the ground, which coincides with the root cause of the fault. Finally, Station 2 was learned to be electrically weaker than Station 1.

9.6 Summary

In summary, this Chapter uses field data collected from utility transmission and distribution networks to demonstrate the following benefits of analyzing fault data:

- *Assess the Relay and Circuit Breaker Performance*

  Intelligent electronic devices record what they "see" during a fault in the form of an event report. These reports can be used to assess the performance of relays and circuit breakers as demonstrated in Case Study 4.

- *Validate the Line Impedance*

  Event reports are a valuable resource for validating the line impedance settings in relays. For example, Case Study 2 and Case Study 4 illustrates how a single or double line-to-ground fault event can be used to validate the zero-sequence impedance of a transmission line. Case Study 1, on the other hand, reveals a possible inaccuracy in the positive-sequence line impedance.

- *Estimate the Fault Resistance*

  Fault data captured at one or both ends of the line can be used to estimate the fault resistance. Interpretation of this value is useful in determining the root cause of the fault. Knowing the fault resistance value also plays a significant role when verifying the accuracy of the circuit model as demonstrated in Case Study 4.

- *Estimate the Thevenin Impedances*

  Estimating the Thevenin impedance during a fault provides valuable feedback about the state of the transmission network upstream from the monitoring location. Case study 2 is an excellent example. During the fault, which lasts for 34.5 cycles, the estimated Thevenin impedances were shown to decrease suddenly. This change suggests that several critical loads upstream from the monitoring location must have tripped offline during this long event.

- *Confirm the Accuracy of the System Circuit Model*

  Another application of analyzing fault data lies in verifying the accuracy of the circuit model as established in Case Study 4.

- *Detect Incorrect Installation of Power System Equipment*

  Analysis of fault data can reveal incorrect setup of power system equipment or incorrect field wiring that was missed during field commissioning tests. Results of the analysis can be used to take corrective action and avoid future misoperations. For example, Case Study 5 detects a CT with incorrect polarity and a digital fault recorder with a missing measurement channel.

Chapter 10

Conclusion

The overall objective of this dissertation is to describe the theory of impedance-based fault location algorithms, identify the sources of fault location error, propose solutions to overcome those error sources, and share lessons learned from analyzing intelligent electronic device data. The goals are to reduce system downtime, prevent protection system misoperations, and improve power quality.

To achieve the above objective, Chapters 2 and 3 present the theory of one- and two-ended impedance-based fault location algorithms and identify their strengths and weaknesses. The simple reactance method is the most straightforward of all fault location algorithms. The accuracy of this method, however, deteriorates due to fault resistance, load current, and remote infeed in a non-homogeneous system. Subsequent fault-locating algorithms address the above sources of error. For example, the Takagi method is robust to load but sensitive to remote infeed. The modified Takagi and Eriksson methods use source impedance parameters to eliminate the fault location error caused by load and remote infeed. Additional sources of error that compromise the accuracy of one-ended algorithms in locating single line-to-ground faults are mutual coupling in double-circuit transmission lines and an uncertain value of zero-sequence line impedance. Two-ended fault-locating algorithms use measurements from both ends of a transmission line to overcome the short-comings of one-ended methods and are an attractive solution for tracking down the exact location of a fault. Unfortunately, measurements captured at the remote end of the line are not always available. Furthermore, both one- and two-ended algorithms require the input of voltage and current phasors to estimate the

distance to a fault. Due to operational constraints or equipment malfunction, voltage measurements may not be available. To perform fault location even in the absence of voltage measurements, Chapter 4 develops current-only fault location algorithms. The discussion so far suggests that data availability is a key criteria in selecting the best approach for fault location.

Another key criteria in selecting the best approach for fault location is the application scenario. As an example, Chapter 3 demonstrates that two-ended algorithms are not suited to locate faults in three-terminal lines. In contrast, one-ended fault locating algorithms applied from one of the three terminals pinpoints the exact location of the fault. Two-ended fault location algorithms fail not because of limitations in the algorithms but because it was not meant for use in a three-terminal line. Moreover, one-ended algorithms designed for application to a distribution feeder assume a radial feeder where the power flows unidirectionally from the substation to the end users. With increased penetration of distributed generators to the grid, this assumption is violated. Distributed generators also contribute to the fault and adversely affect the accuracy of impedance-based algorithms as illustrated in Chapter 5. In such scenarios, improved algorithms developed in Chapter 6 that account for the fault current contribution from distributed generators in the fault location computation must be applied. From this discussion, it is evident that system operators need to be aware of the application scenario, identify possible error sources, and then choose the algorithm most robust to those error sources.

Therefore, based on the analysis conducted in this dissertation, the following criteria are recommended for selecting the most suitable fault location algorithm: (a) data availability, and (b) fault location application scenario. This is illustrated in Fig. 10.1. The fault location suite provides the user with several choices, including one- and two-ended impedance-based fault location algorithms, current-only fault location algorithms, and fault location algorithms that account for distributed generation. Depending on

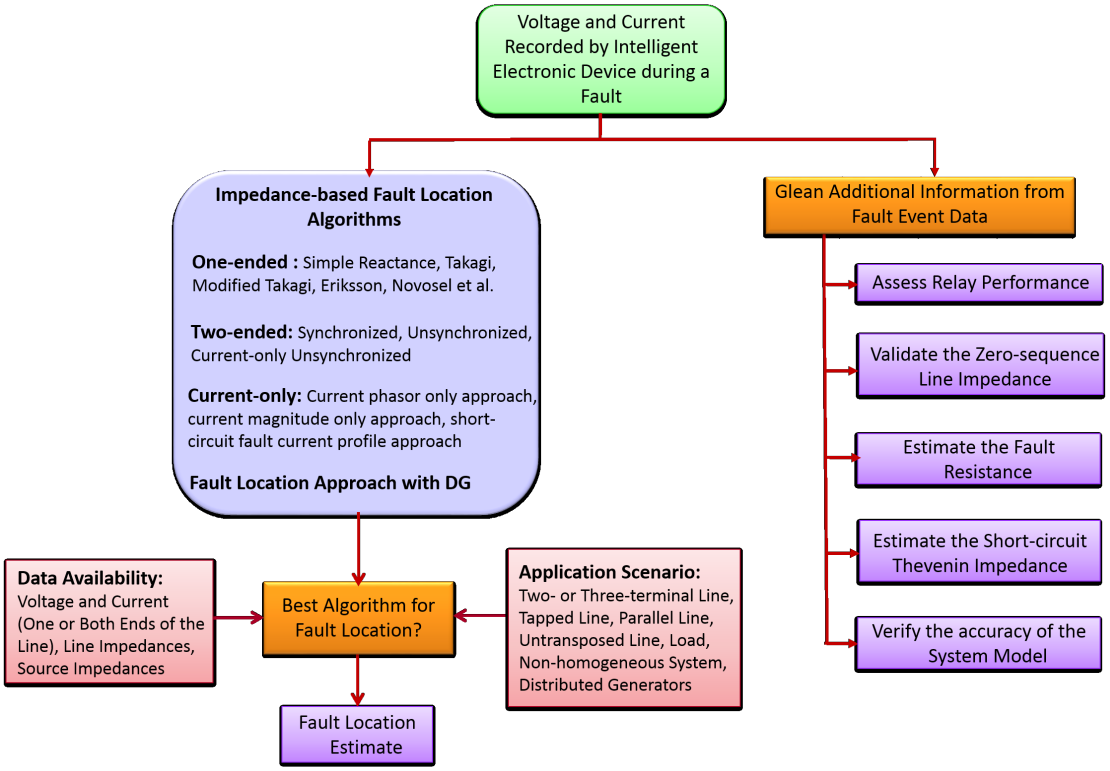

Figure 10.1: Graphical illustration of the objectives of this dissertation.

data availability and the application scenario, the user can apply the best fault-locating approach to the intelligent electronic device (IED) data and determine the location to a fault. The same IED data can be used for other applications that improve power system reliability as described in Chapters 8 and 9. Potential applications include assessing relay performance, evaluating the performance of circuit breakers, validating the zero-sequence impedance of multi-terminal transmission lines, estimating the fault resistance, tracking the response of the upstream transmission network, and confirming the accuracy of the system model.

Key Technical Contributions:

- Provided a comprehensive theory of one- and two-ended impedance-based fault location algorithms, identified the input data requirement and the strengths and

weaknesses of each algorithm.

- Recommended the following criteria for choosing the most suitable fault location algorithm: data availability and application scenario.

- Developed current-only fault location algorithms that use either the fault current magnitude or the fault current phasor to estimate the distance to a fault.

- Demonstrated the adverse impact of distributed generators on impedance-based fault location algorithms.

- Proposed an algorithm that improves fault location accuracy in the presence of distributed generators.

- Modeled a high-resolution time-domain model of a fixed-speed wind turbine that includes a detailed representation of tower shadow and wind shear components.

- Verified the suitability of using the IEC 60909-0 Standard in calculating protective device settings in networks interconnected with distributed generation.

- Proposed algorithms to validate the zero-sequence impedance of two- and three-terminal transmission lines using unsynchronized measurements.

- Demonstrated the potential of intelligent electronic data in assessing relay performance, estimating the fault resistance and identifying the root cause of a fault, tracking the response of the upstream transmission network, and confirming the accuracy of the system circuit model.

Appendix

Appendix A

Line Constant Calculation

Positive- and zero-sequence line impedances play a critical role when computing the distance to a fault. This Chapter explains how to solve for line constants from the arrangement of phase and neutral conductors, and conductor data.

A.1 Self and Mutual Line Impedance

The following three models are commonly used to calculate the self and mutual impedances of an overhead line:

A.1.1 Full Carson's Model

The Full Carson's model assumes the earth to be an infinite, homogeneous solid with a constant resistivity. A method of images is used wherein every conductor above the ground has a fictitious image conductor at the same distance below the ground as illustrated in Fig. A.1. The self and mutual impedances of the line, Z_{ii} and Z_{ik}, are given by [3, 82]

$$\begin{aligned} Z_{ii} &= R_{Ci} + 4\omega PG + j\left[2\omega G\ln(\frac{r_i}{GMR_i}) + 2\omega G\ln(\frac{2h_i}{r_i}) + 4\omega QG\right]\ \Omega/\text{mi} \\ Z_{ik} &= 4\omega PG + j\left[2\omega G\ln(\frac{D_{ik}}{d_{ik}}) + 4\omega QG\right]\ \Omega/\text{mi} \end{aligned} \tag{A.1}$$

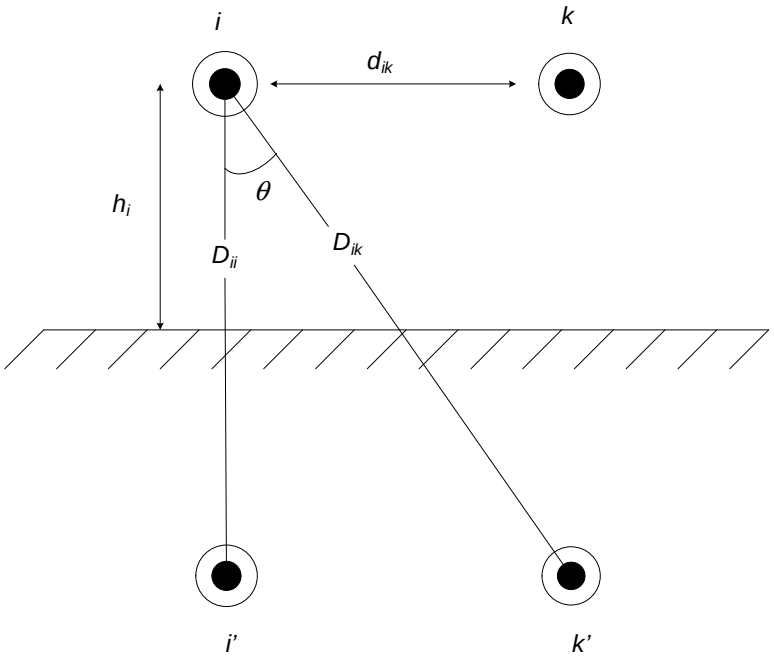

Figure A.1: Conductors and their images in Carson's model.

where P and Q are complex correction factors defined as

$$P = \frac{\pi}{8} - \frac{1}{3\sqrt{2}}k\cos\theta + \frac{k^2}{16}\cos 2\theta\left(0.6728 + \ln\frac{2}{k}\right) + \frac{k^2}{16}\theta\sin 2\theta + \frac{k^3\cos 3\theta}{45\sqrt{2}} - \frac{\pi k^4\cos 4\theta}{1536}$$

$$Q = -0.0386 + \frac{1}{2}\ln\frac{2}{k} + \frac{1}{3\sqrt{2}}k\cos\theta - \frac{\pi k^2\cos 2\theta}{64} + \frac{k^3\cos 3\theta}{45\sqrt{2}} - \frac{k^4}{384}\theta\sin 4\theta \qquad (A.2)$$

$$- \frac{k^4}{384}\cos 4\theta\left(1.0895 + \ln\frac{2}{k}\right) .$$

Constants k and θ in (A.2) can be calculated as

$$\left.\begin{array}{l} k = 1.713\times 10^{-3} h_i\sqrt{\dfrac{f}{\rho}} \\ \\ \theta = 0 \end{array}\right\} \text{for self-impedance}$$

$$\left.\begin{aligned} k &= 0.8565 \times 10^{-3} D_{ik} \sqrt{\frac{f}{\rho}} \\ \theta &= \cos^{-1}\left(\frac{h_i + h_k}{D_{ik}}\right) \end{aligned}\right\} \text{for mutual impedance.}$$

Notations used in the above equations are defined as follows:

Z_{ii}	Self-impedance of conductor i (Ω/mi)
Z_{ik}	Mutual impedance between conductors i and k (Ω/mi)
R_{Ci}	Internal resistance of conductor i (Ω/mi)
ω	System angular frequency (rad/s)
f	System frequency (Hz)
G	Constant = 0.1609347×10^{-3}(Ω/mi)
r_i	Radius of conductor i (ft)
GMR_i	Geometric mean radius of conductor i (ft)
ρ	Earth resistivity (Ω/m)
d_{ik}	Distance between conductors i and k (ft)
D_{ik}	Distance between conductor i and image k' (ft)
D_{ii}	Distance between conductor i and its own image i' (ft)
h_i	Height of conductor i above the ground (ft)
h_k	Height of conductor k above the ground (ft)
θ	Angle between D_{ii} and D_{ik}

A.1.2 Modified Carson's Model

The modified Carson's model, popularly used for power frequency calculations, approximates the full Carson's model by retaining only the first term of correction factor

P and the first two terms of correction factor Q. As a result, the calculation of self and mutual impedance terms simplify down to [3, 82]

$$\begin{aligned} Z_{ii} &= R_{Ci} + 0.00159f + j0.004657f \log_{10}\left(\frac{2160\sqrt{\frac{\rho}{f}}}{GMR_i}\right) \Omega/\text{mi} \\ Z_{ik} &= 0.00159f + j0.004657f \log_{10}\left(\frac{2160\sqrt{\frac{\rho}{f}}}{d_{ik}}\right) \Omega/\text{mi} \ . \end{aligned} \tag{A.3}$$

A.1.3 Deri Model

Equations proposed by Dubanton and implemented by Deri use simple expressions to calculate the line impedances which are valid over a wide frequency range. The earth is replaced by a superconducting earth current return plane located at a complex depth p below the ground. Self and mutual line impedances are given as [82, 83]:

$$\begin{aligned} Z_{ii} &= R_{Ci} + j\omega\frac{\mu_0}{2\pi}\ln\left(\frac{2h_i + 2p}{r_i}\right) \Omega/\text{mi} \\ Z_{ik} &= j\omega\frac{\mu_0}{2\pi}\ln\left(\frac{\sqrt{(h_i + h_k + 2p)^2 + d_{ik}^2}}{\sqrt{(h_i - h_k)^2 + d_{ik}^2}}\right) \Omega/\text{mi} \ . \end{aligned} \tag{A.4}$$

The complex penetration depth p in (A.4) can be calculated as

$$p = \frac{3.28084}{\sqrt{j\omega\mu_0\sigma}} \ . \tag{A.5}$$

where μ_0 is the permeability of free space ($4\pi \times 10^{-7}$ H/m) and σ is the earth conductivity in units of S/m.

A.2 Phase Impedance Matrix

After using one of the three earth return models in Section A.1 to calculate the self and mutual line impedances, construct a primitive impedance matrix, $Z_{primitive}$, of size $N \times N$, where N is the total number of phase and neutral conductors. For example, $Z_{primitive}$ for a three-phase four wire system shown in Fig. A.2 can be written as [3]

$$Z_{primitive} = \left[\begin{array}{ccc|c} Z_{aa} & Z_{ab} & Z_{ac} & Z_{an} \\ Z_{ba} & Z_{bb} & Z_{bc} & Z_{bn} \\ Z_{ca} & Z_{cb} & Z_{cc} & Z_{cn} \\ \hline Z_{na} & Z_{nb} & Z_{nc} & Z_{nn} \end{array}\right] \quad \Omega/\text{mi}$$

Here a, b, and c are phase conductors, and n is the neutral conductor. Denoting phase and neutral conductors by subscripts p and n, respectively, $Z_{primitive}$ can be partitioned as

$$Z_{primitive} = \left[\begin{array}{cc} [Z_{pp}] & [Z_{pn}] \\ [Z_{np}] & [Z_{nn}] \end{array}\right] \quad \Omega/\text{mi}$$

To eliminate the neutral conductor, apply Kirchhoff's circuit law to write the voltage drop across the feeder in Fig. A.2 as

$$\left[\begin{array}{c} [V_{abcg}] \\ [V_{ng}] \end{array}\right] = \left[\begin{array}{c} [V'_{abcg}] \\ [V'_{ng}] \end{array}\right] - \left[\begin{array}{cc} [Z_{pp}] & [Z_{pn}] \\ [Z_{np}] & [Z_{nn}] \end{array}\right] \times \left[\begin{array}{c} [I_{abc}] \\ [I_n] \end{array}\right] \tag{A.6}$$

where V_{ig} is the voltage between conductor i and the ground at one end of the line, V'_{ig} is the voltage between conductor i and the ground at the other end of the line, and I_i

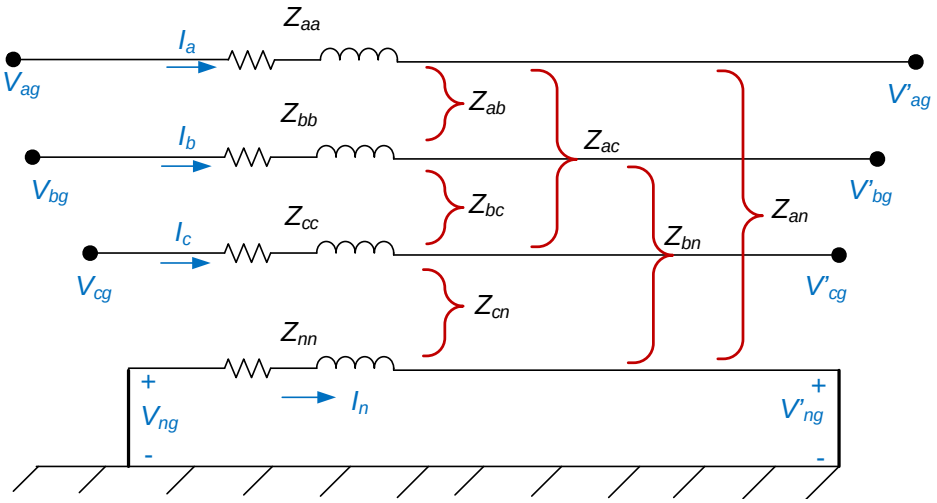

Figure A.2: Kron reduction assumes a perfectly grounded neutral [3].

is the current through conductor i. If the neutral is assumed to be perfectly grounded to the earth, V_{ng} and $V_{ng}^{'}$ can be set to zero. As a result, (A.6) can be rearranged and simplified to obtain a phase impedance matrix, Z_{abc}, of size $M \times M$, where M is the total number of phase conductors as:

$$[Z_{abc}] = [Z_{pp}] - [Z_{pn}][Z_{nn}]^{-1}[Z_{np}] \quad \Omega/\text{mi} \tag{A.7}$$

This process of eliminating the neutral conductor is known as Kron reduction.

A.3 Positive- and Zero-sequence Line Impedances

Although the phase impedance matrix calculated in Section (A.2) is the most accurate representation of an overhead feeder, the impedance-based fault location algorithms characterize a feeder in terms of its positive- and zero-sequence components.

Assuming a transposed line, the sequence line impedances can be determined as [3]

$$[Z_{012}] = [T]^{-1} \times [Z_{abc}] \times [T] = \begin{bmatrix} z_{L0} & 0 & 0 \\ 0 & z_{L1} & 0 \\ 0 & 0 & z_{L2} \end{bmatrix} \quad \Omega/\text{mi} \tag{A.8}$$

where z_{L0}, z_{L1}, and z_{L2} are the zero-, positive-, and negative-sequence line impedances, respectively, and T is the symmetrical component transformation matrix defined as

$$[T] = \begin{bmatrix} 1 & 1 & 1 \\ 1 & a^2 & a \\ 1 & a & a^2 \end{bmatrix}; \quad a = 1\angle 120^\circ$$

A.4 Summary

This Chapter describes how to calculate the series impedance of an overhead transmission or distribution feeder using (a) Full Carson's model, (b) Modified Carson's model, and (c) Deri model. All three models differ in how they account for earth current return. Assumptions made when calculating the positive- and zero-sequence line impedances can be summarized as follows:

1. Neutral conductor is perfectly grounded to the earth

2. Line is completely transposed

Bibliography

[1] H. Markiewicz and A. Klajn, "Earthing systems - fundamentals of calculation and design," in *Power Quality Application Guide*. Hertfordshire, U.K.: Copper Development Association, 2003.

[2] *Distributed generation modeling guidelines*, EPRI, Palo Alto, CA.

[3] W. H. Kersting, *Distribution System Modeling and Analysis*, 3rd ed. Boca Raton, FL, USA: CRC Press, 2012.

[4] M. M. Saha, J. J. Izykowski, and E. Rosolowski, *Fault Location on Power Networks*, 1st ed. New York, NY, USA: Springer-Verlag, 2010.

[5] R. E. Fehr. (2004, May) Sequence impedances of transmission lines. [Online]. Available: http://helios.acomp.usf.edu/~fehr/carson.pdf

[6] N. D. Tleis, *Power Systems Modelling and Fault Analysis: Theory and Practice*, 1st ed. Elsevier Ltd., Jan. 2008.

[7] T. A. Short, *Electric Power Distribution Handbook*. Boca Raton, FL, USA: CRC Press, 2004.

[8] *SEL-551 Instruction Manual*, Schweitzer Engineering Laboratories, Washington, Pullman.

[9] W. H. Kersting, "Radial distribution test feeders," in *IEEE Power Eng. Soc. Winter Meeting*, vol. 2, 2001, pp. 908–912.

[10] *SEL-351R Recloser Control Instruction Manual*, Schweitzer Engineering Laboratories, Washington, Pullman, July 2014.

[11] S. Santoso, *Fundamentals of Electric Power Quality*, Spring ed. Scotts Valley, CA, USA: CreateSpace, 2009.

[12] "Cost of power interruptions to electricity consumers in the United States (U.S.)," Environmental Energy Technologies Division, Ernest Orlando Lawrence Berkeley National Laboratory, Feb. 2006. [Online]. Available: http://emp.lbl.gov/sites/all/files/REPORT%20lbnl%20-%2058164.pdf

[13] *IEEE Guide for Determining Fault Location on AC Transmission and Distribution Lines*, IEEE Std. C37.114-2004, 2005, pp. 1-36.

[14] *Distribution fault location: field data and analysis*, EPRI, Palo Alto, CA: 2006. 1012438.

[15] E. O. Schweitzer III, "A review of impedance-based fault locating experience," in *Proc. 14th Annu. Iowa-Nebraska Syst. Protect. Seminar*, Oct. 1990.

[16] K. Zimmerman and D. Costello, "Impedance-based fault location experience," in *Proc. 58th Annu. Conf. Protect. Relay Eng.*, Apr. 2005, pp. 211–226.

[17] T. Takagi, Y. Yamakoshi, M. Yamaura, R. Kondow, and T. Matsushima, "Development of a new type fault locator using the one-terminal voltage and current data," *IEEE Trans. Power App. Syst.*, vol. PAS-101, no. 8, pp. 2892–2898, Aug. 1982.

[18] L. Eriksson, M. M. Saha, and G. D. Rockefeller, "An accurate fault locator with compensation for apparent reactance in the fault resistance resulting from remote-end infeed," *IEEE Trans. Power App. Syst.*, vol. PAS-104, no. 2, pp. 423–436, Feb. 1985.

[19] D. Novosel, D. Hart, Y. Hu, and J. Myllymaki, "System for locating faults and estimating fault resistance in distribution networks with tapped loads," U.S. Patent 5 839 093, Nov. 17, 1998.

[20] E. O. Schweitzer III, "Evaluation and development of transmission line fault-locating techniques which use sinusoidal steady-state information," *Comput. Elect. Eng.*, vol. 10, no. 4, pp. 269–278, 1983.

[21] D. A. Tziouvaras, J. B. Roberts, and G. Benmouyal, "New multi-ended fault location design for two- or three-terminal lines," in *Proc. IEE 7th Int. Conf. Develop. Power Syst. Protect.*, Apr. 2001, pp. 395–398.

[22] "Loss of ac voltage considerations for line protection," Line Protection Subcommittee of the IEEE Power Engineering Society, Power System Relaying Committee. [Online]. Available: http://www.pes-psrc.org/Reports/Loss_of_AC_Voltage_Considerations_for_Line_Protection.pdf

[23] M. Djurić, Z. Radojević, and V. Terzija, "Distance protection and fault location utilizing only phase current phasors," *IEEE Trans. Power Del.*, vol. 13, no. 4, pp. 1020–1026, Oct. 1998.

[24] Y. Liao, "Fault location using sparse current measurements," in *Proc. 39th North American Power Symp. (NAPS)*, Sept. 2007, pp. 1–6.

[25] N. Kang and Y. Liao, "Fault location estimation using current magnitude measurements," in *Proc. IEEE SoutheastCon*, Mar. 2010, pp. 214–217.

[26] C. Orozco-Henao, J. Mora-Florez, and S. Perez-Londono, "A robust method for single phase fault location considering distributed generation and current compensation," in *Proc. 6th IEEE/PES Transmission Distrib. Conf. Expo., Latin America*, Montevideo, Sept. 2012, pp. 1–7.

[27] R. Agrawal and D. Thukaram, "Identification of fault location in power distribution system with distributed generation using support vector machines," in *Proc. IEEE PES Innovative Smart Grid Technologies (ISGT)*, Feb. 2013, pp. 1–6.

[28] S. M. Brahma, "Fault location in power distribution system with penetration of distributed generation," *IEEE Trans. Power Del.*, vol. 26, no. 3, pp. 1545–1553, Jul. 2011.

[29] J. U. N. Nunes and A. S. Bretas, "A impedance-based fault location technique for unbalanced distributed generation systems," in *Proc. IEEE Trondheim PowerTech*, Trondheim, Jun. 2011, pp. 1–7.

[30] J. I. Marvik, "Fault localization in medium voltage distribution networks with distributed generation," Ph.D. dissertation, Norwegian University of Science and Technology, Norway, Jun. 2011.

[31] F. M. Abo-Shady, M. A. Alaam, and A. M. Azmy, "Impedance-based fault location technique for distribution systems in presence of distributed generation," in *Proc. IEEE Int. Conf. Smart Energy Grid Eng. (SEGE)*, Aug. 2013, pp. 1–6.

[32] *International standard for short-circuit currents in three-phase ac systems - Part 0: Calculation of currents*, IEC Std. 60 909-0, 2001.

[33] P. P. Barker and R. W. De Mello, "Determining the impact of distributed generation on power systems: Part 1 - radial distribution systems," in *Proc. IEEE Power Eng. Soc. Summer Meeting*, vol. 3, 2000, pp. 1645–1656.

[34] N. Samaan, R. Zavadil, J. Smith, and J. Conto, "Modeling of wind power plants for short circuit analysis in the transmission network," in *Proc. IEEE/PES Transmission Distrib. Conf. Expo.*, Apr. 2008, pp. 1–7.

[35] T. N. Boutsika and S. A. Papathanassiou, "Short-circuit calculations in networks with distributed generation," *Electr. Power Syst. Res.*, vol. 78, no. 7, pp. 1181–1191, 2008.

[36] D. Dolan and P. Lehn, "Simulation model of wind turbine $3p$ torque oscillations due to wind shear and tower shadow," *IEEE Trans. Energy Convers.*, vol. 21, no. 3, pp. 717–724, Sept. 2006.

[37] T. Kumano, "A short circuit study of a wind farm considering mechanical torque fluctuation," in *Proc. IEEE Power Eng. Soc. General Meeting*, Montreal, Que., 2006, pp. 1–6.

[38] T. Kumano, "Effects of output power fluctuation on short-circuit current of induction-type wind power generators," in *Proc. Electr. Eng. Jpn.*, vol. 166, no. 3, Feb. 2009, pp. 27–36.

[39] D. Costello, "Understanding and analyzing event report information," in *Proc. Minnesota Power Syst. Conf.*, Nov. 2001, pp. 1–52.

[40] K. Zimmerman and R. McDaniel, "Using power system event data to reduce downtime," in *Proc. IEEE Cement Industry Technical Conf. Rec.*, May 2009, pp. 1–15.

[41] D. Costello, "Lessons learned analyzing transmission faults," in *Proc. 61st Annu. Conf. for Protect. Relay Eng.*, Apr. 2008, pp. 410–422.

[42] J. J. Bian, A. D. Slone, and P. J. Tatro, "Protection system misoperation analysis," in *Proc. IEEE Power Energy Soc. General Meeting Conf.*, National Harbor, MD, Jul. 2014, pp. 1–5.

[43] A. Amberg, A. Rangel, and G. Smelich, "Validating transmission line impedances using known event data," in *Proc. 65th Annu. Conf. Protect. Relay Eng.*, Apr. 2012, pp. 269–280.

[44] K. Zimmerman and D. Costello, "Fundamentals and improvements for directional relays," in *Proc. 63rd Annu. Conf. Protect. Relay Eng.*, Mar. 2010, pp. 1–12.

[45] "The complexity of protecting three-terminal transmission lines," System Protection and Control Task Force of the NERC Planning Commitee, Sept. 2006. [Online]. Available: http://www.nerc.com/comm/PC/System%20Protection%20and%20Control%20Subcommittee%20SPCS%20DL/SPCTF-3TerminalLines091906.pdf

[46] V. Núñez, S. Kulkarni, S. Santoso, and M. Joaquim, "Feature analysis and classification methodology for overhead distribution fault events," in *Proc. IEEE Power Energy Soc. General Meeting*, Jul. 2010, pp. 1–8.

[47] *Applications of PSCAD®/EMTDC™*, Manitoba HVDC Research Center Inc., Winnipeg, MB, Canada.

[48] *CAPE User's Programming Language Reference Manual*, Electrocon International Inc., Jun. 1999.

[49] R. C. Dugan, *The Open Distribution System Simulator (OpenDSS) Reference Guide*, Electric Power Research Institute, Palo Alto, CA, Jun. 2013.

[50] "Lessons learned: Short circuit models (relay settings and equipment specifications," North American Electric Reliability Corporation (NERC), Princeton, NJ, May 2010.

[51] S. Das, S. Santoso, A. Gaikwad, and M. Patel, "Impedance-based fault location in transmission networks: theory and application," *IEEE Access*, vol. 2, pp. 537–557, 2014.

[52] S. Das, S. Santoso, R. Horton, and A. Gaikwad, "Effect of earth current return model on transmission line fault location - a case study," in *Proc. IEEE Power Energy Soc. General Meeting*, Jul. 2013, pp. 1–5.

[53] J. Traphöner, S. Das, S. Santoso, and A. Gaikwad, "Impact of grounded shield wire assumption on impedance-based fault location algorithms," in *Proc. IEEE PES General Meeting Conf. Expo.*, Jul. 2014, pp. 1–5.

[54] N. Karnik, S. Das, S. Kulkarni, and S. Santoso, "Effect of load current on fault location estimates of impedance-based methods," in *Proc. IEEE Power Energy Soc. General Meeting*, San Diego, CA, Jul. 2011, pp. 1–6.

[55] S. Kulkarni, N. Karnik, S. Das, and S. Santoso, "Fault location using impedance-based algorithms on non-homogeneous feeders," in *Proc. IEEE Power Energy Soc. General Meeting*, San Diego, CA, Jul. 2011, pp. 1–6.

[56] S. Das, N. Karnik, and S. Santoso, "Distribution fault-locating algorithms using current only," *IEEE Trans. Power Del.*, vol. 27, no. 3, pp. 1144–1153, Jul. 2012.

[57] S. Das, S. Kulkarni, N. Karnik, and S. Santoso, "Distribution fault location using short-circuit fault current profile approach," in *Proc. IEEE Power Energy Soc. General Meeting*, San Diego, CA, Jul. 2011, pp. 1–7.

[58] S. Das, S. Santoso, and A. Maitra, "Effects of distributed generators on impedance-based fault location algorithms," in *Proc. IEEE PES General Meeting Conf. Expo.*, Jul. 2014, pp. 1–5.

[59] S. Das, N. Karnik, and S. Santoso, "Time-domain modeling of tower shadow and wind shear in wind turbines," *ISRN Renewable Energy*, vol. 2011, no. 890582, Jul. 2011.

[60] S. Das and S. Santoso, "Effect of wind speed variation on the short-circuit contribution of a wind turbine," in *Proc. IEEE Power Energy Soc. General Meeting*, Jul. 2012, pp. 1–8.

[61] R. Živanović, "Evaluation of transmission line fault-locating techniques using variance-based sensitivity measures," in *Proc. 16th Power Syst. Comput. Conf.*, Jul. 2008, pp. 1–6.

[62] E. O. Schweitzer III and D. Hou, "Filtering requirements for distance relays," in *Proc. American Power Conf.*, Apr. 1993, pp. 296–301.

[63] J. Jiang, "Elevated neutral-to-earth voltage in distribution systems including harmonics," Ph.D. dissertation, Clemson University, Clemson, SC, Dec. 2006.

[64] J. Horak, "Zero sequence impedance of overhead transmission lines," in *Proc. 59th Annu. Conf. Protect. Relay Eng.*, Apr. 2006, pp. 1–11.

[65] A. Apostolov, D. Tholomier, S. Sambasivan, and S. Richards, "Protection of double circuit transmission lines," in *Proc. 60th Annu. Conf. Protect. Relay Eng.*, Mar. 2007, pp. 85–101.

[66] *SEL-251D Instruction Manual*, Schweitzer Engineering Laboratories, Washington, Pullman.

[67] *SEL-351A Protection System Instruction Manual*, Schweitzer Engineering Laboratories, Washington, Pullman.

[68] *SEL-351S Protection System Instruction Manual*, Schweitzer Engineering Laboratories, Washington, Pullman.

[69] R. Baldick, *Applied Optimization: Formulation and Algorithms for Engineering Systems*, 1st ed. Cambridge, England: Cambridge University Press, 2009.

[70] G. Lampley, "Fault detection and location on electrical distribution system," in *Proc. IEEE Rural Electric Power Conf.*, May 2002, pp. B1–1 – B1–5.

[71] E. Ebrahimi, A. J. Ghanizadeh, M. Rahmatian, and G. B. Gharehpetian, "Impact of distributed generation on fault locating methods in distribution networks," in *Proc. Int. Conf. Renewable Energies and Power Quality (ICREPQ'12)*, Spain, Mar. 2012, pp. 1–5.

[72] T. El-Fouly and C. Abbey, "On the compatibility of fault location approaches and distributed generation," in *Proc. CIGRE/IEEE PES Joint Symp. Integration of Wide-Scale Renewable Resources Into the Power Delivery Syst.*, Jul. 2009, pp. 1–5.

[73] *IEEE Standard for Interconnecting Distributed Resources with Electric Power Systems*, IEEE Std. 1547.2-2008, 2009.

[74] M. Aghaebrahimi, M. Amiri, and M. Moghaddam, "A short circuit study of an induction generator wind farm considering wind speed changes," in *Proc. 40th North American Power Symposium (NAPS)*, Sept. 2008, pp. 1–6.

[75] M. Papadopoulos, S. Papathanassiou, S. Tentzerakis, and N. Boulaxis, "Investigation of the flicker emission by grid connected wind turbines," in *Proc. 8th Int. Conf. Harmonics And Quality of Power*, vol. 2, Oct. 1998, pp. 1152–1157.

[76] E. Muljadi, N. Samaan, V. Gevorgian, J. Li, and S. Pasupulati, "Short circuit current contribution for different wind turbine generator types," in *Proc. IEEE Power Energy Soc. General Meeting*, Jul. 2010, pp. 1–8.

[77] W. D. Stevenson, Jr., *Elements of Power System Analysis*, 4th ed. McGraw Hill, 1982.

[78] T. A. Loehlein, "Calculating generator reactances," White Paper, Power Topic # 6008, Cummins Power Generation, 2006. [Online]. Available: http://www.cummins.co.kr/board/DATA/pt-6008%20Calculating%20generator%20reactances%20%28900-0292%29.pdf

[79] T. Ackermann, *Wind Power in Power Systems*, 2nd ed. John Wiley and Sons Ltd., 2012.

[80] S. Santoso and H. T. Le, "Fundamental time-domain wind turbine models for wind power studies," *Renewable Energy*, vol. 32, no. 14, pp. 2436–2452, Nov. 2007.

[81] *SEL-251-3 Instruction Manual*, Schweitzer Engineering Laboratories, Washington, Pullman.

[82] R. Horton, W. Sunderman, R. Arritt, and R. Dugan, "Effect of line modeling methods on neutral-to-earth voltage analysis of multi-grounded distribution feeders," in *Proc. IEEE/PES Power Syst. Conf. Expo. (PSCE)*, Mar. 2011, pp. 1–6.

[83] A. Deri, G. Tevan, A. Semlyen, and A. Castanheira, "The complex ground return plane a simplified model for homogeneous and multi-layer earth return," *IEEE Trans. Power App. Syst.*, vol. PAS-100, no. 8, pp. 3686–3693, Aug. 1981.

Vita

Swagata Das received her B.Tech degree in Electrical and Electronics Engineering from SRM University, India in May 2009 and the M.S.E and PhD degrees in Electrical Engineering from The University of Texas at Austin in May 2011 and 2015, respectively. Her research interests include power system protection, fault location, power quality, and smart grid technologies. In 2014, she became an Engineering-in-Training (EIT) in the state of Texas. During her studies, she has interned with Hubbell Power Systems, Baker Hughes, and Schweitzer Engineering Laboratories. She is currently working for Schweitzer Engineering Laboratories as an Associate Application Engineer (Protection).

Permanent address: swagata@utexas.edu

This dissertation was typeset with LaTeX[†] by the author.

[†]LaTeX is a document preparation system developed by Leslie Lamport as a special version of Donald Knuth's TeX Program.